Dynamics of groundwater flow in an unconfined aquifer

Adrien Guérin

▶ **To cite this version:**

Adrien Guérin. Dynamics of groundwater flow in an unconfined aquifer. Fluid mechanics [physics.class-ph]. Université Paris Diderot (Paris 7), Sorbonne Paris Cité, 2015. English. NNT : . tel-01884762

HAL Id: tel-01884762
https://hal.science/tel-01884762

Submitted on 1 Oct 2018

HAL is a multi-disciplinary open access archive for the deposit and dissemination of scientific research documents, whether they are published or not. The documents may come from teaching and research institutions in France or abroad, or from public or private research centers.

L'archive ouverte pluridisciplinaire **HAL**, est destinée au dépôt et à la diffusion de documents scientifiques de niveau recherche, publiés ou non, émanant des établissements d'enseignement et de recherche français ou étrangers, des laboratoires publics ou privés.

UNIVERSITÉ SORBONNE PARIS CITÉ

Thèse préparée
à l'UNIVERSITÉ PARIS DIDEROT
École doctorale STEP'UP – ED 560
IPGP–Laboratoire de Dynamique des Fluides Géologiques

Dynamique de l'écoulement dans un aquifère non confiné

par
Adrien Guérin

Thèse de doctorat de Sciences de la Terre et de l'Environnement
dirigée par Olivier Devauchelle & Éric Lajeunesse

présentée et soutenue publiquement le
23 Octobre 2015

devant le jury composé de :

Pascale Aussillous	Rapporteur
Tanguy Le Borgne	Rapporteur
Julien Bouchez	Examinateur
Ghislain de Marsily	Examinateur
Daniel H. Rothman	Examinateur
Olivier Devauchelle	Directeur de thèse
Éric Lajeunesse	Directeur de thèse

Remerciements

Tout d'abord, je tiens à remercier Olivier et Éric. Votre curiosité, votre enthousiasme, votre bonne humeur m'ont guidé tout au long de ces trois ans de thèse. Au tableau, en salle de manip ou en Guadeloupe, votre sens aigu de la critique ne s'est jamais départi de la volonté que ce travail soit avant tout un plaisir. Ce manuscrit est d'abord le fruit de ce plaisir, et j'en suis fier.

Ce travail a aussi beaucoup été influencé par François, le grand gourou de l'équipe géomorpho du DFG. J'ai beaucoup apprécié nos discussions, toujours stimulantes, autour d'un bon café ou d'une nouvelle manip, fraîchement montée sur un coin de table.

Le DFG est un laboratoire extrêmement chaleureux, où il fait bon être thésard. Je remercie tout particulièrement Angela, toujours disponible pour aider à trouver LA pièce qui manque pour finir une manip; et Hélène qui, outre son aide précieuse pour monter la manip, m'a appris à utiliser dans les règles de l'art quantité d'outils dont j'ignorais l'existence auparavant. Je pense également, bien sûr, aux amis thésards et post-doc avec qui j'ai partagé de nombreux bons moments, autour d'un café ou (parfois) d'une bière : Loïc, Pauline, Samuel, Anaïs, Alberto, Kenny, Céline, Clémentine, Gaurav, Hugo, Laure, Guillaume, Morgane, Grégoire, Navid, Gao, Maylis, Fanny...

Les missions en Guadeloupe ont à chaque fois été un immense plaisir, et je garderai un excellent souvenir des moments passés à la Maison de la forêt avec Thierry, Olivier ou Vincent, et de l'accueil toujours chaleureux à l'Obs. Les Lyonnais ont aussi contribué à pimenter ces missions (ainsi que la ratatouille) : Pascal, Philippe, Amélie, Vincent, Christophe. Je tiens également à remercier le Parc national de la Guadeloupe pour son soutien à nos travaux dans la Ravine Quiock.

J'ai eu la chance de faire un peu d'enseignement, et surtout la chance de les faire avec Alexandre et Édouard, qui ont tous les deux su me conseiller, mais aussi m'écouter. J'ai été heureux de faire partie, de manière éphémère, de cette TP team. La double (ou triple ?) correction restera comme un moment fort de ma thèse.

Je remercie chaleureusement Pascale Aussillous et Tanguy Le Borgne d'avoir rapporté ce manuscrit; et Julien Bouchez, Ghislain de Marsily et Dan Rothman d'avoir alimenté la soutenance de remarques constructives.

Un travail scientifique est aussi le fruit de nombreuses interactions. Je tiens ici à remercier toutes les personnes qui se sont intéressées à ma thèse et ont alimenté ma curiosité scientifique : Adrian Daerr, Christophe Josserand, François James, Patrick Meunier, Pierre-Yves Lagrée, Stéphanie Deboeuf.

Philippe Davy a été une source d'inspiration continue, depuis la prépa (et les voyages Sainte-Thérèse Beaulieu) jusqu'à maintenant. Il est à l'origine de mon goût pour les géosciences, et je lui suis infiniment reconnaissant de m'avoir guidé, tout au long de ces années, jusqu'ici.

Enfin, tout ceci n'aurait aucun sens sans la famille et les amis. Clément, les moments passés ensemble sont à chaque fois source d'inspiration et de motivation. Nos chemins se suivent et se ressemblent depuis un moment déjà, et j'espère que ce sera le cas pendant encore longtemps. Merci aux Lyonnais pour tous les week-ends et vacances passés en

votre compagnie, de Marseille ou Montpellier au Tadjikistan, en passant par Freiburg et Nantes : Mylène, Simon, Clémentine, Marion, Amélie, Fabian, Pauline, Elara et tous les autres. Merci à Pierre, mon ami de toujours, et à Hugo, Guillaume et PA, les trois autres “vieux Rennais”, d’être encore et toujours là. Après toutes ces années, vous comptez toujours autant.

Merci à mes parents, qui sont toujours là pour me soutenir et apprécier mes choix. Je veux aussi remercier ma belle-famille, qui m’a toujours accueilli à bras ouverts — Claude, vos observations conjointes du niveau de la Bézonde, de la mare et du puits ont été un soutien moral de poids.

Guillaume, tu es présent à chaque instant : merci d’être là. Je ne saurais comment faire sans toi, Florie, Lucien, et maintenant Siméon.

Lucie : je ne te dirai jamais assez combien ta présence est importante. Merci.

Contents

Introduction

Le cycle de l'eau est un acteur majeur de l'histoire de la Terre. Chaque année, plus de quatre cent mille kilomètres cubes d'eau s'évaporent des océans, dont un quart précipite ensuite à la surface des continents, sous forme de pluie ou de neige (figure 1, Rotaru et al. (2006)). Une partie de ces précipitations s'évapore à nouveau par l'évapotranspiration, et le reste se répartit en deux réservoirs principaux. La glace des calottes polaires et des glaciers représente environ 69% des stocks d'eau douce (Gleick, 1996). Le reste est essentiellement enfoui dans le sous-sol qui, lorsqu'il est suffisamment poreux et perméable, forme un aquifère.

Les aquifères représentent une ressource essentielle pour l'Homme, fournissant environ la moitié de l'eau potable sur Terre et 20% des eaux d'irrigation (Darnault, 2008). L'eau contenue dans les aquifères alimente aussi de nombreux écosystèmes (Le Maitre et al., 1999; Naumburg et al., 2005). Enfin, les aquifères alimentent les rivières, qui ne représentent que 0.6% des stocks d'eau douce, mais qui assurent l'essentiel des transferts

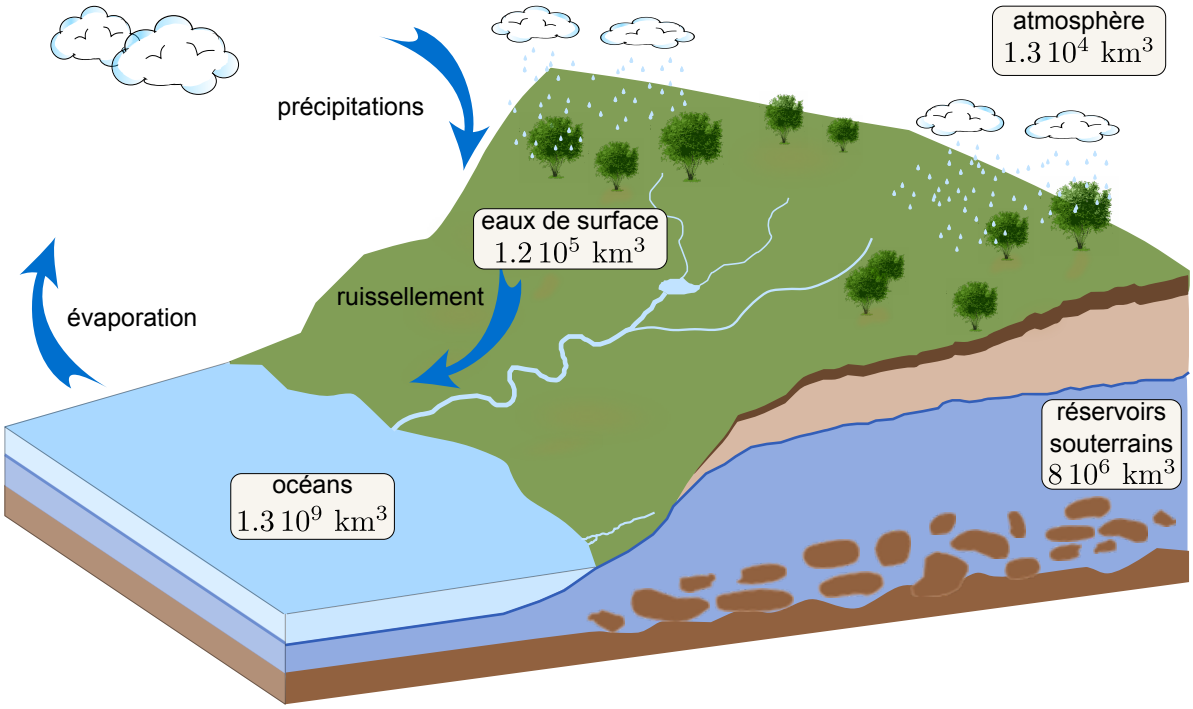

Figure 1: Le cycle de l'eau.

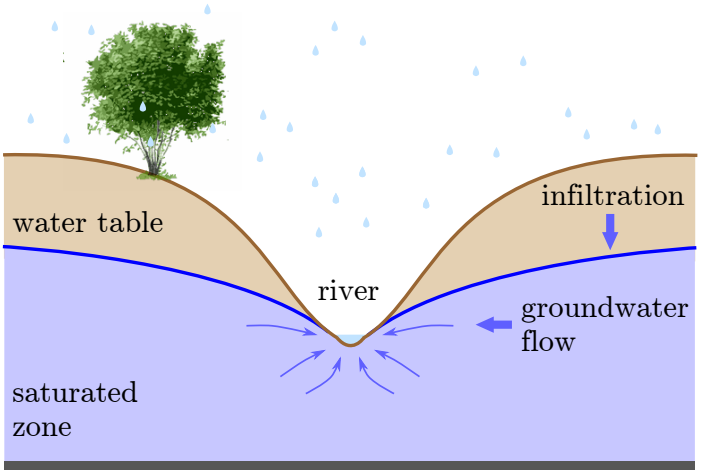

Figure 2: Une rivière est souvent la partie affleurant à la surface terrestre d'une nappe phréatique étendue dans tout le sous-sol environnant. Si la surface de la nappe est au-dessus de la rivière, la pression pousse l'eau souterraine vers la rivière.

d'eau, de minéraux dissous et de matières organiques (Maher and Chamberlain, 2014).

Lorsqu'une goutte de pluie atteint le sol, deux chemins s'offrent à elle. Si le sol n'est pas suffisamment perméable, elle reste à sa surface, et ruisselle pour s'écouler dans une rivière. Si le sol est suffisamment perméable, l'eau s'infiltre sous l'effet de la gravité, et alimente les aquifères. Les nappes phréatiques, situées à faible profondeur, ne sont pas confinées: leur surface supérieure (*water table*) est libre de s'adapter aux conditions de l'écoulement.

Lorsqu'une nappe est alimentée par la pluie, sa surface s'élève, la pression dans l'aquifère augmente, et l'eau s'écoule vers les zones de moindre pression. Là où la surface de la nappe s'élève suffisamment pour atteindre celle du sol, l'eau affleure et forme une rivière (figure 2). C'est ainsi que l'eau des nappes phréatiques rejoint le réseau de drainage qui l'entraîne vers les océans.

Les nappes phréatiques sont le théâtre de réactions chimiques qui altèrent les roches qui constituent l'aquifère. L'ensemble de ces réactions chimiques transforme les roches primaires en minéraux secondaires non solubles, en général des argiles, qui les remplacent pour former un sol mobile et propice à la végétation (Brantley and Lebedeva, 2011). Les ions dissous, quant à eux, sont emportés par les nappes phréatiques vers les rivières puis les océans, où ils précipitent et forment des roches sédimentaires (Gaillardet et al., 1999; Lloret et al., 2013).

Avant de précipiter au fond des océans, les minéraux solubles issus de l'altération sont déversés par les nappes phréatiques dans les rivières, sous forme d'ions. Ils représentent donc un moyen d'observer l'écoulement dans les nappes phréatiques. Pour mesurer la quantité de minéraux dissous dans une rivière, on mesure la conductivité électrique de l'eau, proportionnelle à sa concentration en ions. La figure 3 montre le débit et la conductivité de la rivière Bras-David (Guadeloupe) en fonction du temps, ainsi que le

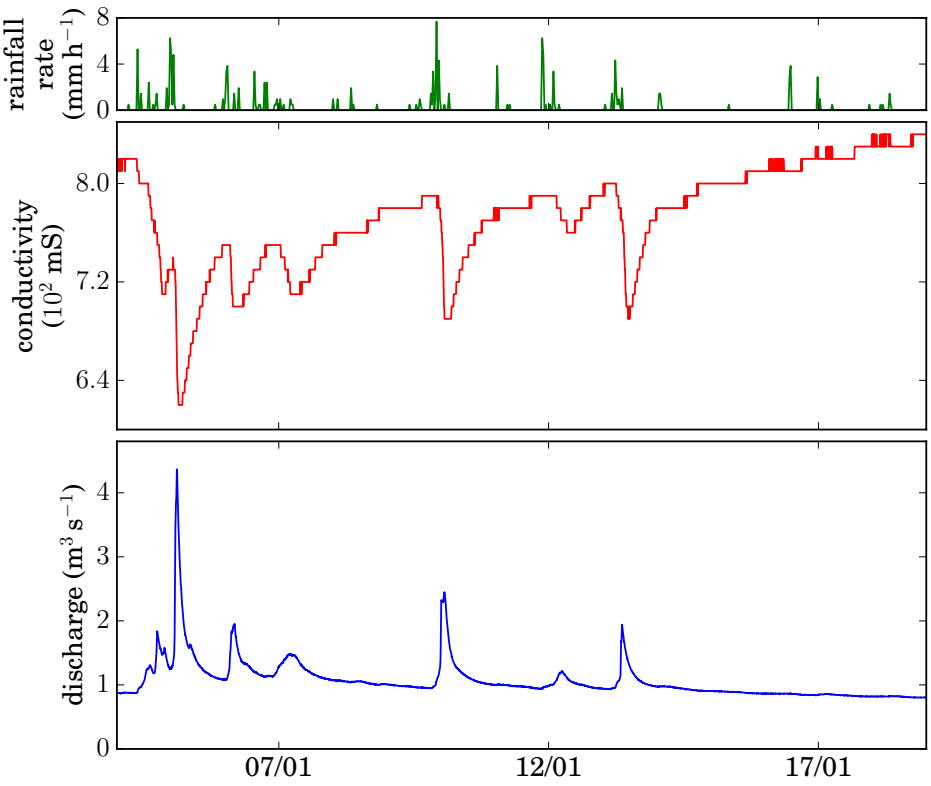

Figure 3: Taux de précipitations (—, *haut*), conductivité électrique (—, *milieu*), et débit (—, *bas*) de la rivière Bras-David (Guadeloupe), en Janvier 2014. La conductivité électrique croît avec la concentration en ions. Lorsque le débit de la rivière augmente, la conductivité diminue.

taux de précipitation. Lorsqu'il pleut, le débit de la rivière augmente, et la conductivité diminue rapidement. L'explication la plus simple attribue ces variations au ruissellement de surface, dont l'écoulement est beaucoup plus rapide que celui des nappes phréatiques. En effet, l'eau du ruissellement ne traverse pas la nappe, et ne se charge donc pas en éléments dissous. Le ruissellement, de faible concentration, dilue l'eau de la rivière, et la concentration de cette dernière diminue donc en période de crue (Johnson et al., 1969).

Cependant, dans la plupart des cas, les mesures de concentration en période de crue sont supérieures à la concentration attendue pour une simple dilution (Neal and Rosier, 1990; Kirchner et al., 2000). Cela signifie que l'eau de pluie, avant d'arriver dans la rivière, s'est écoulée dans la nappe et s'est chargée en ions (McDonnell, 1990; Kirchner, 2009). Des transferts rapides ont donc lieu au sein des nappes phréatiques, ce qui leur permet de délivrer aux rivières des quantités d'ions importantes lors des crues.

L'origine physique ou chimique de cette surprenante rapidité demeure débattue à l'heure actuelle (Kirchner, 2003; McDonnell, 2003). D'une part, il s'agit d'évaluer la vitesse des réactions d'altération (Maher, 2010). Celles-ci peuvent-elles être suffisamment rapides pour expliquer la grande concentration en ions observée dans les rivières en temps de crue ? D'autre part, il s'agit d'évaluer la vitesse et la dynamique des écoulements souterrains. Les nappes phréatiques peuvent-elles réagir suffisamment rapidement à la pluie pour augmenter de manière significative le débit, et donc la quantité d'ions délivrés à la rivière en temps de crue ?

Dans cette thèse, nous nous intéresserons à la dynamique des écoulements dans les nappes phréatiques, et à l'influence de cette dynamique sur le débit des rivières. Lorsqu'il pleut, la surface d'une nappe phréatique s'élève, ce qui augmente la pression au sein de la nappe et entraîne une augmentation du débit délivré aux rivières (Sophocleous, 2002; Bresciani et al., 2014). Lorsqu'il ne pleut plus, l'aquifère se vide lentement, la surface de la nappe décroît progressivement, et avec elle le débit de la rivière qu'elle alimente (Troch et al., 1993; Chapman, 2003; Troch et al., 2013).

Comme les écoulements en milieu poreux sont lents, une nappe continue d'alimenter sa rivière longtemps après la fin de la pluie, maintenant ainsi son débit d'étiage (*drought flow*). Ce mécanisme a fait l'objet de nombreuses études (Ibrahim and Brutsaert, 1965; Sanford et al., 1993; Brutsaert and Nieber, 1977; Szilagyi and Parlange, 1998; Brutsaert and Lopez, 1998). En revanche, le comportement d'une nappe et de sa surface libre en réaction à la pluie est bien moins documenté (Beven, 1981; Pauwels and Troch, 2010). Ce manuscrit sera majoritairement consacré à la réponse rapide d'une nappe phréatique à un événement de pluie. Nous focaliserons notamment notre attention sur le début de cette réponse transitoire (régime asymptotique). Dans ce but, notre approche consistera à simplifier le système au maximum. Cette simplification nous permettra d'élaborer un modèle analytique, que nous testerons dans une expérience de laboratoire. Une fois validé en laboratoire, nous pourrons ensuite évaluer la pertinence de ce modèle et tester ses prédictions dans des aquifères naturels, plus complexes.

Le manuscrit s'organisera autour de quatre parties. Nous présenterons tout d'abord un état des connaissances sur les écoulements souterrains (partie I). Le chapitre 1

présentera, de manière générale, les modèles actuels, essentiellement numériques. Dans le chapitre 2, nous présenterons, de manière plus spécifique, comment le problème peut être traité analytiquement et expérimentalement. Dans une deuxième partie, nous montrerons comment une nappe phréatique génère une crue (partie II). Pour cela, nous travaillerons dans le cadre de l'approximation de Dupuit-Boussinesq, qui permet de réduire la description de notre écoulement souterrain à une seule dimension (approximation de l'eau peu profonde). Nous comparerons notamment un régime asymptotique de montée de crue, dérivé de la théorie de Dupuit-Boussinesq, aux résultats d'une expérience de laboratoire (chapitre 3). Dans une troisième partie, nous présenterons une expérience de terrain destinée à identifier ces régimes dans un petit bassin versant (partie III). Nous vérifierons tout d'abord que la nappe se comporte bien, qualitativement, comme dans notre expérience de laboratoire (chapitre 4). Nous présenterons ensuite plusieurs méthodes pour évaluer les caractéristiques hydrauliques de l'aquifère (chapitre 5). Nous analyserons enfin la dynamique du débit de la rivière à l'aide de régimes asymptotiques dérivés de la théorie de Dupuit-Boussinesq (chapitre 6). Nous comparerons enfin ces régimes asymptotiques à des hydrographes d'autres bassins versants (chapitre 7). Enfin, la dernière partie montrera comment la théorie de Dupuit-Boussinesq peut être mise en défaut, même dans une géométrie simple (partie IV, chapitre 8).

Part I

State of the art

Chapter 1

Groundwater flows

Contents

This manuscript is devoted to the dynamics of groundwater flow. The present chapter attempts to present how groundwater flow is modelled in the hydrogeology literature. Through their storage capacities, aquifers act as filters between the rainfall signal and its output as streamflow. Lumped-parameter models reduce this filter to a single-valued function, generally relating the discharge delivered by the aquifer to the volume of water stored in the aquifer. Yet, this filter can also be described on a physical basis, and distributed models attempt to simulate the flow continuously within the whole aquifer. Distributed models reproduce reality more accurately, but are more time-consuming than lumped-parameter models.

1.1 Aquifers as filtering reservoirs: lumped-parameter models

1.1.1 Storage-Discharge relationships

Lumped-parameter models consider an aquifer as a black box, which transforms an input signal (as rainfall) into an output signal (as the river discharge). They are generally used to study large-scale processes, such as the response of large aquifers to climatic change, or the influence of pumping or dams on groundwater sustainability. In these models, the aquifer is a module among others, such as vegetation, overland flow or climate. As an example, the Hydrologiska Byråns Vattenbalansavdelning (HBV) model (Bergström et al., 1995) has allowed to study the impact of snowmelt on a stream discharge in Turkey, or the impact of climatic change on river flooding in a small river in France (Şorman et al., 2009; Booij, 2005).

As they attempt to simulate numerous complex processes at the same time, lumped-parameter models must reduce these processes to simple behaviours. The aquifer module is generally used to assess groundwater sustainability through the volume S of water stored in the aquifer, and the discharge Q delivered to the river. The simplest way to estimate both is to relate them with a single function:

$$Q = f(S)\,. \tag{1.1}$$

The function f varies according to the different models, but is often a power law.

An exponent of one simply models the aquifer as a linear reservoir (Alcamo et al., 2003; Döll et al., 2003). However, this linear representation of an aquifer is generally not satisfactory (Tallaksen, 1995). Lindström et al. (1997) or Kirchner (2009) thus propose to represent the function f with a general power law

$$Q = k\,S^n\,, \tag{1.2}$$

where k and the exponent n are fitting parameters, characterising the aquifer. Chapman (1999) adds further complexity, and proposes to separate the groundwater reservoir into two reservoirs: a shallow storage S_s and a deep storage S_d. This separation into two reservoirs is supposed to reflect the variations of the hydraulic properties with depth. The discharge is then the sum of the shallow discharge $Q_s = k_s\,S_s$ and of the deep discharge $Q_d = k_d\,(S_s + S_d)$. Tallaksen (1995) finally states that the exponent itself could also depend on the storage:

$$Q = k\,S^{1+\alpha\,S}\,, \tag{1.3}$$

where α is a fitting parameter.

Tallaksen (1995), in a review of drought flow analysis, lists all the functions proposed to relate Q and S. However, Chapman (1999) argues that these storage-discharge relationships do not give full satisfaction during rainfall events. Finally, Sloan (2000) observes hysteretic behaviours between the discharge and the storage of an aquifer, and shows that a single-valued storage-discharge function cannot reproduce such behaviours.

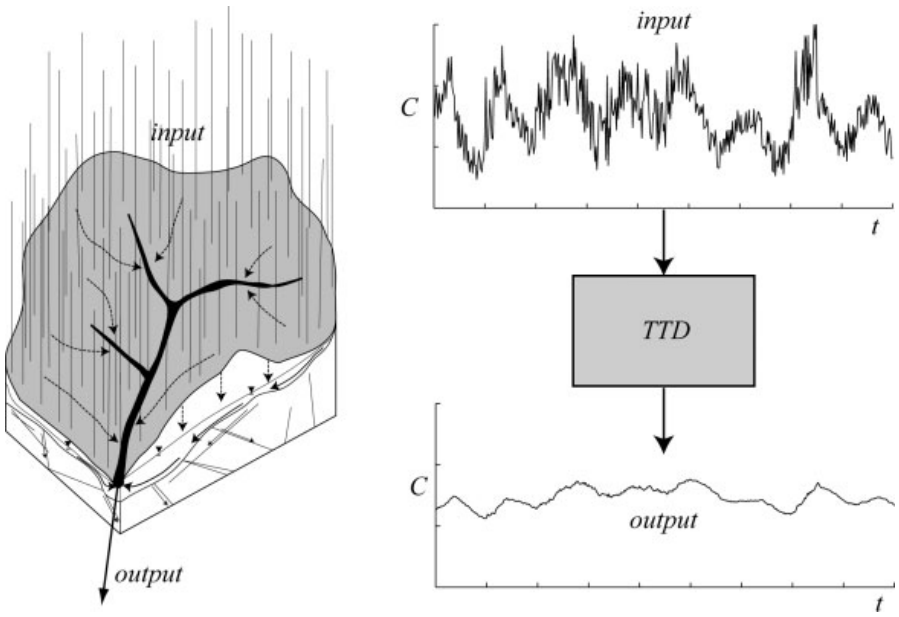

Figure 1.1: Illustration of a catchment as a filter, which receives and processes an input signal (rainfall, but also chemicals), and delivers an output signal into a stream.

1.1.2 Transit-time models

The transit-time distribution is another way to represent the flow within an aquifer (figure 1.1). The transit (or residence) time is defined as the time water spends flowing within an aquifer, from the moment it enters the aquifer to the moment it exits the aquifer, generally into a river (McDonnell et al., 2010). The transit time of a water droplet thus depends on its distance to the river when it enters the aquifer. The area drained by the river defines the catchment. The latter is characterised by a spatial distribution of distinct transit times. These transit times depend on many factors such as the permeability or the geology of the aquifer. A catchment can thus be represented by a transit time distribution, which provides important information to describe its filtering process.

Three generic distributions are usually used to represent the transit-time distribution of a catchment (McGuire and McDonnell, 2006). The simplest one, called the piston-flow model, considers that the flow pathways to the river all have the same velocity and path length. The distribution thus consists of a single transit time, calculated as the ratio of the catchment storage over its outflow discharge. This model is rather unrealistic (McGuire and McDonnell, 2006).

The exponential model simply uses an exponential distribution of transit times. Haitjema (1995) shows that this distribution can be inferred from a physical description of the groundwater flow, in the specific case where the shallow water (or Dupuit-Boussinesq) approximation holds, and where the Dupuit-Boussinesq equation can be linearised (see chapter 2, section 2.3).

The third common model is the dispersion model, inferred from the one-dimensional advection-dispersion equation (Kreft and Zuber, 1978; Małoszewski and Zuber, 1982).

Yet, this solution assumes a unique flow path. Integrating spatially this solution over all the pathways of the catchment, this model can account for fractal distributions of chemical tracers, suggesting a fractal distribution of flow paths (Kirchner et al., 2000, 2001).

These three transit-time distributions are generally used in lumped-parameter models. For example, McGuire et al. (2005) analyse the composition of $\delta^{18}O$ as an age tracer for water, and use these models to fit their data. As a result, these fits yield the mean residence time in the catchment. Comparing their results on seven different catchments, McGuire et al. (2005) find that the exponential model yields the best results.

Most transit time distribution models are based on a common assumption: linearity. In addition to provide simple transit time distributions, linearity allows frequency-domain analyses, and defines a mean residence time. Yet, Cardenas (2007) shows that the full resolution of the two-dimensional flow equations also results in a power-law distribution. Power-law distributions are not associated with any mean or characteristic residence time (McGuire et al., 2005). In the previous section, we also noted that the assumption of linear reservoirs is generally not satisfactory, and would deserve further evaluation (Tallaksen, 1995). For this purpose, we must describe physically the groundwater flow.

1.2 Flow in a porous aquifer

To understand the groundwater flow, we must first describe its reservoirs.

1.2.1 Groundwater reservoirs

A great variety of rocks constitute Earth's surface, which thus presents varied landscapes. All areas of Earth have their own history, yet most share the ability to store water. An underground permeable layer of rock which contains water is called an aquifer. The storage capacity of an aquifer depends on the properties of the rock. For instance, the ground near Plœmeur, Brittany, was studied to better understand the flow in underground fracture networks (Le Borgne et al., 2004, 2006b). The igneous and metamorphic rocks composing this aquifer are referred to as crystalline rocks, because they are highly impermeable. A very productive source yet reveals significant groundwater storage (Le Borgne et al., 2006a). In this specific case, groundwater infiltrates into fractures between blocks of impervious rocks. At the other end of the spectrum, the Apalachicola Bluffs and Ravine Preserve, located in North Florida, present ramified stream networks which shape could be related to groundwater flow (Petroff et al., 2011; Devauchelle et al., 2012; Petroff et al., 2013). The ground is composed of a rather homogeneous quartz sand. It is obviously porous and permeable to water (Devauchelle et al., 2011). The geology of these two sites is different, yet both contain groundwater.

The capacity of an aquifer to store water is primarily controlled by its porosity s, defined as the volume V_{void} of voids contained in a given volume V_{tot} of solid:

Type of rock	Porosity
Unaltered granite and gneiss	$0.02 - 1.8\%$
Quartzite	0.8%
Shales, slates, mica-shists	$0.5 - 7.5\%$
Limestones, primary dolomites	$0.5 - 12.5\%$
Secondary dolomites	$10 - 30\%$
Chalk	$8 - 37\%$
Sandstones	$3.5 - 38\%$
Volcanic tuff	$30 - 40\%$
Sands	$15 - 48\%$
Clays	$44 - 53\%$
Swelling clays, silt	Up to 90%
Tilled arable soils	$45 - 65\%$

Table 1.1: Typical porosity of several types of rocks and granular materials. Fractures are not taken into account, and can significantly increase the porosity in some cases. Table reproduced from De Marsily (1986).

$$s = \frac{V_{\text{void}}}{V_{\text{tot}}} \,. \tag{1.4}$$

By definition, the porosity ranges between zero and one. Its value varies significantly from one aquifer to another (figure 1.2). As an example, the random packing of perfect spheres with uniform size has a porosity of about $s \simeq 0.4$ (Andreotti et al., 2012). In sand aquifers, which generally have a non-uniform grain-size distribution, the small grains fill the pores between larger grains, and consequently the volume of void decreases (figure 1.2b): sand aquifers have a porosity of the order of a few dozens of per cent (De Marsily, 1986). In fractured aquifers, where the ground is made of large blocks of rock, the porosity can be due to both the porosity of the rock itself, and to the fractures between the rocks (figure 1.2c). Depending on the porosity of the rocks, the number and the volume of the fractures, the porosity can be as low as a few per cent, or even lower (Halley and Schmoker, 1983; De Marsily, 1986; Andermann et al., 2012). Table 1.1 lists the typical porosity of several types of rocks and granular materials.

As a consequence of this porosity, the ground can store water. In general, we define three zones of groundwater storage (De Marsily, 1986). Near the surface, the vadose zone is unsaturated: it contains both water and air (figure 1.3). The water content progressively increases with depth, until the ground becomes fully saturated. Under the vadose zone, two distinct layers form the saturated zone. The capillary fringe defines the upper layer, in which surface tension lowers the water pressure below atmospheric pressure (Abdul and Gillham, 1984). Under the capillary fringe, the phreatic zone is saturated with water, and its pressure is higher than atmospheric pressure. The virtual

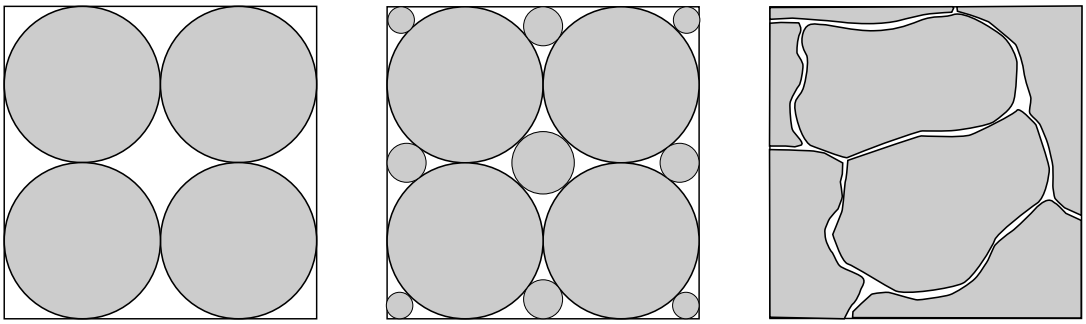

(a) (b) (c)

Figure 1.2: Influence of the grain-size distribution and grain shape on an aquifer porosity. *(a):* Packing of monodisperse spheres. *(b):* Packing of polydisperse spheres. The small grains fill the pores between larger grains, and the resulting porosity is lower. *(c):* Fractured aquifer.

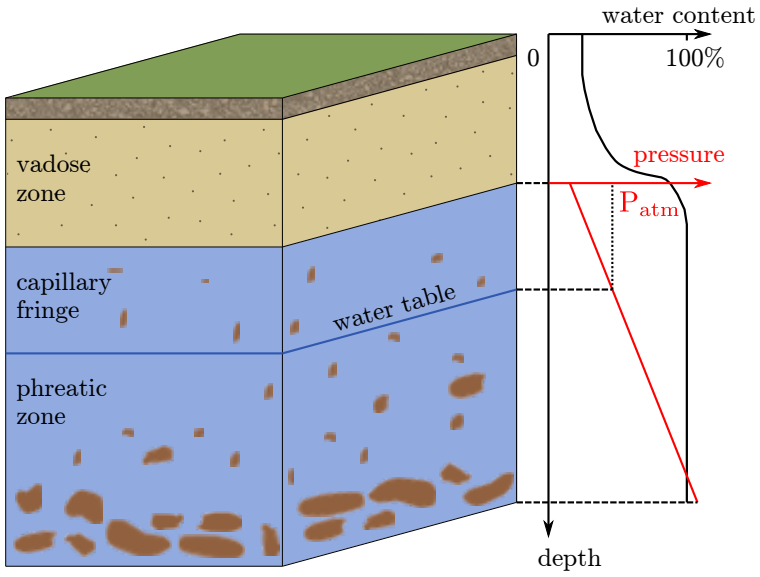

Figure 1.3: The three groundwater reservoirs. The vadose zone is not saturated, the capillary fringe is saturated and at "negative pressures" (less than atmospheric), and below the water table the ground is saturated and at "positive" pressures.

surface at which the water pressure is atmospheric is the water table.

Both the vadose zone and the capillary fringe are dominated by surface tension. In the vadose zone, surface tension causes part of the water to adhere to the walls of the rocks, inducing spatial and temporal variations of water content. In the saturated zone, the capillary rise of water is due to surface tension. According to Jurin's law, the smaller the size of the pores in the ground, the higher the capillary fringe (Guyon et al., 2001). In a layer of clay, the capillary fringe may be as high as a few metres (Polubarinova-Kochina, 1962). In sand, where the pore size is larger, the capillary rise is of the order of a few centimetres.

Surface tension induces problems of wetting and of hysteresis, and is sensitive to the geometry of the pores (de Gennes et al., 2002; Marchand et al., 2011; Snoeijer and Andreotti, 2013). Its consequences are uneasy to quantify. Richards (1931) and Brutsaert (1968) described the vertical flow of water within the unsaturated zone with Darcy's law (see next section), and a permeability which depends on the water content. This approach is equivalent to treating the unsaturated zone as a saturated zone of varying permeability. Parlange and Brutsaert (1987) estimate the influence of such flow on the drainage of an initially saturated aquifer. Chapman (2003) assumes that the unsaturated zone drains as a linear reservoir, and estimates its influence on the flow in the saturated zone. Finally, Abdul and Gillham (1984) investigate experimentally the effects of the capillary fringe on streamflow generation, and conclude that a large capillary fringe may accelerate streamflow generation.

Under the water table, water is moved by the combined action of pressure and gravity. In the next section, we will describe more precisely the mechanisms which drive the motion of a fluid in a saturated porous material, when surface tension can be neglected.

1.2.2 Fluid motion in a saturated porous material

Darcy (1856) was the first to investigate the flow of a fluid through a porous material, with an experiment represented in figure 1.4. In his experiment, water flows steadily through a column of sand. The water pressure is imposed at both ends of the column, and measured as a water height ΔH, also called pressure head. Measuring the discharge Q flowing out of the column, Darcy observed that it is proportional to the pressure head and inversely proportional to the length L of the column:

$$Q = K\,S\,\frac{\Delta H}{L}, \tag{1.5}$$

where S is the section of the column and K is the proportionality coefficient. This proportionality coefficient, expressed in $\mathrm{m\,s^{-1}}$, is the hydraulic conductivity of the porous material. It depends on the material properties, but also on the fluid properties.

The empirical result (1.5) obtained by Darcy is very robust. It has been generalised to three-dimensional flows:

$$\mathbf{q} = -\frac{k}{\eta}\,(\nabla p - \rho\,\mathbf{g}), \tag{1.6}$$

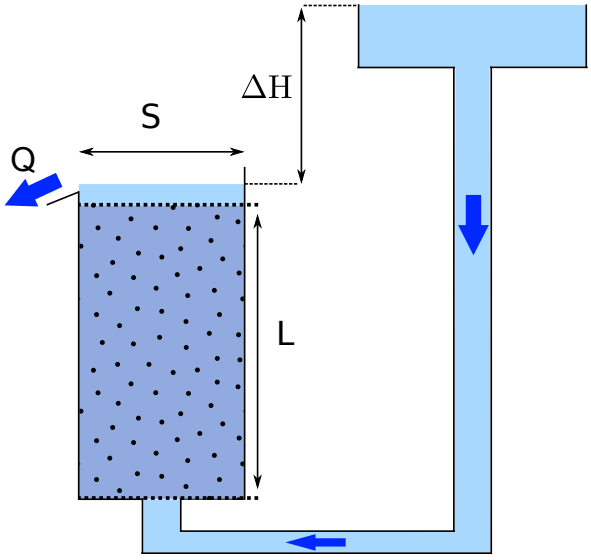

Figure 1.4: Darcy experiment. The discharge Q is proportional to the pressure head ΔH.

where η is the dynamic viscosity of the fluid, P is the pressure, ρ is the density of the fluid, and $\mathbf{g}$ is the acceleration of gravity. Here, $\mathbf{q}$ is the specific flux, or discharge per unit area. It has the dimensions of a velocity, but is not equal to the actual velocity $\mathbf{v}$ of the fluid. Because only a fraction of the total volume is available for the flow, the specific flux is lower than the actual velocity of the fluid within the pores. Both are related through the porosity s of the material: $\mathbf{q} = s\,\mathbf{v}$. Finally, the proportionality coefficient k is the permeability of the porous medium. With the dimension of a surface (m^2), it characterises the geometry of the porous material only, and is roughly proportional to the square size of the pores, and to porosity (Guyon et al., 2001). It is related to the hydraulic conductivity K through the following relationship:

$$K = \frac{k\,\rho\,g}{\eta}. \tag{1.7}$$

Several limitations hinder the validity of Darcy's law (1.6). First, it is valid only for laminar flows. When the Reynolds number increases beyond order one, the discharge deviates from its linear relationship with the pressure gradient (Brutsaert, 2005). Second, equation (1.6) only concerns isotropic materials. Some porous materials, made of lamellar grains for example, may exhibit preferential directions (Dagan, 1967). When this is the case, the permeability is a 3D tensor which takes into account anisotropy.

Natural aquifers provide several examples where Darcy's law is not valid. In karstic aquifers, water flows within cavities as large as a few metres, such that the flow is not laminar (Aquilina et al., 2006). In fractured aquifers, some fractures may also be so large that the Reynold's number would increase beyond the limit of validity of Darcy's law (Long et al., 1982; Renard and De Marsily, 1997). In some regions, fractures are oriented preferentially in a specific direction, and the aquifer is not isotropic (Neuman et al., 1984).

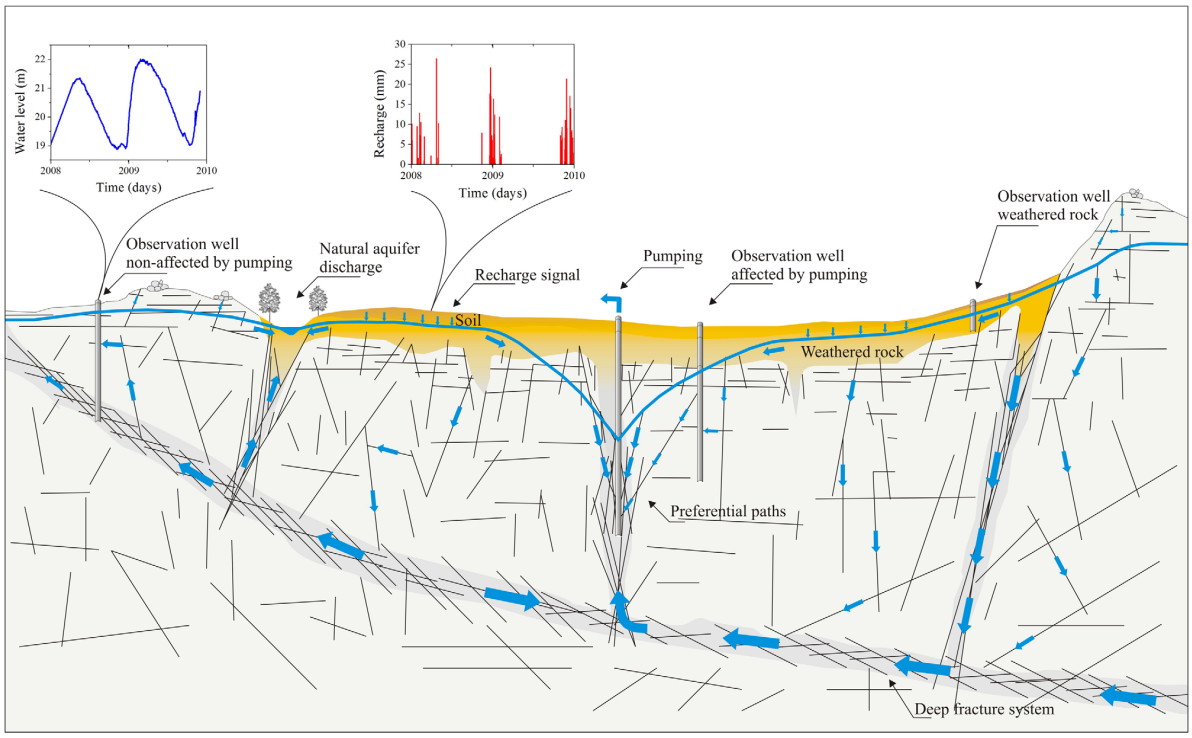

Figure 1.5: Conceptual scheme of a fractured aquifer. Fracture networks are characterized by a multi-scale heterogeneity. Arrow size represents the relative contribution to the flow of the different structures. From Jiménez-Martínez et al. (2013).

In the next section, we briefly present how one can model the groundwater flow within fractured aquifers.

1.2.3 Flow inside fractures

Fractured aquifers are composed of large blocks of impermeable rocks, separated by a network of interconnected fractures (figure 1.5). The scale of these fractures can be highly variable, even within a single aquifer. Inferring general hydraulic properties from such aquifers therefore raises difficulties. The multi-scale nature of fractures networks in fractured aquifer induces strong heterogeneities (Davy et al., 2006). Modelling the consequently heterogeneous flow field generally requires statistical and numerical methods (Berkowitz et al., 2006; Le Borgne et al., 2008). As an example, the software MPFRAC (see on the platform H2OLAB[1]) is devoted to stochastic simulations of groundwater flow into fractured aquifers (Le Goc, 2009; Erhel et al., 2009). It simulates a random network of fractures (with given properties, such as a fracture-length distribution), and then simulating the flow within these fractures.

Yet, numerous studies try to simplify these highly heterogeneous structures, looking for equivalences with classical porous media. One can thus define an equivalent permeability, and study how it is influenced by the distribution of fractures scales (de Dreuzy

[1] `http://h2olab.inria.fr/`

et al., 2004; Davy et al., 2006). Within this approach, one focuses on the average properties of the flow (Le Borgne et al., 2004).

The average properties are then often modelled with lumped-parameter models. The simplest one is to model the aquifer as a linear reservoir (Gelhar, 1993). A second model is the Dupuit model, based on the theory of flow into porous media (linearised Dupuit-Boussinesq equation, see section 2.3) (Jiménez-Martínez et al., 2013). A third class of models, called combined model, considers two flow components: a rapid flow component corresponding to a shallow reservoir, and a linear or Dupuit model describing the contribution of a deep reservoir (Molenat et al., 1999; Trinchero et al., 2011).

The hydrological properties of fractured aquifers are often studied with frequency domain analysis and transfer functions (Gelhar, 1986; Molenat et al., 1999; Jiménez-Martínez et al., 2013). This method assumes a linear relationship between the input and the output.

Porous media are simpler to cope with, because one can model the flow continuously.

1.3 Groundwater flow in a homogeneous aquifer

As opposed to fractured aquifer, classical porous aquifers are composed of a large amount of small grains of rock, like a granular material at rest. These aquifers are simpler to cope with, because one can model the flow continuously at the scale of the aquifer.

1.3.1 Laplace equation

Unconfined aquifers generally present a thickness of several metres. At this scale, we consider water as incompressible. As a consequence, continuity ensures that the divergence of the velocity $\mathbf{q}$ vanishes:

$$\nabla \cdot \mathbf{q} = 0 \,. \tag{1.8}$$

Combined with Darcy's law (1.6), the continuity equation induces that there exists a scalar field ϕ, the velocity potential, which satisfies the Laplace equation

$$\nabla^2 \phi = 0 \,, \tag{1.9}$$

where ∇^2 refers to the the Laplace operator. Stemming from Darcy's law (1.6), the velocity potential reads

$$\phi = \frac{p}{\rho\, g} + y \,, \tag{1.10}$$

where y is the vertical coordinate oriented upwards. In the hydrogeology literature, the velocity potential is often referred to as the hydraulic head h.

The Laplace equation (1.9) has been largely studied, in many different fields of physics. As a non exhaustive list of examples:

- In the absence of electric charges, the electric field **E** satisfies the Laplace equation. Around a point charge for example, the solution to the Laplace equation is inversely proportional to the radius r squared:

$$E \sim 1/r^2 \,. \tag{1.11}$$

- The temperature in a heat conductor and in steady state satisfies the Laplace equation. For example, let's consider a 1D conducting rod thermally isolated, which extremities temperatures are T_1 in $x = 0$ and T_2 in $x = L$. The Laplace equation results in a linear temperature field:

$$T(x) = T_1 + (T_2 - T_1)\,\frac{x}{L} \,. \tag{1.12}$$

- The velocity potential of a viscous fluid flowing between two closely spaced plates (Hele-Shaw cell) satisfies the Laplace equation. When a viscous fluid pushes a more viscous fluid, the laplacian potentials of the two fluids interact with each other. This interaction acts on the fluids interface, which can deform into a wide range of shapes, from fingers to fractals (Saffman and Taylor, 1958; Arneodo et al., 1989; Lajeunesse and Couder, 2000).

These three examples, in which the Laplace equation leads to entirely different results, only differ by their boundary conditions.

Natural aquifers offer a wide range of different boundary conditions, yet one usually classifies aquifers into two types:

- when the upper surface of the saturated zone is bounded by an impermeable layer, the aquifer is referred to as *artesian* — or confined. Confined aquifers typically lie deep into the ground. Because of their confinement, artesian aquifers respond linearly to changes in pressure — according to Darcy's law.

- when the upper surface of the saturated zone is connected to the atmosphere through the pores of the vadose zone (as in figure 1.3), the aquifer is said to be *unconfined*. Contrary to confined aquifers, the upper surface of unconfined aquifers is not fixed by any physical boundary, and adapts its shape to the flow conditions. The water table acts therefore as a free surface. Being a free surface, the water table possibly induces non-linear behaviours.

In this manuscript, we focus on unconfined aquifers. As rainwater infiltrates into the aquifer, the water table rises to accommodate more water, until it reaches a drain — generally a river or a spring. Moved by pressure gradients, groundwater then flows towards the river. The aquifer progressively empties, until it receives rainwater again. The rainfall fluctuations thus induce variations in the groundwater flow, which in turn cause variations of the river discharge. To study these fluctuations, we must solve the Laplace equation for the velocity potential.

Figure 1.6 represents the groundwater flow and its boundaries in a typical unconfined aquifer. Hereafter, we describe these boundaries.

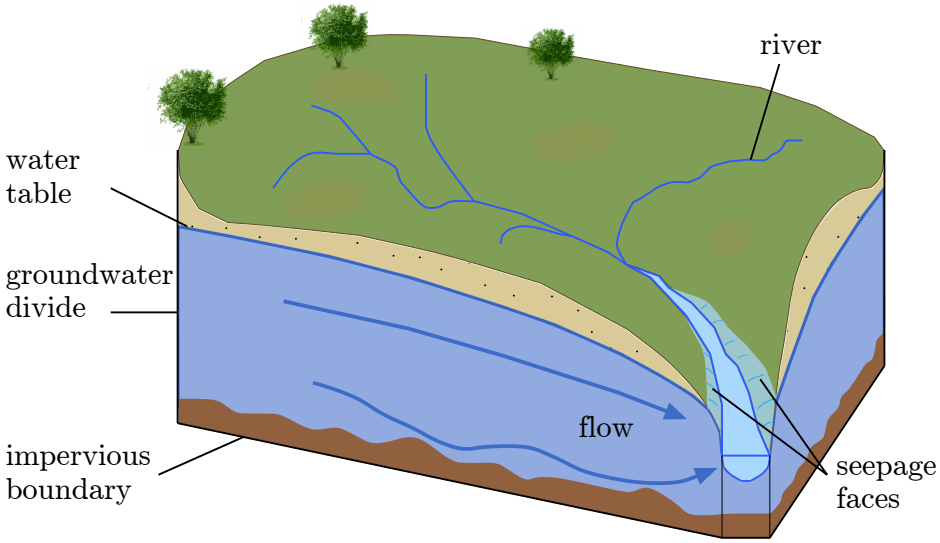

Figure 1.6: Three-dimensional unconfined aquifer. Five boundaries delimit the groundwater flow towards the river: the water table, the water divide, the river, the seepage face and the bottom.

Groundwater divide. The area drained by the river is coloured in green. It is called a catchment (or watershed). This area is delimited by the groundwater divide: outside of this limit, groundwater flows towards another river. If we call $\mathbf{n}$ the unit vector normal to the water divide, this condition formally reads

$$\partial_n \phi = 0\,. \tag{1.13}$$

The location and shape of the groundwater divide mainly depend on the shapes of the river network and of the adjacent rivers. However, in general, the groundwater divide is distinct from the topographic divide (Haitjema and Mitchell-Bruker, 2005). Figure 1.7 illustrates this distinction. In a symmetric system, where the water table connects two similar rivers at the same altitude, the ground elevation is likely to be similar to the water table shape. In contrast, when the system is not symmetric, their shapes can differ considerably. In practice, it is often difficult to determine the position of the groundwater divide. It is underground, it can vary in time, and two-dimensional effects can even induce non-vertical groundwater divides (see figure 8.1). Due to these difficulties, this problem is often neglected, and one often assimilates topography and groundwater divides to estimate drainage areas (see sections 7.1 and 7.2).

Impermeable bottom. At the bottom, the flow is generally bounded by an impermeable layer — although this bottom is not always well-defined. In some cases, the permeability progressively decreases with depth, and the transition from the permeable aquifer to the impermeable bottom is smooth (Godsey et al., 2009). Sometimes this transition is even considered to occur at infinite depth (Goderniaux et al., 2013). For the sake of simplicity, we consider that a sharp interface separates the aquifer, of

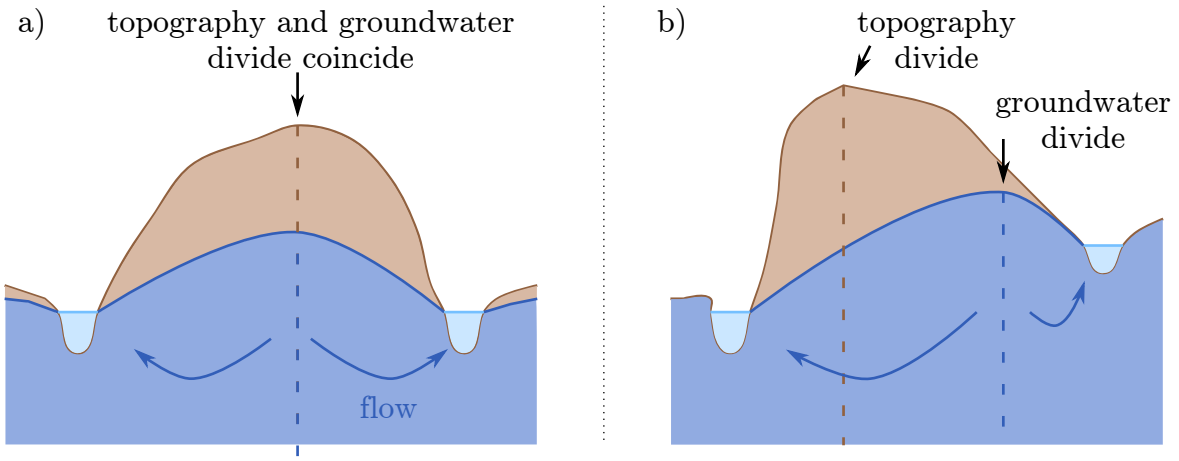

Figure 1.7: Difference between topography (or water) divide and groundwater divide. *a)* In a symmetric system, the topography approximately reflects the water table shape. *b)* In an asymmetric system, the water table and the topography differ considerably.

homogeneous permeability, from its impermeable bottom. The flow cannot cross this boundary, which formally reads

$$\partial_n \phi = 0\,. \tag{1.14}$$

Free surface. The water table, being a free surface, concentrates the difficulties of our problem. In particular, its moving location makes the flow time-dependent and non-linear (figure 1.6). This situation, referred to as a Stefan problem, requires two boundary conditions for a free boundary. Here, the first condition is that the water table must accommodate rainwater. The mass balance describes its evolution:

$$(s\,\partial_t h - R)\,n_y = K\,\nabla\phi \cdot \mathbf{n}\,. \tag{1.15}$$

Here, R denotes the rainfall rate, h the water table elevation, $\mathbf{n}$ the unit vector perpendicular to the water table, and n_y its vertical component. We chose to note y the vertical coordinate, oriented upwards. A single condition is not sufficient to determine a free surface, and this mass balance must be supplemented with the condition that the water table must be at atmospheric pressure. For the velocity potential, this condition formally reads

$$\phi = h \quad \text{on the free surface.} \tag{1.16}$$

Seepage face. When the water table rises sufficiently high, it may reach the ground surface (see figure 2.2). In this case, water simply flows over the surface, following its topography. The water table therefore adopts the shape of the Earth surface: it is not a free surface any more. This fixed surface, called a seepage face, must satisfy the atmospheric pressure condition only:

$$\phi = h \quad \text{on the seepage face.} \tag{1.17}$$

Drainage network. Finally, groundwater flows towards a network of channels. Along this network, the river imposes its pressure to the groundwater flow, exactly as the atmosphere imposes its pressure to the seepage face. As the other boundaries, the river network imposes its shape to the groundwater flow. Recent studies suggest that the geometry of a river network, in turn, is sometimes determined by the groundwater flow field, through seepage erosion (Devauchelle et al., 2012; Petroff et al., 2013).

Due to these boundary conditions, the flow in a natural aquifer depends on many factors, among which: the ground elevation, the shape of the river network, the shape of the other boundaries such as the water divide or the impervious bottom. Taking into account all the parameters which uniquely determine the groundwater flow in a specific aquifer requires numerical models. We now briefly present these models, often referred to as distributed models.

1.3.2 Distributed models

Even in numerical methods, the free surface causes major difficulties. It is non-linear, and contains the time-dependency of the problem. Several simplifications allow to tackle the problem analytically, under simplified conditions — this is the subject of the present manuscript. However, to account for more realistic conditions, one generally resorts to numerical models. However, even numerical models require simplifications, which vary according to the desiderata of the study. On the one hand, some models take full account of the non-linearity of the free-surface condition — but they let aside the time-dependency. On the other hand, some models allow to study the transients properties of a groundwater flow — often requiring some linearisation of the free surface condition. Hereafter, we attempt to establish a list of numerical methods used to solve this problem, classifying them based on the simplifications they adopt.

Transient, Dupuit-Boussinesq approximation. Very popular in hydrogeology, the Dupuit-Boussinesq (or shallow-water) approximation assumes that the flow is parallel to the aquifer bottom. This removes one dimension to the problem — transforming the Laplace equation into the Dupuit-Boussinesq equation (chapter 2). Sloan (2000) solves numerically this equation to show that the discharge delivered by an aquifer is not a single-valued function of its storage. Beven and Freer (2001) also use the shallow water approximation, and linearise it for the TOPMODEL[2]. This model predicts the evolution of the groundwater flow in any type of catchment, given its topography. This model is popular because its simplicity adapts to many field situations. It is mainly designed to predict floods.

Transient, linearised free surface. Younes et al. (2010) developed a numerical model which solves the two-dimensional diffusion equation, taking into account compressibility and volumetric source terms. Without source term, the diffusion equation

[2] `http://csdms.colorado.edu/wiki/Model:TOPMODEL`

becomes the Laplace equation. However, they do not consider the water table as a free surface, thus discarding the non-linearity of the problem.

Fully non-linear, steady state. Darbandi et al. (2007) present a numerical scheme to solve the Laplace equation in a vertical two-dimensional plane, taking full account of the non-linearity of the free-surface condition. Bresciani et al. (2012) propose an alternative scheme, which allows them to simulate the groundwater flow in two and three dimensions. With this model, they evaluate the validity of the Dupuit-Boussinesq approximation in a specific geometric configuration (Bresciani et al., 2014).

Fully non-linear, transient. Finally, MODFLOW[3] is a very popular model which solves the diffusion equation with the non-linear and time-dependent free-surface condition (Harbaugh, 2005). MODFLOW can be used as a lumped-parameter model to study water balances in a specific catchment, but also to study groundwater flow structures. Goderniaux et al. (2013) use it to study the location of a two-dimensional flow in a deep aquifer, and show that it can distribute over several scales, from first-order streams to lower rivers. Woessner (2000) uses MODFLOW to study the water exchange between the groundwater flow and a fluvial stream. However, MODFLOW suffers from problems of convergence, and the water table is not always treated accurately (Naff and Banta, 2008; Bresciani, 2011).

1.4 Objective of the study

Numerical models have the advantage to take into account complex natural configurations, such as spatial heterogeneities of the aquifer, or of the ground surface. However, accounting for this complexity has a cost: these models are generally designed to model the behaviour of a specific aquifer, and must be adapted to any new situation. In addition, many models assume linearity, as a simplification allowing to take into account the natural complexity. However, several studies criticise this simplification (Tallaksen, 1995; Cardenas, 2007).

Are aquifers linear reservoirs? Is it possible to linearise the free-surface condition, and what does it change? Are there generic features, which would be common to many aquifers?

These questions particularly concern the transient behaviours of groundwater flow. To address these questions, we choose to focus on simplified systems. The study of simplified systems allows us to perform more simple mathematics, potentially leading to analytic predictions. In addition, simplified systems can also be easily reproduced in laboratory experiments, under controlled and reproducible conditions. Finally, once a simplified system is understood, it is then easier to single out the prominent features of its behaviour. The parsimony of simplified systems then allows us to answer general questions, and to identify generic features.

[3] `http://water.usgs.gov/ogw/modflow/`

In the next chapter, we present several ways to simplify the groundwater flow, both analytically and experimentally.

Chapter 2

The Dupuit-Boussinesq theory

Modelling the groundwater flow in a natural aquifer is complicated, and requires simplifications. In the previous chapter, we have presented the common simplifications used in numerical models: assumption of steady state, or of linearity. In the present chapter, we discuss how the Dupuit-Boussinesq approximation simplifies the study of groundwater flows.

2.1 Vertical two-dimensional flow

A first step towards simplification of natural aquifers is to reduce the complexity of the drainage network. A drainage network is often a complex ramification of channels (figure 2.1). A common simplification is to reduce this network to a simple linear channel, halving the aquifer into two symmetric parts around the channel. The channel is further considered as infinitely long, such that groundwater flows perpendicularly to the channel. In this simplified configuration, the groundwater flow can be reduced to a vertical plane perpendicular to the river channel.

Figure 2.2 illustrates this two-dimensional groundwater flow. As we will see in part IV, a theory based on complex analysis allows us to model the two-dimensional groundwater flow in various geometries, although only in steady state (Polubarinova-Kochina, 1962). We now concentrate on the dynamical behaviour of the groundwater flow. To take the dynamics into account, we further remove one dimension, and adopt the shallow-water approximation. In hydrogeology, this approximation is known as the Dupuit-Boussinesq (or Dupuit-Forchheimer) approximation.

2.2 Reduction to one dimension: Dupuit-Boussinessq approximation

The Dupuit-Boussinesq approximation combines Darcy's law with the shallow-water approximation to describe the groundwater flow in an unconfined aquifer (Boussinesq, 1903). Based on the observation that the horizontal dimension of the flow is often much

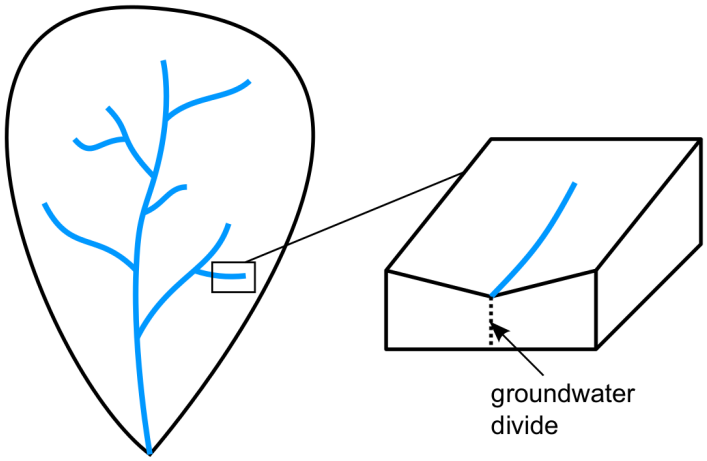

Figure 2.1: A river network is a complex ramified network of channels (left). To simplify the problem of groundwater flow, we reduce the network to a simple linear channel. The channel halves the aquifer into two symmetric parts, equally feeding the river. In this simplified configuration, the groundwater flow is confined to a vertical plane perpendicular to the river. Figure from Bresciani et al. (2014).

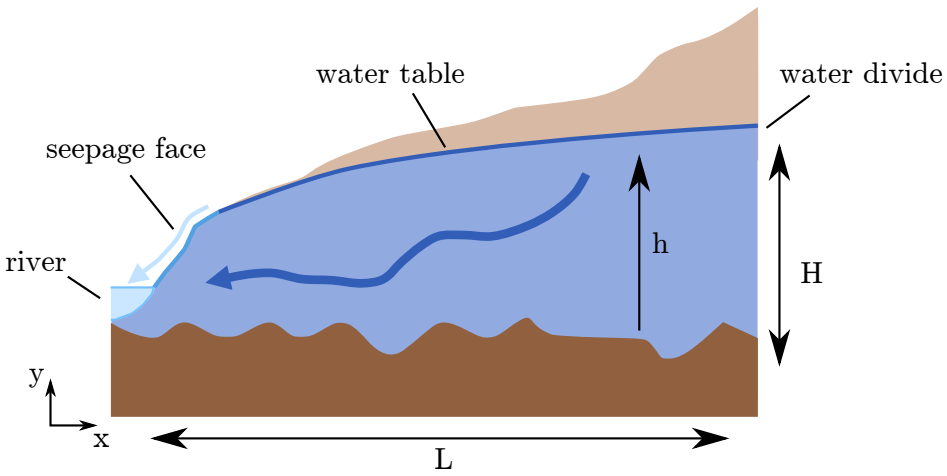

Figure 2.2: Two-dimensional groundwater flow towards a river, in a vertical section perpendicular to the river channel.

larger than its vertical dimension ($L \gg H$), the shallow-water approximation assumes that the velocity is almost horizontal, and that the vertical component of the velocity vanishes: $v_y \sim 0$. Through Darcy's law (1.6), this is equivalent to assuming that the pressure is hydrostatic:

$$p = \rho\, g\, (h - y)\,. \tag{2.1}$$

Accordingly, the horizontal velocity v_x is proportional to the water table slope $\partial_x h$, and the total flux q of fluid through a vertical line halving the aquifer reads (figure 2.2)

$$q = -K\, h\, \frac{\partial h}{\partial x}\,. \tag{2.2}$$

The mass balance then leads straightforwardly to the Dupuit-Boussinesq equation:

$$\boxed{s\, \frac{\partial h}{\partial t} = \frac{K}{2}\, \frac{\partial^2 h^2}{\partial x^2} + R}\,, \tag{2.3}$$

where s is the drainable porosity of the aquifer. The drainable porosity is the volume of water that gravity would extract from a porous material in the absence of a pressure gradient, divided by the total volume of porous material (De Marsily, 1986). Due to surface tension, it differs slightly from the geometric porosity.

A major part of this manuscript will be devoted to solutions of the Dupuit-Boussinesq equation, and their implications on the discharge of a river (parts II and III). The Dupuit-Boussinesq equation is non-linear, and does not have any general analytical solution. In the next section of this chapter, we present several analytical solutions to the Dupuit-Boussinesq equation which have already been derived in the literature (section 2.3). Here, we first analyse qualitatively this equation, by solving it numerically with Mathematica.

We supplement the Dupuit-Boussinesq equation with two boundary conditions. The first condition states that the water table elevation h vanishes at the river, that is in $x = 0$:

$$h(0, t) = 0\,. \tag{2.4}$$

Then, the groundwater divide, which we fix in $x = 1$, imposes that the horizontal velocity vanishes. Combined with Darcy's law and the Dupuit-Boussinesq approximation, it formally reads

$$\partial_x h(1, t) = 0\,. \tag{2.5}$$

Finally, we begin the numerical experiment with an empty aquifer:

$$h(x, 0) = 0\,. \tag{2.6}$$

We then impose a constant rainfall rate $R = 1$ at $t = 0$, and stop the rainfall at $t = 0.25$. The parameters of the equation, s and K, are set to one. The numerical resolution then gives the shape $h(x, t)$ of the water table from $t = 0$ to $t = 5$. Combining equation (2.2) with this solution in $x = 0$, we obtain the discharge delivered by the aquifer to the river (figure 2.3).

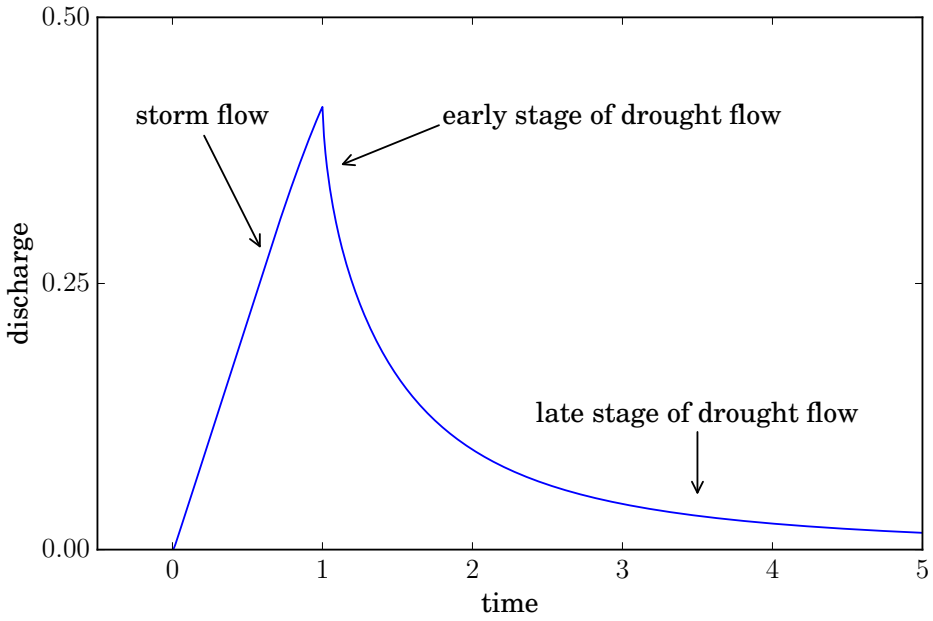

Figure 2.3: Discharge given by a numerical resolution of the Dupuit-Boussinesq equation (2.3), with the parameters s and K set to one. A constant rainfall rate $R = 1$ is imposed from $t = 0$ to $t = 0.25$, and then stopped.

The numerical hydrograph is qualitatively similar to typical river hydrographs (see figures 4.9, 7.3 and 7.9 for comparisons). The discharge increases rapidly during rainfall, decreases rapidly just after the rainfall has stopped, and then progressively relaxes towards zero. The discharge starts increasing instantaneously when rainfall starts, showing that the flow adjusts instantly to the shape of the water table. The variations of the water table elevation, due to variations of the rainfall rate, induce changes in the pressure field within the saturated zone, therefore acting on the groundwater flow. Even though groundwater flows slowly, the pressure field propagates rapidly. On the contrary, the groundwater reservoir created during rainfall takes a long time to empty. At the end of the experiment, at $t = 5$, a small discharge still persists.

Based on this numerical hydrograph, we define three regimes in a hydrograph: the storm flow, the early stage of the drought flow, and the late stage of the drought flow. The first stage, when the discharge increases during rainfall, is generally referred to as the storm flow. When rainfall has stopped, the discharge decrease is generally referred to as the drought flow. Here, we emphasise the distinction between the rapid discharge decrease during the early stage of drought flow, and the long tail of the discharge decrease. This long tail will be referred to as the late stage of drought flow.

2.3 The drought flow regimes

The drought flow of a Dupuit-Boussinesq groundwater flow has attracted much more attention in the literature, and several analytical solutions are known since the late

nineteenth century (Dupuit, 1863; Boussinesq, 1877). We now focus on these solutions.

To understand how groundwater dynamics can influence the discharge of a river, we first present laboratory experiments which reproduce a Dupuit-Boussinesq drought flow. After the theoretical investigations of Dupuit and Boussinesq, the first laboratory studies were, to our knowledge, performed by Todd (1954) and, a few years later, by Ibrahim and Brutsaert (1965). Here, we first describe Ibrahim and Brutsaert's experiment, which simulates the drainage of an initially fully saturated aquifer. They measure the position of the water table and compute, from these measurements, the discharge based on the Dupuit-Boussinesq approximation (equation (2.2)). They compare this discharge with the discharge measured experimentally, concluding to a good agreement. Here, we will rather compare their measurements with asymptotic regimes of the Dupuit-Boussinesq theory (section 2.3.2). Asymptotic regimes yield analytic predictions and scaling laws. These scaling laws are a robust way to test a theory in the laboratory and on the field, and to evaluate its limitations. We finally compare these asymptotic regimes with field measurements of river discharge (section 2.3.3).

2.3.1 The experiment of Ibrahim and Brutsaert

2.3.1.1 Experimental setup

To design their experiment, Ibrahim and Brutsaert (1965) use the well-known analogy between Darcy's law and a Poiseuille flow in a Hele-Shaw cell. In a Hele-Shaw cell, a viscous fluid flows between two parallel plates closely spaced (Hele-Shaw, 1898). If the gap between the two plates is sufficiently small, the flow is laminar. Like in a Darcy flow, the velocity is then proportional to the pressure gradient (Guyon et al., 2001). According to Poiseuille's law, the mean velocity of a viscous fluid flowing in a Hele-Shaw cell reads:

$$\mathbf{v} = -\frac{\rho\, W^2\, g}{3\,\eta}\, \nabla \left(\frac{p}{\rho\, g} + y \right) , \tag{2.7}$$

where W is the width of the tank. This flow is indeed analogue to Darcy's law, with

$$K = \frac{\rho\, W^2\, g}{3\,\eta} . \tag{2.8}$$

The only difference is that the hydraulic conductivity K is analytically determined in a Poiseuille configuration, whereas it must be measured in a porous medium.

Using this analogy, they simulate a two-dimensional aquifer with two closely spaced parallel plates, forming a $0.147 \times 52 \times 243$ cm tank (figure 2.4). This Hele-Shaw cell contains a viscous fluid (96% glycerine, which viscosity η was measured to be 0.355 $\mathrm{Pa\,s^{-1}}$) between a vertical impermeable wall (right), a horizontal impermeable bottom, and a vertical impermeable gate (left) which opens into a large outflow tank. The outflow tank acts as a draining reservoir and roughly represents a river. A pipe of adjustable height h_c fixes a constant outflow level h_c. The right-hand wall represents the water divide, and the bottom represents an impervious layer on which groundwater flows. In this configuration, the river is supposed to flow on the same impermeable layer as the

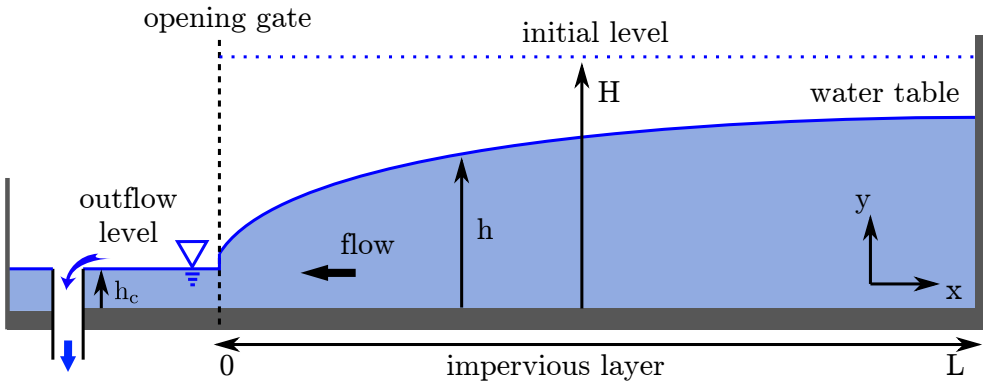

Figure 2.4: Ibrahim and Brutsaert's experiment. A two-dimensional tank (Hele-Shaw cell) holds a viscous fluid between an impermeable wall (right) and an impermeable gate (left). When the gate opens, the asymmetry of the boundary conditions causes the fluid to flow towards the outflow tank.

groundwater flow. In the literature, this simplified configuration is referred to as a fully-penetrating stream. This simplification is important, because it ensures the correctness of the Dupuit-Boussinesq approximation (chapter 8).

2.3.1.2 Observations

An experiment consists in suddenly opening the gate of a tank initially filled with fluid up to the elevation H. Figure 2.5 shows the decline of the water table for two experiments performed with an outflow height fixed at zero (top) and at $h_c/H = 0.25$ (bottom). As the water table is higher than the outflow reservoir, a pressure discontinuity arises at the outlet. The fluid tends to smooth out this discontinuity by flowing towards the outlet, pushed by the pressure gradient. As a result, the water table declines. Because the fluid velocity is proportional to the pressure gradient, the fluid is faster near the outlet, where the pressure gradient is higher. Far from the outlet, the water table is almost horizontal, and the fluid flows more slowly.

The decline of the water table generates a discharge Q, flowing out of the experimental aquifer. Figure 2.6 shows the discharge of three experiments performed with the same outflow height $h_c = 0$, but with three different initial elevations H. The higher the initial elevation, the larger the initial pressure difference with the outlet, and the larger the initial discharge. Then, as the water table declines, the pressure gradient decreases, and the outflow discharge decreases. At long times, the discharges of all three experiments seem to collapse on the same trend. Like in the numerical hydrograph, these experimental drought flows result in two regimes: the early stage, where the discharge decreases quickly, and the late stage, where it decreases more slowly.

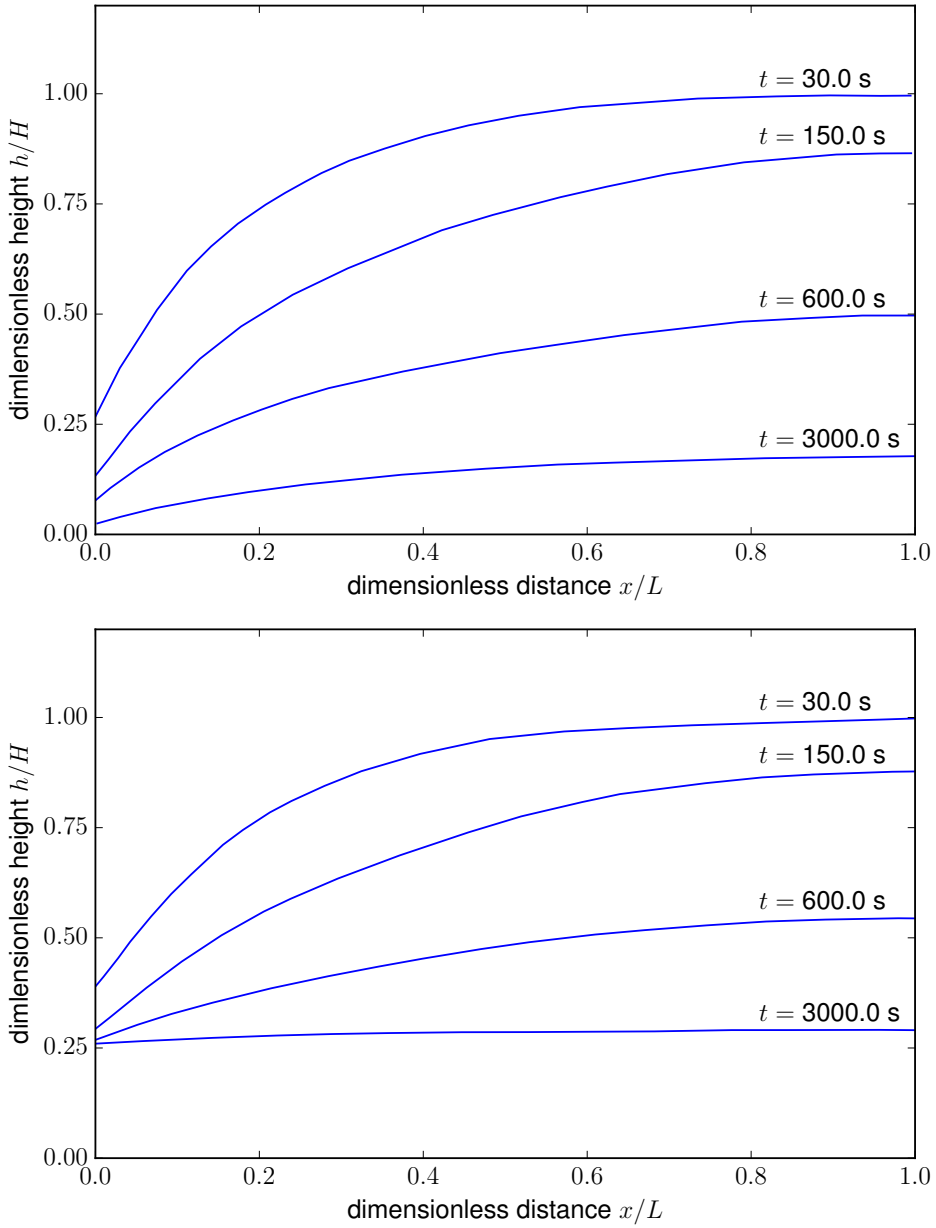

Figure 2.5: Decline of the water table as observed in two of Ibrahim and Brutsaert's experiments. *Top:* $h_c = 0$. *Bottom:* $h_c/H = 0.25$.

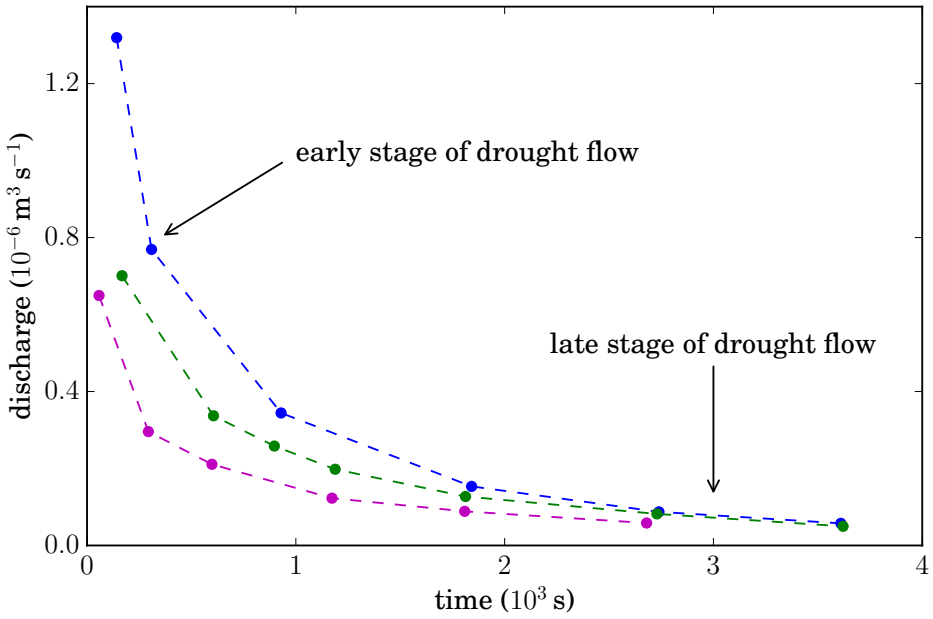

Figure 2.6: Outflow discharge recorded in some of the Ibrahim and Brutsaert's experiments. The experiments shown here are made with $h_c = 0$. The blue points are made with initial level $H = 40\,\text{cm}$ (●), the green points with $H = 30\,\text{cm}$ (●) and the magenta points with $H = 20\,\text{cm}$ (●).

2.3.2 Discharge exiting the aquifer: comparison of the experiment of Ibrahim and Brutsaert with asymptotic regimes of the Dupuit-Boussinesq equation

In this section we discuss several analytical solutions to the Dupuit-Boussinesq equation (2.3) previously derived in the literature. We then compare these solutions, which correspond to asymptotic regimes of the Dupuit-Boussinesq equation, with the experimental results of Ibrahim and Brutsaert (1965). To our knowledge, this approach — comparing the asymptotic regimes of the Dupuit-Boussinesq equation with experiments — is new. Indeed, Ibrahim and Brutsaert (1965) computed a semi-theoretical discharge from measurements of the water table position (as we did for our numerical hydrograph), and compared it with the discharge measured experimentally. The few other experimental studies of fully-penetrating aquifers also favoured other approaches (Todd, 1954; Hewlett and Hibbert, 1963; Abdul and Gillham, 1984).

As it is of second order in space, the Dupuit-Boussinesq equation must be supplemented with two boundary conditions. First, the flux vanishes at the water divide:

$$\frac{\partial h}{\partial x} = 0 \quad \text{for} \quad x = L\,, \tag{2.9}$$

where $x = L$ is the length of the aquifer (figure 2.2).

The second boundary condition is less straightforward. If we neglect surface tension, the outflow reservoir imposes its hydrostatic pressure under the outflow level (for $h \leq$

h_c), whereas the outlet imposes atmospheric pressure to the fluid above the outflow level (for $h \geq h_c$). In the Dupuit-Boussinesq framework, this approximation translates into

$$h = h_c \quad \text{for} \quad x = 0\,. \tag{2.10}$$

When $h_c = 0$, this boundary condition generates a singularity at the outlet. Indeed, if q_o is the flux of groundwater exiting the aquifer, then equation (2.2) implies that the water table elevation behaves like

$$h \sim \sqrt{\frac{2\,q_o\,x}{K}}\,. \tag{2.11}$$

The square root implies that the slope of the water table diverges near the outlet, which is incompatible with the Dupuit-Boussinesq approximation. Indeed, the measurements of the water table show that this condition does not hold in reality (figure 2.5). Even in the experiments with $h_c \neq 0$, the condition (2.10) is not exactly satisfied (figure 2.5). This boundary condition, inherent to the Dupuit-Boussinesq approximation, is one of the limitations of this theory.

2.3.2.1 Linearisation: $h_c \neq 0$

The Dupuit-Boussinesq equation (2.3) is non-linear. The simplest way to solve it consists in linearising it around an equilibrium value. During the experiment, the water table declines and tends to the outflow reservoir level h_c:

$$h \to h_c \quad \text{for} \quad t \to \infty\,. \tag{2.12}$$

If $h_c \neq 0$, we can write the water table elevation as

$$h = h_c + \delta h\,, \tag{2.13}$$

where $\delta h \ll h_c$. Combining (2.13) with (2.3), we only keep the first order terms to obtain the linearised Dupuit-Boussinesq equation:

$$s\,\frac{\partial\,\delta h}{\partial t} = K\,h_c\,\frac{\partial^2\,\delta h}{\partial x^2}\,. \tag{2.14}$$

To solve this equation, Boussinesq (1904) assumes that the shape of the water table gradually assumes the first harmonic solution to (2.14), leading to the long-time solution (see Brutsaert (2005) for the complete derivation):

$$h \sim h_c + 4\,\frac{H - h_c}{\pi}\,\sin\left(\frac{\pi\,x}{2\,L}\right)\,\exp\left(\frac{-\pi^2\,K\,h_c\,t}{4\,s\,L^2}\right)\,, \tag{2.15}$$

where we recall that H is the initial level of saturation of the aquifer (figure 2.4). The discharge delivered to the river by this linearised groundwater flow, given by equation (2.2) taken in $x = 0$ and multiplied by the width W of the aquifer, thus reads

$$Q(t) \sim 2\,W\,h_c\,K\,\frac{H - h_c}{L}\,\exp\left(\frac{-\pi^2\,K\,h_c\,t}{4\,s\,L^2}\right)\,. \tag{2.16}$$

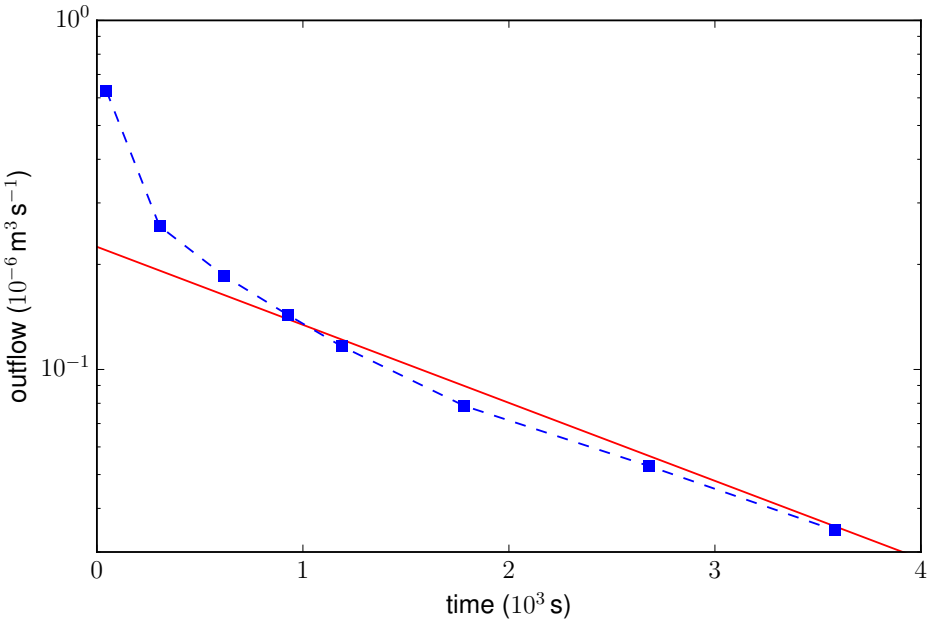

Figure 2.7: Outflow discharge measured in an experiment with $h_c = 0.05\,\mathrm{m}$ and $H = 0.2\,\mathrm{m}$ (■). (—) is the exponential decrease predicted in equation (2.16), without any fitting parameter.

The experimental results conform well with this long-time solution (figure 2.7). With no fitting parameter, the measurements nearly collapse on the theoretical prediction. Despite the slight discrepancy between the outlet boundary condition and the level observed in the experiments (figure 2.7), the Dupuit-Boussinesq approximation seems to be relevant in this particular configuration, where $h_c \neq 0$.

However, natural hydrographs hardly ever exhibit any exponential behaviour, even long after the last rain event (Wittenberg, 1994; Chapman, 2003). As equation (2.16) is a long-time solution, it is possible that natural rivers never reach this long-time behaviour, and rather exhibit series of sub-harmonic solutions. An other possibility is that, in the conditions of natural aquifers, one cannot linearise the Dupuit-Boussinesq equation. As a matter of fact, it is very likely that the depth of most aquifers is much larger than the depth of their river. As an example, the Quiock Creek studied in part III is at most about 10 cm deep, whereas the elevation of the water table is a few metres higher than the river. In this particular case at least, the height h_c of the river is negligible compared to the elevation of the water table. In what follows, we will consider that the depth of the river can be neglected: $h_c \to 0$.

2.3.2.2 Early stage of drought flow ($h_c = 0$)

When $h_c = 0$, one cannot linearise the Dupuit-Boussinesq equation (2.3). To solve this non-linear equation, we look for similarity solutions.

At the very beginning of the experiment, that is at the exact moment when the gate is opened, the experimental aquifer is fully saturated, whereas the outflow reser-

voir imposes atmospheric pressure at the outlet. In the frame of the shallow-water approximation, this corresponds to a singular initial condition:

$$\begin{cases} h = 0 & \text{for} \quad x = 0\,, \\ h = H & \text{for} \quad x > 0\,. \end{cases} \tag{2.17}$$

This initial condition suggests that, as soon as the aquifer starts draining, the singularity in $x = 0$ diffuses in the aquifer. As it diffuses, it progressively moves towards the other extremity of the aquifer in $x = L$, like the front of a wave. This wave does not feel the influence of the water divide until it reaches it. We consequently consider the water divide as being infinitely far from the outlet:

$$h = H \quad \text{for} \quad x \to \infty\,. \tag{2.18}$$

These initial and boundary conditions, combined with the left-hand condition (2.10) $h = 0$ for $x = 0$, suggest the use of Botzmann's variable $x\,t^{-1/2}$ to solve the Dupuit-Boussinesq equation. Indeed, Polubarinova-Kochina (1962) shows that the elevation of the water table adopts a self-similar shape of the form

$$h = H\,f\left(\frac{\sqrt{s}\,x}{2\sqrt{K\,H\,t}}\right)\,. \tag{2.19}$$

The similarity function f satisfies the following ordinary differential equation

$$2\,\xi\,f' + f\,f'' + f'^2 = 0\,, \tag{2.20}$$

where ξ is the Boltzmann similarity variable:

$$\xi = \frac{\sqrt{s}\,x}{2\sqrt{K\,H\,t}}\,. \tag{2.21}$$

The boundary conditions (2.10) and (2.18) translate into $f = 0$ for $\xi = 0$ and $f = 1$ for $\xi \to \infty$, respectively. By comparing equation (2.20) to the Blasius equation (theory of viscous boundary layers), Polubarinova-Kochina (1962) shows (p. 507) that the self-similar solution of the water table has a square root shape close to the outlet:

$$f(\xi) \sim a_{\text{esdf}}\,\sqrt{\xi} \quad \text{for} \quad \xi \to 0\,, \tag{2.22}$$

where $a_{\text{esdf}} \approx 1.152$ is a numerical integration constant borrowed from the theory of the boundary layer of a plate. This result is in good agreement with a numerical resolution of equation (2.20), which exhibits a square root shape close to the outlet and tends to 1 for $\xi \to \infty$ (figure 2.8).

The shape of the water table gives us access to the theoretical discharge flowing out of the aquifer through equation (2.2), and we obtain the following short-times asymptotic behaviour for the discharge:

$$q(t) \sim \frac{a_{\text{esdf}}^2}{4}\,\frac{(s\,K\,H^3)^{1/2}}{\sqrt{t}}\,. \tag{2.23}$$

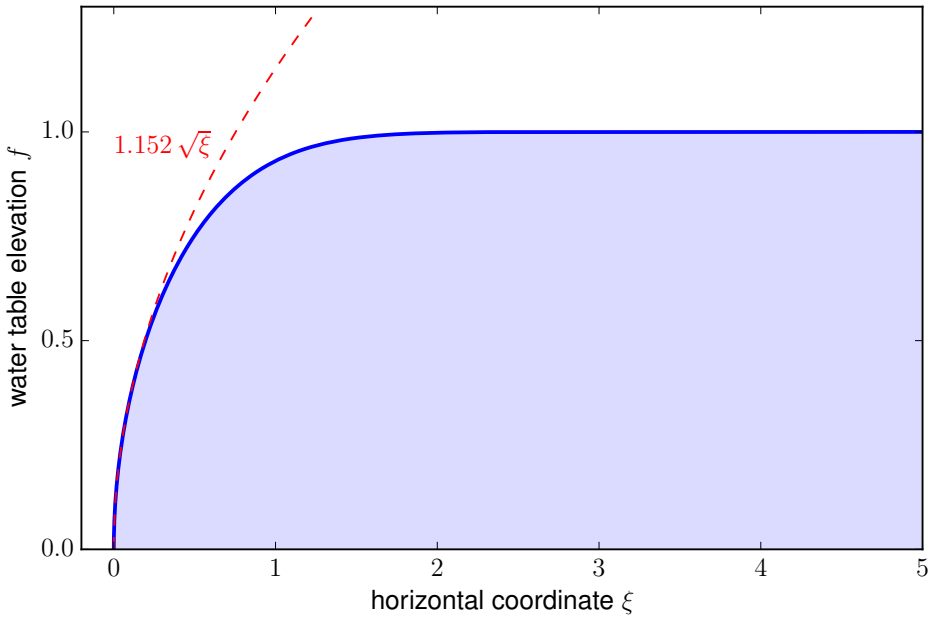

Figure 2.8: Numerical solution of (2.20) corresponding to the self-similar shape of the water table during the early stage of the drainage (—). Its behaviour near the outlet is $1.152\sqrt{\xi}$ (- - -).

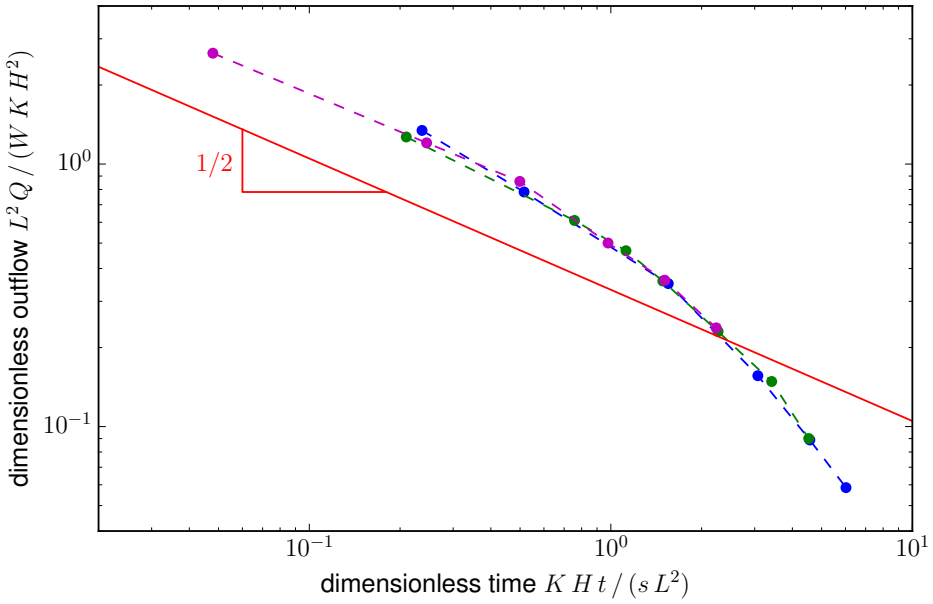

Figure 2.9: Dimensionless discharge recorded in the three experiments with $h_c = 0$, as a function of dimensionless time (following equation (2.24)). The blue points were made with the initial level $H = 40\,\text{cm}$ (●), the green points with $H = 30\,\text{cm}$ (●) and the magenta points with $H = 20\,\text{cm}$ (●). The red line is the short time asymptotic $1/\sqrt{t}$ behaviour (—), with no adjustable parameters (equation (2.23)).

We expect this asymptotic regime to be valid until the wave front reaches the water divide, that is until

$$t \sim \frac{s\,L^2}{K\,H}\,. \tag{2.24}$$

The three experiments by Ibrahim and Brutsaert (1965) with $h_c = 0$ conform well with this prediction (figure 2.9). Once the time is rescaled with equation (2.24) and the discharge with (2.23), the data of the three experiments merge on the same $-1/2$ power law. As expected, when the dimensionless time roughly equals one, the discharge deviates from the early-time asymptotic regime.

Fitting a $-1/2$ power law to the experimental data before the dimensionless time equals one yields a prefactor of 0.56, that is about 1.7 times the theoretical prefactor of 0.332. This slight mismatch could be due to the breakdown of the Dupuit-Boussinesq approximation at the outlet.

2.3.2.3 Late stage of drought flow ($h_c = 0$)

The asymptotic regime (2.23) relies on the hypothesis that the aquifer is initially fully saturated, and holds only during the beginning of the experiment. As seen on figure 2.9, the discharge rapidly deviates from this $1/\sqrt{t}$ behaviour.

Dupuit (1863) and Boussinesq (1877) show that the Dupuit-Boussinesq equation (2.3) has an other self-similar solution compatible with the boundary conditions (2.9) and (2.10):

$$h(x,t) = \frac{L^2\,s}{K\,t}\,H_d\left(\frac{x}{L}\right)\,, \tag{2.25}$$

where L is the length of the aquifer, and the shape H_d of the water table satisfies

$$H_d\,H_d'' + H_d'^2 + H_d = 0\,. \tag{2.26}$$

We can then directly translate conditions (2.9) and (2.10) to obtain the two boundary conditions: $H_d'(1) = 0$ and $H_d(0) = 0$. The solution to this equation can be approximated by a square root close to zero:

$$H_d \sim a_d\sqrt{\frac{x}{L}}\,, \tag{2.27}$$

where a_d is a mathematical constant expressed in terms of the Euler gamma function Γ (Brutsaert, 2005):

$$a_d = \sqrt{\frac{8}{3}}\left(\frac{\Gamma(7/6)}{\sqrt{\pi}\,\Gamma(2/3)}\right)^{3/2} \approx 1.177\,. \tag{2.28}$$

A numerical resolution of equation (2.26) shows the shape of this self-similar solution (figure 2.10).

The discharge associated to this self-similar solution reads

$$Q \sim \frac{a_d^2}{2}\,\frac{s^2\,W\,L^3}{K\,t^2}\,. \tag{2.29}$$

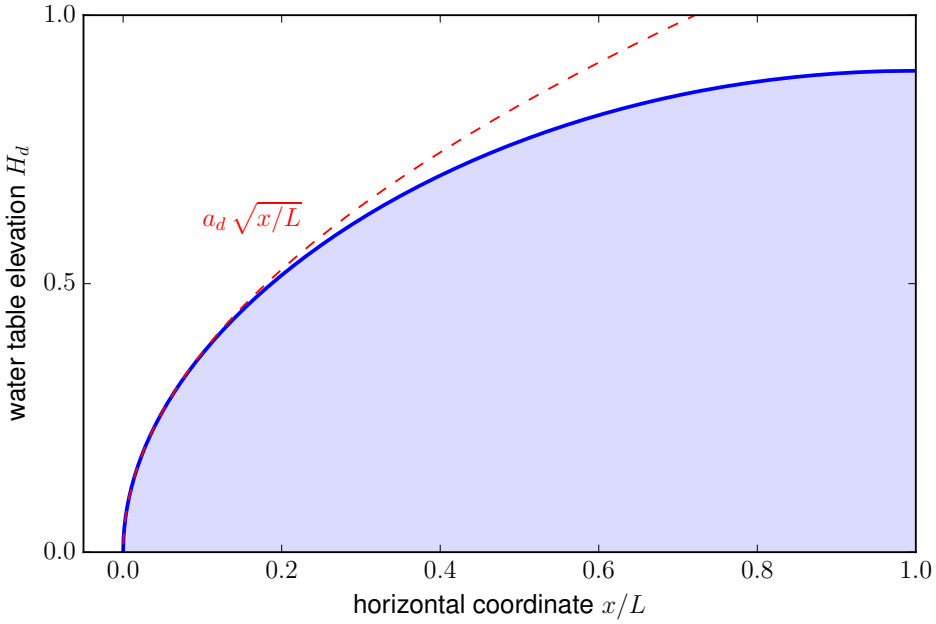

Figure 2.10: Numerical solution of (2.26) corresponding to the self-similar shape of the water table during the late stage of the drainage (—). Its behaviour near the outlet is $a_d\sqrt{x/L}$ (- - -).

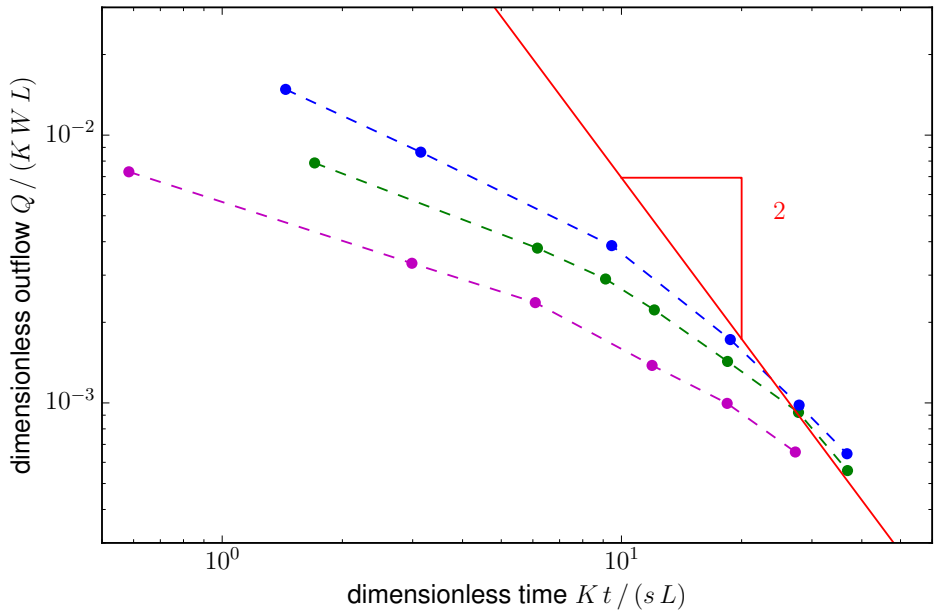

Figure 2.11: Outflowing discharge recorded in the three experiments made with $h_c = 0$. (●) was made with the initial level $H = 40\,\text{cm}$, (●) with $H = 30\,\text{cm}$ and (●) with $H = 20\,\text{cm}$. (—) is the long times asymptotical $1/t^2$ power law, with no adjustable parameters.

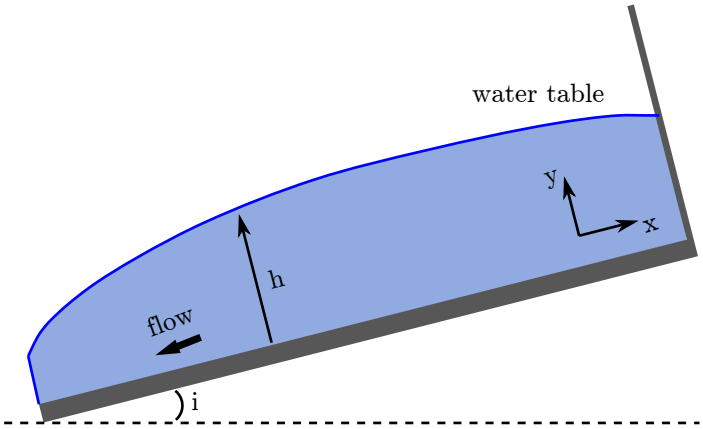

Figure 2.12: Sketch of a sloping aquifer flowing towards a river which flows on the same impermeable layer.

By analogy with the linear heat equation, we expect most solutions of the Dupuit-Boussinesq equation to tend towards the self-similar solution H_d at long times, regardless of the initial conditions. The drought flow of a fully-penetrating stream is therefore expected to decrease as the inverse time squared at long times. In contrast with the early stage of drought flow, the late stage of drought flow depends on the length of the aquifer.

The experiments of Ibrahim and Brutsaert (1965) with $h_c = 0$ did not last long enough to decide positively whether they will eventually reach a -2 power law of time (figure 2.11). The three experiments seem to tend towards the same asymptotic behaviour, which seems to have a slope -2. Longer experiments would be necessary to confirm this result.

2.3.2.4 Sloping aquifers

So far in this section we have considered the discharge exiting a horizontal fully-penetrating aquifer. Yet some aquifers, generally located in mountaneous areas, lie along inclined hillslopes. A large part of the literature, which can be referred to as hillslope hydrology, assumes that the aquifer bottom reflects the ground elevation, and consequently presents large slopes. Here, we briefly expose some results concerning sloping aquifers draining into a fully-penetrating stream (figure 2.12). In such case, Childs (1971) uses the Dupuit-Boussinesq approximation, which translates here into the hypothesis that the flow is parallel to the sloping bed of the aquifer. As a consequence, the flux of water flowing along the x direction reads

$$q = -K\,h\left(\frac{\partial h}{\partial x}\cos i + \sin i\right), \tag{2.30}$$

Type of aquifer	Stage of drought	Discharge regime	Exponent in a Q $\dot{Q}$ plot
Horizontal, $h_c \neq 0$	Late	$Q \propto \exp(-t)$	1
Horizontal, $h_c = 0$	Early	$Q(t) \propto 1/\sqrt{t}$	3
Horizontal, $h_c = 0$	Late	$Q(t) \propto 1/t^2$	3/2
Sloping, $h_c \neq 0$	Early	$Q(t) \propto 1/\sqrt{t}$	3
Sloping, $h_c \neq 0$	Late	$Q \propto \exp(-t)$	1

Table 2.1: Summary of all the asymptotic regimes of an aquifer presented in this chapter concerning the drought flow. See Rupp and Selker (2006b) for a larger review of the existing asymptotic regimes. These asymptotic regimes are associated to specific exponents in the Q $\dot{Q}$ plane, as discussed in section 2.3.3.

where i is the angle of the aquifer. Mass balance then straightfordwardly leads to a new Dupuit-Boussinesq equation:

$$s\,\frac{\partial h}{\partial t} = \frac{K}{2}\left(\frac{\partial^2 h^2}{\partial x^2}\,\cos\,i + 2\,\frac{\partial h}{\partial x}\,\sin\,i\right). \tag{2.31}$$

One can find many solutions to this equation in the literature (Zecharias and Brutsaert, 1988; Sanford et al., 1993; Troch et al., 2013). The solving techniques do not vary much from those already exposed in this section, and most solutions consist in linearising this equation (Brutsaert, 1994). The main results are an early-time drought-flow self-similar regime where the discharge behaves like the inverse square root of time, and a long-time regime where the river discharge behaves exponentially (see table 2.1, which lists all the predictions presented in this chapter). To our knowledge, there is no experimental verification of these results in the literature.

Even though other derivations exist, we have presented the majority of the analytical models which lead to the prediction of the discharge delivered by an aquifer during drought. Comparing the asymptotic regimes of a horizontal aquifer feeding a fully-penetrating stream with the experimental results of Ibrahim and Brutsaert (1965), we conclude to a good agreement with the Dupuit-Boussinesq theory. Yet, the long-times asymptotic regime (2.29) would deserve longer experiments to be tested. In the next section we analyse the discharge of natural rivers, and compare them to the Dupuit-Boussinesq asymptotic regimes.

2.3.3 Comparison with natural rivers: the Q $\dot{Q}$ plot method

In this section, we look for the behaviour of natural rivers in the absence of rainfall using data from the literature. Based on the analytic results of the previous section, we

expect the discharge to decrease exponentially or as a power law of time. To discriminate between these different regimes, Brutsaert and Nieber (1977) have developed a now widespread method: the $Q\ \dot{Q}$ plot.

The simple semi-log plot of a river hydrograph reveals whether the river discharge decreases exponentially or not. However, as discussed previously, discharge recessions seem to be hardly ever exponential, and we shall rather seek power-law behaviours:

$$Q = A\ (t - t_0)^{-B}\,, \tag{2.32}$$

where A and B depend on the characteristics of the system, and t_0 depends on the initial conditions. Such power law strongly depends on t_0. Unfortunately, we do not know *a priori* the value of t_0, and looking for such power law is equivalent to a three parameters fit — A, B, and t_0 — whereas we are only interested in A and B.

Brutsaert and Nieber (1977) circumvent this problem by examining the behaviour of the time derivative of the discharge $\dot{Q}$ versus the discharge Q, instead of examining directly the relationship $Q = f(t)$. Equation (2.32) thus becomes

$$\dot{Q} = -A\,B^{-1/B}\,Q^{1+1/B} = -a\,Q^b, \tag{2.33}$$

which does not depend on t_0. As a consequence, the three-parameters fit in the t/Q plane becomes a two-parameters fit in the $Q/\dot{Q}$ plane. Table 2.1 lists the theoretical asymptotic regimes derived in this chapter, and the exponent b in the $Q\ \dot{Q}$ plane to which they correspond.

Brutsaert and Nieber (1977) developed this method to analyse the discharge of several rivers in the Finger Lakes region, in the United States. Figure 2.13a illustrates their result for the Fall Creek. Although their data do not span much more than one decade of discharge measurements, their field measurements seem to be consistent with a $b = 3/2$ slope. Following equations (2.33) and (2.32), this result would imply that the discharge decreases as the inverse time squared: $Q \sim t^{-2}$. This behaviour is consistent with the analytical result (2.29) derived in the previous section.

Brutsaert and Nieber (1977) inspired many later studies (Troch et al., 1993; Szilagyi and Parlange, 1998; Brutsaert and Lopez, 1998; Huyck et al., 2005). Figure 2.13b shows the result of the same analysis performed for a spring in the Philippines (Malvicini et al., 2005), and figure 2.13c for a river in central Oklahoma (Brutsaert and Lopez, 1998). Both analyses show that a large scatter may hinder the $Q\ \dot{Q}$ analysis. Brutsaert and Nieber (1977) assume that this scatter is due to other sources of discharge decrease. According to them, the main component of the discharge decrease is the decline of the water table, but if there is evapotranspiration for example, the discharge decreases faster. As a consequence, the asymptotic regimes of groundwater flow represent the smallest discharge decrease $|\dot{Q}|$ possible at a given discharge Q. According to this argument, the asymptotic regimes presented in this chapter should therefore represent the lowest envelopes of a $Q/\dot{Q}$ plot.

On the contrary, Kirchner (2009) estimates that the scatter is inherent to field measurements, and calculates averages of his $Q/\dot{Q}$ measurements. Fitting his averaged data,

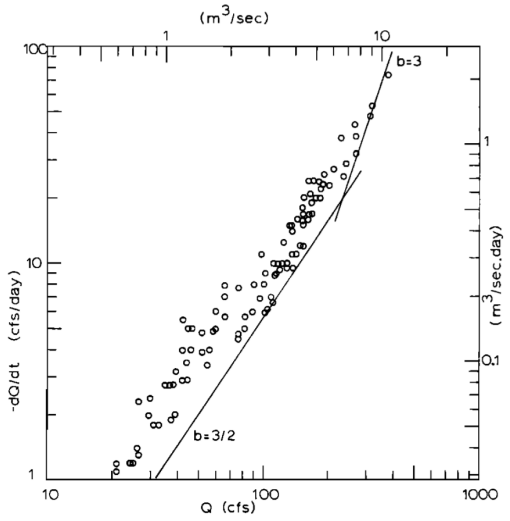

(a) Brutsaert and Nieber (1977) analysis.

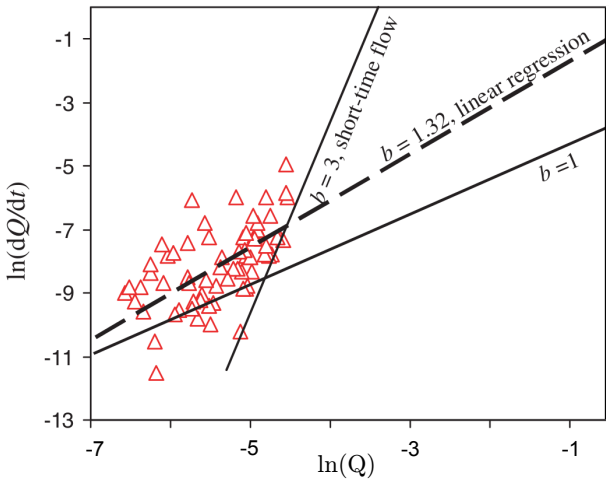

(b) Malvicini et al. (2005) analysis.

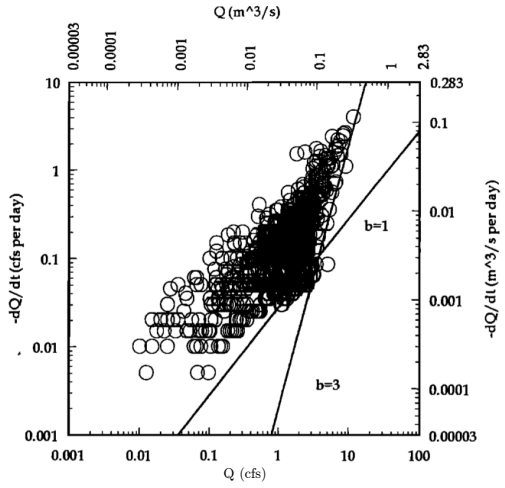

(c) Brutsaert and Lopez (1998) analysis.

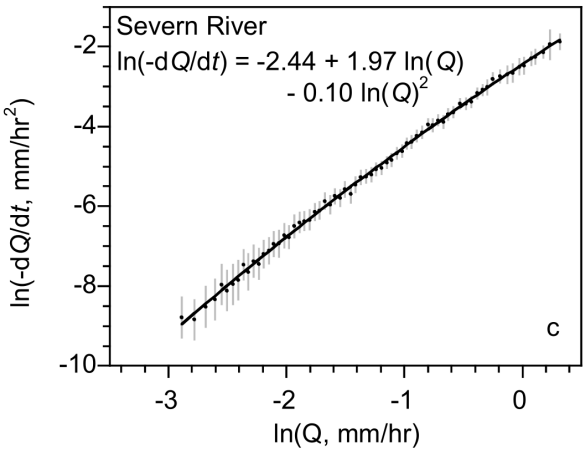

(d) Kirchner (2009) analysis.

Figure 2.13: River discharge recession analysis of several rivers found in the literature. The straight lines indicate exponential or power laws: a 3/2 slope indicates that $Q \sim 1/t^2$, a slope of 3 indicates $Q \sim 1/\sqrt{t}$, and a slope of 1 indicates exponential behaviour (table 2.1).

he obtains a slope $b \approx 2$, implying that the discharge decreases as the inverse of time: $Q \sim 1/t$ (figure 2.13d). Strictly speaking, the latter power law is not integrable, which implies an infinite volume of water. Yet, a slightly larger exponent would be integrable.

The interpretation of the large scatter of the Q $\dot{Q}$ plots is not clear yet. However, the exponential decrease of the discharge predicted by the linearised Dupuit-Boussinesq equation corresponds to an exponent $b = 1$ in a Q $\dot{Q}$ plot (table 2.1). This exponent is hardly ever found in the literature. This observation is consistent with the fact that semi-log plots of river hydrographs hardly ever exhibit straight lines. We may conclude from this observation that, in most cases, aquifers do not behave as linear reservoirs.

The decline of a water table after rainfall has been widely studied, in many different configurations. Here, we have chosen to focus on scaling laws derived analytically, which requires strong simplifications (table 2.1). Among these simplifications, perhaps the most important ones are: the reduction to two dimensions, the assumption of a homogeneous porous medium, a simple geometry, negligible surface tension, and the assumption of a fully-penetrating stream. The failure of these approximations can explain, at least partly, the scatter of field measurements (figure 2.13).

2.4 The storm flow

Surprisingly, the behaviour of an aquifer during a rainfall event has been much less studied. Contrary to most studies of the drought flow, most works treating this question have assumed that the impermeable bottom of the aquifer is inclined towards the river. In this section we summarise their main results, before treating the case of the linearised Dupuit-Boussinesq equation in a horizontal aquifer.

2.4.1 Sloping aquifers.

When it rains, the Dupuit-Boussinesq equation for a sloping aquifer reads

$$s\,\frac{\partial h}{\partial t} = \frac{K}{2}\left(\frac{\partial^2 h^2}{\partial x^2}\,\cos\,i + 2\,\frac{\partial h}{\partial x}\,\sin\,i\right) + R\,, \tag{2.34}$$

where the only difference with equation (2.31) is the presence of the rainfall rate R. Henderson and Wooding (1964) show that the single dimensionless parameter

$$\lambda = \frac{4\,R\,\cos i}{K\,\sin^2 i} \tag{2.35}$$

determines the solution to equation (2.34). When $\lambda < 1$, that is essentially for large slopes, the problem can be formulated as a kinematic wave (Beven, 1981) (figure 2.14). In the kinematic wave framework, at the beginning of the rain event, the river has no influence on the groundwater flow. As groundwater flows downhill, the water divide, at the top of the hill, fully determines the groundwater flow. Before it feels the effects of the river, the water table, at the river, rises linearly with time and proportionally to the

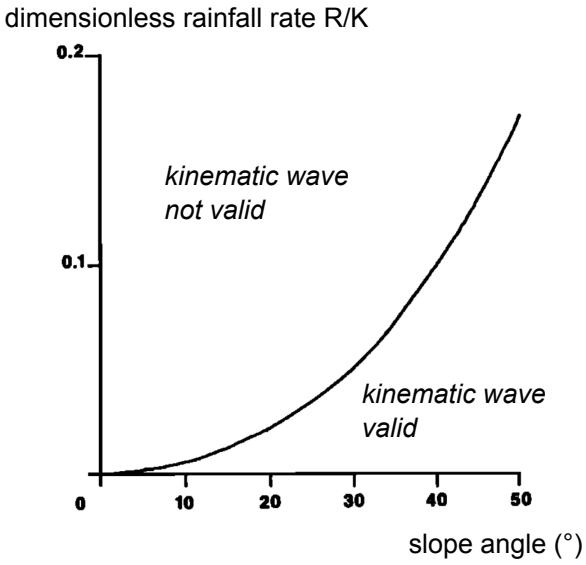

Figure 2.14: Domain of validity of the kinematic wave approximation for the groundwater flow on a hillslope. Figure adapted from Beven (1981).

rainfall rate: $h \sim R\,t$ in $x = 0$. This asymptotic regime only works at the early stage of the rainfall event, until the groundwater flow feels the effect of the river. For larger values of λ, the water table deviates from this asymptotic behaviour.

The discharge associated to this self-similar solution is linear in time (Beven, 1981):

$$Q \sim K \, \sin i \, R\, t \,. \tag{2.36}$$

Numerical solutions to equation (2.34) show that this solution is indeed reasonable for small values of λ (figure 2.15). The smaller the value of λ, the better the approximation. For small slopes, which means large values of λ, this approximation does not work.

2.4.2 Horizontal aquifers.

Pauwels and Troch (2010) are the only one to have addressed analytically the behaviour of a horizontal aquifer submitted to rainfall. Primarily considering sloping aquifers, their model also provides a solution when the aquifer has no slope, as a specific case of more general solutions.

The Dupuit-Boussinesq equation, in the limit where the river depth is neglected ($h_c = 0$ in figure 2.4), is non-linear. However, Pauwels and Troch (2010) linearise the flux following Brutsaert (1994):

$$q = K\, h\, \frac{\partial h}{\partial x} \simeq K\, p\, D\, \frac{\partial h}{\partial x}\,, \tag{2.37}$$

where D is the constant aquifer depth, and p is a fitting parameter. Following this technique, the Dupuit-Boussinesq equation is linearised:

$$\frac{\partial h}{\partial t} = \frac{K\, p\, D}{s}\, \frac{\partial^2 h}{\partial x^2} + \frac{R}{s}. \tag{2.38}$$

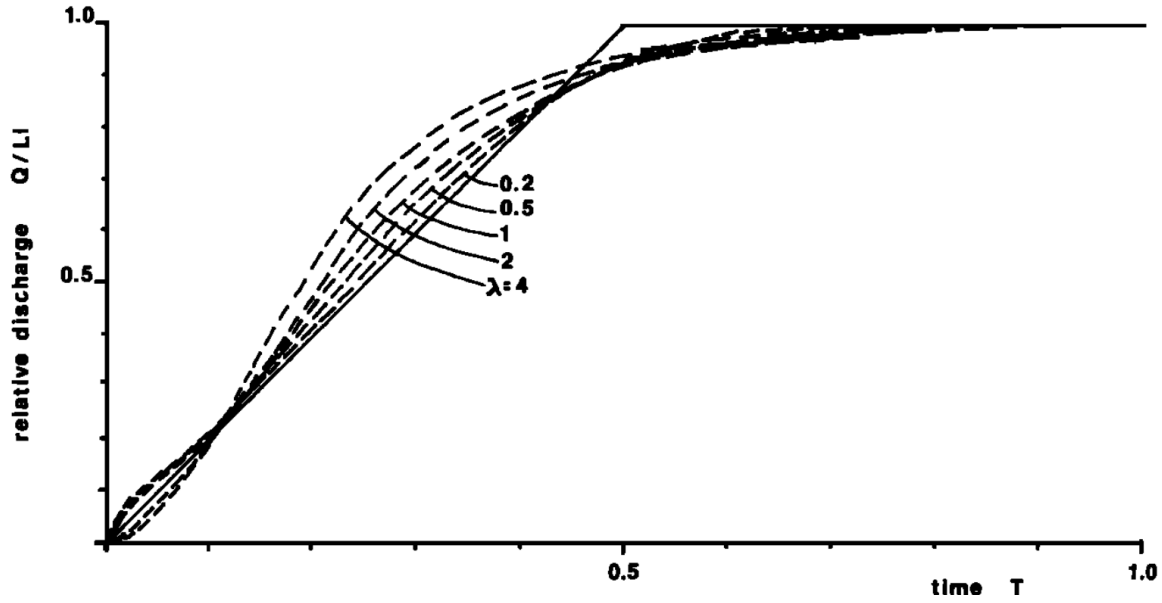

Figure 2.15: Discharge delivered by a sloping aquifer, predicted by the extended Dupuit-Boussinesq equation (2.34) solved numerically for different values of λ (broken lines), and kinematic wave solution (solid line). Figure from Beven (1981).

To this equation are associated two boundary conditions: no flux at the water divide, that is $\partial h/\partial x = 0$ for $x = L$, and $h = 0$ at the river, for $x = 0$. At last, they assume it has not rained for a long time, and that the aquifer is initially empty: $h = 0$ for $t = 0$. Through a Laplace transform, they state that the solution to equation (2.38) leads to

$$Q(t) = 4\,W\,R\sqrt{\frac{K\,p\,D}{s}}\,\sqrt{t}. \tag{2.39}$$

To check this result, Pauwels and Troch (2010) produce a synthetic hydrograph by numerically solving equation (2.38), with a varying rainfall rate. The analysis of the rising limbs of several floods of this synthetic hydrograph conforms well to their asymptotic result (2.39).

The two models presented here use asymptotic solutions to the linearised Dupuit-Boussinesq equation. As a result, both discharge predictions depend linearly on the rainfall rate. However, to our knowledge, there is no comparison to experimental studies, nor to field measurements.

2.5 Conclusions

Since Dupuit and Boussinesq, several authors have studied theoretically the dynamics of a water table declining after a rainfall event. In particular, several asymptotic regimes of the Dupuit-Boussinesq equation emerge from the literature. According to these asymptotic regimes, the discharge delivered by an aquifer to a fully-penetrating

stream evolves as the inverse of the square root of time at the beginning of the drought flow ($Q \sim 1/\sqrt{t}$), and then exponentially or as the inverse of the square of time ($Q \sim 1/t^2$). The Q $\dot{Q}$ plot method, developed to test these regimes, revealed that most aquifers do not behave as linear reservoirs. Natural aquifers compare relatively well with the Dupuit-Boussinesq asymptotic regimes, but the large scatter of field data hinders to draw definitive conclusions. Additional tests, such as separate measurements of the hydraulic parameters, water table measurements or the analysis of the storm flow, could help to confirm whether natural aquifers could be described by the generic features of a Dupuit-Boussinesq groundwater flow.

In contrast, the behaviour of an aquifer during storm flow has been less studied. Most analytical studies assumed linearity, but they were not tested against laboratory experiments or field data.

To our knowledge, the asymptotic regimes of the Dupuit-Boussinesq equation were never tested against laboratory experiments. Systematic laboratory experiments are necessary to confirm that an aquifer behaves non-linearly, even in a simplified configuration. Moreover, field studies need to confront their scattered results with separate measurements. For instance, we are not aware of any measurement of the water table decline during drought periods in natural conditions. The dynamics of a groundwater flow during storm flow could also add information on the behaviour of the groundwater flow in natural aquifers.

In this manuscript, we will address the question of the linearity of aquifers in simplified configurations, with a strong emphasis on the groundwater dynamics during rain events. In chapter 3, we design a laboratory aquifer to further study the Dupuit-Boussinesq model and its asymptotic regimes. We first confirm the $1/t^2$ late stage of drought flow. We then observe its behaviour during rainfall, additionally deriving a new asymptotic regime for the early reaction to rainfall.

We then test the Dupuit-Boussinesq asymptotic regimes in natural aquifers in part III, which is divided into four chapters. We begin with a field experiment, especially designed to test qualitatively and quantitatively the influence of the groundwater flow on the river dynamics. We first present the field installation and qualitative observations (chapter 4). We then measure separately the hydraulic parameters of the aquifer (chapter 5). We finally compare the river dynamics with the Dupuit-Boussinesq asymptotic regimes (chapter 6). We end part III by testing these regimes against hydrographs of other catchments (chapter 7).

In the last part of this manuscript, we explore the influence of two-dimensional flow on the dynamics of groundwater (part IV, chapter 8).

Part II

Dupuit-Boussinesq theory: comparison with a laboratory experiment

Chapter 3

Response of a laboratory aquifer to rainfall

Contents

How does groundwater react to rainfall? Can groundwater generate rapid floods? Our numerical resolution of the Dupuit-Boussinesq equation (section 2.2) suggests that the flow in an unconfined aquifer can react quickly to a storm. Yet, the dynamics of groundwater in response to rainfall has been much less studied than its drought flow.

In this chapter, we reproduce an aquifer in a fully-penetrating configuration in a simplified laboratory experiment, with a threefold objective. We first want to determine

whether an aquifer can qualitatively reproduce the dynamics observed in rivers hydrographs. Then, we intend to evaluate the validity of the Dupuit-Boussinesq drought flow asymptotic behaviour against experiment. Finally, we plan to apply the same method (experiment and asymptotic regime) to the groundwater flow induced by a storm.

Most of this chapter has been previously published in an abbreviated form (Guérin et al., 2014).

3.1 Why a laboratory experiment?

In this manuscript, we will attempt to isolate generic features of the response of an aquifer to rainfall. For that purpose, we will emphasise the asymptotic regimes of the Dupuit-Boussinesq equation. Indeed, asymptotic regimes yield scaling laws, which constitute robust results to test a theory, and provide a simple and efficient way to assess the influence of the various parameters. Asymptotic regimes depend on hypotheses, and must be tested against experiments.

The Dupuit-Boussinesq theory requires simplifying hypotheses. Unfortunately, theses hypotheses are often difficult to assess in the field. For example, to study the groundwater flow in a natural aquifer, we need to know the geometry of the aquifer. Indirect imaging techniques, like electrical resistivity tomography or seismic tomography, may allow to identify some underground structure; but they do not give access to permeability (Kalinski et al., 1993; Dannowski and Yaramanci, 1999; Chevigny, 2014). Yet, direct laboratory measurement of the permeability of a ground sample is unreliable: it is impossible to know whether collecting a sample of ground changes its structure; furthermore, sampling provides a local permeability, which could be totally different from the permeability at the aquifer scale.

To these technical difficulties must be added physical hypotheses, which are also difficult to test. For example, it is much easier to study the groundwater flow if we neglect surface tension. In the field, its influence is uneasy to quantify.

Finally, a physical model such that the Dupuit-Boussinesq theory also relies on mathematical hypotheses. Indeed, the dynamics of a vertical two-dimensional groundwater flow has never been investigated so far and, for the moment, we must reduce the problem to a one-dimensional flow. This simplification requires that the aquifer be connected to a fully-penetrating stream.

On the whole, many hypotheses are necessary to study the dynamic behaviour of a groundwater flow. A laboratory experiment offers the possibility to satisfy some of them. The geometry of the aquifer is well-defined, and we can even chose to satisfy one of the Dupuit-Boussinesq conditions, the fully-penetrating geometry. Furthermore, we can measure independently porosity and permeability. Finally, we can reduce to a reasonable level the influence of surface tension. Last but not least, small laboratory setups allow to reduce the duration of the experiments, to reproduce experiments as many times as necessary, and to vary the parameters independently. In such controlled conditions, we can assess the validity of the physical and mathematical model.

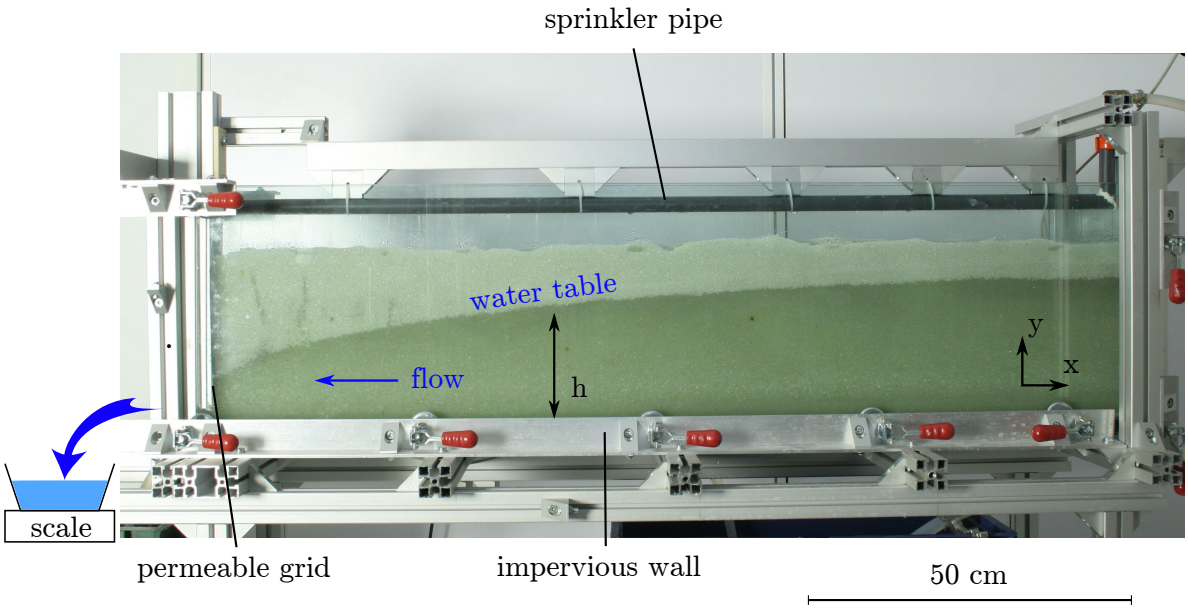

Figure 3.1: Experimental aquifer. The water table separates the unsaturated zone of porous material (light zone, above) from its saturated zone (darker zone, bottom). At the outlet, we collect water in a bucket weighed every second.

3.2 Laboratory aquifer compatible with the Dupuit-Boussinesq theory

3.2.1 Geometry

The simplest configuration of a free-surface aquifer consists of a homogeneous porous medium partly filled with water, the flow of which is confined to a vertical plane. We approximate this idealistic representation with a quasi two-dimensional tank filled with glass beads (figure 3.1). Two vertical glass plates ($143 \times 40\,\text{cm}$) separated by a 5 cm gap hold the glass beads between an impervious vertical wall (right-hand side), an impervious horizontal bottom, and a permeable grid through which water can exit the experiment (left-hand side). The impervious wall corresponds to the drainage divide of a natural aquifer, whereas the outlet of the experiment is a rough representation of the drainage network.

As we pour water onto this experimental aquifer, water infiltrates downwards, into the aquifer. As water reaches the aquifer impervious bottom, a groundwater reservoir forms and rises, and groundwater begins to exit the aquifer through the outlet.

At the outlet, we collect the water exiting the experiment with a rectangular spout about 10 cm long to drive water from the outlet to a bucket (figure 3.2). Along the vertical outlet grid, the water table height is finite — in contrast with the Dupuit-Boussinesq outlet condition (equation (2.10)). This height adjusts to the discharge it must accommodate. Typically, it is of the order of 1 mm for small discharges, up to approximately 1 cm for large discharges.

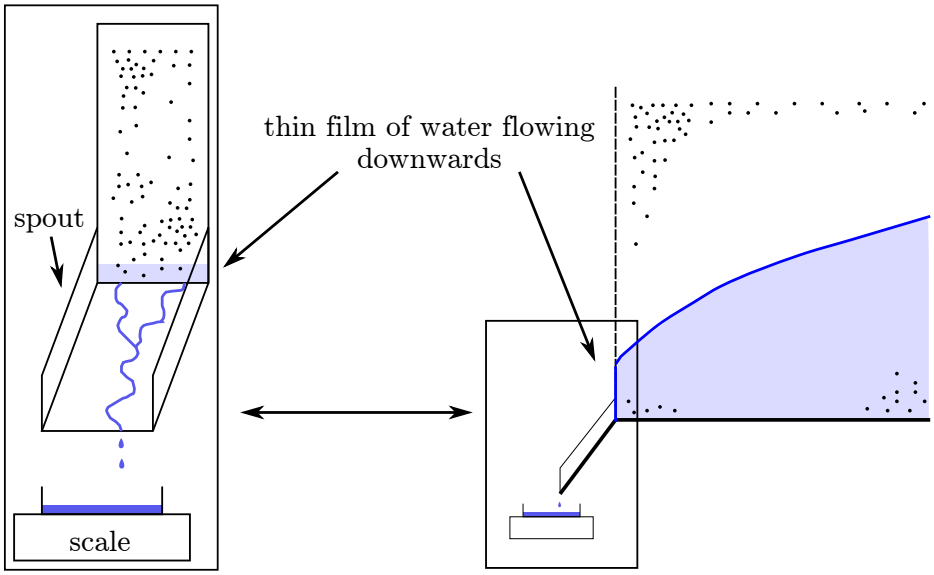

Figure 3.2: Outlet device to collect the water exiting the aquifer. Along the vertical grid, a thin film of water flows downwards, due to the finite elevation of the water table.

3.2.2 Porous material

We performed two series of experiments with different glass beads (1 mm and 4 mm), to test the influence of permeability.

3.2.2.1 Porosity

We measure the porosity of a porous material by pouring $P = 7.609\,\mathrm{kg}$ of 1 mm glass beads into a 5-litres bucket. The density of glass is $\rho = 2.5\ \mathrm{kg\,l^{-3}}$, and we thus calculate a volume of 3.04 l actually occupied by the glass beads. We then totally saturate this random packing of beads with 1.98 l of water. We thus roughly estimate the porosity $s \approx 0.39$ of the medium made with 1 mm beads. With the same procedure, we estimate $s \approx 0.42$ for the 4 mm beads.

3.2.2.2 Hydraulic conductivity

To measure the hydraulic conductivity of a porous material, we use a Darcy column. It consists of a vertical cylinder of section $S = 63.62\,\mathrm{cm^2}$, and height $H = 50\,\mathrm{cm}$ (figure 3.3). In this column, we pour a height L of glass beads. This column is supplied with water by a water tower, imposing a constant pressure at the bottom of the column. At the top of the column, a small pipe drives water towards a bucket, weighed every second to measure the discharge Q flowing out of the column (see section 3.2.4). The principle of Darcy's experiments is to impose a constant pressure head ΔH between the bottom and the top of the column, such that the discharge Q is proportional to this

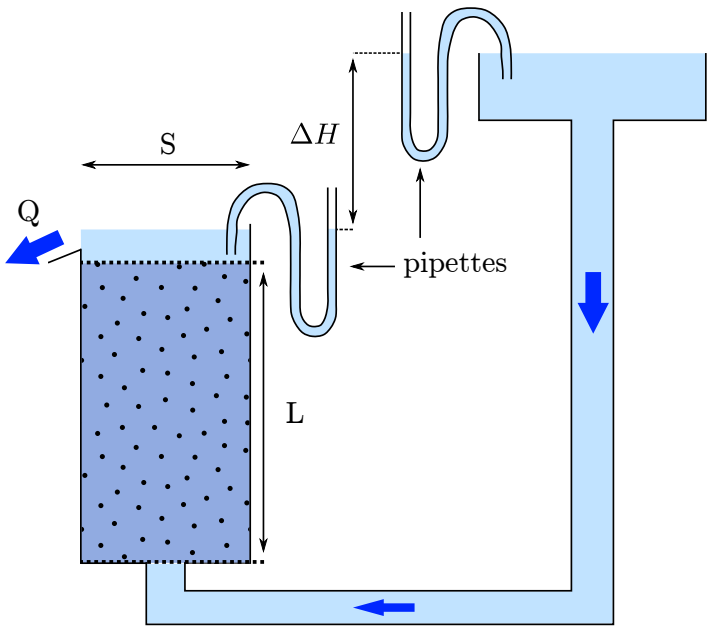

Figure 3.3: Experimental setup used to measure the permeability of the porous media.

pressure head:

$$Q = K\,S\,\frac{\Delta H}{L}. \tag{3.1}$$

The proportionality coefficient K is the hydraulic conductivity of the porous material.

To measure the pressure head difference ΔH, we connect both the water tower and the top of the column to small transparent pipettes (7 mm in diameter) with tubes filled with water, such that the water level in both pipettes reflect the water levels in both reservoirs (figure 3.3).

For a given height L of porous material, we collect a set of data points as follows. We start from a pressure head difference $\Delta H = 0$. We then progressively increase ΔH, step by step. At each step, we wait for the discharge to stabilise into a steady state regime, and measure the steady state discharge during approximately two minutes. We thus measure Q with the average discharge of this steady state, estimating the measurement error with the standard error of the measurements. During this steady state regime, we then take a picture of the pipettes and measure ΔH. Repeating this procedure at each step, we progressively increase the imposed pressure head. To avoid hysteresis, we then decrease the pressure head progressively and also perform measurements during this decrease.

For each bead size, we thus collect two data sets, with two distinct column heights L (figure 3.4). In the four data sets, the discharge increases linearly with the hydraulic head, at least for small hydraulic heads. Fitting a linear relationship over the linear parts of the data sets, and comparing the proportionality coefficient to equation (3.1), we thus obtain two measurements of K for each beads size (table 3.1).

Yet, all experiments seem to deviate from a linear relationship at large values of the pressure head. The largest the beads and the lowest the height L of porous column, the

	1 mm beads		4 mm beads	
	$L = 24.8\,\mathrm{cm}$	$L = 46\,\mathrm{cm}$	$L = 24.7\,\mathrm{cm}$	$L = 45.4\,\mathrm{cm}$
K (linear fit)	1.01	1.00	5.10	7.37
K (polynomial fit)	0.91	1.02	4.76	6.34
K (average)	0.97 ± 0.06		$K = 5.7 \pm 1$	

Table 3.1: Results of the Darcy experiments, in $\mathrm{cm\,s^{-1}}$.

strongest the deviation. We attribute this deviation to a departure from a laminar flow. Indeed, we estimate that the Reynolds number $R_\mathrm{e} = 1$ for $Q \approx 0.6\,\mathrm{g\,s^{-1}}$ with the 4 mm beads, and $Q \approx 2.5\,\mathrm{g\,s^{-1}}$ with the 1 mm beads. We thus make a second estimate of the linear part of the data sets by fitting a polynom of order two (Forchheimer, 1901). The linear component of this polynom yields a second estimate of the hydraulic conductivity for each data set, and we end up with four estimates of the hydraulic conductivity of the porous material for each beads size. Taking the mean values and maximum difference of the measurements, we thus measure a conductivity K of $0.97 \pm 0.06\,\mathrm{cm\,s^{-1}}$ for the 1 mm glass beads and $K = 5.7 \pm 1\,\mathrm{cm\,s^{-1}}$ for the 4 mm glass beads.

3.2.3 Rainfall

To simulate rainfall, a sprinkler pipe of diameter 2.5 cm is held above the tank. A series of 31 holes of diameter 1 mm spreads regularly along it, and distributes water evenly over the aquifer surface. The internal diameter is about 2.1 cm. The 31 holes are therefore tubes of length ≈ 2 mm. Limescale deposits sometimes partly plug some holes, but overall the rainwater spatial distribution is homogeneous.

As a distance of about 4.5 cm separates neighbouring holes, the spatial distribution of rainwater is discretised. Yet, as a jet of rainwater infiltrates downwards to join the groundwater reservoir, it forms a plume of width about 3 cm. This makes the groundwater recharge almost homogeneous.

Finally, we measure the rainfall rate with an electromagnetic flowmeter (Kobold, MIK-5NA10AE34R). It measures the rainfall discharge with a precision of 2%, for discharges from $0.05\,\mathrm{l\,min^{-1}}$ to $1\,\mathrm{l\,min^{-1}}$.

3.2.4 Discharge measurement

The flow exiting the aquifer is collected in a bucket weighted every second (scale Ohaus, Explorer 22) with a precision of 0.1 g. The time interval between each measurement is not exactly one second and slightly varies, so we need to record the time of each measurement. The water discharge is then simply the derivative of the bucket weight with respect to time.

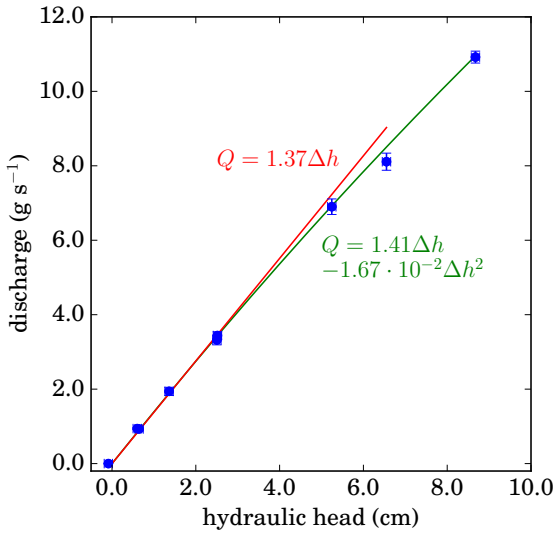

(a) 1 mm beads, $L = 46\,\text{cm}$.

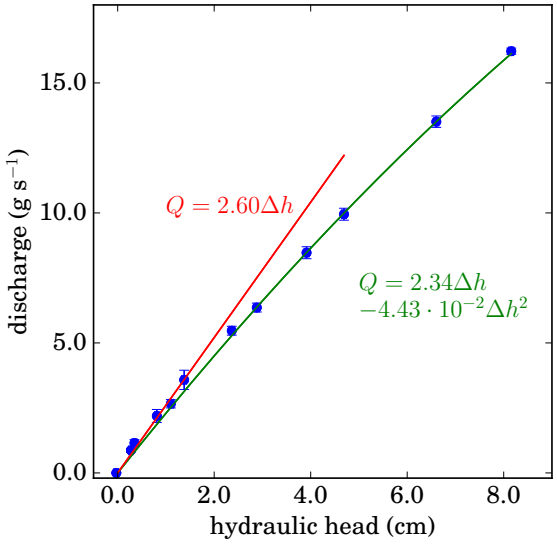

(b) 1 mm beads, $L = 24.8\,\text{cm}$.

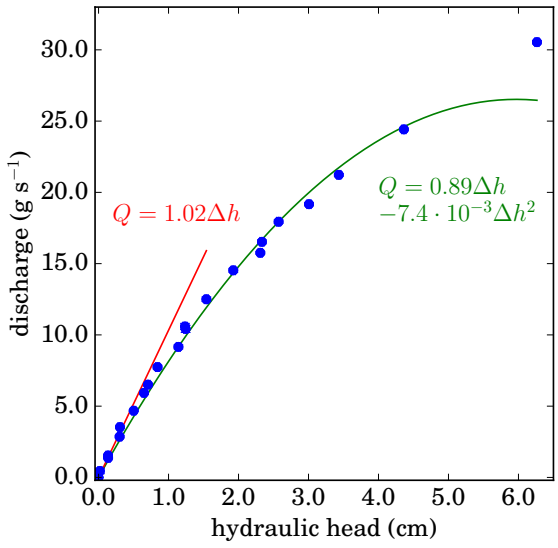

(c) 4 mm beads, $L = 45.4\,\text{cm}$.

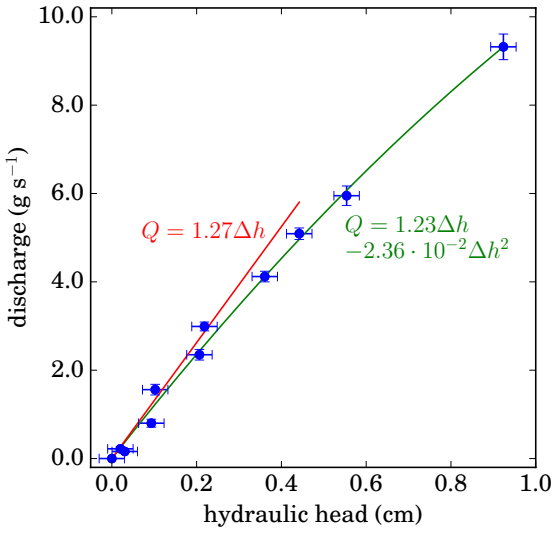

(d) 4 mm beads, $L = 24.7\,\text{cm}$.

Figure 3.4: Results of the Darcy experiments. The blue points are measurements (●), the red lines are linear fits over the first part of the data (—), and the green lines are polynomial fits of order 2 of all the data (—).

3.2.5 Surface tension

Above the groundwater reservoir, air connects the porous material to atmospheric pressure, thus maintaining the water it contains under capillary tension. For the 1 mm (resp. 4 mm) glass beads, this tension creates a capillary fringe of thickness about 4 cm (resp. 1 cm). This capillary fringe is particularly visible at the end of an experiment, when the discharge exiting the aquifer has vanished. A fringe of porous material, at the bottom of the aquifer, is still saturated with water. Capillary tension hinders this reservoir to exit the aquifer.

Surface tension exhibits a strong hysteresis (de Gennes et al., 2002). A visible consequence is that the angles of contact of a moving droplet on a solid are different at the front and at the rear (Le Grand et al., 2005; Snoeijer and Andreotti, 2013). As a result, we expect the capillary fringe height to be higher when the water table declines, and lower when the water table rises. This prevents us from locating the water table visually with good accuracy.

Finally, surface tension also plays a role at the outlet. We have chosen a grid which holes are slightly smaller than the beads. Yet, if the grid were in direct contact with air, surface tension would induce a pressure jump at the outlet. To avoid this inconvenience, we spread a soft plastic sheet over the outside of the grid. This device maintains a thin film of water at atmospheric pressure over the grid surface (suggestion of A. Daerr).

In what follows we neglect surface tension, and assume that the upper surface of the saturated reservoir is at atmospheric pressure. This free surface is referred to as the water table.

3.3 Observations

A typical experiment begins with an empty aquifer. We then switch on the rainfall and maintain its rate R constant for a few tens of seconds. Rainwater infiltrates vertically through the porous material until it reaches the bottom of the tank, where its accumulation forms a reservoir. As the water table expands to accommodate more rainwater, the asymmetry of the boundary conditions causes it to curve towards the aquifer outlet. The resulting pressure field pushes the water out of the aquifer, generating a discharge Q.

We performed two series of experiments, with the rainfall ranging from $1.67\,\mathrm{ml\,s^{-1}}$ to $42\,\mathrm{ml\,s^{-1}}$ for the 1 mm beads, and from $2\,\mathrm{ml\,s^{-1}}$ to $35\,\mathrm{ml\,s^{-1}}$ for the 4 mm beads.

We observed the same behaviour in all cases: a few seconds after the beginning of rainfall, the water discharge exiting the aquifer rises quickly, until the rainfall stops (figure 3.5a). At this point, the discharge suddenly decreases, and then relaxes slowly towards zero. As observed in the hydrograph predicting by the Dupuit-Boussinesq theory (figure 2.3), we observe three regimes: a storm flow, an early stage of drought flow where the discharge decreases rapidly, and a late stage of drought flow where the discharge decreases slowly. This laboratory hydrograph resembles both the numerical hydrograph, and typical river hydrographs (figures 4.9, 7.3 and 7.9).

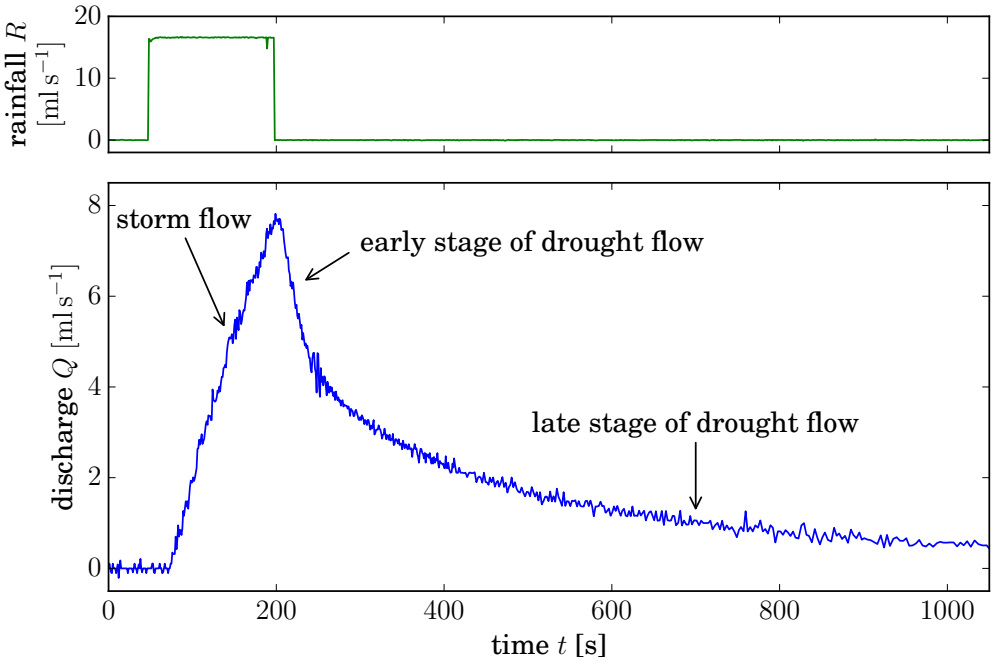

(a) Hydrograph realised by stopping rainfall during the storm flow.

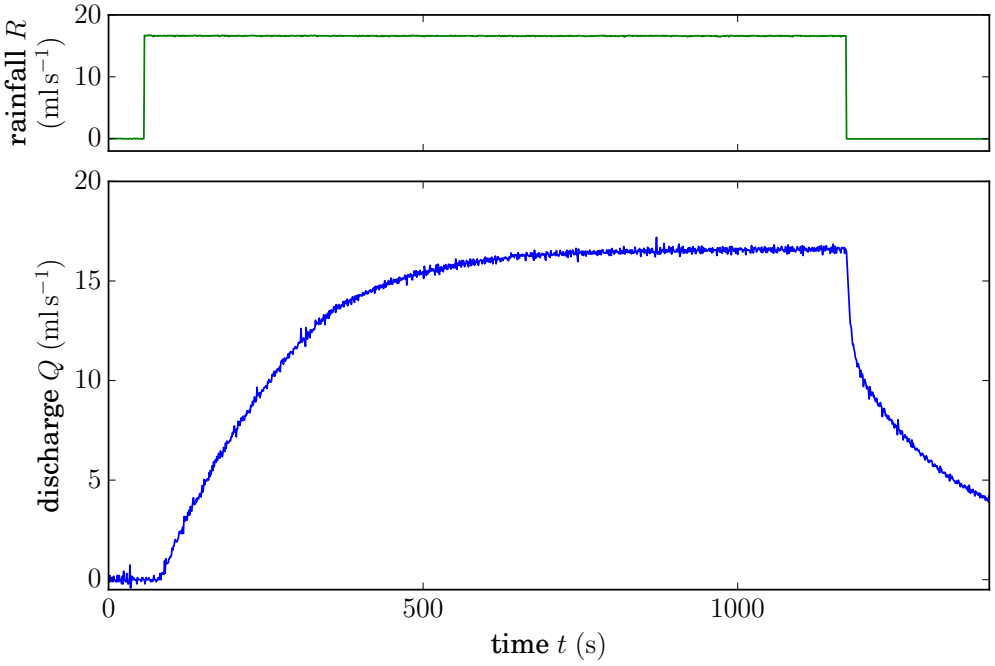

(b) Hydrograph realised by imposing a constant rainfall rate until saturation of the discharge.

Figure 3.5: Rainfall rate R imposed to our laboratory aquifer (green line, top), and water discharge Q exiting the experiment (blue line, bottom). Measurements are collected at 1 Hz, with a precision of about 0.1 g s^{-1}. In this experimental run, the porous reservoir is made of 1 mm glass beads.

Of course, if we maintain a constant rainfall during a sufficiently long time (about 4 minutes for the 4 mm beads, and 15 minutes for the 1 mm beads), the water discharge will eventually saturate to equal the rainfall input (figure 3.5b). At this point, the water table shape is stationary. At the groundwater divide (right-hand side), its maximum elevation increases with the rainfall rate. Yet, it reaches approximately 10 cm (respectively 25 cm) for the 4 mm (respectively the 1 mm) beads.

In the experiment of figure 3.5a, the water discharge increases about 40 s after the beginning of the rain. We observe a similar time lag in every experiment. We interpret it as the travel time of rainwater trough the 40 cm of unsaturated porous medium which separate the aquifer's surface from its bottom. This would imply that the rainwater infiltration velocity through the unsaturated porous material is about $1\,\mathrm{cm\,s^{-1}}$. This velocity is indeed consistent with the measured conductivity of the saturated aquifer, although one could expect the porous media to be less permeable when unsaturated.

In the next section, we focus on the drought flow of this laboratory aquifer. The purpose is to confirm experimentally the asymptotic regime of the Dupuit-Boussinesq theory concerning the late stage of the drought flow (equation (2.29)).

3.4 Experimental drought flow: comparison with the Dupuit-Boussinesq theory

When the rain stops, the water discharge relaxes slowly towards zero. Here, we compare this drought flow with the Dupuit-Boussinesq asymptotic regimes derived in section 2.3. Reproducing the early stage of the drought flow which corresponds to the early-times asymptotic regime (equation (2.23)) requires to saturate completely the experimental aquifer with water, as in section 2.3.2.2. This condition was difficult to realise with our experimental setup, and we only reproduced the late stage of the drought flow.

In a fully-penetrating configuration, the Dupuit-Boussinesq theory predicts that the discharge decreases as $1/t^2$ during this drainage regime (section 2.3, equation (2.29)). More precisely, the asymptotic regime at long times reads:

$$Q \sim a_d \frac{s^2\, W\, L^3}{K\, t^2} \tag{3.2}$$

where $a_d \approx 0.693$ is a mathematical constant, s is the porosity, W and L are the width and the length of the aquifer, and K is the hydraulic conductivity.

We test this prediction by imposing a constant rainfall rate $R = 34\,\mathrm{ml\,s^{-1}}$ during several minutes, until we reach steady state. We then stop the rainfall, and measure the discharge during more than one day for the 1 mm beads, and almost two days for the 4 mm beads. With the two porous materials, we perform two drainage experiments. Figure 3.6 shows the discharge evolution averaged over two experiments, for the two porous materials.

At the end of the experiments, the discharge reaches $10^{-5}\,\mathrm{ml\,s^{-1}}$, which corresponds approximately to one droplet every ten minutes (for a droplet of radius 1 mm). The scale

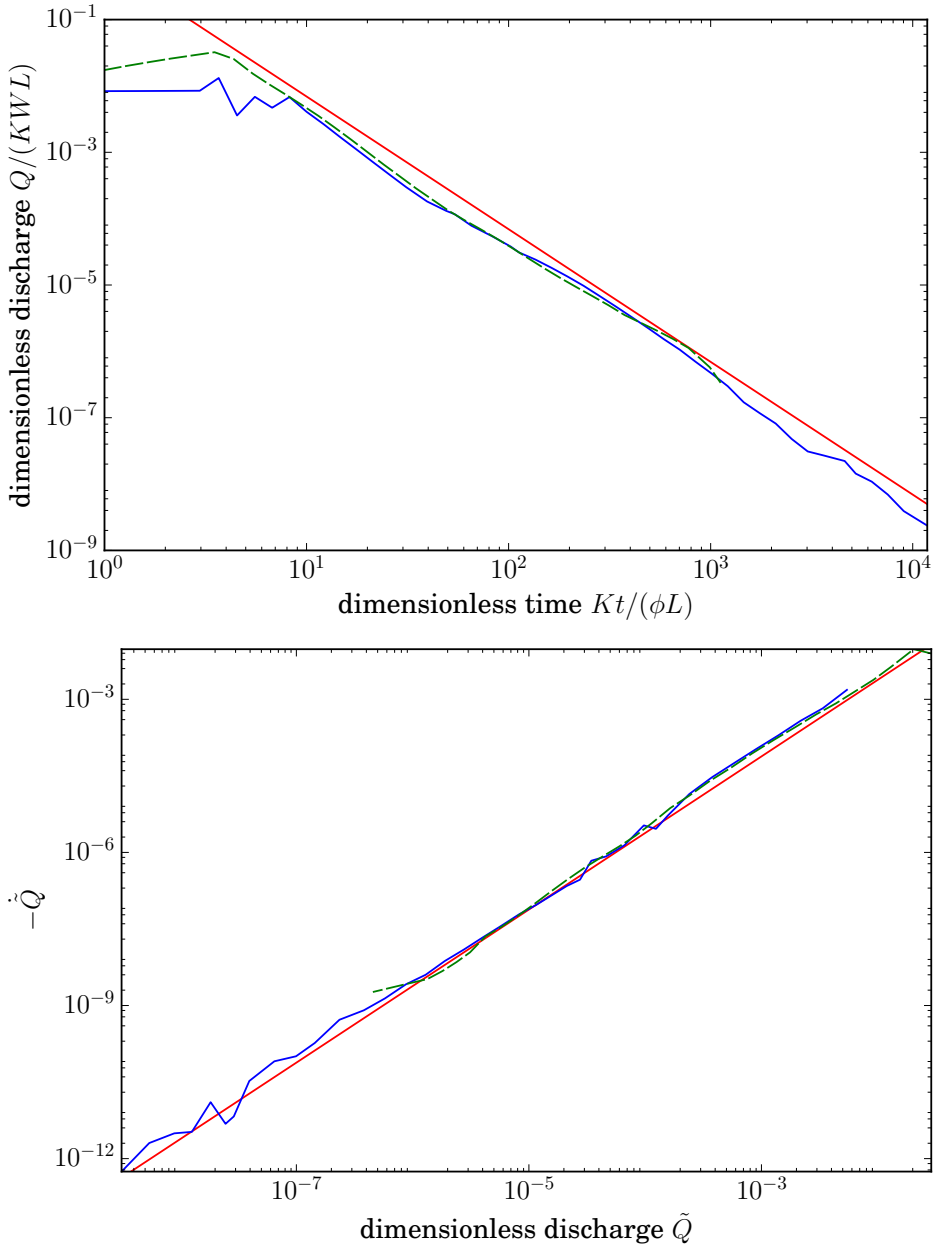

Figure 3.6: *Top:* Evolution of the water discharge after rainfall has been switched off (blue solid line (—): 4 mm glass beads, green dashed line (- - -): 1 mm glass beads). The red line represents the asymptotic regime (3.2). *Bottom:* Negative time derivative of the discharge with respect to the discharge, as suggested by (Brutsaert and Nieber, 1977) (see section 2.3.3). The red line is the 3/2 power law of equation (3.2), without any fit parameter.

cannot measure such a low discharge. As a consequence, we increase logarithmically the time between each measurement. At the beginning the measurement time interval is one second. After two days of experiment, the time interval is about three hours.

At the end of one experiment (with 1 mm beads), the measured discharge is (slightly) negative, of the order of $3 \cdot 10^{-4}\,\mathrm{ml\,s^{-1}}$. This is certainly due to evaporation in the outlet bucket.

To compare the drainage regime of the two porous materials, we scale out the the permeability in equation (3.2):

$$\frac{Q}{K\,W\,L} = a_d \left(\frac{s\,L}{K\,t}\right)^2 . \tag{3.3}$$

Our experimental aquifer conforms well with the drought flow of the Dupuit-Boussinesq theory (figure 3.6). After appropriate rescaling, the relaxation of the water discharge appears to be independent of the aquifer permeability. Without any fit parameter, the two drainage regimes conform well to the theoretical prediction. Fitting a power law to the data after the transient ($Kt/(sL) > 10$) yields an exponent of -1.87 ± 0.03, comparable with the theoretical exponent. We estimate the error on the exponent by estimating a lowest and highest value of the exponent. The lowest value is obtained with the minimisation of the horizontal distance of the data points to the fit function, and the highest value with the vertical distance. Now assuming the exponent is exactly -2, the data is best fitted with a prefactor of 0.48 ± 0.2, again in reasonable agreement with the theoretical value of $a_d = 1.177$.

Based on Brutasert and Nieber's method (section 2.3.3), we also plot the negative time derivative of the rescaled discharge with respect to the discharge (figure 3.6). In this plot, we expect the late stage drought flow to conform to a 3/2 power law (table 2.1). Fitting a power law to the data after the transient ($Kt/(sL) > 10$) yields an exponent of 1.502 ± 0.002, in good agreement with the theoretical exponent. Assuming this exponent is exactly 1.5, the data is best fitted with a prefactor of 3.10 ± 0.1, again in reasonable agreement with the theoretical value of $2/\sqrt{a_d} = 2.402$.

The mismatch between theory and observation is hardly distinguishable from the experimental noise, thus supporting the use of the Dupuit-Boussinesq approximation to interpret the drought flow of our experimental aquifer. Yet, the breakdown of the Dupuit-Boussinesq approximation near the outlet indicates that the two-dimensionality of the flow might play a significant role there (section 2.3, equation (2.11)). Indeed, a two-dimensional description of the flow could account for the finite height of the water table observed along the outlet grid, as described in section 3.2.1. We will show, in section 8.3.1.4, how matching asymptotically a two-dimensional flow near the outlet with the Dupuit-Boussinesq solution far from the outlet could alter the prefactor of equation (3.2).

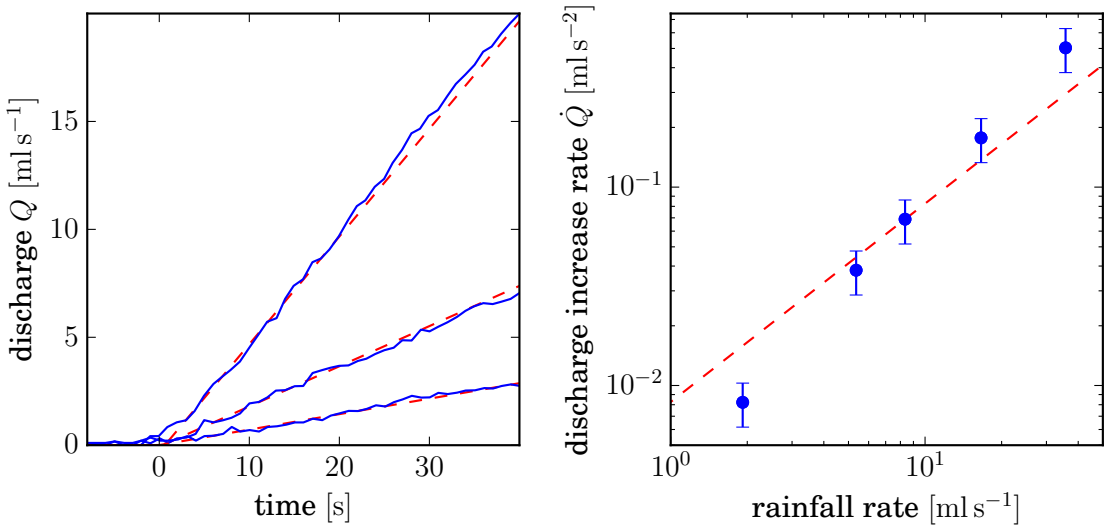

Figure 3.7: *Left*: Increase of the water discharge just after the beginning of rainfall for various rainfall rates (solid blue lines, $R = 36.7$, 16.8 and 8.3 mL s^{-1} from top to bottom). The curves are shifted horizontally so that time is zero at the beginning of the discharge increase. For each run, a linear increase is fitted to the data (dashed red lines). *Right*: Dependence of the discharge increase rate on the rainfall rate (blue dots). A linear relationship is fitted to the data for comparison (dashed red line). In this series of experiments, the porous reservoir is made of 4 mm glass beads.

3.5 Experimental storm flow

We now focus on the storm flow of our laboratory hydrograph. After the rainfall rate has started, rainwater infiltrates downwards through the porous material. Once the rainwater has reached the bottom of the aquifer, the discharge at the experiment's outlet appears to increase linearly with time (figure 3.7). This observation holds over the entire range of rainfall rates we were able to investigate (from 2.4×10^{-5} to 5.8×10^{-4} m s^{-1}).

A simple reasoning might explain the linear increase of the discharge during rainfall: far from the outlet, the water table moves upwards in proportion to the water input, that is Rt, and arguably so does the pressure in the reservoir. Assuming discharge is simply proportional to the pressure in the reservoir, we conclude that the discharge increase rate should be constant, and proportional to the rainfall rate R.

We can measure the discharge increase rate $\dot{Q}$ by fitting a linear relation to the data, at the beginning of an experimental run (figure 3.7). Repeating this procedure for various rainfall rates, we find that the discharge increase rate is a growing function of the rainfall rate. This relationship, however, is not linear, and resembles a power law with an exponent larger than one (figure 3.7, right). This finding contradicts the simple reasoning based on the linear pressure increase, thus suggesting that the discharge is not proportional to the elevation of the water table far from the outlet.

The non-linear relation between discharge and pressure is likely to be the signature of a free-surface flow. Indeed, when the geometry of the flow is confined, Darcy's law

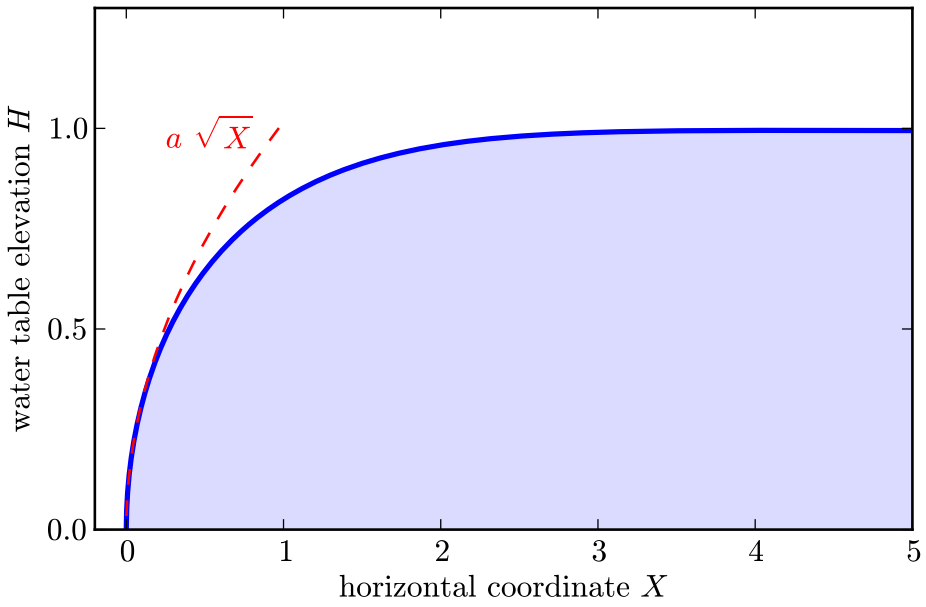

Figure 3.8: Numerical solution of equation (3.7), corresponding to the self-affine shape of the water table during the early stage of a rain event (blue line). Its behaviour near the aquifer outlet is $a\sqrt{X}$ (red dashed line).

leads to a linear response of the aquifer. To the contrary, when the shape of the water table adjusts to the flow conditions, its dynamics influences the aquifer's response to rainfall.

3.6 Early response to rainfall: asymptotic regime of the Dupuit-Boussinesq equation

The Dupuit-Boussinesq equation reads

$$s\,\frac{\partial h}{\partial t} = \frac{K}{2}\,\frac{\partial^2 h^2}{\partial x^2} + R\,, \tag{3.4}$$

where R is the rainfall rate. Our experiments suggest a power-law relationship between the discharge increase rate and the rainfall rate during the early stage of a rain event (figure 3.7). This is an incentive to look for the asymptotic behaviour of the Dupuit-Boussinesq equation at the beginning of rainfall.

We expect the groundwater flow to be insensitive to the boundary far from the outlet, and therefore the water table elevation should increase as Rt/s, where the time t is set to zero when rainwater reaches the bottom of the experiment. In contrast with the simple reasoning of section 3.5, we now propose a self-affine shape for the water table:

$$h(x,t) = \frac{Rt}{s}\,H\left(X\right)\,, \tag{3.5}$$

where X is a new variable, which depends on x and t. The purpose of this new variable is to transform the partial differential equation (3.4) into an ordinary differential equation. For that purpose, we assume a self-affine expression $X = x/t^\beta$, and introduce the self-affine shape (3.5) into the Dupuit-Boussinesq equation (3.4). We thus find $\beta = 1$. Finally, the self-affine variable

$$X = \frac{s\,x}{t}\sqrt{\frac{2}{K\,R}}\,, \tag{3.6}$$

together with the self-affine shape H, transform the Dupuit-Boussinesq equation into a parameterless ordinary differential equation:

$$H\,H'' + H'^2 + \frac{1}{2}\,(X\,H' - H + 1) = 0\,. \tag{3.7}$$

The boundary condition at the outlet (equation (2.10) in section 2.2) translates into $H(0) = 0$, while the steady rise of the water table far from the outlet formally reads

$$\lim_{X\to+\infty} H = 1\,. \tag{3.8}$$

This boundary condition is valid as long as the impervious boundary is far from the outlet, compared to the characteristic length of the flow. Mathematically, $t \ll s\,L/\sqrt{K\,R}$ (for the experiment of figure 3.5a, $t \ll 400\,\mathrm{s}$).

We are not aware of any analytical solution to the above problem, and therefore we approximate H numerically (figure 3.8). With the same arguments as in section 2.3.2, we expect a singularity in $X = 0$: as $H = 0$, the slope H' must be infinite to accommodate a finite discharge. In equation (3.7), we therefore expect, at first order, the two left terms to dominate close to zero:

$$H\,H'' \sim H'^2 \quad \text{when} \quad X \to 0\,. \tag{3.9}$$

This implies that H adopts a square root shape near the outlet:

$$H \sim a\,\sqrt{X} \tag{3.10}$$

where a is a constant adjusted to satisfy the far-field boundary condition (3.8). Using a numerical shooting method to do so, we find $a \approx 1.016$.

To the self-affine regime of the groundwater flow at early time corresponds the following water discharge, in dimensional form:

$$Q(t) \sim a^2\,\frac{W}{s}\,\sqrt{\frac{K}{2}}\,R^{3/2}\,t \tag{3.11}$$

where W is the width of the aquifer. The above expression is encouraging, as it features the linear time dependence of the discharge we observe in experiments. Furthermore, the prefactor of this relation includes the rainfall rate R to a power larger than one, again in qualitative agreement with observations (figure 3.7).

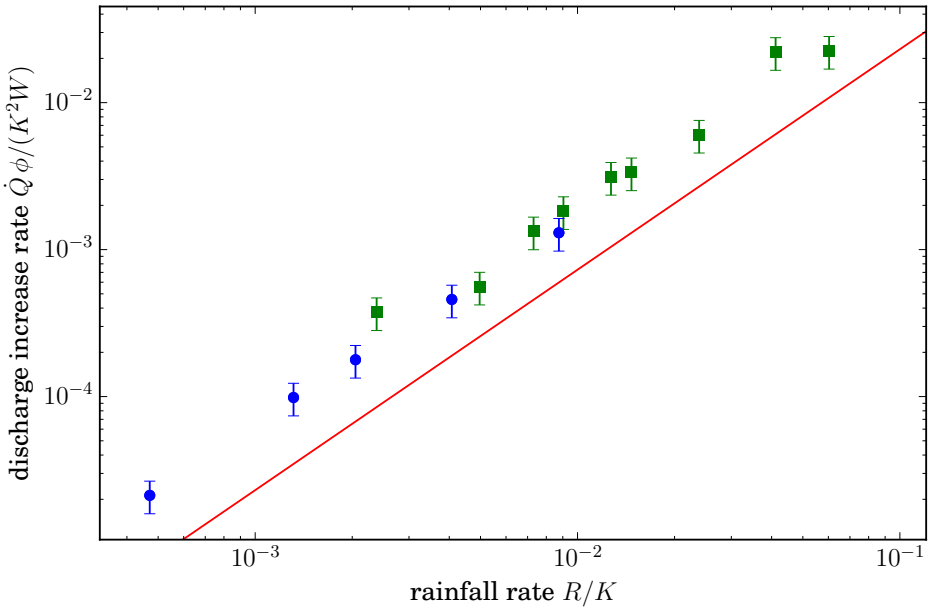

Figure 3.9: Dependence of the discharge increase rate with respect to the rainfall rate, for two series of experiments: 4 mm glass beads (blue dots) and 1 mm glass beads (green squares). The red line represents the asymptotic regime (3.12).

To further compare this asymptotic regime to observation, we supplement the data of figure 3.7 with similar experiments involving a less permeable aquifer, made of 1 mm glass beads. Equation (3.11) suggests that the permeability K be scaled out of the data:

$$\frac{\dot{Q}\,s}{K^2\,W} \sim \frac{a^2}{\sqrt{2}}\left(\frac{R}{K}\right)^{3/2}. \tag{3.12}$$

Indeed, when rescaled according to the above expression, the discharge increase rate and the rainfall rate from all experiments gather around the same relation, regardless of permeability (figure 3.9). Fitting a power law through the data yields an exponent of 1.47 ± 0.01, in reasonable accordance with the $3/2$ exponent of the asymptotic regime. Here again, we estimate the error on the exponent by estimating a lowest and highest value of the exponent. The lowest value is obtained with the minimisation of the horizontal distance of the data points to the fit function, and the highest value with the vertical distance. Assuming the asymptotic exponent is correct, the data are best fitted with a prefactor of 2.0 ± 0.1, that is about three times the theoretical value of 0.73.

The asymptotic regime resulting in equation (3.12) explains the scaling of the discharge increase rate with both the rainfall rate and the conductivity, throughout the range of parameters we were able to explore experimentally. The overestimate of the drainable porosity could explain part of the mismatch between the theoretical prefactor and our measurements, though not all of it (section 2.2).

This mismatch does not depend on the rainfall rate, nor on the conductivity of the aquifer, which points to a geometrical effect. The breakdown of the Dupuit-Boussinesq approximation near the outlet could play a significant role here, which could affect

boundary condition (2.10) and alter the prefactor of equation (3.11).

3.7 Conclusion

The experiment presented here supports the use of the Dupuit-Boussinesq approximation to describe the response of an aquifer to a rainfall event. In particular, it correctly predicts the increase of the groundwater discharge at the beginning of rainfall, and reveals an unexpected asymptotic behaviour: the discharge increase is proportional to the rainfall rate to the power 3/2.

If its validity extends to field situations, this strong dependence would induce a fast groundwater contribution to the discharge of rivers, especially under intense rainfall. Therefore its consequences in terms of flood predictions deserve detailed scrutiny. An ideal field site to assess the contribution of this asymptotic regime would be dominated by groundwater hydrology, with negligible surface run-off. In such site, our new asymptotic regime could contribute to determine the hydrological parameters of the aquifer, adding a supplementary constraint to the drought flow analysis developed by Brutsaert and Nieber (1977).

However, even in a simplified laboratory experiment, the fast dynamics of a free-surface aquifer requires more investigations. Indeed, our experiment shows a slight mismatch between the numerical factors yielded by the Dupuit-Boussinesq approximation and measurements. We speculate that the two-dimensionality of the flow might come into play near the outlet, thus changing the effective boundary condition there.

Finally, under natural conditions, various phenomena excluded from the present analysis, such as surface tension, heterogeneities of the aquifer and evapotranspiration, are likely to play a significant role. In the next chapter, we present a field experiment to assess the Dupuit-Boussinesq theory in the field.

Part III

Response of a natural aquifer to rainfall

Chapter 4

The Quiock Creek field experiment

Contents

In the previous chapter, we have studied the dynamics of a groundwater flow in controlled and simplified conditions, and assessed the validity of asymptotic regimes of the Dupuit-Boussinesq equation. These asymptotic regimes resulted in predictions on the dynamics of the discharge delivered by an aquifer to a river. In field situations, the complexity of natural aquifers could break several of the hypotheses satisfied in the laboratory experiment. This questions the validity of our predictions in natural aquifers.

To test these predictions, we need to measure simultaneously the discharge of a river, the water table profile, and the rainfall rate. These measurements must be acquired at high frequency to capture quick flood events. They must also cover a duration long enough to analyse many events. To our knowledge, there exists no such data set in the literature. This is why we have developed a field experiment in the Quiock Creek catchment, in Guadeloupe.

The first objective of this field experiment is to observe qualitatively the behaviour of the groundwater flow. To do so, we measure a water table profile perpendicularly

to the river. Second, the analysis of the Dupuit-Boussinesq equation suggests that a groundwater flow reacts rapidly to rainfall events, and can generate quick floods. We measure the water table elevation and the river discharge at short time intervals, to confirm that their dynamics is comparable.

In this chapter, we present our field set-up, and qualitative results from this experiment.

4.1 Field site

4.1.1 Catchment

The Quiock Creek is located on Basse-Terre, a volcanic island of the Guadeloupe archipelago, in the French West Indies. It is a small tributary of the Bras-David river, in the center of the primary tropical rainforest of the Guadeloupe National Park. Where both rivers join, the Bras-David river drains approximately nineteen km^2, with a mean discharge of $8.5\,m^3\,s^{-1}$ (figure 4.1).

The Quiock Creek flows over a heavily weathered aquifer. A 12.5-metres deep ground profile revealed a very homogeneous material mostly composed of clay (about 70%, mainly halloysite and kaolinite) and of secondary minerals (essentially Fe(III)-hydroxides (about 19%)) (Buss et al., 2010). The rest is composed of primary minerals (quartz, feldspar and cristobalite), predominantly found in the first 30 cm beneath the surface. This ferralitic regolith, which develops on Pleistocene andesitic pyroclastic deposits, is often thicker than 15 metres on the Basse-Terre island (Clergue, 2015). It is considered to be reasonably permeable (Colmet-Daage and Lagache, 1965).

Using the Whitebox Geospatial Analysis Tool[1], we find that the drainage area of the Quiock Creek is 7.86 hectares at the point where we record the discharge, with about 979 m of channels (section 6.2.5). To calculate these values, this software uses a digitised elevation model (DEM), which gives the earth surface elevation on a $5 \times 5\,m$ grid[2]. An algorithm associates each point of the grid with a flow direction: towards its lowermost neighbour (or, equivalently, towards the maximum slope). Then, a specific point of the drainage network collects the flow from a given number of pixels. All these pixels define the catchment associated to this specific point. This catchment is therefore associated to overland flow. However, nothing forces groundwater to flow in the direction of the ground surface maximum slope. The area drained by the groundwater flow and the overland flow catchment therefore possibly differ (figure 1.7). In the following, we assume that their orders of magnitude are comparable.

Overall, the Quiock Creek catchment combines several characteristics favourable to test the asymptotic regimes of the Dupuit-Boussinesq equation. First, the Quiock Creek drains a small area on homogeneous ground, limiting the possible influence of heterogeneities. Moreover, as the channels are relatively short, the flood waves within the stream are likely to play a minor role on the floods dynamics. Second, the smooth

[1] `http://www.uoguelph.ca/~hydrogeo/Whitebox/`

[2] This model results from a Litto3D campaign (`http://professionnels.ign.fr/litto3d`).

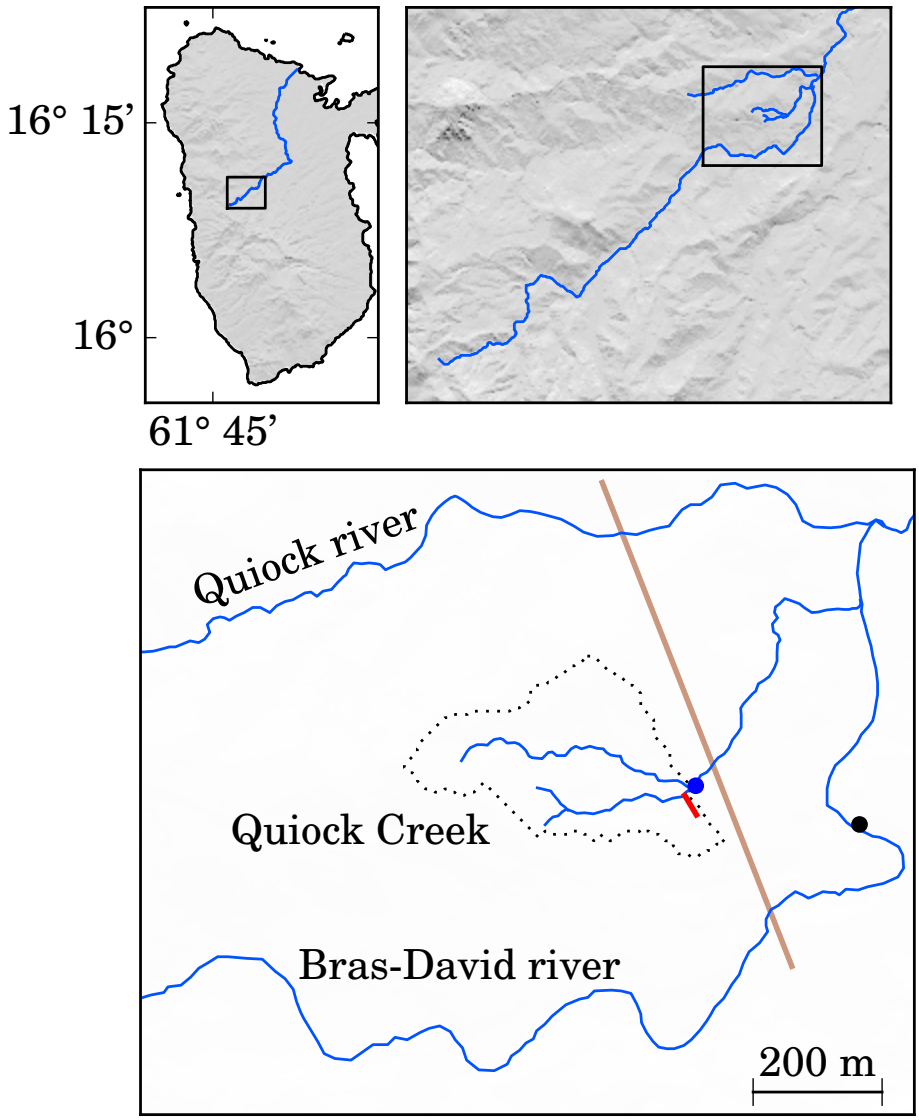

Figure 4.1: Field installation in the Basse-Terre island (Guadeloupe, lesser Antilles). We measure the discharge of the Quiock Creek with a Venturi flume (●). Where we measure the discharge, the river approximately drains eight hundred metres of channels over about eight hectares (catchment area delimited by the dotted line (···)). We measure the water table with six piezzometers located besides the Ravine Quiock river along the transect (—) (see figures 4.7 and 4.10). A rain gauge measures the rainfall rate close to the piezzometers. A station additionally measures the Bras-David river discharge continuously, as well as the rainfall rate outside the forest (●). At last, figure 4.2 shows the topography around the Quiock Creek along the transect (—), seen from the left (see section 4.1.2).

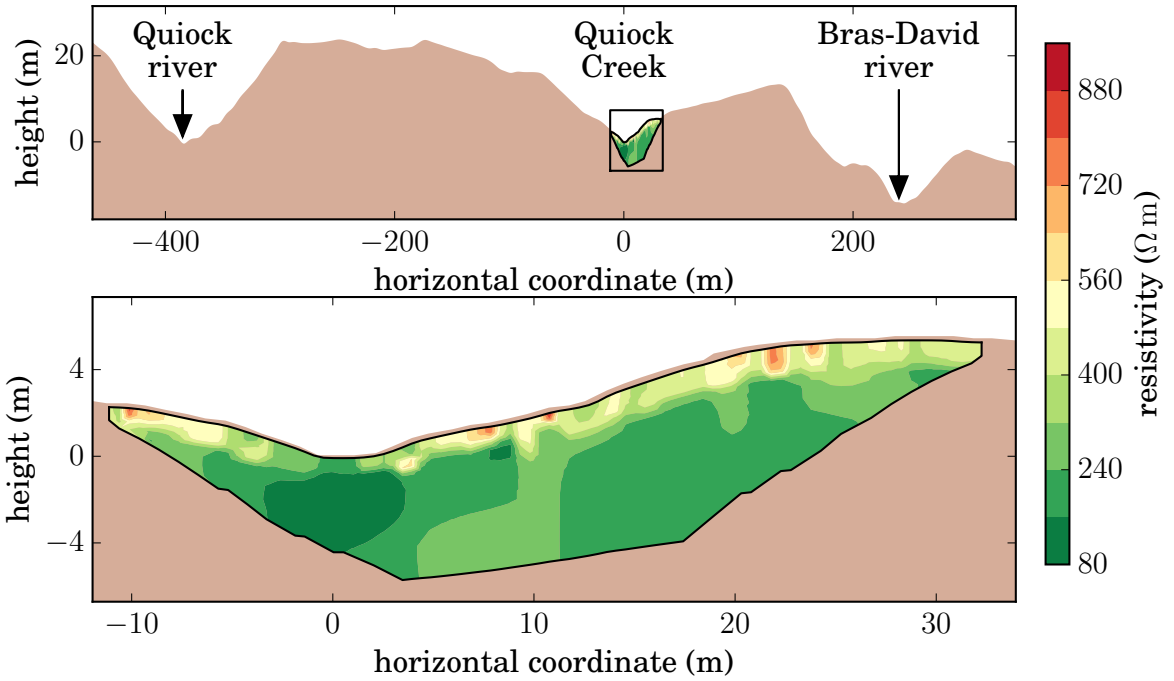

Figure 4.2: Surface topography along a transect perpendicular to the river (see figure 4.1) (*top*) and tomographic profile (*bottom*). In the top graph, the surface topography is derived from a 5×5 m digitised elevation model (DEM). We measured the topography of the bottom graph more precisely, with a laser pointer (which measures the distance and angle to a given target).

topography of the ground does not present any mark of overland flow. In addition, the creek flows throughout most of the year, even after long drought periods. These two points suggest a significant contribution of groundwater to the discharge of the Quiock Creek. Third, the loose constitution of the weathered rock allows to dig easily into the ground, which facilitates the monitoring of the water table. Finally, the Observatoire de l'eau et de l'érosion aux Antilles (ObsErA[3]) has been studying chemical weathering on this site for four years now (Lloret, 2010; Clergue, 2015). The existence of this INSU-CNRS observatory allows to maintain the site and to collect data frequently (thanks to C. Dessert, T. Kitou, V. Robert and O. Crispi). Moreover, our hydrological data should soon be complemented with chemical data.

4.1.2 Aquifer geometry

The geometry of an aquifer strongly influences the groundwater flow. In particular, the Dupuit-Boussinesq theory assumes a fully-penetrating stream. To investigate the structure of the Quiock Creek aquifer, we used electric resistivity tomography (ERT). With this technique, one can assess the homogeneity of the aquifer and localise the hypothetic aquifer impervious bottom. We performed this tomography profile in a field

[3] `https://morpho.ipgp.fr/Obsera/Home`

campaign in collaboration with A. Quiquerez (Université de Bourgogne), V. Langlois, P. Allemand and P. Grandjean (Université Lyon 1).

The ERT method consists in imposing an electrical current in the ground with a pair of electrodes (Chevigny, 2014). The electrical potential is then measured at various locations on the ground surface with a second pair of electrodes. Repeating this procedure along a transect, we end up with an inverse problem which solution yields an estimate of the electrical resistivity in the ground (Loke, 1999).

The resistivity of a ground layer depends on its mineral composition, on its structure, and on its water content. Typically, the resistivity of groundwater is expected to be between 10 and 100 Ω m (Samouëlian et al., 2005). The resistivity of an unsaturated ground is generally larger, but highly variable, and depends strongly on its water content. Typically, the resistivity of clay varies from 10 Ω m with a high water content, up to a few hundreds of Ω m if it is dry (Samouëlian et al., 2005). The resistivity also depends on the soil properties, such as its structure or its mineralogy. We therefore expect a resistivity profile to show abrupt variations at interfaces between two layers of different composition.

We placed 24 electrodes spread every two metres along a transect perpendicular to the river. With this set-up, we could measure the resistivity of the ground down to 6 m below the ground surface (figure 4.2). The soil profile reveals a surface layer of about 0.5 - 1 m in depth with a relatively high resistivity, between 400 and 900 Ω m. This surface layer probably corresponds to the organic material extracted at the beginning of the drillings (section 4.2.3), although it could also be due to biased measurements close to the electrodes (A. Quiquerez personal communication). Under this surface layer, the resistivity profile shows little variation, between 80 and 320 Ω m. This range of resistivity is consistent with the dry clay observed in the material extracted from the boreholes (section 4.2.3), and reported by Buss et al. (2010). The resistivity profile thus suggests that the Quiock Creek aquifer is homogeneous, in agreement with Buss et al. (2010).

However, this soil profile also points to the absence of a bottom layer below the river. In addition to this tomography profile, we have drilled six boreholes along this transect, at several distances from the river. The boreholes depth reached up to six metres down the ground surface, and the material extracted from drilling appeared homogeneous to the eye. This second observation supports the idea that the aquifer impervious bottom, along this particular transect, is deeper than four metres below the river.

4.2 Field installation

We developed this field experiment to collect high-frequency measurements of the water table elevation, of the river discharge and of the rainfall rate, to compare their dynamics. Here, we present our measurement procedure.

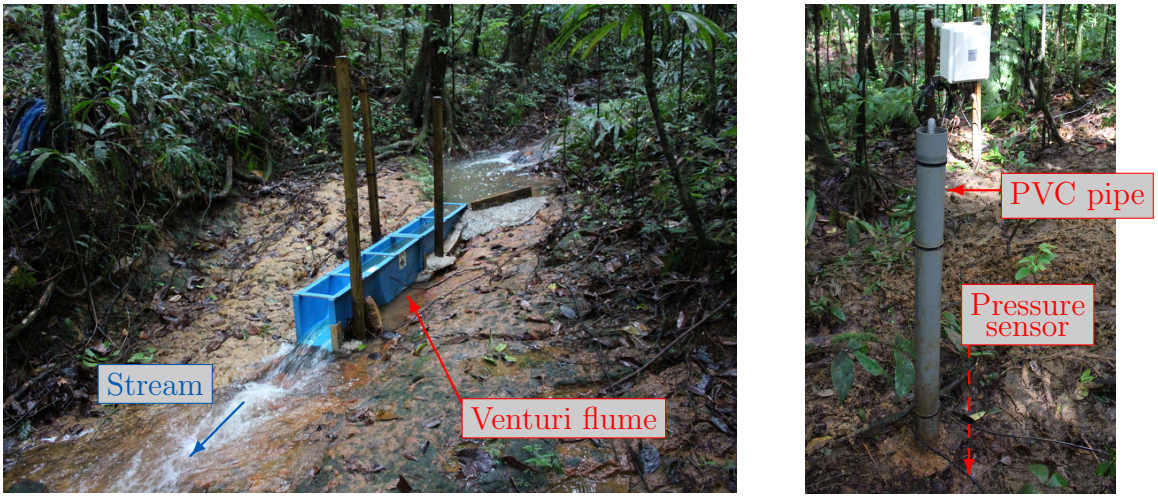

Figure 4.3: *Left:* Measurement of the river discharge with a Venturi flume. The relation between water height and water discharge is calibrated. *Right:* A PVC pipe is introduced in a borehole to prevent its collapse. At the bottom of the borehole, a pressure sensor measures the water level (see figure 4.7).

4.2.1 Rainfall measurement

We measure the rainfall rate with a tipping-bucket rain gauge. Rainfall fills a bucket which tips over after 0.2 mm of cumulated rainfall. Every minute, we record how many times the bucket has tipped over, obtaining a volume of rainfall every minute. We then sum this volume over a sampling period of five minutes, and divide it by the sampling period to obtain the rainfall rate.

A dense vegetation covers the catchment, and large trees intercept part of the rainfall. As a result, a rainfall rate measured within the forest of the catchment could differ from the actual rainfall rate. To test the influence of the forest on our rainfall measurements, we measure the rainfall rate at two different locations. A first weather station is located within the forest, near the Quiock Creek (figure 4.1). A second weather station is located outside the forest, near the Bras-David river station (black point in figure 4.1), and a few hundred meters far from the Quiock Creek. This station is close enough to the Quiock Creek catchment to assume that it records the local rainfall rate.

Outside the forest, the Bras-David weather station has been measuring the rainfall rate outside the forest since November 2011. These measurements confirm the Météo France estimations of an average 3500 $\mathrm{mm\,yr^{-1}}$, with small seasonal variations (the wet season, from July to December, can be twice as rainy as the dry season) (Lloret et al., 2013). Estimations by Clergue (2015) reveal that the volume recorded outside the forest is only 12% larger than within the forest. Hereafter, we use the "within-forest" measurements.

Finally, the evapotranspiration is estimated to be around 60%, typical of tropical rainforests (Clergue, 2015).

4.2.2 Discharge measurement

We began to monitor discharge of the Quiock Creek in September 2014. To do so, we force the stream to flow through a Venturi flume (ISMA, exponential cross section Type III, measurement range) (figure 4.3). The Venturi flume is a $19 \times 26.6 \times 250\,\mathrm{cm}$ epoxy channel. Its rectangular cross section contracts about 62.5 cm upstream from its outlet, and expands again to a rectangular shape about 40 cm upstream from its outlet. The principle of such flume is to measure the height of water upstream of the contraction. This height h depends on the stream discharge Q, in a relationship which has been calibrated by the manufacturer (figure 4.4). A polynomial fit of the calibration data points made by the manufacturer reads

$$Q \approx -0.597\,h + 1156.49\,h^2 - 1126.96\,h^3 + 6552.4\,h^4\,, \tag{4.1}$$

where the discharge is in $\mathrm{m^3\,h^{-1}}$, and the height in m. The stream level consequently rises as the discharge flowing into the flume increases. Fitting a power law to these data points yields an exponent of 1.93, i.e. close to 2. Manufacturing defects can induce measurement errors of about 3%.

The exponential cross section of the contraction allows to measure a large range of discharges. The minimum height giving a reliable discharge is 2.9 cm and corresponds to a discharge of $0.93\,\mathrm{m^3\,h^{-1}}$, and the maximum height is 26.6 cm and corresponds to a discharge of $93.26\,\mathrm{m^3\,h^{-1}}$.

We focus the stream into the canal with a concrete dam (figure 4.5). Up to a height $h \approx 24.7\,\mathrm{cm}$, the entire flow enters the flume but, above this threshold value, the stream overflows the dam. For this reason we do not consider measurements above 24.7 cm, which correspond to a maximum discharge of about $76.01\,\mathrm{m^3\,h^{-1}}$.

We measure the water height in the flume with a pressure sensor (CS451, Campbell Scientific, precision δh =0.7 mm). As the discharge is approximately proportional to the height squared, the measurement error on the discharge δQ reads:

$$\delta Q \sim 2\,Q\frac{\delta h}{h} \sim 2\,\sqrt{Q}\,\delta h\,. \tag{4.2}$$

The discharge measurement error therefore increases with the square root of the discharge.

With this installation, we measure the evolution of the water height in the canal (figure 4.6), and convert it into a water discharge (figure 4.9). We have measured the creek discharge every five minutes from September 9th, 2014 to September 26th, 2014 and every minute from October 10th, 2014 to June 30th, 2015. Over almost ten months (from September 2014 to May 2015), we measured a mean discharge of $9.9\,\mathrm{m^3\,h^{-1}}$. Divided by the drainage are, the mean discharge is about $0.12\,\mathrm{mm\,h^{-1}}$.

4.2.3 Measurement of the water table elevation

We measure the profile of the water table along a transect perpendicular to the river, located approximately 20 m upstream of the Venturi flume. Using an auger, we drilled

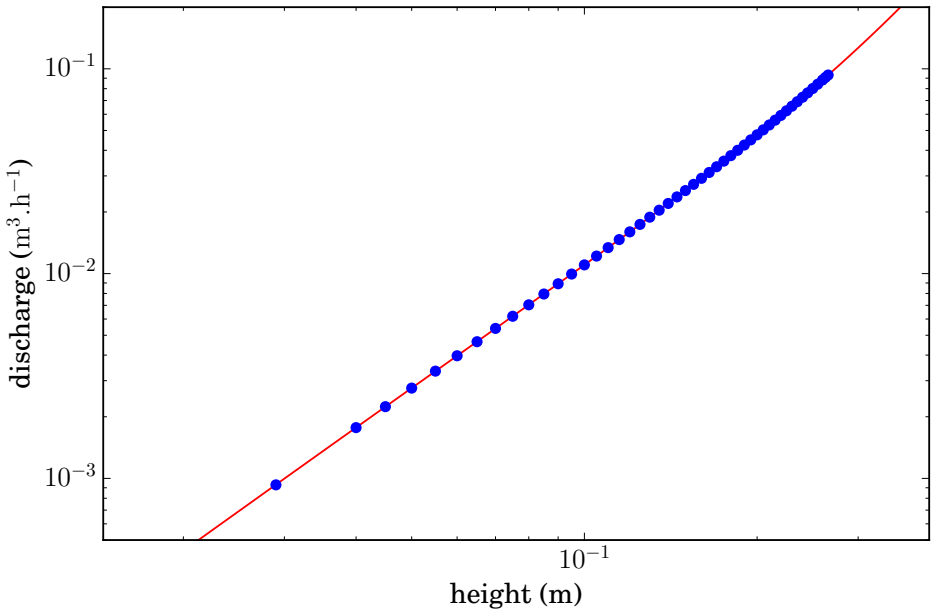

Figure 4.4: Calibration relationship between the height of water in the Venturi flume, and the river discharge. The blue points are the calibration points by the manufacturer (●), and the red line is their provided fit (equation (4.1)) (—).

Figure 4.5: Picture of the concrete dam which focuses the stream into the Venturi flume, up to a water height of about 24.7 cm.

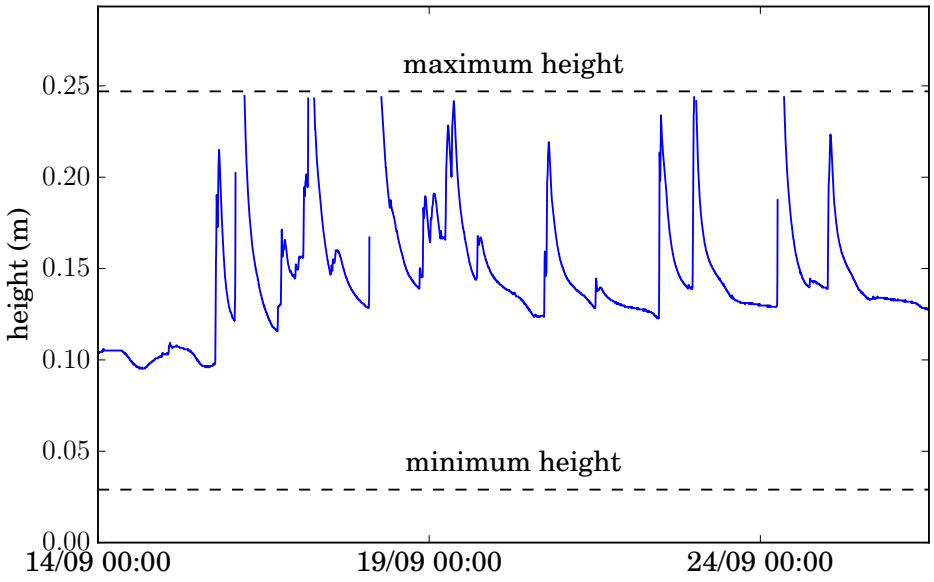

Figure 4.6: Evolution of the height measured in the Venturi flume in September 2014.

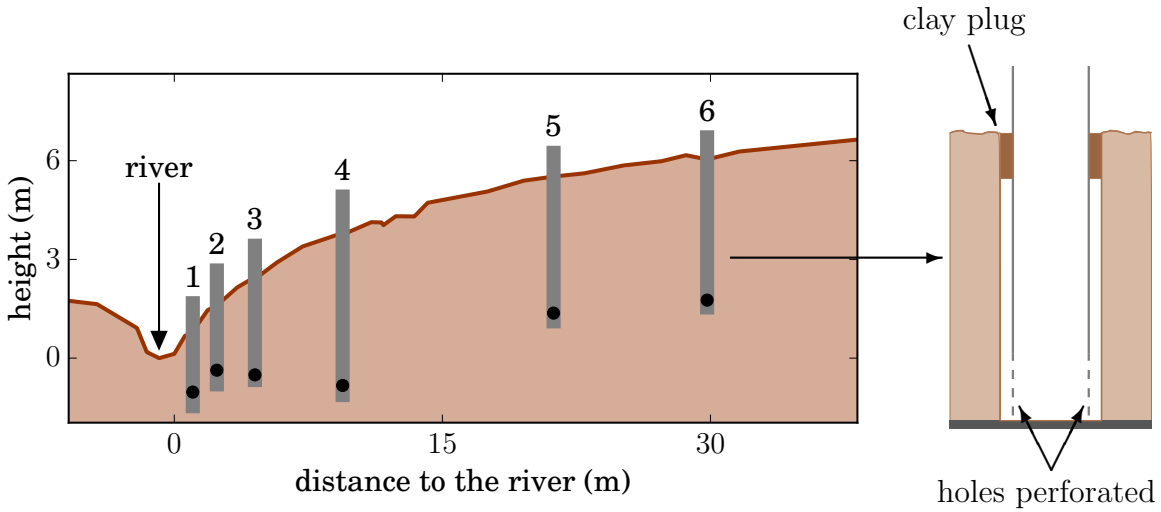

Figure 4.7: *Left:* Side view of the field installation. Along a transect perpendicular to the river bed, six pressure sensors (●) are located at the bottom of boreholes (▬), 1, 2.4, 4.5, 9.4, 21.2 and 29.8 m away from the river. The ground topography was measured with a laser pointer. *Right:* A borehole. At the top, we fill the gap between its wall and the PVC pipe with a clay plug, to prevent overland flow from filling the borehole. Near the bottom, the PVC pipe is perforated, to allow water to enter through its sides.

six boreholes (10 cm in diameter) along this transect, at six distinct locations: 1, 2.4, 4.5, 9.4, 21.2 and 29.8 m away from the river (figure 4.7). We number these boreholes from one to six, respectively.

The drilling procedure was similar for all boreholes. After roughly 50 cm of muddy and organic clay, the ground material become homogeneous during the whole drilling process, corresponding to the homogeneous ferralitic regolith described in Buss et al. (2010). The ground material was similar in all boreholes, confirming the homogeneity of the aquifer (section 4.1.2). In boreholes number 4, 5 and 6, we drilled until we reached a more resistant material, which hindered drilling. This resistant layer set the depth of these boreholes, which is why the bottom of boreholes 5 and 6 is higher than the river. In contrast, near the river (boreholes number 1, 2 and 3), we stopped drilling before reaching any resistant layer.

To prevent any collapse, we inserted PVC pipe into the borehole (8 cm in diameter). The borehole is two centimetres larger in diameter than the PVC pipe, such that a one-centimetre gap separates its wall from the tube. In order to prevent any overland flow to enter the borehole through this gap, we plugged the gap with clay over the uppermost dozen centimetres (schematic in figure 4.7). We eventually overcome the potential formation of a mud plug at the bottom of the PVC tube by drilling small holes evenly over the lowermost twenty centimetres of the tube.

Near the bottom of the boreholes, we placed a pressure sensor connected to a data logger (Campbell Scientific, CR800). Each sensor is approximately 15 cm above the borehole bottom, to prevent clogging by residual mud. By measuring the length of the cable from the top of the PVC pipe to the sensor, we estimate the depth of the sensors relative to the ground surface. We then measured the topography of the transect with a laser pointer, which measures the distance and angle of a given target. From this accurate topography and the depth of the sensors, we estimate the elevation of the sensors relative to the river elevation, which we arbitrarily fix to zero. As a result, as we measure the water height in the boreholes, we obtain the water table profile relative to the river. We have measured this water table profile every minute during almost six months, from January 2015 to June 2015.

4.3 Behaviour of the groundwater flow

The field set-up presented in the previous section allows us to observe the behaviour of groundwater in the Quiock Creek catchment. The water-table profile allows us to estimate the direction of the groundwater flow.

4.3.1 Average water table profile

Figure 4.8 shows the water table profile averaged over almost six months, from 15th January 2015 to 28th June 2015. During this period, boreholes 5 and 6 happened to be dry during several drought periods (almost 40 days in total). In the averaging procedure of the six boreholes, we did not take into account data from this period.

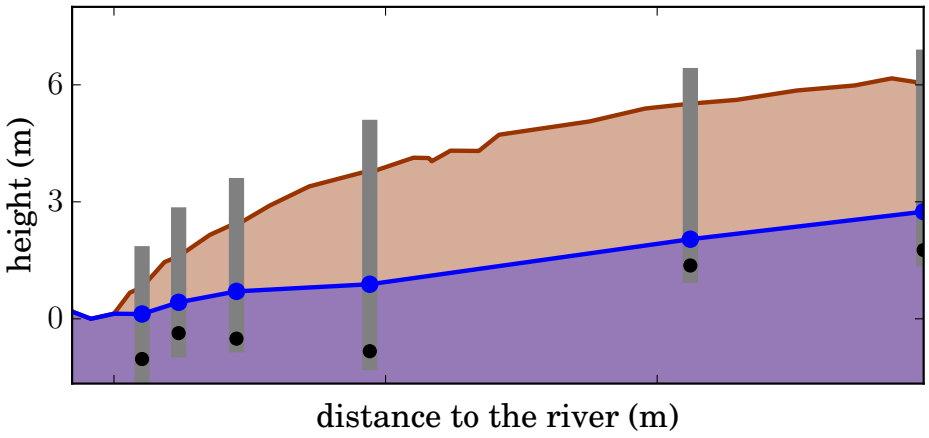

Figure 4.8: Average water table profile between 15th January and 28th June 2015. The blue points represent the measured water level (●), and we then interpolate the water table between each borehole (—).

The averaged water table profile resembles the experimental water tables observed in Ibrahim and Brutsaert's laboratory experiment (section 2.3), and in our's (chapter 3). It is above the river, and slopes towards the river. This slope implies that the pressure gradient is oriented towards the river. On average, along this specific profile, the groundwater of the Quiock Creek aquifer feeds the Quiock Creek.

We now investigate dynamics of the water table and the river discharge. For the sake of clarity, we first observe the water table dynamics through a single borehole. In section 4.3.3, we will extend our observations to the entire profile.

4.3.2 River discharge and water table elevation

Figure 4.9 shows the evolution of the water table level and of the river discharge during ten days. Submitted to several rainfall events, the water level recorded in the borehole strikingly resembles the river discharge. We can identify six distinct rainfall events, five of which cause a fast increase of both the water table and the river discharge. On the contrary, one of the rainfall events (on 6th Feb.) is too small to trigger a water table reaction and, similarly, the river discharge does not react.

Moreover, the reaction times of the water table and the river discharge are similar. As they start increasing, both reach their maximum after a comparable duration, of the order of a dozen minutes. When rainfall stops, both start decreasing rapidly, and slowly relax to their initial stage. Yet, the discharge signal is slightly narrower than the water table level signal.

Both the water table and the river discharge react slightly after the rainfall event has started, generally a few dozen minutes. Like in our laboratory experiment (chapter 3), we interpret this time shift by the infiltration time of the rainwater down to the water table. Considering that the water table is about 1 m below the ground surface at the beginning of the event, and that the water table starts increasing about ten minutes

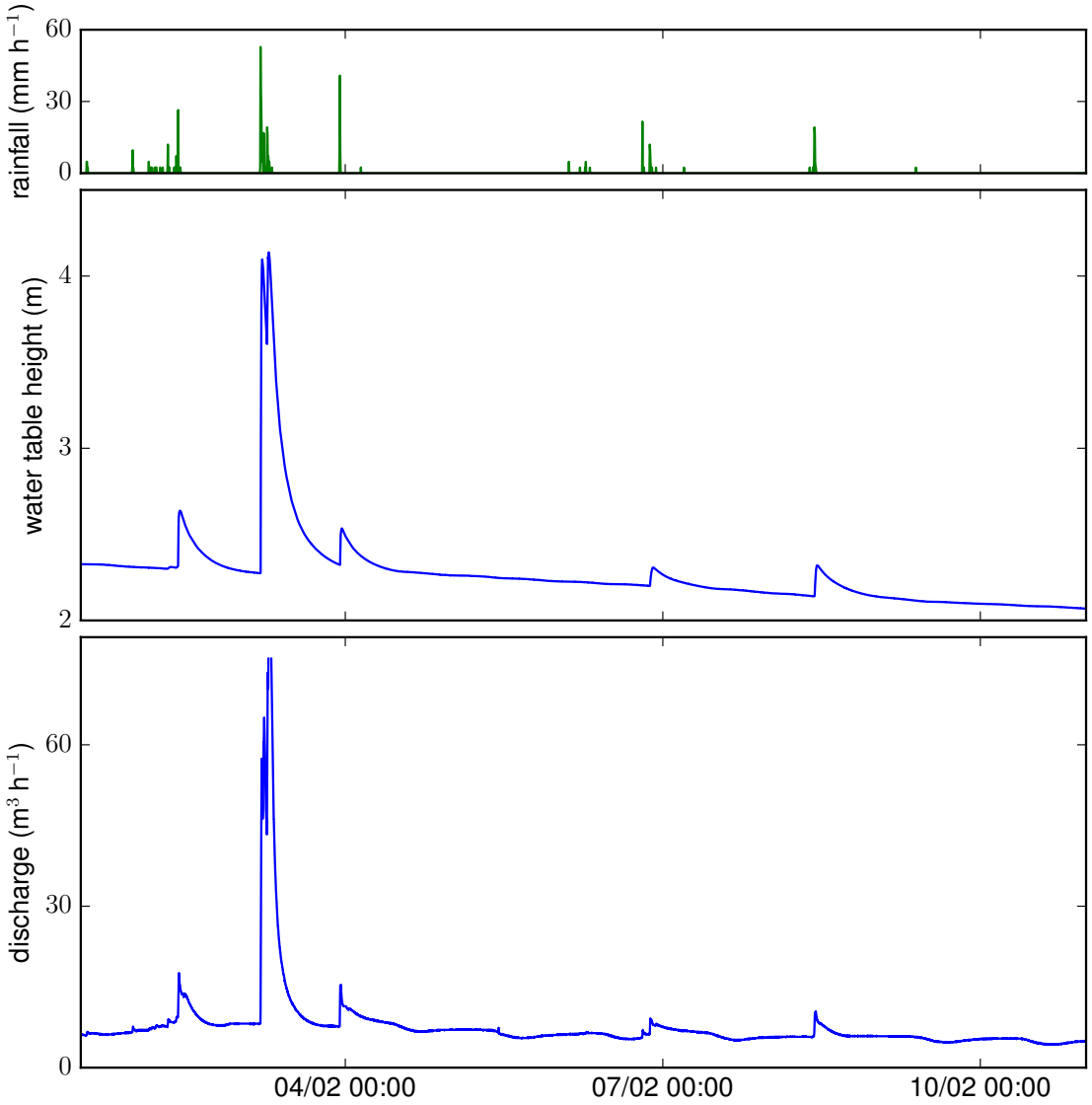

Figure 4.9: Rainfall rate (*top*), water level in the borehole 5 (compared to the river elevation, *middle*) and river discharge (*bottom*) during ten days in February 2015. The water level in the borehole and the river discharge are strongly correlated: both increase very rapidly during rainfall events, and decrease slowly afterwards. Moreover, the water table elevation is more than two metres higher than the river, indicating that groundwater flows towards the river.

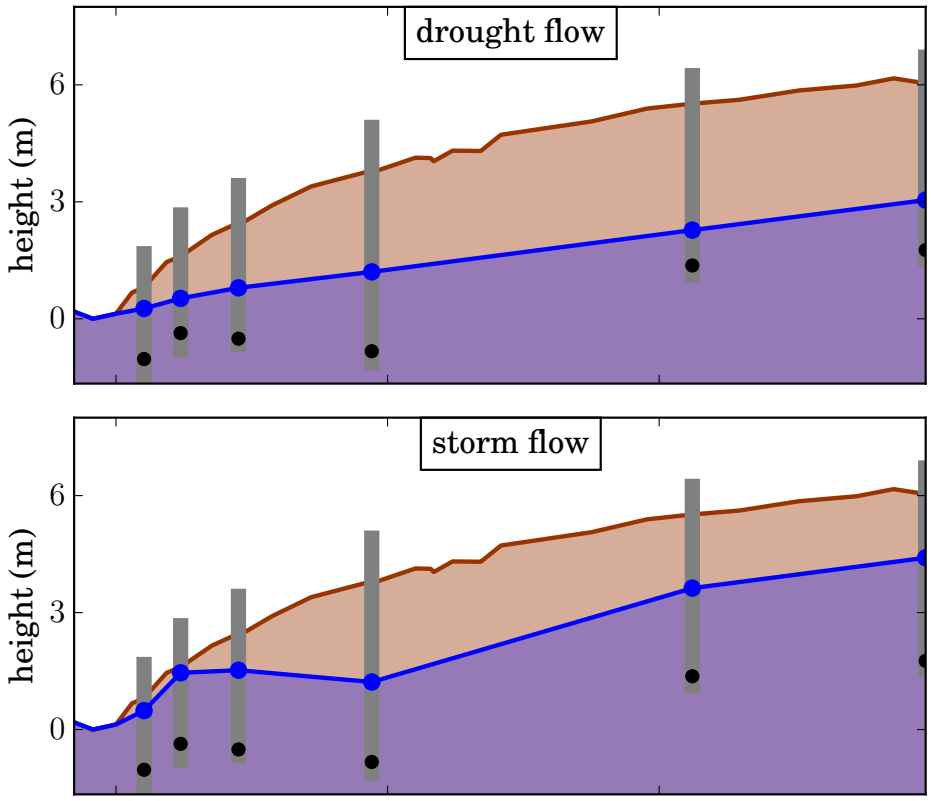

Figure 4.10: *Top:* water table profile recorded on 3rd February 2015 at 04:45 am, in a period of low discharge — at the very beginning of a flood (see figure 4.9). *Bottom:* profile recorded exactly three hours later, during the river discharge peak. In the boreholes, the water level has increased of 0.22, 0.93, 0.73, 0.02, 1.35 and 1.36 m respectively.

after the beginning of the event, we conclude that rainwater seeps down at the velocity of about $1\,\mathrm{mm\,s^{-1}}$.

Combined with the slope of the water table towards the river, the similarity between the water table level and the river discharge evolutions suggests that the Quiock Creek groundwater flow is able to generate quick floods. One needs not invoke overland flow to explain the quick floods observed on the Quiock Creek hydrograph.

4.3.3 Water table dynamics

We now briefly extend our observations over the entire profile of the water table.

Figure 4.10 shows two snapshots of the water table profile. The top profile was recorded during a period of relatively low discharge, a few minutes before the flood event of 3rd Feb. (see also figure 4.9). This snapshot profile is similar to the averaged profile, and indicates that groundwater flows towards the river.

The bottom graph shows the water table profile recorded three hours later, during the river discharge peak. The water level has increased in all boreholes — except number 4. Moreover, the further away from the river, the larger the water level increase — except

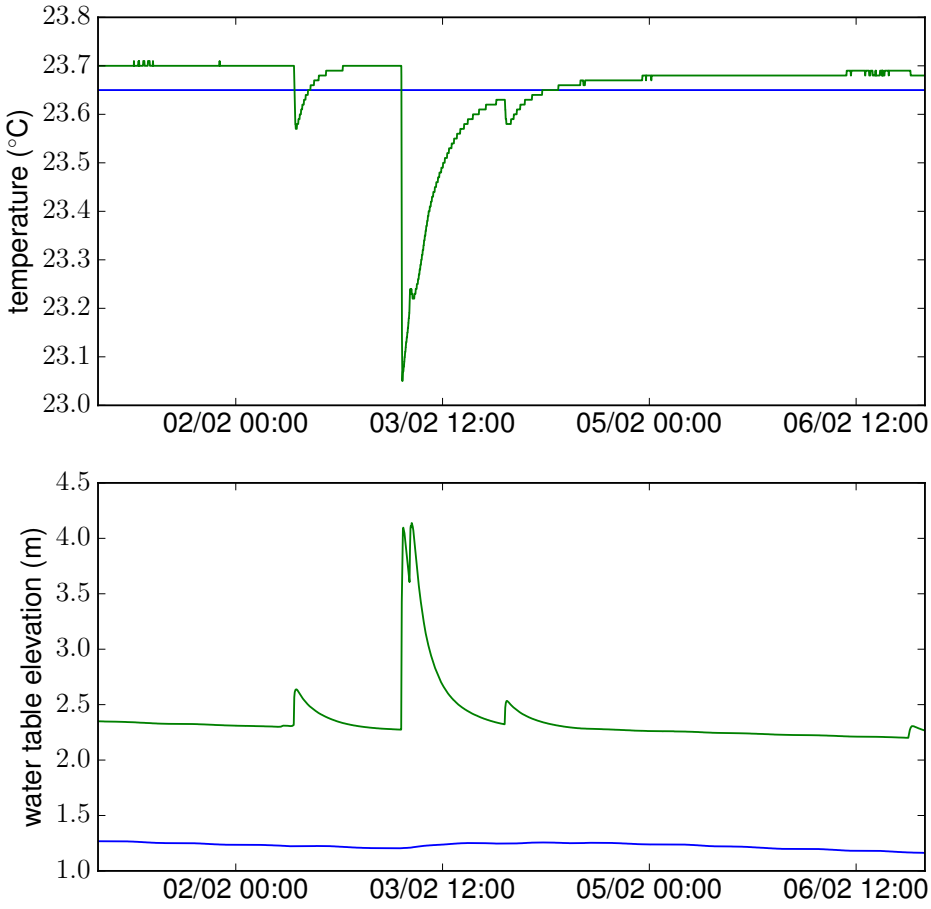

Figure 4.11: *Top:* Temperature recorded in boreholes 4 (—) and 5 (—) during six days in February 2015. *Bottom:* Water level in the same boreholes. In borehole 5, the temperature decreases strongly when the water level rises. In borehole 4, the water level does not rise and, accordingly, the temperature is steady.

in borehole 4. This indicates that, during the storm, the pressure gradient increases, thus accelerating the groundwater flow. This observation again supports the idea that the groundwater flow of the Quiock Creek catchment generates quick floods.

Yet, the water level in the fourth borehole has only risen by two centimetres during this storm event. The quasi-absence of reaction recorded in this borehole was observed for all recorded floods. The reaction time in this borehole is much longer than in the others. In the present example, the quasi-absence of reaction in the fourth borehole causes its water level to be lower than on its left and on its right. If our measurements are correct, this means that the groundwater flow changes direction between the boreholes 3 and 5. We rather invoke a biased measurement, and suggest that borehole 4 was drilled in a less permeable material. This biased measurement seems to be confirmed by temperature measurements in the boreholes (figure 4.11). When the water level in a borehole rises, the temperature in the borehole varies. In borehole 4, the temperature is almost steady, as the water level.

At the beginning of July 2015, we have drilled an additional borehole close to this defective point, to better understand this odd behaviour. We are waiting for the results.

In all boreholes but number 4, the water level increases rapidly during flood events, in a way similar to figure 4.9. Moreover, the water level during floods elevates to higher levels further away from the river. Therefore, the pressure difference between the river and groundwater is higher during floods, thus accelerating the groundwater flow, and increasing the discharge delivered by the aquifer.

4.4 Conclusion

The field experiment presented here looks suitable to test the asymptotic regimes of the Dupuit-Boussinesq equation, which concern the storm flow and the drought flow delivered by an aquifer to a river.

First, an electric tomography profile revealed a relatively homogeneous aquifer. Second, the water table slopes towards the river, which indicates that groundwater flows towards the river. Third, simultaneous measurements of the water table and of the river discharge revealed a comparable dynamics. In particular, the water table rises quickly during rainfall events.

Overall, our field observations indicate that the groundwater flow of the Quiock Creek is able to generate quick floods. As we measure the rainfall rate and the river discharge with a high frequency, we can now test the storm flow regime derived in section 3.6. For that purpose, we must first measure the hydraulic properties of the aquifer.

Chapter 5

Characterisation of the hydraulic properties of the Quiock Creek aquifer

Contents

In the previous chapter, we have presented the Quiock Creek field site, where the groundwater flow behaves similarly as in our laboratory experiment. This site seems suitable to test the Dupuit-Boussinesq asymptotic regimes concerning the drought flow (section 2.3) and the storm flow (section 3.6). These regimes depend on the porosity and hydraulic conductivity of the aquifer. As the hydraulic properties of an aquifer are difficult to measure, these parameters are often fitting parameters of groundwater flow models. Here, we present our attempts to estimate these parameters independently.

5.1 Aquifer porosity

Estimating the porosity of an aquifer is a difficult task, because direct measurements on ground samples are generally not reliable (Bresciani, 2011). Indeed, it implies to collect an aquifer sample and measure its porosity in the laboratory. This method has three major drawbacks. First, a single sample may not be representative of the porosity

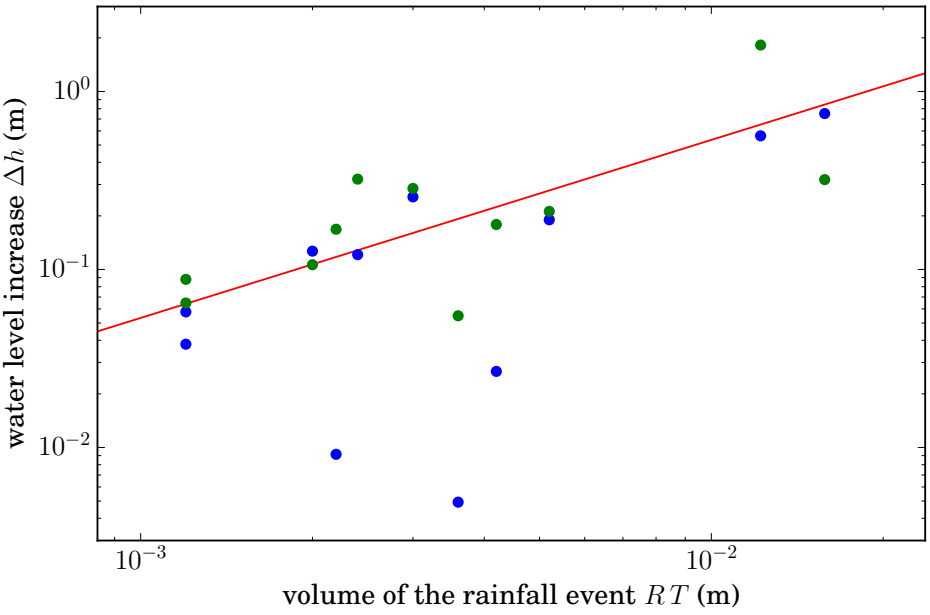

Figure 5.1: Water level rise Δh with respect to the volume $V = RT$ of a rainfall event, in the boreholes number 5 (●) and 6 (●). The red line is the fit of a linear relationship (—), yielding a prefactor 53.4. The inverse of this prefactor provides an evaluation of the porosity $s = 1.87 \cdot 10^{-2}$.

of the whole aquifer. Second, the actual porosity of a sample may differ from the effective porosity, which only accounts for the pores actually filled with water. Third, the sampling process may alter the structure of the material, inducing biased measurements in the laboratory. As a result, the porosity is often a fitting parameter, integrated in a groundwater flow model (Brutsaert and Nieber, 1977).

Here, we propose a method to evaluate in situ the effective porosity s of an aquifer. This method, inspired from the asymptotic analysis of the storm flow in chapter 3, requires high frequency measurements of the water table.

At the very beginning of a rainfall event, we assume that, far from the river, the groundwater flow is insensitive to the river. As a consequence, the water table rises steadily, in proportion with the volume $V = Rt$ it receives from rainfall:

$$h = \frac{V}{s}\,. \tag{5.1}$$

The assumption of a steady rise of the water table far from the river was the boundary condition (3.8) of the storm flow asymptotic regime. This condition requires the Dupuit-Boussinesq assumption. If the groundwater flow is two-dimensional, groundwater may flow downwards, which could break the approximation of a steady rise (chapter 8).

During ten distinct flood events, we measured the water table increase Δh in boreholes 5 and 6. We then plot it against the volume V of the corresponding rainfall event (figure 5.1). As expected, Δh is positively correlated with the volume of rainfall. If we except a few points, a linear relationship is compatible with the data. Fitting a

linear relationship to the data yields a prefactor 53.4, which corresponds to a porosity $s = 1.87 \cdot 10^{-2}$.

Despite a large uncertainty, this estimation is in reasonable agreement with values from the literature. The porosity of clays is generally considered to be of the order of a dozen of per cents, but one per cent remains reasonable (De Marsily, 1986).

Yet, our measurements are much scattered, which hinders our ability to positively decide whether the relationship is indeed linear. In particular, fitting a power law to the data yields an exponent 1.67 ± 1.2, and several measurement points in borehole 6 exhibit a strong departure from the linear relationship. This can be due to spatial heterogeneities of the rainfall rate, or to differences in the initial conditions prior to the rainfall event.

5.2 Hydraulic conductivity: the slug test

We now measure the second hydraulic parameter which characterises an aquifer: the hydraulic conductivity.

The hydraulic conductivity of an aquifer is a key parameter to model groundwater flow. Yet, as for the porosity, measuring it in the laboratory leads to large uncertainties. As a result, several in-situ methods have been developed to measure it in the field, generally requiring the measurement of the water table level in boreholes. A classical method involves the steady pumping of water from a borehole, and the measurement of the water table profile around this borehole (Theis, 1935). Assuming a given groundwater model — Dupuit-Boussinesq for example —, one can estimate the conductivity of the aquifer. This method provides a value of the conductivity at the catchment scale. However, it requires heavy field installations.

Here we use another classical method, involving only light equipment. It consists in pouring a known volume of water into a borehole, and then recording the rate of decline of the water level in the borehole. This method, generally referred to as the slug test in the literature, measures the permeability only locally, i.e. just around the borehole.

5.2.1 The slug test

The slug test consists in adding a volume (a "slug") of water in a borehole and analysing the evolution of the water level (figure 5.2). Figure 5.3 shows the water level in borehole 6, where we suddenly added a volume $V_0 \approx 2.5\,\mathrm{L}$ of water. After a sudden increase, the water level decreases rapidly at the beginning, and then slowly relaxes towards its initial level. Unfortunately, a rainfall event starts approximately 4.5 hours after the beginning of our experiment, stopping the experiment before we could observe the late stage of the water level decline.

To measure the conductivity of the aquifer, we need to interpret the decline rate of the water level in the borehole. Figure 5.2 illustrates the principle of the slug test. As the water level in the borehole increases due to the slug, this creates a pressure difference between the borehole and the surrounding groundwater. In response to this pressure

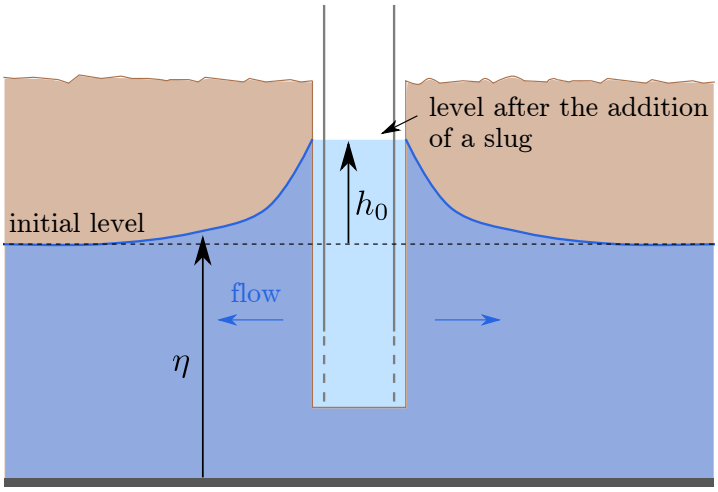

Figure 5.2: Principle of a slug test. A slug of water is added into a borehole, perturbing the groundwater flow around it. As groundwater flows away from it, the water level in the borehole declines.

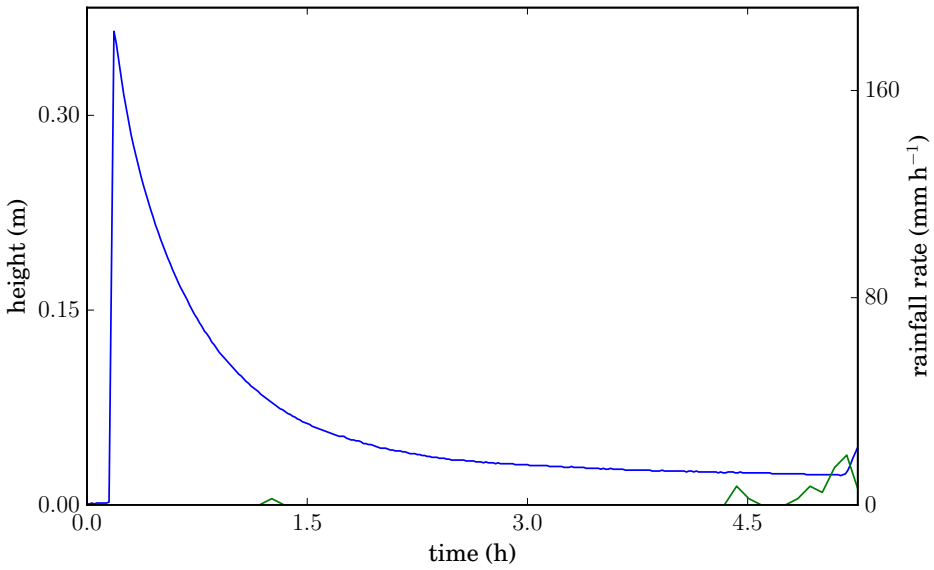

Figure 5.3: Evolution of the water level (—) recorded in borehole 6, after we added a slug $h_0 = 0.36\,\mathrm{m}$ of water. We measure the height relative to its initial level. A significant rainfall event (—) starts 4.5 hours after the beginning of the test, therefore stopping the experiment.

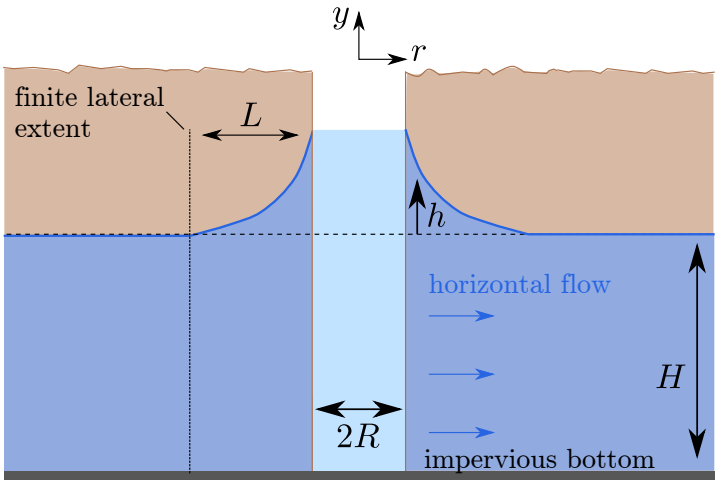

Figure 5.4: Idealised configuration of the classical approach. The flow is assumed to be horizontal. The water table is assumed to recover its initial level $h = 0$ at the ad-hoc distance L from the borehole.

increase, groundwater flows away from the borehole. The water table accommodates this new flow condition, joining the borehole water surface to the initial water table level far from the borehole. This last point implies that the slug should not perturb the groundwater flow far from the borehole, which is supposed to be initially at rest. This assumption is reasonable if the slug volume is small enough. This is why a slug test only gives a local measurement of the conductivity.

The interpretation of the water level decline in the borehole therefore requires a theoretical model. Several flow regimes are possible. In what follows, we propose three different interpretations. We first begin with the classical interpretation of slug tests in unconfined aquifers (section 5.2.2). We then present another classical approach, which was originally intended for confined aquifers (section 5.2.3). We finally propose a third method, which models a two-dimensional groundwater flow.

In the three methods presented hereafter, we consider a homogeneous porous aquifer, where the groundwater flow can be described by Darcy's law. We also assume a radial symmetry: groundwater flows only radially, and there is no variation in the circular component.

5.2.2 One-dimensional flow with finite lateral extent

In the classical approach, one assumes that the aquifer presents a horizontal impervious bottom, a finite depth H below the water table. Figure 5.4 illustrates this idealised configuration.

Mass balance combined with the shallow-water approximation leads to the Dupuit-Boussinesq equation for the water-table elevation η:

$$s\,\frac{\partial \eta}{\partial t} = \frac{K}{2\,r}\,\frac{\partial}{\partial r}\left(r\,\frac{\partial \eta^2}{\partial r}\right), \tag{5.2}$$

expressed here in radial coordinates. Far from the borehole, the slug has no influence on the groundwater flow, and the water table elevation remains at its original level H:

$$\partial_r \eta = 0 \quad \text{for} \quad r \to \infty \,. \tag{5.3}$$

At the boundary of the well (i.e. in $r = R$), a mass balance relates the discharge of water escaping the borehole to the flux of groundwater flow:

$$\pi R^2 \, \partial_t \eta = 2 \pi R \, \eta \, K \, \partial_r \eta \quad \text{for} \quad r = R \,. \tag{5.4}$$

We now consider that, at long times, the slug of water only slightly perturbs the water table. We thus linearise both the Dupuit-Boussinesq equation (5.2) and the boundary condition (5.4) by writing $\eta = H + h$, where $h \ll H$. The Dupuit-Boussinesq equation thus becomes:

$$s \, \frac{\partial h}{\partial t} = \frac{K \, H}{r} \, \frac{\partial}{\partial r} (r \, \frac{\partial h}{\partial r}) \,, \tag{5.5}$$

and the condition at the borehole boundary reads:

$$\partial_t h = 2 \, K \, \frac{H}{R} \, \partial_r h \quad \text{for} \quad r = R \,. \tag{5.6}$$

We now rescale our length variables with the characteristic length H, and the time $\tilde{t} = t/T$ with the characteristic time

$$T = \frac{H}{K}. \tag{5.7}$$

The system of equations describing the decline of the water table around the borehole thus becomes

$$\begin{cases} s \, \partial_t h = \dfrac{1}{r} \, \partial_r (r \, \partial_r h) & \\ \epsilon \, \partial_t h = 2 \, \partial_r h & \text{for} \quad r = \epsilon \,, \\ \partial_r h = 0 & \text{for} \quad r \to \infty \,, \end{cases} \tag{5.8}$$

where all variables are dimensionless, and $\epsilon = R/H$. Two dimensionless parameters determine our system: the aspect ratio ϵ and the porosity s. Both tend to be small in the field. Indeed, the porosity is always inferior to unity and, in the present case, of the order of a few per cents (see section 5.1). In our case, the diameter of the well is 10 cm, and we do not know the depth of the aquifer. However we suppose it is of the order of a few metres, and we have $\epsilon \approx 10^{-1} - 10^{-2}$. In our case, both parameters therefore have the same order of magnitude.

The classical theoretical treatment of slug tests involves the hypothesis that $s \ll \epsilon$ (Bouwer and Rice, 1976; De Marsily, 1986). With this hypothesis, Bouwer and Rice (1976) assume that the water decline in the borehole is the limiting factor of the process. This leads to the quasi-static approximation for the water table profile around the borehole:

$$\partial_r (r \, \partial_r h) = 0 \,. \tag{5.9}$$

A generic solution to this equation is $h = a + b \, \ln(r)$. However, such solution cannot satisfy the far-field boundary condition $\partial_r h = 0$ for $r \to \infty$. To avoid this problem,

Bouwer and Rice (1976) assume that the flow does not extend beyond a finite lateral extent L:

$$h = 0 \quad \text{for} \quad r = L\,. \tag{5.10}$$

Bouwer and Rice (1976) discuss the exact value of L, and find that it approximately corresponds to the depth H of the water level. In dimensionless variables (length variables rescaled with H), we can thus consider $L \approx 1$.

In $r = \epsilon$, the discharge Q escaping the borehole determines the slope of the water table. This condition allows us to determine the integration constants a and b as a function of the rescaled discharge $\tilde{Q}$:

$$\tilde{Q} = -2\,\pi\,\epsilon\,\partial_r h\,. \tag{5.11}$$

Satisfying these two boundary conditions, we obtain the quasi-static water table profile as a function of the discharge:

$$h = -\frac{\tilde{Q}}{2\,\pi}\,\ln(r) \quad \text{for} \quad r \geqslant \epsilon\,. \tag{5.12}$$

In the same time, $\tilde{Q}$ also determines the water level decline in the well: $\tilde{Q} = -\pi\,\epsilon^2\,\partial_t h$ for $r = \epsilon$. Combined with the water table profile (5.12), this leads to a differential equation on the height in the borehole:

$$\partial_t h = \frac{2\,h}{\epsilon^2\,\ln(\epsilon)}\,. \tag{5.13}$$

We straightforwardly integrate this equation, and obtain that the water height in the borehole declines exponentially (as $\epsilon < 1$, $\ln(\epsilon) < 0$):

$$h = \exp\left(\frac{2\,t}{\epsilon^2\,\ln(\epsilon)}\right)\,. \tag{5.14}$$

Dimensionally, the water level in the borehole therefore reads:

$$h(t) = h_0 \exp\left(\frac{-2\,K\,H\,t}{R^2 \ln(H/R)}\right)\,. \tag{5.15}$$

Figure 5.5 shows the slug test we performed in the sixth borehole on a semi-logarithmic plot. The curve we obtain does not seem to be exponential. We momentarily ignore this inconsistency, and fit an exponential law to the curve. The fit yields a characteristic time of $\approx 3000\,\mathrm{s}$, which leads to a hydraulic conductivity $K \approx 8.74 \cdot 10^{-7}\,\mathrm{m\,s^{-1}}$. The same procedure applied to the five other boreholes gives an average value $K = 5.2 \cdot 10^{-7}\,\mathrm{m\,s^{-1}}$ (see figure 5.9 and table 5.1).

The solution (5.15) derived here depends on the arbitrary choice of the length L, which fixes the water table level at a finite distance from the borehole. In a domain of finite size, when the solution of a linear partial differential equation relaxes towards an equilibrium value, it often tends exponentially towards this equilibrium value at asymptotically long time. The time constant of this exponential function is generally

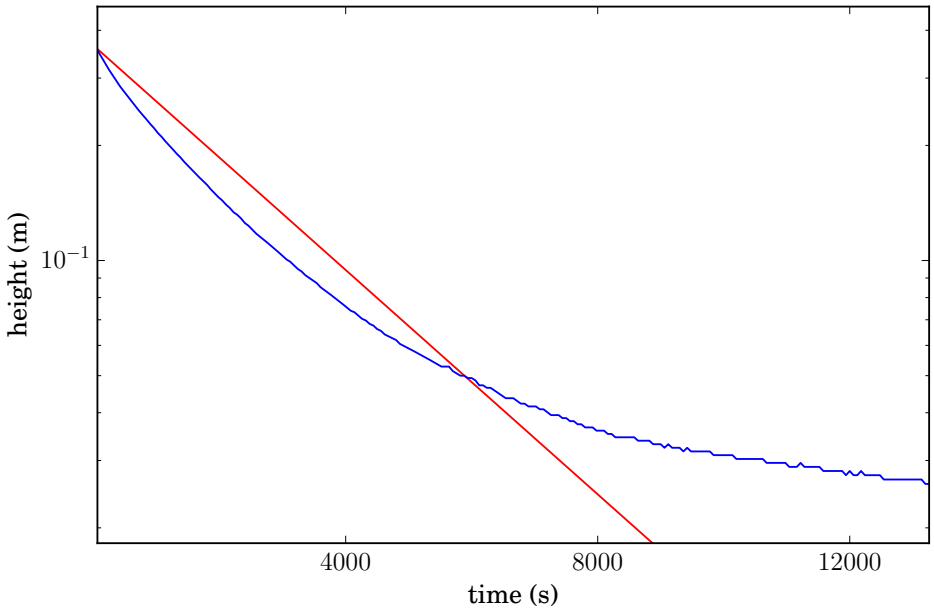

Figure 5.5: Water level decline in the well (—), and fit of an exponential law (—), as predicted by the classical theory (5.15). The fit yields a characteristic time of $\approx 3000\,\mathrm{s}$.

determined by the size of the domain. For instance, this is the case with the linear heat equation (Carslaw and Jaeger, 1959). However, exponential declines after a slug test seem to be rarely observed, as pointed by Bouwer himself (Bouwer, 1989). In fact, any size L would give an acceptable solution to the equation system (5.8). If we sum all these solutions, in a Laplace transform for example, one can obtain a non-exponential decline.

5.2.3 One-dimensional, infinite flow

If we relax the hypothesis of a finite lateral extent, the slug perturbation propagates away from the borehole. After a sufficiently long time, the radius of the borehole becomes negligible compared to the characteristic length of the flow. In this case, we can investigate the behaviour of the equation system (5.8) in the limit where $\epsilon \ll s$ (figure 5.6).

To do so, we use the same hypotheses as in the previous section, except that the horizontal extension of the domain is now infinite. This reduces the borehole to a line source at long times. The present situation is identical to the one depicted in Cooper et al. (1967), except that they consider a confined aquifer, which allows them to linearise the Dupuit-Boussinesq equation (5.5). Yet in an unconfined aquifer of finite depth, the Dupuit-Boussinesq equation can also be linearised at long times.

Introducing a new characteristic time

$$T = \frac{s\,H}{K}\,, \tag{5.16}$$

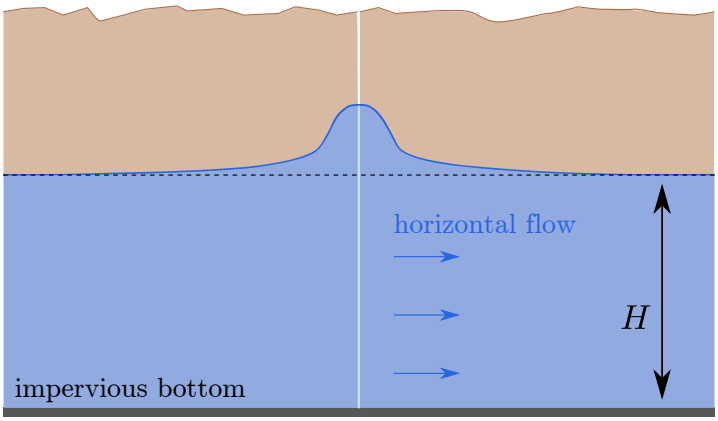

Figure 5.6: When the radius of the borehole can be neglected, the water table is a declining gaussian mound (equation (5.19). The flow is assumed to be horizontal (Dupuit-Boussinesq approximation).

we rescale the system of equations (5.8). This slightly changes equation (5.8) into

$$\begin{cases} \partial_t h = \dfrac{1}{r}\,\partial_r(r\,\partial_r h) & \\ \dfrac{\epsilon}{s}\,\partial_t h = 2\,\partial_r h & \text{for} \quad r = \epsilon\,, \\ \partial_r h = 0 & \text{for} \quad r \to \infty\,. \end{cases} \tag{5.17}$$

The only difference with respect to the system (5.8) is that the porosity s now stands on the left-hand side of the boundary condition at $r = \epsilon$. We now consider the limit $\epsilon/s \ll 1$ such that the left-hand side of the boundary condition in the well vanishes. The system becomes comparable to the heat equation:

$$\begin{cases} \partial_t h = \dfrac{1}{r}\,\partial_r(r\,\partial_r h) & \\ \partial_r h = 0 & \text{for} \quad r = 0\,, \\ \partial_r h = 0 & \text{for} \quad r \to \infty\,, \end{cases} \tag{5.18}$$

with a Dirac delta function $h = h_0$ for $r = 0$ as initial condition. The solution to this system reads (Carslaw and Jaeger, 1959):

$$h(r,t) = \frac{V_0}{4\,\pi\,t}\,\exp\left(\frac{-r^2}{4\,t}\right)\,, \tag{5.19}$$

where V_0 represents the dimensionless volume injected into the well. This solution represents the spreading of a Gaussian mound.

As the borehole is not a perfect Dirac delta function, we expect its water level to tend towards the heat equation solution (5.19) at sufficiently long times. Then, the water level in the borehole, i.e. in $r = 0$, is supposed to decline as the inverse of time. Returning to physical dimensions, the water level in the borehole thus reads

$$h = \frac{s\,h_0\,R^2}{4\,H\,K\,t} \quad \text{for} \quad r = 0\,. \tag{5.20}$$

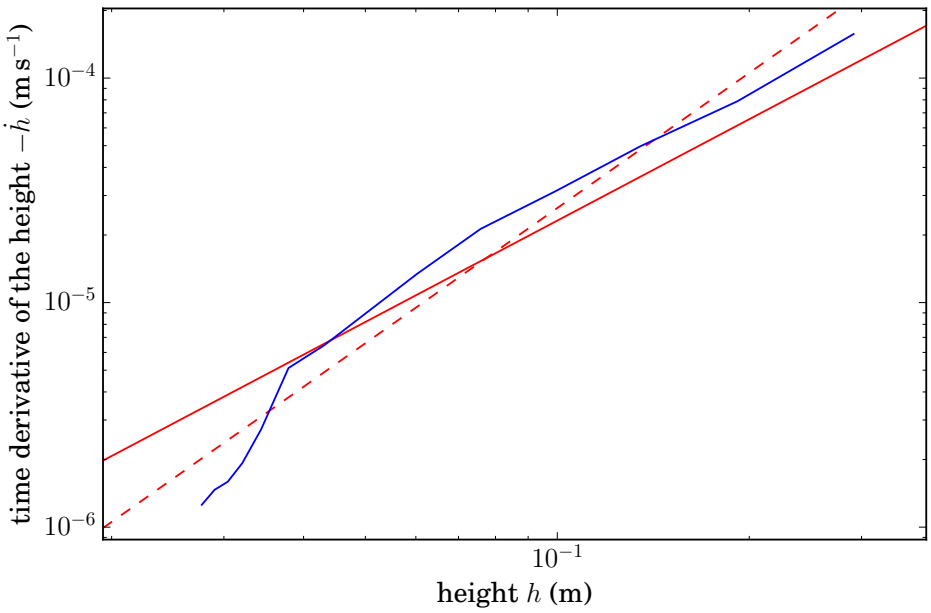

Figure 5.7: Time derivative $\dot{h}$ of the water level decline as a function of the water level h (—). The fit of a power law 2 (- - -), as predicted by the Dupuit-Boussinesq theory (equation (5.21)), yields a prefactor of $2.64 \cdot 10^{-3}\,\mathrm{m}^{-1}\,\mathrm{s}^{-1}$. It corresponds to a declining gaussian mound (section 5.2.3). The fit of a power law 3/2 (—), as predicted by the two-dimensional flow theory (equation (5.40)), yields a prefactor of $7.3 \cdot 10^{-4}\,\mathrm{m}^{-1/2}\,\mathrm{s}^{-1}$. It corresponds to a two-dimensional flow in an infinitely deep aquifer (section 5.2.4).

Like in the analysis of the drought flow of natural rivers in section 2.3.3, we are now looking for a power law which initial time is unknown. We avoid this problem by computing the time derivative of the height, supposed to be proportional to the height squared:

$$-\dot{h} = \frac{s\,h_0\,R^2}{4\,H\,K\,t^2} = \frac{4\,H\,K}{s\,h_0\,R^2}\,h^2\,. \tag{5.21}$$

Our field data are consistent with the power law 5.21 within the limited range of heights we were able to measure (figure 5.7). Indeed, fitting a power law to the data yields an exponent 2.09. Assuming that the exponent is exactly 2, the data are best fitted with a prefactor of $2.64 \cdot 10^{-3}\,\mathrm{m}^{-1}\,\mathrm{s}^{-1}$. Using equation (5.21), we find a permeability of $K = 9.73 \cdot 10^{-9}\,\mathrm{m\,s}^{-1}$.

We measured the hydraulic conductivity around the five other boreholes with the same procedure (see figure 5.10 and table 5.1). We obtain an average value $K = 4.6 \cdot 10^{-9}\,\mathrm{m\,s}^{-1}$.

Finally, the two methods presented so far rely on the shallow-water approximation, which is a one-dimensional description of the problem. We end this section by investigating a situation where the Dupuit-Boussinesq approximation is relaxed.

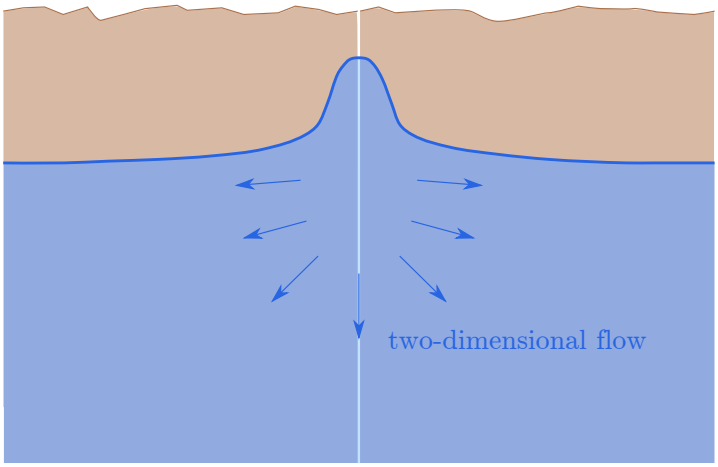

Figure 5.8: In a two-dimensional slug test, the borehole radius is considered infinitely small, and the aquifer bottom infinitely deep. The slug acts as a perturbation propagating horizontally and vertically outwards and downwards.

5.2.4 Two-dimensional flow in an infinitely deep aquifer

So far in this section, we have used the Dupuit-Boussinesq — or shallow-water — approximation. This method is possible only if the aquifer presents an impermeable bottom, at a finite depth H below the water table. This is one of the main assumptions we made, not only in the present section, but also in the entire manuscript so far. Yet, the electrical resistivity tomographic soil profile (figure 4.2) challenges this hypothesis. In fact, the slug acts as a perturbation of the groundwater flow, which propagates horizontally but also vertically (figure 5.8). Before this propagation wave reaches the aquifer bottom, the flow induced by the slug is therefore two-dimensional. In this section, we investigate the response to a slug test of a groundwater flow in an infinitely deep aquifer.

For this purpose, we invoke Darcy's law again:

$$\mathbf{v} = -K\,\nabla\phi \quad \text{where} \quad \phi = \frac{p}{\rho\,g} + y\,. \tag{5.22}$$

Combined with the mass balance, we consider that the groundwater flow is laplacian. In radial coordinates,

$$\Delta_r\phi = \frac{1}{r}\,\partial_r(r\,\partial_r\phi) + \partial_{yy}\phi = 0\,, \tag{5.23}$$

where we assume that the problem is radially symmetric.

The Laplace equation must be supplemented by boundary conditions. In the present situation, the bottom and lateral boundaries are sent to infinity, where the flow is considered to be at rest:

$$\phi = 0 \tag{5.24}$$

at infinity.

We further simplify this system, and consider the borehole radius as infinitely small, such that it can be considered a line source. We therefore neglect its influence on the flow.

The water table is a free surface and requires two conditions. The first condition is that the pressure is atmospheric:

$$\phi = h \quad \text{for} \quad y = h\,, \tag{5.25}$$

where h is the deviation of the water table height with respect to its initial level. Mass balance leads to the second condition on the free surface:

$$s\,\partial_t h = K\left(\partial_r \phi\,\partial_r h - \partial_y \phi\right) \quad \text{for} \quad y = h\,. \tag{5.26}$$

An obvious solution to the equation system (5.23) to (5.26) is

$$\begin{cases} \phi = 0 & \text{and} \\ h = 0\,, \end{cases} \tag{5.27}$$

and corresponds to the initial state of the system, which is at rest before we perturb it.

We now consider the slug V_0 added in the borehole as a small perturbation of this initial state. We therefore consider

$$h = \varepsilon\, h_1 \quad \text{and} \quad \phi = \varepsilon\, \phi_1\,, \tag{5.28}$$

where $\varepsilon \ll 1$ is a small parameter (different from the aspect ratio ϵ). Linearising the free surface condition, we obtain

$$s\,\partial_t h_1 = -K\,\partial_y \phi_1 \quad \text{for} \quad y = h_1\,. \tag{5.29}$$

We choose $L = V_0^{1/3}$ as the characteristic length of the problem, and

$$T = \frac{s\,L}{K} \tag{5.30}$$

as the characteristic time. Rescaling the variables

$$\hat{t} = \frac{t}{T}\,, \quad \hat{r} = \frac{r}{L}\,, \quad \hat{y} = \frac{y}{L} \quad \text{and} \quad \hat{\phi} = \frac{\phi}{L}\,, \tag{5.31}$$

we obtain the following dimensionless and linear system of equations:

$$\begin{cases} \Delta_r \phi = 0 & \\ \partial_t h = -\partial_y \phi & \text{at the free surface}\,, \\ \phi = h & \text{at the free surface}\,, \end{cases} \tag{5.32}$$

where we have removed the hats from the rescaled variables.

We now look for a self-similar solution of the form

$$\begin{cases} h = t^\alpha\, \tilde{h}\left(\dfrac{r}{t^\beta}\right) \\[2ex] \phi = t^\alpha\, \tilde{\phi}\left(\dfrac{r}{t^\beta}, \dfrac{r}{t^\beta}\right)\,. \end{cases} \tag{5.33}$$

The mass balance $\partial_t h = -\partial_y \phi$ on the free surface imposes $\beta = 1$, but the system (5.32) yields no constraint on α. We determine α from the integral of the mass balance: at any time, the total volume of the perturbation must be conserved. This condition formally reads

$$\frac{V_0}{L^3} = 2\,\pi \int_0^\infty h(r,t)\, r\, dr = 2\,\pi\, t^\alpha \int_0^\infty \tilde{h}(r/t)\, r\, dr. \tag{5.34}$$

Within the integrand, we substitute $r/t = \tilde{r}$ and obtain

$$\frac{V_0}{L^3} = 2\,\pi\, t^{\alpha+2} \int_0^\infty \tilde{h}(\tilde{r})\, \tilde{r}\, d\tilde{r}\ . \tag{5.35}$$

The integral of the mass balance therefore imposes $\alpha = -2$. This reasoning suggests that, if a self-similar solution to our problem exists, then

$$h = \frac{1}{t^2}\,\tilde{h}\left(\frac{r}{t}\right) \quad \text{and} \quad \phi = \frac{1}{t^2}\,\tilde{\phi}\left(\frac{r}{t}, \frac{y}{t}\right)\ , \tag{5.36}$$

where the self-similar problem reads

$$\begin{cases} \Delta_r \tilde{\phi} = 0 & \\ 2\,\tilde{h} + \tilde{r}\,\tilde{h}' = \partial_{\tilde{y}} \tilde{\phi} & \text{for} \quad \tilde{y} = 0\,, \\ \tilde{\phi} = \tilde{h} & \text{for} \quad \tilde{y} = 0\,. \end{cases} \tag{5.37}$$

We have not found any analytical solution to this system.

However, let us assume that a solution exists. Then, the self-similar height $\tilde{h}$ must tend to a finite value γ near the borehole:

$$\tilde{h} \sim \gamma \quad \text{for} \quad \tilde{r} \to 0\,. \tag{5.38}$$

The mathematical constant γ must be determined by a resolution of the system of equations (5.37). For this linear system, it should be accessible numerically.

As a result of this finite value near the borehole, the dimensionless water level in the borehole ($r = 0$) declines proportionally to the inverse time squared: $h \sim 1/t^2$. Returning to physical dimensions, we obtain

$$h \sim \gamma\, V_0^{1/3} \left(\frac{s\, h_0}{K\, t}\right)^2\ . \tag{5.39}$$

Once again, we end up with a power-law relationship between the water level in the borehole and time. In order to evaluate this new regime against our observations, we measure the time derivative of the water level $\dot{h}$ as function of h, and expect a $3/2$ power law relationship:

$$\dot{h} = -2\,\gamma\, V_0^{1/3} \left(\frac{s\, V_0^{1/3}}{K}\right)^2 \frac{1}{t^3} = -2\,\frac{K}{s\,\gamma^{3/2}\, V_0^{1/2}}\, h^{3/2}\,. \tag{5.40}$$

Figure 5.7 shows how a $3/2$ power law compares with our slug test. Once again, the range of height measurements is too small to observe a clear tendency. In particular,

we cannot discriminate between a 3/2 power law and the squared relationship derived in the previous section. Both seem to be compatible with our data.

Assuming that solution (5.39) holds, and that $\gamma = 1$, the fit of a 3/2 power law yields a prefactor of $7.3 \cdot 10^{-4}\,\mathrm{m}^{-1/2}\,\mathrm{s}^{-1}$. Comparing with expression (5.40), we measure a hydraulic conductivity $K = 2.23 \cdot 10^{-6}\,\mathrm{m\,s}^{-1}$. With the same procedure, we measure the hydraulic conductivity around the five other boreholes (figure 5.10 and table 5.1). We obtain an average value of $1.14 \cdot 10^{-6}\,\mathrm{m\,s}^{-1}$.

Of course, this method requires more investigation, especially because we must still find a solution to the system of equations (5.37).

5.2.5 Discussion

To conclude, the three methods presented in this section yield three significantly different values of the permeability. These values are larger than what we would expect from the literature (10^{-9} to $10^{-13}\,\mathrm{m\,s}^{-1}$ (De Marsily, 1986)). Yet, the volcanic clays of Guadeloupe are expected to be more permeable than usual (Colmet-Daage and Lagache, 1965). On the whole, the three methods presented here present advantages and drawbacks.

First, the classical method relies on the definition of an arbitrary length and predicts an exponential decline, which is not observed in any of the boreholes. The choice of this method is therefore questionable.

The second method assumes that, at long times, the borehole radius can be considered as infinitely small. As a consequence, the water table is a spreading Gaussian mound. This is certainly true at long times, but our experiment was stopped after 4.5 hours. 4.5 hours correspond to a dimensionless time $K\,t/(s\,H) \approx 0.01 \ll 1$, if we take the average value of this method, $K \approx 5 \cdot 10^{-9}\,\mathrm{m\,s}^{-1}$. This very short dimensionless time does not support the use of the long-times asymptotic regime (5.20) in this specific case.

The third method presented here assumes a borehole of infinitely small radius, and an infinitely deep aquifer. These assumptions imply that it corresponds to an intermediate asymptotic regime: we consider times sufficiently long for the radius of the borehole to be neglected, but sufficiently short that the perturbation has not reached the aquifer bottom. In the present case, with the average value $K \approx 10^{-6}\,\mathrm{m\,s}^{-1}$, the duration $t = 4.5$ hours corresponds to a dimensionless time $K\,t/s\,h_0 \approx 1$. This dimensionless time seems more reasonable than in the previous section, and supports the use of this method. However, this method requires further investigation, as we have no information about the depth of the aquifer bottom, and we still need to solve a system of equations.

A physical argument, concerning the seeping velocity of rainwater, also supports the latter method. Based on the present measurements and on the estimation of the porosity ($s \approx 10^{-2}$, section 5.1), we can roughly estimate the velocity v of the fluid seeping into the ground. It is the ratio of the hydraulic conductivity over the porosity: $v \sim K/s$. If we take $K \approx 10^{-6}\,\mathrm{m\,s}^{-1}$, the downwards infiltration velocity of rainwater into the ground is $v \approx 0.1\,\mathrm{mm\,s}^{-1}$. This is about one order of magnitude lower than what we observed

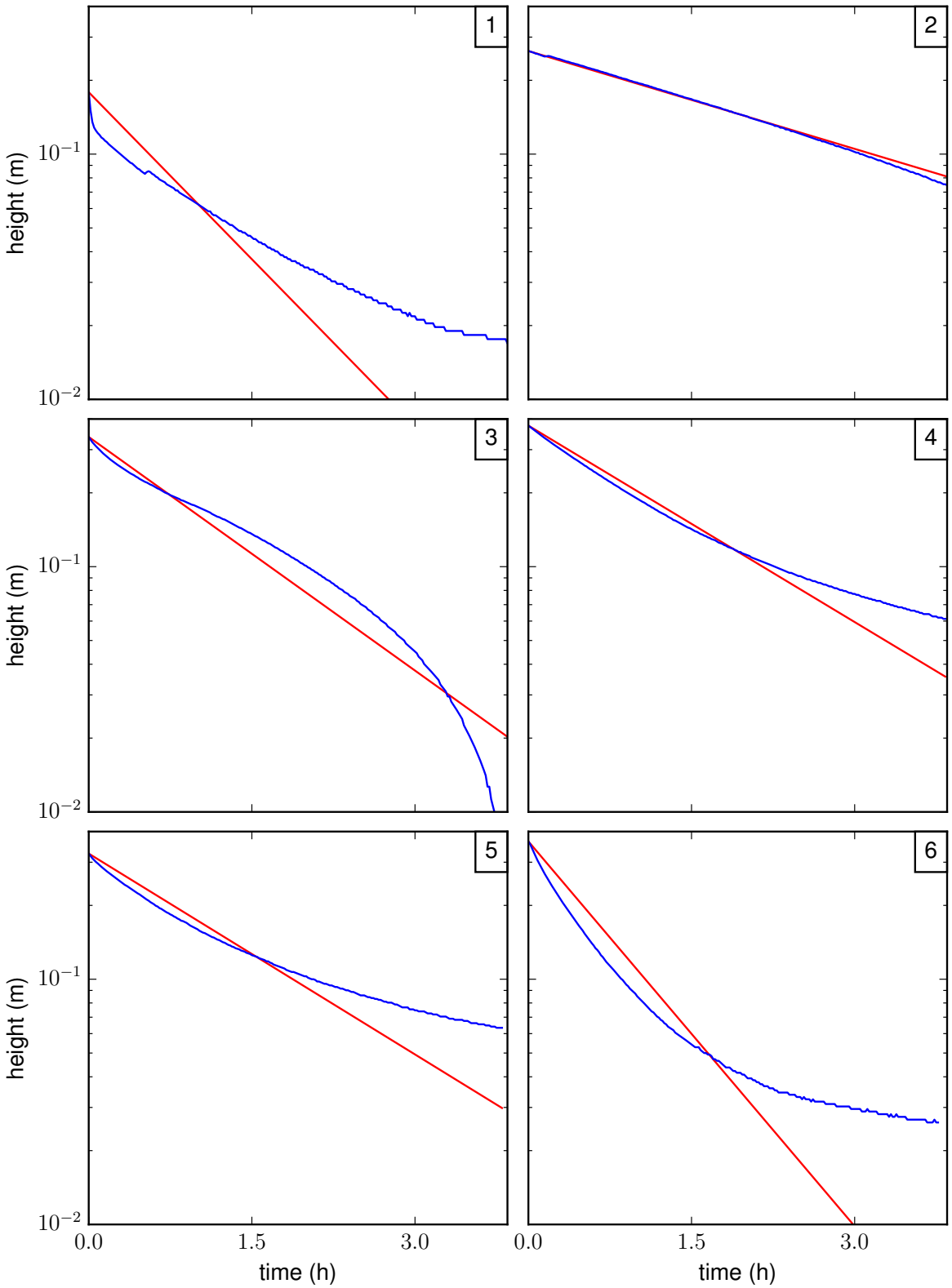

Figure 5.9: Time derivative $-\dot{h}$ of the water level decline as a function of the water level h in the six boreholes (—). The red lines are exponential fits (—), as predicted by equation (5.15), and corresponding to a declining gaussian mound (section 5.2.2).

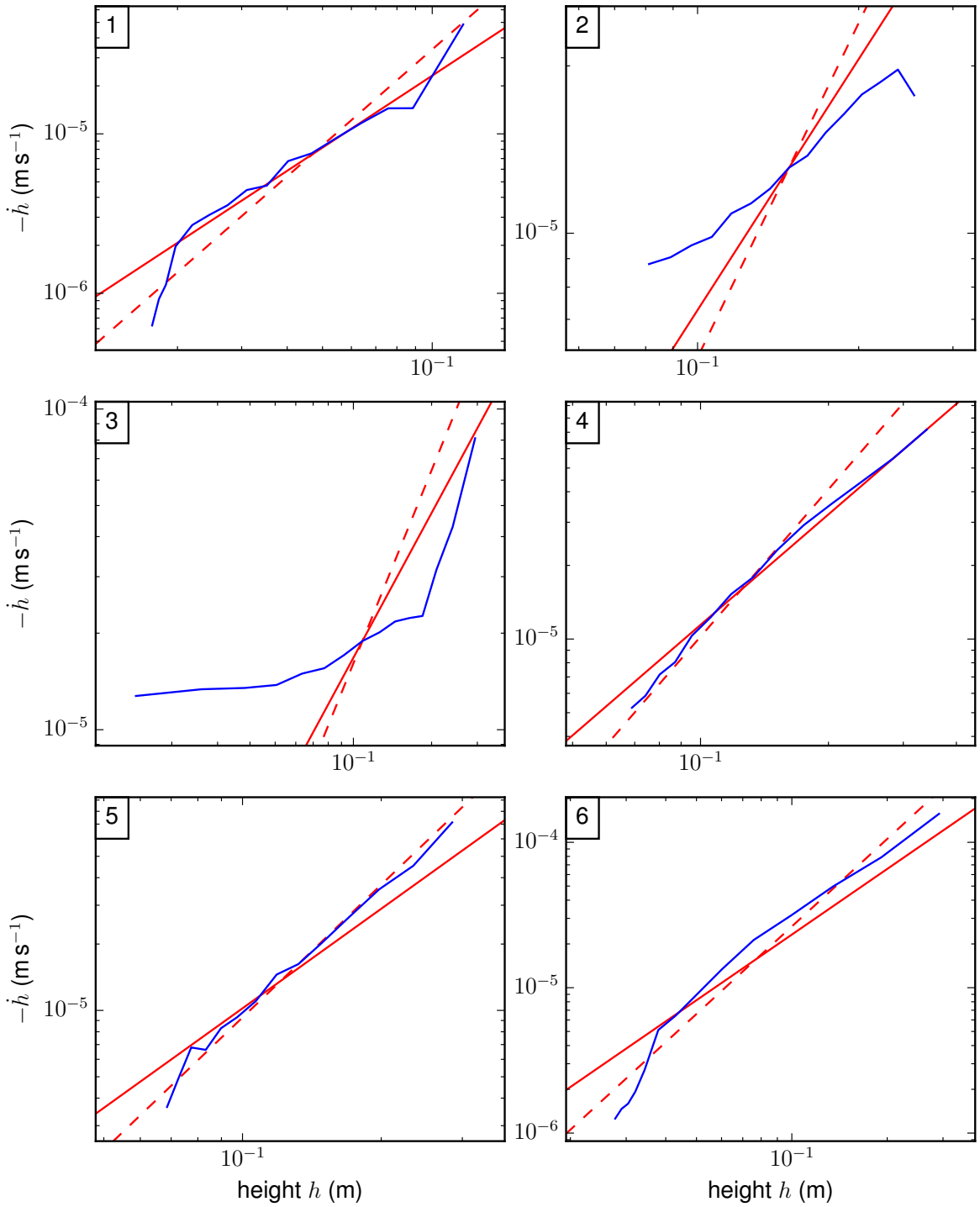

Figure 5.10: Time derivative $-\dot{h}$ of the water level decline as a function of the water level h in the six boreholes (—). The red dashed lines are power law 2 fits (- - -), as predicted by equation (5.21), and corresponding to a spreading Gaussian mound (section 5.2.3). The red lines are 3/2 power law fits (—), as predicted by equation (5.40), and corresponding to a two-dimensional flow in an infinitely deep aquifer (section 5.2.4).

Method	Borehole number						Average
	1	2	3	4	5	6	
Finite lateral extent (section 5.2.2) ($\times 10^{-6}\,\mathrm{m\,s^{-1}}$)	0.72	0.23	0.42	0.32	0.55	0.87	0.52
Infinite lateral extent (section 5.2.3) ($\times 10^{-9}\,\mathrm{m\,s^{-1}}$)	5.66	1.69	4.14	2.43	3.95	9.73	4.6
2D flow, infinitely deep aquifer (section 5.2.4) ($\times 10^{-6}\,\mathrm{m\,s^{-1}}$)	0.76	0.43	1.44	1.15	0.83	2.23	1.14

Table 5.1: Hydraulic conductivity K. Summary of all the results on the aquifer hydraulic conductivity.

in section 4.3.2. A larger conductivity K would better conform to the observations of section 4.3.2. The relatively large difference between these observations and our local estimations also provides an estimate for uncertainties on the measurements of K and s.

All these observations call for a dedicated investigation in controlled conditions — in the laboratory, or numerically. For instance we could build a homogeneous laboratory aquifer with finite depth H and radial extent L, into which we pour a slug h_0 in a borehole of negligible radius. We consider $h_0 \ll H \ll L$. At the beginning, we expect the slug to perturb the groundwater flow only locally around the borehole, and close to the water table. During this early regime, the groundwater flow is insensitive to the bottom of the aquifer, which can be considered as infinitely deep. Equation (5.39) is therefore expected to hold during early times. As the slug spreads, the perturbation hits the aquifer bottom. At this moment, the Dupuit-Boussinesq approximation progressively replaces the early-times regime. We therefore expect the long-times regime (5.20) to hold, and the water level within the borehole to progressively adopt a $1/t$ behaviour. All these speculations would deserve detailed scrutiny in a dedicated experiment.

5.3 Conclusion

In this chapter, we presented new methods to estimate separately the porosity and the hydraulic conductivity of an aquifer. These methods rely on interpretations involving a groundwater flow model.

To estimate the porosity of the aquifer, we assume the geometric configuration of a fully-penetrating stream. In this configuration, we can use the Dupuit-Boussinesq approximation and assume that, far from the river and at the beginning of a rainfall event, the flow is insensitive to the river. The water table thus rises steadily, in proportion to the rainfall rate and to the inverse of the porosity. Analysing ten rainfall events, we estimated a porosity of $1.87 \cdot 10^{-2}$. If confirmed, this method could be a simple way to

measure in-situ the porosity of an aquifer.

The slug test used to estimate the hydraulic conductivity is difficult to interpret. The duration of the slug tests presented in this chapter is relatively short, such that we favour an intermediate asymptotic regime involving a two-dimensional flow in an infinitely deep aquifer. This new method leads to an estimate of $K \approx 10^{-6}\,\mathrm{m\,s^{-1}}$. Yet, it needs further investigation.

With the estimates of the porosity and of the hydraulic conductivity, we can now analyse the Quiock Creek hydrograph.

Chapter 6

The Quiock Creek hydrograph

Contents

In chapter 4, we have presented our field experiment in the Quiock Creek catchment. The measurements of the water table elevation and of the river discharge showed that the groundwater flow reacts quickly to rainfall events, and is likely to generate rapid flood events. Having measured the hydraulic properties of the aquifer in the previous chapter, we can now assess quantitatively to what extent the Quiock Creek hydrograph results from the groundwater flow dynamics.

Figure 6.1 shows the evolution of the Quiock Creek discharge. Like our numerical and experimental hydrographs (figures 2.3 and 3.5a), this hydrograph clearly defines three regimes: the storm flow, where the creek discharge increases rapidly during rainfall; the early stage of drought flow, where the discharge decreases rapidly; and the late stage of drought flow, where the discharge decreases much more slowly.

In this chapter, we analyse these regimes with the Dupuit-Boussinesq asymptotic regimes.

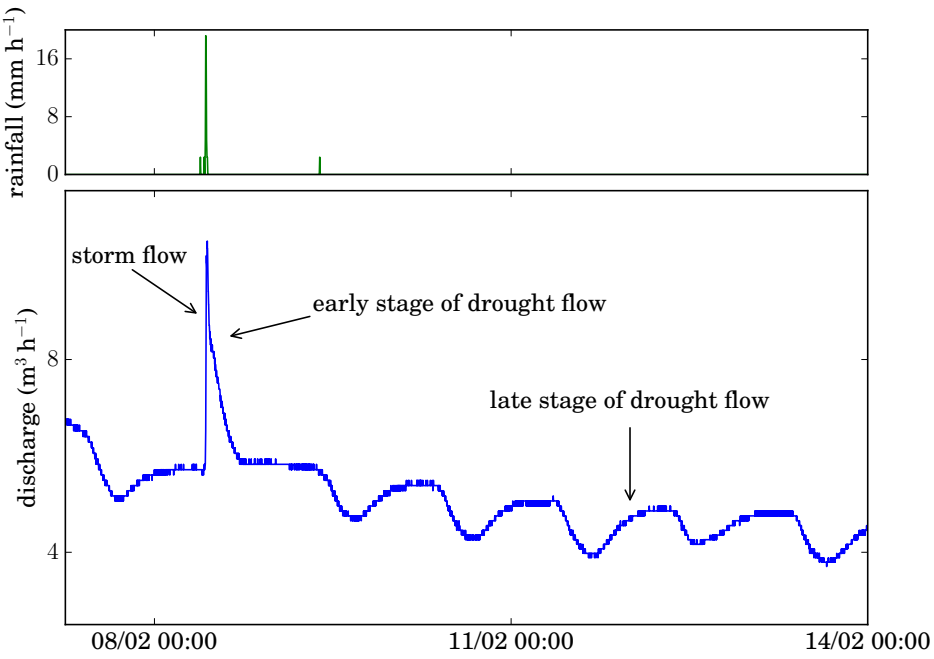

Figure 6.1: Discharge of the Quiock Creek river (—) and rainfall rate (—) measured during twenty-five days in February 2015.

6.1 Drought flow

6.1.1 Early stage of the drought flow

We analyse the Quiock Creek drought flow with the method developed by Brutsaert and Nieber (1977), and which we described in details in section 2.3.3. To identify a power law, we plot the negative time derivative of the discharge $-\dot{Q}$ versus the discharge Q. If it holds, the Dupuit-Boussinesq theory predicts a power law relationship between $-\dot{Q}$ and Q, with an exponent 3 for the early stage of the drought flow ($Q \sim 1/\sqrt{t}$, equation (2.23)), and an exponent 3/2 for the late stage of the drought flow ($Q \sim 1/t^2$, equation (2.29)) (see table 2.1).

The hydrograph of figure 6.1 illustrates a feature often encountered during the late stage of the drought flow: daily cycles, most probably due to vegetation. In the present analysis, we examine only the early stages of drought flows to avoid these daily cycles. We accordingly select twenty-three drought events in the Quiock Creek, most of which last less than one day (figure 6.2). Most of the drought events selected happened during the wet season, and span from 15th September 2014 to 12th January 2015. We do not have any water table measurement for this period.

The discharge variations during drought are still relatively low, and measuring straightforwardly $-\dot{Q}$ as the difference between two consecutive measurements leads to large measurement artefacts (figure 6.3). Indeed, if we name δQ the discharge measurement precision and δt the measurement time interval, the smallest possible value of $\dot{Q}$ is $\delta Q/\delta t$. From equation (4.2), as $\delta h/\delta t$ is a constant, this induces that $\dot{Q}$ varies with

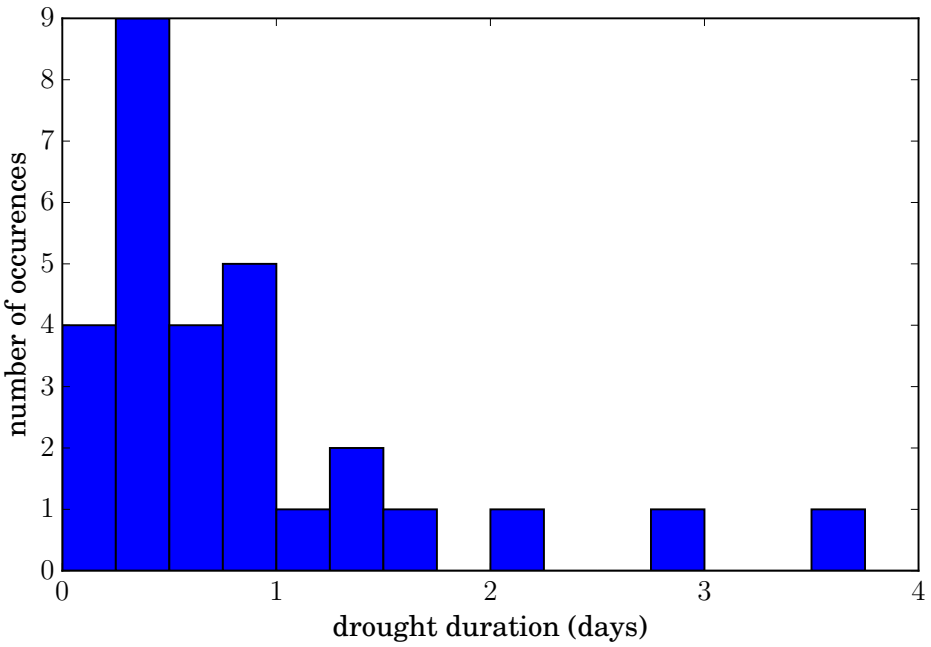

Figure 6.2: Distribution of the duration of droughts.

$\sqrt{Q}$. As a result, our $\dot{Q}$ measurements are attracted towards straight lines of slope 1/2 in a logarithmic plot.

A way to avoid this artefact is to increase the time interval δt between two discharge measurements, as in the left-hand graph of figure 6.4. The resulting data points are the average discharge versus the average slope of the discharge decrease over $\delta t =$ 15 minutes. Another possibility, suggested by Rupp and Selker (2006a), is to adapt the time interval δt such that the discharge difference between two data points is always larger than a given value (right-hand graph of figure 6.4). The discharge is a function of the water height h in the Venturi flume, and we measure the height with a precision of $\delta h = 0.7\,\mathrm{mm}$. We therefore adapt the time interval $t_{i+1} - t_i$ between two measurements such that the height difference $h_{i+1} - h_i$ is larger than $k\,\delta h$, where $k > 1$ is arbitrarily chosen. Choosing a large k reduces measurement noise. On the other hand, a small k preserves more data points at small discharge. The right-hand graph of figure 6.4 illustrates this method on a specific drought event. For illustrative purposes, we have chosen a large height difference ($k = 30$): the time interval $t_{i+1} - t_i$ is adapted such that $h_{i+1} - h_i > 2\,\mathrm{cm}$.

In practice, we performed this analysis with a less restrictive criterion: $h_{i+1} - h_i >$ 2.1 mm, which is three times the measurement precision (figure 6.5). As typically observed in this kind of plots, our data points are much scattered. We reduce this scatter by averaging the data over bins of Q, and then calculate the average values of Q and $-\dot{Q}$ into these bins. The resulting averaged points conform surprisingly well to a straight line in a logarithmic plot (figure 6.5). Fitting a power law to this average data yields an exponent of 2.81 ± 0.02. With the other measurement technique ($\delta t = 15\,\mathrm{minutes}$), we obtain an exponent 3.08 ± 0.02. As in chapter 3, we estimate the error on the exponents

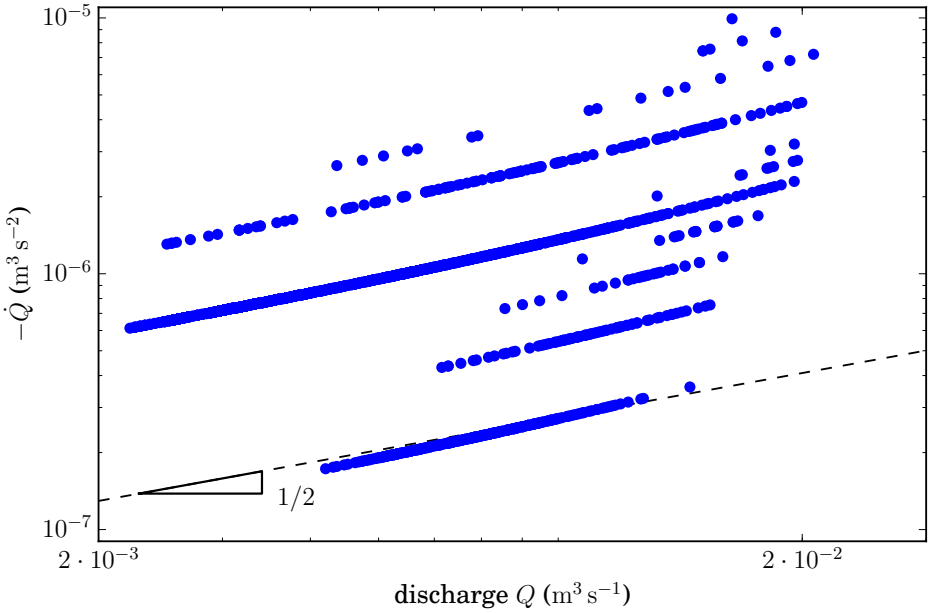

Figure 6.3: Measurement artefacts in the estimation of the time derivative of the discharge $\dot{Q}$ as a function of the discharge Q.

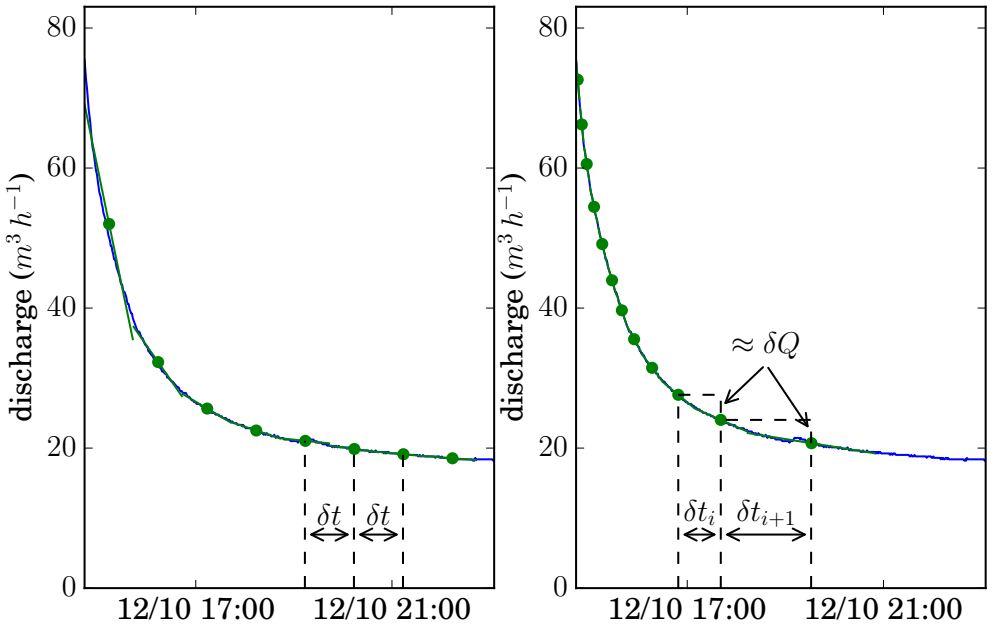

Figure 6.4: Two different methods to calculate the time derivative of the discharge. In both plots, the blue line (—) is the measured discharge and the green line (—) is the mean slope corresponding to a mean discharge (●). *Left:* A time interval δt is fixed, and we calculate the mean slope between each time interval. *Right:* A mean discharge Q_i is calculated over a time interval δt_i such that $Q_i - Q_{i+1} \geqslant \delta Q$, where δQ is arbitrarily chosen. Accordingly, the time interval between two points $(Q_i, -\dot{Q}_i)$ increases as the discharge decreases.

by estimating a lowest and highest value of the exponent. The lowest value is obtained with the minimisation of the horizontal distance of the data points to the fit function, and the highest value with the vertical distance.

These exponents are close to the exponent 3 predicted by the early-times asymptotic regime of the Dupuit-Boussinesq equation. If confirmed, this result implies that the early stage of the Quiock Creek drought flow is well described by the Dupuit-Boussinesq theory.

We can further assess this result with the prefactor of this power law. Within the Dupuit-Boussinesq framework, the early stage of the drought flow (equation (2.23)) reads:

$$Q(t) \sim 2 \times \frac{a_{\text{esdf}}^2}{4} W \frac{(s\,K\,H^3)^{1/2}}{\sqrt{t}}\,, \tag{6.1}$$

where $a_{\text{esdf}} \approx 1.152$ is a mathematical constant, W is the length of the stream, and H is the depth of the aquifer. This equation differs from equation (2.23) by a factor two. Indeed, our laboratory aquifer simulates only one side of a river, whereas a natural stream is obviously fed from both sides. In the $\dot{Q}/Q$ plane, this equation translates into the following relationship:

$$-\dot{Q} = \frac{1}{2}\,\frac{a_{\text{esdf}}^2}{2}\,W\,\frac{(s\,K\,H^3)^{1/2}}{t^{3/2}} = \frac{2}{(a_{\text{esdf}}^2\,W)^2\,s\,K\,H^3}\,Q^3\,, \tag{6.2}$$

In chapter 5, we estimated $s = 1.87 \cdot 10^{-2}$ and $K \approx 10^{-6}\,\mathrm{m\,s^{-1}}$. We also estimated the total stream length $W \approx 979$ m. Finally, the maximum altitude difference between the ground topography and the river is about 6 m, along the profile we measured (figure 4.2). We thus roughly estimate the depth of the aquifer $H \approx 6\,\mathrm{m}$. We assume that the aquifer is initially fully saturated over this whole depth, as required to derive the early-times asymptotic regime (2.23).

The early-times asymptotic regime therefore predicts a prefactor of $0.293\ \mathrm{s\,m^{-6}}$ for the power law (6.2). In comparison, fitting a power law with an exponent 3 to the data yields a prefactor of $0.638\ \mathrm{s\,m^{-6}}$. The Quiock Creek early stage drought flow is therefore in good agreement with the Dupuit-Boussinesq prediction.

Being a short-times regime, the early stage of the drought flow (6.1) has a finite duration. In section 2.3, we showed that this regime is valid until the front reaches the divide, that is

$$t \approx \frac{s\,L^2}{K\,H}\,. \tag{6.3}$$

In the present case, the drainage area A is about eight hectares ($A \approx 8 \cdot 10^4\,\mathrm{m^2}$) and the channel length W is about a thousand metres. We therefore estimate that the lateral extension of the aquifer $L \approx 40\,\mathrm{m}$ (see also section 6.2.5). Using our local estimations of the hydraulic parameters $K \approx 10^{-6}\,\mathrm{m\,s^{-1}}$ and $s = 1.87 \cdot 10^{-2}$, we obtain a regime validity of about 70 days. As all the drought events examined in this section last less than 4 days, they are therefore within the range of validity of the Dupuit-Boussinesq regime.

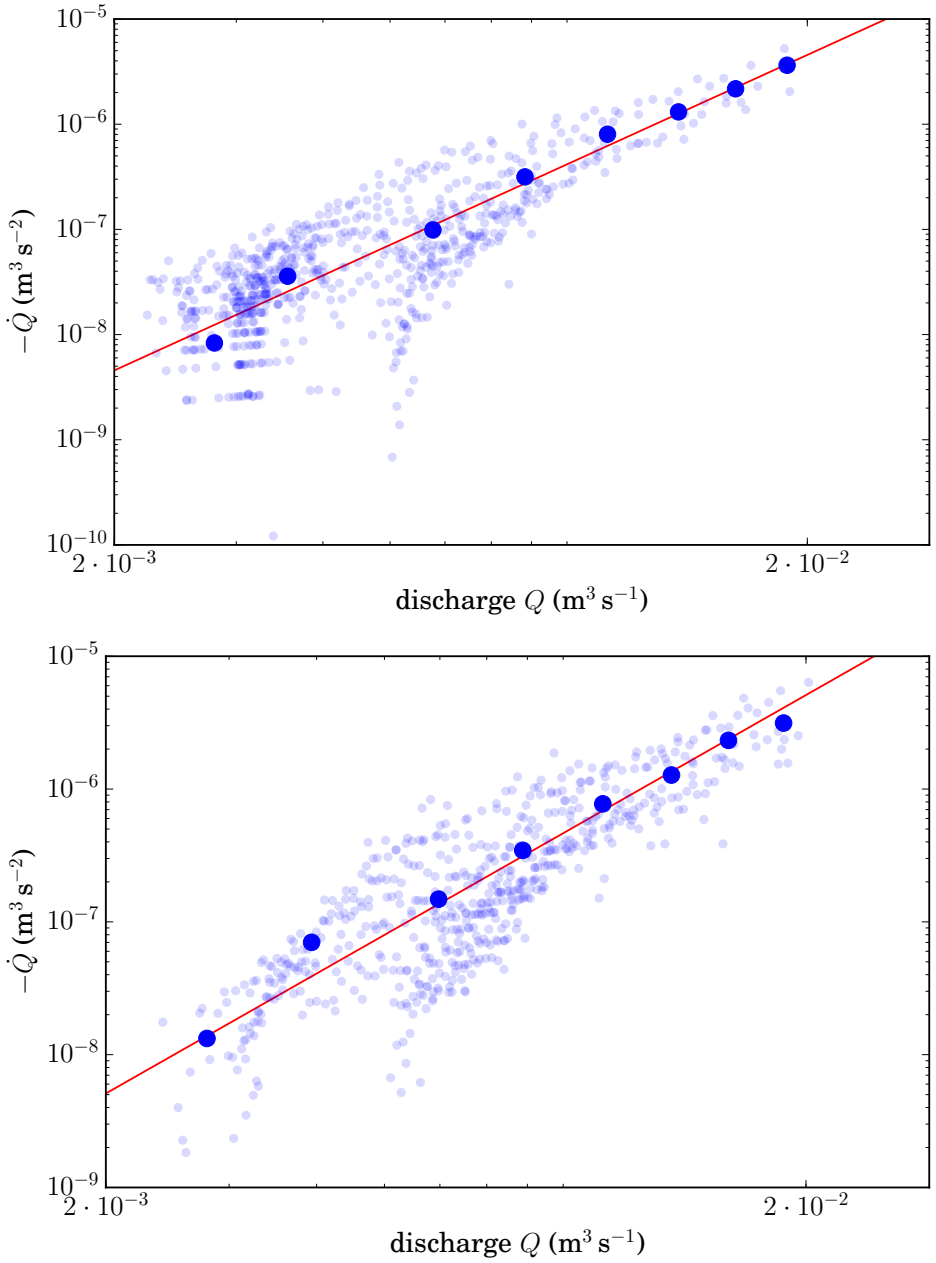

Figure 6.5: Time derivative of the discharge $-\dot{Q}$ as a function of the discharge Q. The small transparent blue points are the raw data points, and the blue points (●) are averaged bins. *Top:* $\dot{Q}$ is calculated over a fixed time interval. The fit of a power law with an exponent of 3 (—) yields a prefactor of 0.570 s m^{-6}. *Bottom:* $\dot{Q}$ is calculated over a time interval $t_{i+1} - t_i$ such that the discharge difference $Q_i - Q_{i+1}$ between two measurements is three times larger than the discharge measurement precision δQ: $Q_i - Q_{i+1} > 3\,\delta Q$ (see text). A power law with an exponent of 3 (—) fitted to the binned data yields a prefactor of 0.638 s m^{-6}.

6.1.2 Late stage of the drought flow

The early-times regime is expected to last during approximately 70 days. As drought periods rarely exceed two weeks, we could expect this regime to hold for all droughts. Yet, this flow regime implies that the aquifer does not empty far from the river. This situation is not possible, as the groundwater flow is often being recharged. There must be periods where the discharge quits this early flow regime.

During the dry season — since January 2015 (to July 2015) — the rainfall events are scarce. We consequently observe more late stages of drought flow, characterised by daily variations. We did not have time to analyse these late drought flows yet.

6.2 Storm flow

As a result of intense rainfall events, the Quiock Creek discharge can increase by a factor of 20 or more in less than an hour. The purpose of this section is to evaluate quantitatively the contribution of groundwater to these flood events. In section 5.1, we analysed the water table dynamics during rainfall events, in order to measure the aquifer porosity. This analysis showed that, far from the river, the water table rise during rainfall is compatible with a linear relationship with the rainfall rate, and therefore compatible with the Dupuit-Boussinesq theory.

In this section, we analyse the discharge dynamics of the Quiock Creek during rainfall events. We compare this analysis with the storm-flow asymptotic regime (3.11) of the Dupuit-Boussinesq equation derived in section 3.6, which relates the discharge Q of the river with the rainfall rate R through a 3/2 power law:

$$Q(t) \sim 2\,a^2\,\frac{W}{s}\,\sqrt{\frac{K}{2}}\,R^{3/2}\,t\,, \tag{6.4}$$

where W is the length of the stream, s is the porosity, K is the hydraulic conductivity, and $a \approx 1.016$ is a mathematical constant. Equation (6.4) differs from equation (3.11) by a factor two because our laboratory aquifer simulates only one side of a river.

Prediction (6.4) results from the condition that the aquifer is empty before the beginning of the rainfall event. In fact, the Quiock Creek discharge never vanished during the period analysed here, and the aquifer certainly never totally empties. In the present section, we ignore this inconsistency. However, we carefully select the floods to be analysed, such that they are as close as possible from ideal conditions. Three criteria are required to select a flood. First, the river discharge prior to the flood should be sufficiently low, such that the initial state of the aquifer prior to the flood be close to be empty. In practice, the initial discharge of all selected floods is inferior to $22.5\,\mathrm{m^3\,h^{-1}}$. Second, the rainfall event should be isolated from other rainfall events; and with only one local maximum (see figure 6.9). Finally, the discharge signal should be regular enough to evaluate discharge increase rate $\dot{Q}$ (figure 6.7).

In total, we selected 84 flood events for this analysis. As equation (6.4) only describes the early response to rainfall, its validity is limited in time. We first evaluate this validity in our data set.

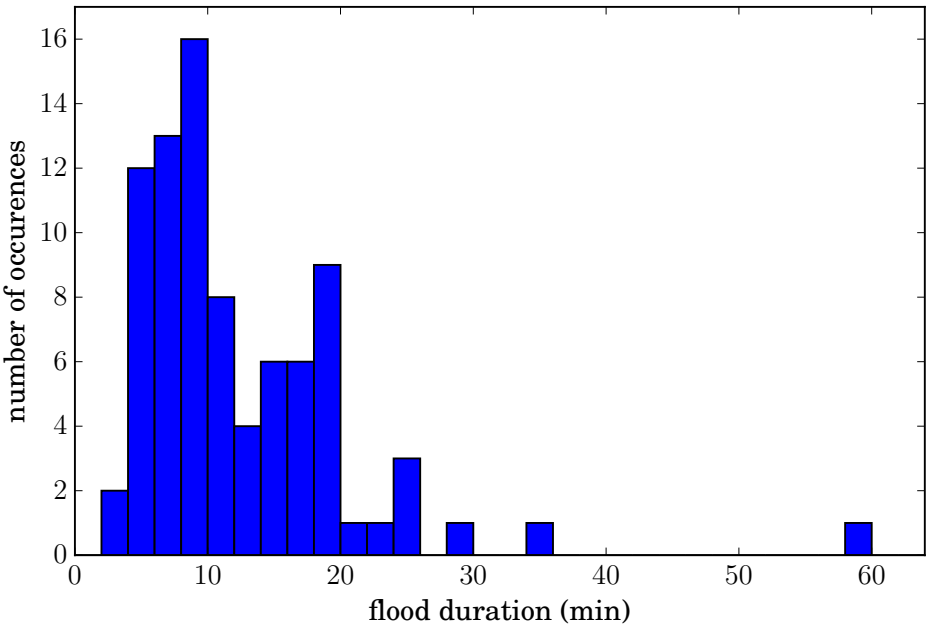

Figure 6.6: Distribution of the duration of the floods of our data set.

6.2.1 Flood duration

Equation (6.4) derives from an early-times asymptotic regime. In chapter 3, we showed that this regime is valid until the front reaches the divide, that is until

$$t \approx \frac{s\,L}{\sqrt{K\,R}}\,. \tag{6.5}$$

As the drainage area A is about eight hectares ($A \approx 8 \cdot 10^4\,\mathrm{m}^2$) and the channel is about a thousand metres long, we estimate that the lateral extension of the aquifer is about $L \approx 40\,\mathrm{m}$. For a rainfall rate $R \approx 10^{-5}\,\mathrm{m\,s}^{-1}$ (our most intense event), the asymptotic regime is valid about three days.

Figure 6.6 shows the distribution of storm duration. All storms lasted less than one hour, and the average duration is thirteen minutes (figure 6.6). The selected floods therefore satisfy the early times condition.

According to equation (6.4), the discharge increase rate $\dot{Q}$ is expected to be proportional to the rainfall rate at the power of 3/2:

$$\dot{Q} \propto R^{3/2}\,. \tag{6.6}$$

We now present our procedure to measure $\dot{Q}$ and R during storm events.

6.2.2 Measurement of the discharge increase rate

Figure (6.7) shows a typical flood, to illustrate how we measure the discharge increase rate and the rainfall rate, and how we estimate the measurement errors.

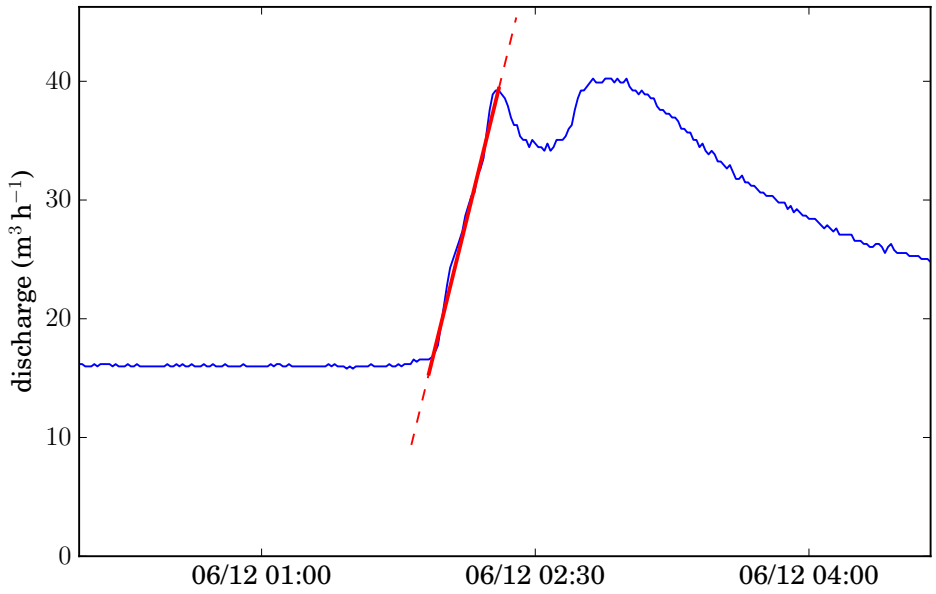

Figure 6.7: Example of a flood in the Quiock Creek (—), during December 2014. The mean slope of the discharge over the whole duration of the discharge increase yields the discharge increase rate $\dot{Q}$ (—).

We estimate the discharge increase rate by recording the time at which the discharge starts increasing, and the time at which it starts decreasing. We thus estimate the duration over which the discharge increases. We then fit an affine function to the discharge over this duration. The slope of this linear function is the discharge increase rate $\dot{Q}$. This method reduces the influence of discharge measurement errors.

As the measurement of a time derivative may be sensitive to the way it is computed, we have also tested four other procedures. For each flood, we have measured the maximum slope over ten minutes, the slope over the first half of the flood, and the slope over the middle half of the flood. In addition, we have estimated visually the discharge increase rate. The comparison of these four measurement methods with the average slope method reveals that the five methods are roughly equivalent, but individual data points may differ up to a factor of two (figure 6.8). For each data point, we calculated the standard deviation between the five measurement techniques. The average standard deviation over all our data points is 23%. Our evaluations are therefore rather insensitive to the procedure we use.

6.2.3 Rainfall rate during the flood events

We now present the procedure we follow to evaluate the rainfall rate. In the asymptotic theory of section 3.6, we assumed that the rainfall rate is constant during a flood event. This is obviously not true in the field. To approximate this assumption, we measure the rainfall rate by fitting a rectangular function to the rainfall signal (figure 6.9). We impose that the fitting function preserves the volume of rainwater of each event. We

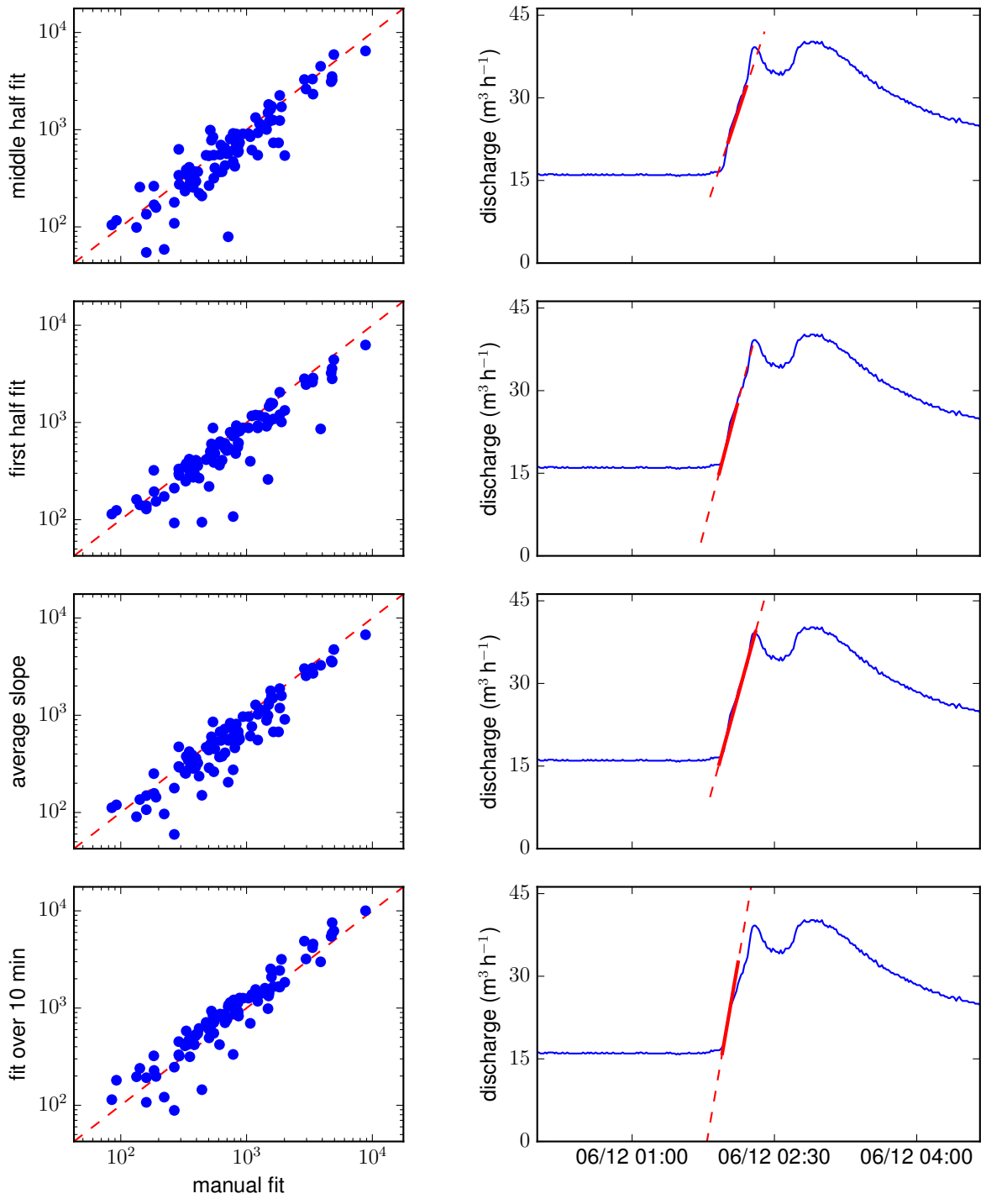

Figure 6.8: Comparison of the four methods used to measure the discharge increase rate. We compare four different automated procedures with a visual estimate of the slope.

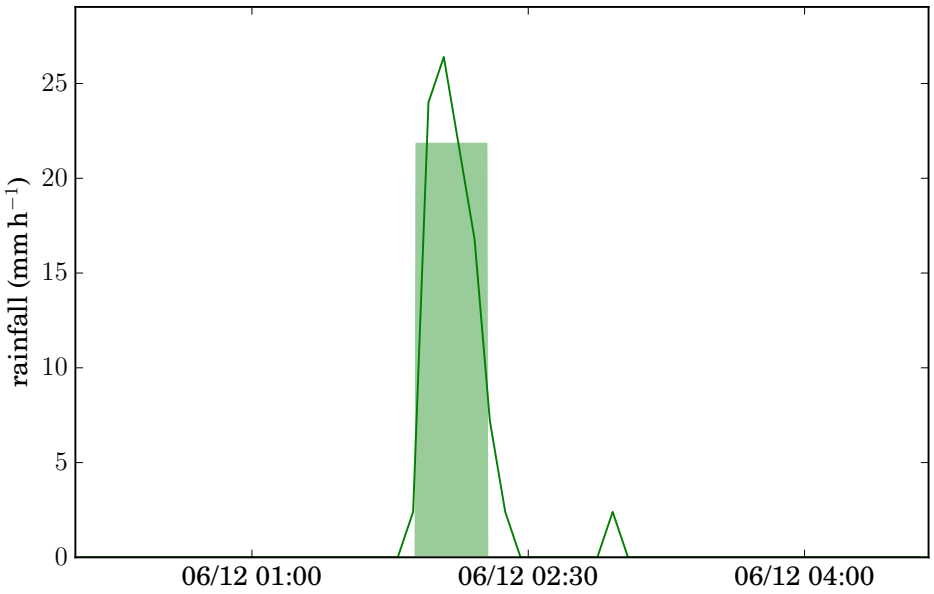

Figure 6.9: Rain event causing a flood (—), and the associated rectangular fit (▬).

thus fit two parameters: the time of the event and its duration.

To assess the robustness of this procedure, we compare these measurements with visual estimations of the rainfall rates (figure 6.10). The data follow a linear trend with moderate fluctuations. For each data point, we calculated a standard deviation between the two techniques of 11% in average.

Another issue might stem from the choice of the sampling period, which influences strongly the rainfall signal. Figure 6.11 illustrates this influence. The same rainfall event is recorded with three different sampling periods: one minute, five minutes and fifteen minutes. To these three signals, we have applied our fitting procedure to evaluate the average rainfall intensity. Not surprisingly, the shorter the sampling period, the larger the rainfall intensity. Figure 6.12 illustrates this artefact by comparing the results of the three signals. With a sampling period of one minute (top graph), we observe a minimum threshold $R_{\min} \approx 10\,\mathrm{mm\,h^{-1}}$, which corresponds to the rain gauge volume (0.2 mm) divided by one minute. This very short sampling period is therefore not adapted to measure moderate rainfall events. On the contrary, the rainfall rates measured with sampling periods of fifteen and five minutes are, on average, proportional. Fitting a power law to the data yields an exponent of 1.19, and the average standard deviation is 34%. Fitting a linear relationship between the two signals, we find that the rainfall intensity obtained with a sampling period of fifteen minutes is, on average, lower by a factor two. In what follows, we consider the five-minutes signal.

Finally, we also compared our measurements with the intensity of the rainfall events outside the forest. Not surprisingly, the rainfall rate measured outside the forest is slightly larger. The discrepancy between the two signals is slightly larger for small rainfall rates, suggesting that the measurement error in the Quiock Creek catchment is larger for small rainfall events.

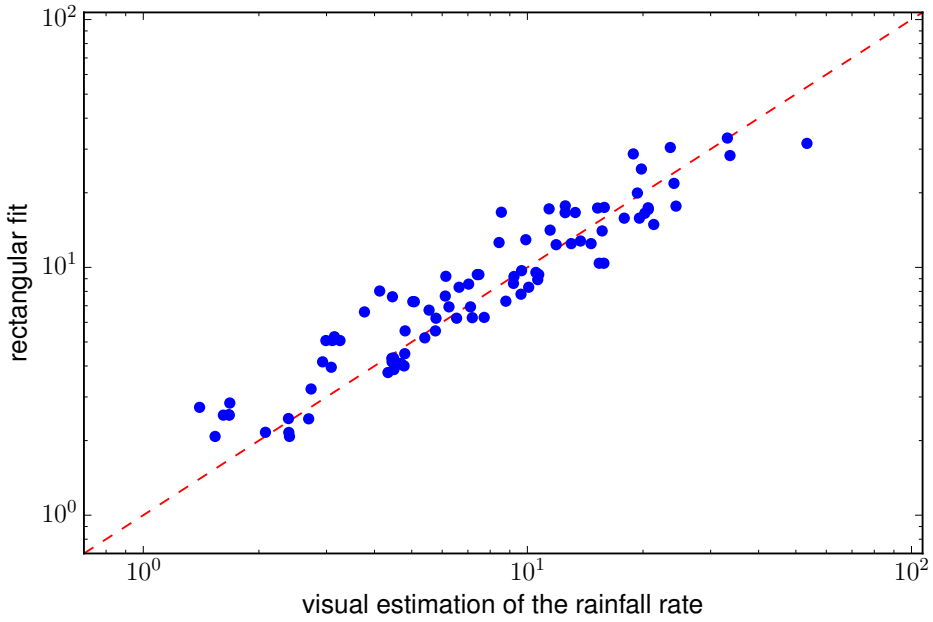

Figure 6.10: Rainfall rate measured by a rectangular fit as a function of a visual estimate of the rainfall rate of the event (●). The red dashed line (- - -) is identity.

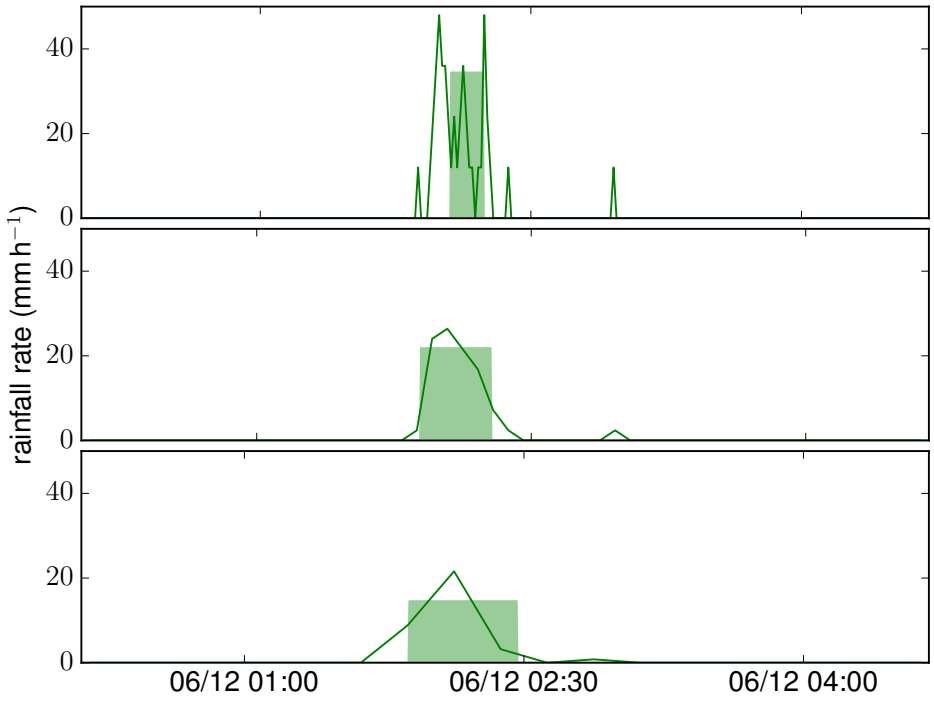

Figure 6.11: Rainfall rate (—) measured with three different sampling periods: one minute (*top*), five minutes (*middle*) and fifteen minutes (*bottom*). The rainfall rate R (▬) associated to a flood event depends on the sampling period.

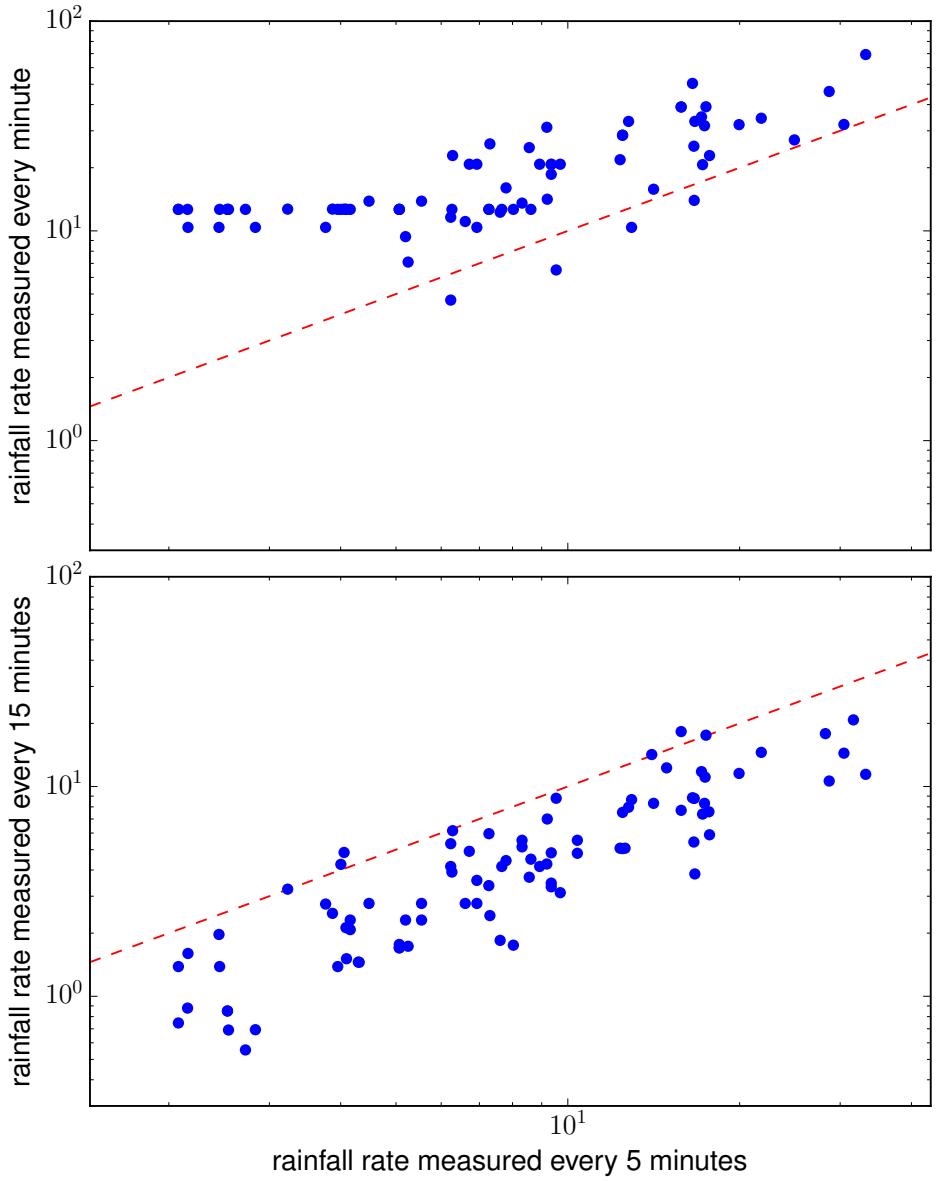

Figure 6.12: Influence of the sampling time on the measurement of the rainfall rate causing a flood. The red dashed line (- - -) corresponds to identity.

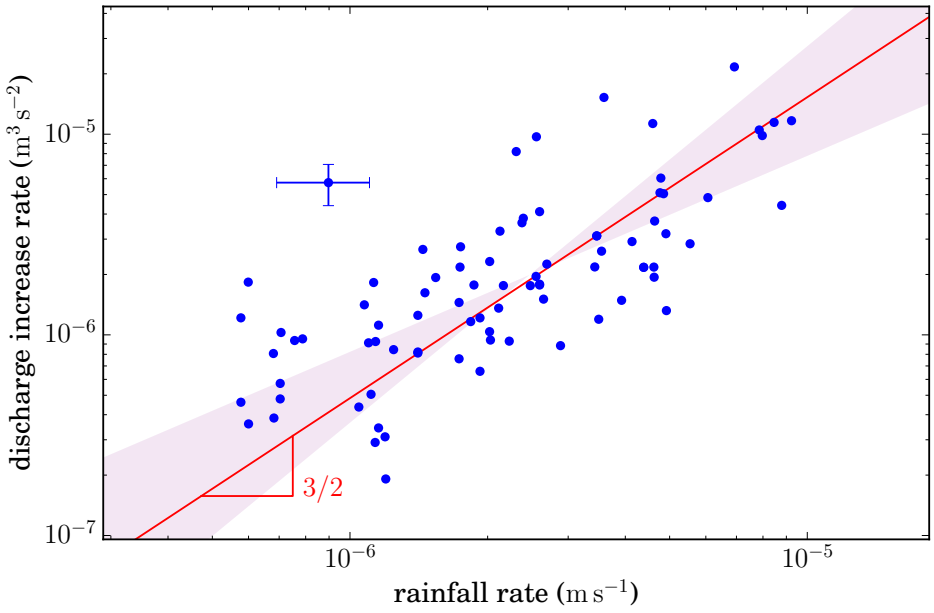

Figure 6.13: Discharge increase rate as a function of the rainfall rate in the Quiock Creek (●). The red line (—) represents a 3/2 power law fitted to the data, yielding a prefactor of 483.60 $m^{3/2} s^{-1/2}$. The shaded area represents the least-square fit based on each axis.

6.2.4 Asymptotic regime of the Dupuit-Boussinesq theory

For the eighty-four floods thus analysed, we plot the discharge increase rate $\dot{Q}$ as a function of the rainfall rate R (figure 6.13). As expected, the discharge increase rate is a growing function of the rainfall rate. This growing function is not linear, and resembles a power law with an exponent larger than one. Fitting a power law to the data yields an exponent of 1.35 ± 0.45. The minimum and maximum fits are estimated with a lest-square fit based on x-axis and on the y-axis, respectively. These exponents are in reasonable agreement with the 3/2 exponent of the asymptotic regime predicted from the Dupuit-Boussinesq theory (equation (6.4)).

Assuming that the prediction (6.4) holds and fitting a 3/2 power law to all the data (figure 6.13) yields a prefactor of 483.60 $m^{3/2} s^{-1/2}$. Using our estimates of the hydraulic parameters $K \approx 10^{-6} m s^{-1}$ and $s = 1.87 \cdot 10^{-2}$, and our estimate of the total drainage length $W = 979 m$, we obtain a theoretical prefactor of 76.43 $m^{3/2} s^{-1/2}$. Our measurements therefore compare reasonably with the asymptotic regime (6.4) of the Dupuit-Boussinesq equation.

Yet, the theoretical prefactor is about six times lower than our measurement. Three reasons could explain this mismatch besides disqualifying the Dupuit-Boussinesq theory. First, our experiments already resulted in a prefactor three times larger than the theoretical prefactor (chapter 3). To explain this mismatch, we pointed to the possible breakdown of the Dupuit-Boussinesq approximation near the outlet. This remark still holds here. Second, our local estimates of K and s may slightly differ from the aquifer

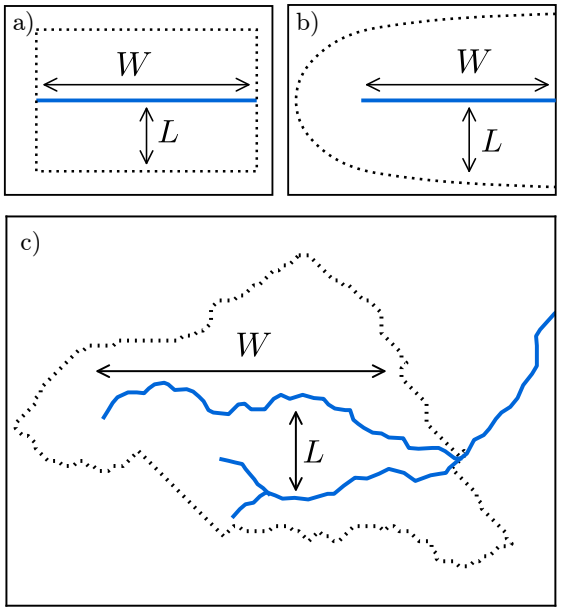

Figure 6.14: Influence of the drainage-network geometry on the flow. *a)* Configuration adopted in this manuscript. A single lateral extent characterises the network, and the flow is one-dimensional. *b)* A single lateral extent characterises the network, but the flow is two-dimensional near the tip of the channel. *c)* Drainage network of the Quiock Creek. Multiple tributaries define multiple lateral extents, and the flow is two-dimensional around the network.

hydraulic properties at the catchment scale (yet, these values yielded a good agreement with the drought flow analysis). Third, the one-dimensional approach we used here and in our experiment neglects the influence of the drainage network on the hydrograph, reducing it to a single straight channel. In the next paragraph, we investigate this influence.

6.2.5 Influence of the drainage-network geometry

Most natural drainage networks are ramified collections of streams, and the typical lateral extent of a drainage divide depends on scale. In addition, the network induces horizontal two-dimensional flows near tips, ramifications and sharp curves (Devauchelle et al., 2012; Petroff et al., 2013). In this manuscript, we reduced the network to a single channel, with a single lateral length (figure 6.14). As a result, the flow was confined to a line perpendicular to the river. In reality, the geometry of the network affects the dynamics of the groundwater flow.

Provided the flow is shallow enough, the Dupuit-Boussinesq approximation still holds in two dimensions:

$$s\,\partial_t h = \frac{K}{2}\,\nabla^2 h^2 + R\,, \tag{6.7}$$

and we need to solve it around the network. How do the asymptotic regimes of this

equation compare with their one-dimensional counterparts?

Storm flow. The self-affine rescaling of the storm flow (equations (3.5) and (3.6)) affects the space coordinates. This rescaling cannot match the river boundary condition in two dimensions, and therefore is not an exact solution to equation (6.7).

However, the one-dimensional solution corresponds to a front propagating away from the river. This solution is valid as long as this front has not reached another boundary. Thus, the one-dimensional storm flow is likely to be a reasonable approximation of the two-dimensional flow, until the thickness of the front becomes comparable to the lateral extent L of the aquifer.

In that case, we expect the storm-flow discharge to depend on the drainage length W only:

$$Q(t) \sim a^2 \, \frac{W}{s} \sqrt{\frac{K}{2}} \, R^{3/2} \, t \, . \tag{6.8}$$

The lateral extent L of the divide only affects the duration of the asymptotic-regime validity.

Early drought flow. The rescaling of the early-drought-flow regime also corresponds to a front propagating away from the river. Following the same reasoning as above, we also expect the one-dimensional asymptotic regime to provide a reasonable approximation of the discharge, as long as the front is thinner than the lateral extent L of the aquifer:

$$Q(t) \sim W \, \frac{a_{\text{esdf}}^2}{4} \, \frac{(s \, K \, H^3)^{1/2}}{\sqrt{t}} \, . \tag{6.9}$$

Again, the discharge is proportional to the drainage length.

Late drought flow. Contrary to the two above regimes, the rescaling of the late-drought-flow regime does not affect the space coordinates. Indeed, substituting

$$h(x, y, t) = \frac{L^2 \, s}{K \, t} H_d \left(\frac{x}{L}, \frac{y}{L} \right) \tag{6.10}$$

into the two-dimensional Dupuit-Boussinesq equation (6.7) yields

$$\nabla^2 H^2 + H = 0 \tag{6.11}$$

which is but the extension of equation (2.26) to two dimensions. The length L is the typical extension of the entire catchment. The non-linear Helmholtz equation (6.11) depends on space only, and can be supplemented with a boundary condition along the drainage network. Based on the one-dimensional case, we expect it to admit a single solution for any given geometry of the network. If this is true, the late-drought-flow regime is an exact solution of the two-dimensional Dupuit-Boussinesq equation. The corresponding discharge is the integral of the groundwater flux along the entire drainage network:

$$Q \sim \tilde{a}_d \, \frac{s^2 \, L^4}{K \, t^2} \, , \tag{6.12}$$

where $\tilde{a}_d$ is a dimensionless constant which depends on the network geometry only.

In conclusion, the three asymptotic regimes of the Dupuit-Boussinesq equation can be generalised to two dimensions. However, the planform geometry of the drainage network is likely to affect the integration constant of an asymptotic regime, and the duration of its validity. Therefore, we cannot expect to predict accurately the prefactor of the corresponding discharge expression. We can only expect its order of magnitude to compare with observations.

6.2.6 Sources of variability in the measurements

Our analysis supports the use of the Dupuit-Boussinesq theory to describe the Quiock Creek discharge evolution. Yet, our measurements show a large scatter (figure 6.13). Here, we try to evaluate possible sources of variability.

Our error bars are smaller than the scatter of the data. This suggests that this scatter comes from the heterogeneity of natural conditions, rather than from measurement errors. Among the most obvious sources of variability are the heterogeneity of the ground, of the rainfall rate, or the fact that the initial state prior to a flood slightly varies from one flood to another.

Figure 6.15 points to the influence of seasons on our measurements. Indeed, all the points measured in September (in purple) lie into the lower part of the data cloud. If we select only the floods recorded in September, we are left with fourteen data points (figure 6.16). The resulting graph appears much less scattered, although these fourteen points almost cover the same range of rainfall rate measurements. Fitting a power law to these data points yields an exponent of 1.74 ± 0.1. However, a 3/2 power law could also fit the data within the error bars. Moreover, fitting a 3/2 power law to these fourteen data points yields a prefactor of 284.29 $\mathrm{m}^{3/2}\,\mathrm{s}^{-1/2}$, which is closer to the theoretical prefactor calculated with equation (6.4).

Finally, we also estimate the influence of the sampling period on our results. The high frequency of our discharge measurements, collected every minute, allows a good temporal resolution of the quick storm events, but it can induce measurement noise. Decreasing the measurement frequency reduces this noise but, in turn, it can lower the number of floods observed, or affect the discharge increase rate measurement. To estimate the influence of the discharge measurement frequency, we artificially increase the sampling time of the measurements. We then select flood events, based on the same criteria as described at the beginning of this section, and measure $\dot{Q}$. We repeat this procedure with sampling times of 15 minutes, one hour and five hours (figure 6.17). As expected, we observe less floods when we increase the sampling time. Fitting a power law to the three new data sets, we obtain the exponents 1.36, 1.54 and 2.02, all in reasonable agreement with the Dupuit-Boussinesq prediction. Yet, the measurement error on the exponent increases with the sampling time. Of course, the sampling time should not be larger than the average duration of flood events.

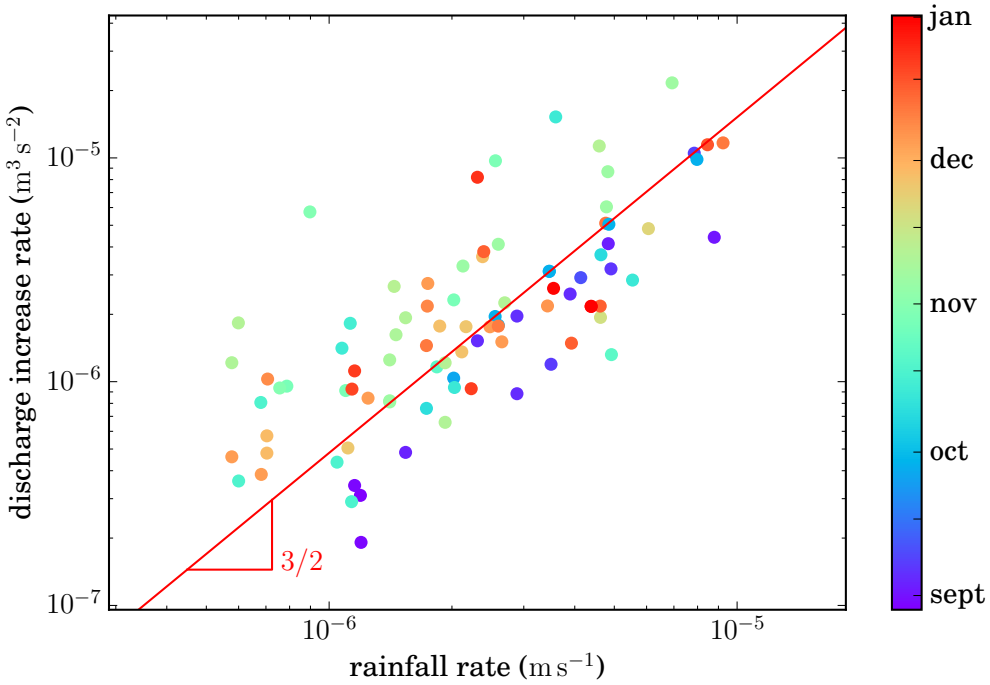

Figure 6.15: Influence of the season on our results. September is the very beginning of the wet season, which ends in December - January.

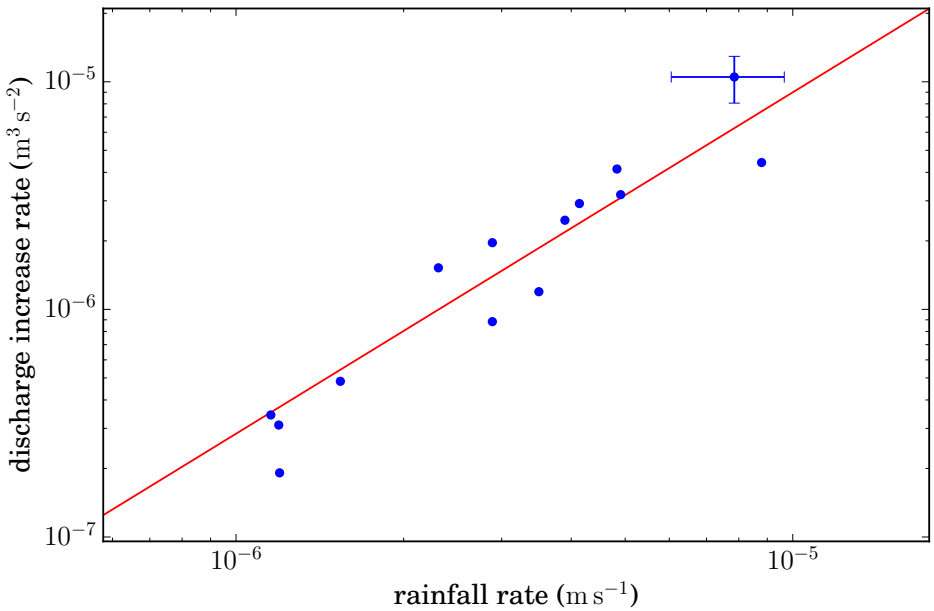

Figure 6.16: Discharge increase rate as a function of the rainfall rate in the Ravine Quiock (●). On this graph, only the points recorded in September 2014 are represented. The red line (—) represents a 3/2 power law fitted to the data, yielding a prefactor of 284.29 $m^{3/2} s^{-1/2}$.

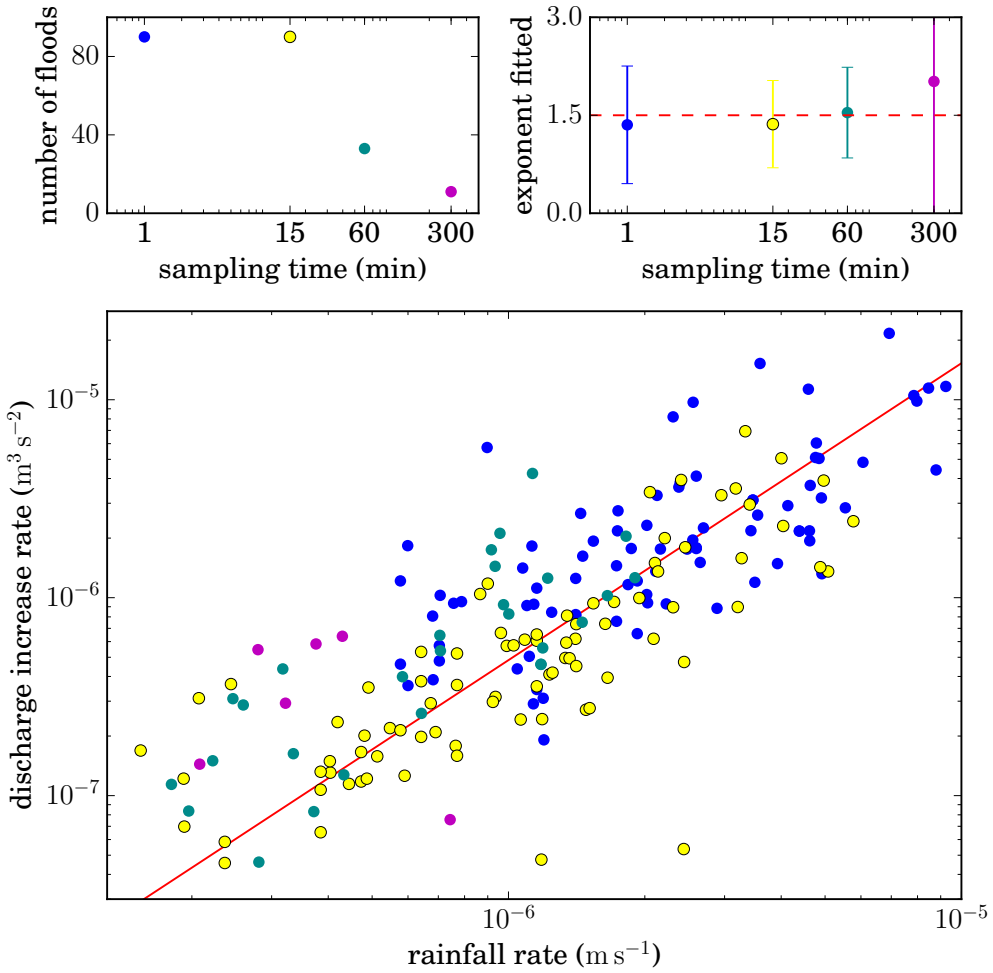

Figure 6.17: Influence of the sampling time on the relationship between the discharge increase rate and the rainfall rate.

6.3 Discussion

Our measurements of the water table elevation indicated that groundwater can generate quick floods in the Quiock Creek (chapter 4). In the present chapter, we have analysed the Quiock Creek discharge dynamics with high-frequency measurements. We compared this dynamics with asymptotic regimes of the Dupuit-Boussinesq equation, using the methods developed for our laboratory aquifer (chapter 3).

Both the analyses of the drought flow and of the storm flow revealed a non-linear behaviour. During the drought flow, the Quiock Creek discharge decreases as a power law of time. During the storm flow, the discharge increase grows with the rainfall rate more than linearly. This suggests that the Quiock Creek aquifer is a non-linear reservoir.

The early stage of the river drought flow seems compatible with the asymptotic regime of the Dupuit-Boussinesq equation. This implies that the river discharge decreases as the inverse square root of time. The prefactor of this scaling law also conforms to the prediction, indicating that our measurements of the aquifer hydraulic properties are reasonable. It would be interesting to compare the river discharge and water table decline to the long-times asymptotic regime of the Dupuit-Boussinesq equation. Unfortunately, we could not observe drought flows over a period long enough to do so, due to the presence of strong daily variations during periods of low discharge, and to a lack of time.

The river discharge increase rate during rainfall events grows with the rainfall rate in a non-linear power-law relationship. The exponent of this relationship is close to $3/2$, in agreement with the early-times asymptotic regime derived in chapter 3. The theoretical prefactor of this scaling law also reasonably conforms with our measurements. The Dupuit-Boussinesq asymptotic regimes therefore describe the Quiock Creek discharge dynamics reasonably well, during storm events and during drought events. This suggests that the Quiock Creek is mostly fed by groundwater. There is no need to invoke overland flow to explain the quick floods which affect its discharge.

Finally, we developed in this chapter a new method to analyse a river hydrograph: plotting the discharge increase rate $\dot{Q}$ with respect to the rainfall rate R during storm flow. In complement to the Q $\dot{Q}$ plot method of Brutsaert and Nieber (1977) for drought flow analysis (section 2.3.3), this method could contribute to determine the flow processes within a catchment. In this chapter, we showed that a power law with an exponent of $3/2$ could be the signature of a groundwater-dominated catchment where the Dupuit-Boussinesq approximation holds. As the prefactor of this power law depends on the hydraulic properties of the aquifer, the $\dot{Q}$ R plot method is also a way to estimate the porosity and hydraulic conductivity of an aquifer, if associated to a known asymptotic regime.

Yet, the asymptotic regimes of a two-dimensional groundwater flow in a deep aquifer are still to be known. Whereas the mathematics of a groundwater flow feeding a fully-penetrating stream is easier to grasp, nothing justifies this assumption in general. In the Quiock Creek aquifer, an electrical resistivity soil profile did not reveal any bottom (chapter 4). Moreover, the most convincing interpretation of the slug tests performed in

section 5.2 corresponds to an infinitely deep aquifer. The two-dimensional groundwater flow in a deep aquifer certainly deserves a detailed scrutiny.

Before addressing this question in chapter 8, we first test the $\dot{Q}\ R$ plot method to analyse, in the next chapter, the hydrograph of natural rivers.

Chapter 7

Hydrographs from other catchments

Contents

In the last three chapters, we have shown that a natural groundwater flow can react quickly to rainfall events, and generate floods. In the present chapter, we analyse the hydrograph of other natural catchments, and evaluate their compatibility with the Dupuit-Boussinesq asymptotic regimes. In particular, we analyse the river floods by plotting the discharge increase rate $\dot{Q}$ with respect to the rainfall rate, expecting a 3/2 power law if the catchment is dominated by groundwater and the latter conforms to the Dupuit-Boussinesq theory.

The ideal site to test the Dupuit-Boussinesq theory is a small catchment, where the geologic and climatic conditions are homogeneous. We further require high-frequency measurements of the discharge. We found three instrumented catchments which satisfy these two conditions: the two catchments of the Severn and of the Wye rivers, known as the Plynlimon catchments, in mid-Wales, UK; and the Draix catchment, in the French

Préalpes. As these two sites are geologically different, we separate the analyses of the Plynlimon catchments and of the Draix catchment.

7.1 The fractured aquifers of the Plynlimon catchments, Wales

Figure 7.1: A gauging station of the Severn river, Wales (*picture*: J. Kirchner, from `http://www.ethlife.ethz.ch/archive_articles/130812_Wasserqualitaet_aj/index_EN`).

7.1.1 Field sites

Known as the Plynlimon catchments, the headwaters of the Severn and of the Wye rivers are a historical landmark for hydrological research. For more than four decades, these two neighbouring catchments were extensively instrumented to study the chemistry of groundwater, the impact of vegetation on evapotranspiration, or to evaluate long-term water balances (Calder, 1977; Kirby et al., 1991; Neal, 1997; Neal et al., 1997b; Marc and Robinson, 2007). The two catchments lie in the Cambrian Mountains and share very similar geological features. Their upland massif is composed of Ordovician and Silurian mudstones, sandstones, shales, and slates. The bulk of these hard stones is virtually impermeable, but boreholes revealed extensive groundwater circulation through fractures (Neal et al., 1997a; Haria and Shand, 2004; Kirchner, 2009). The upper layer of the soil is mostly composed of blanket peat (> 40 cm thick) at

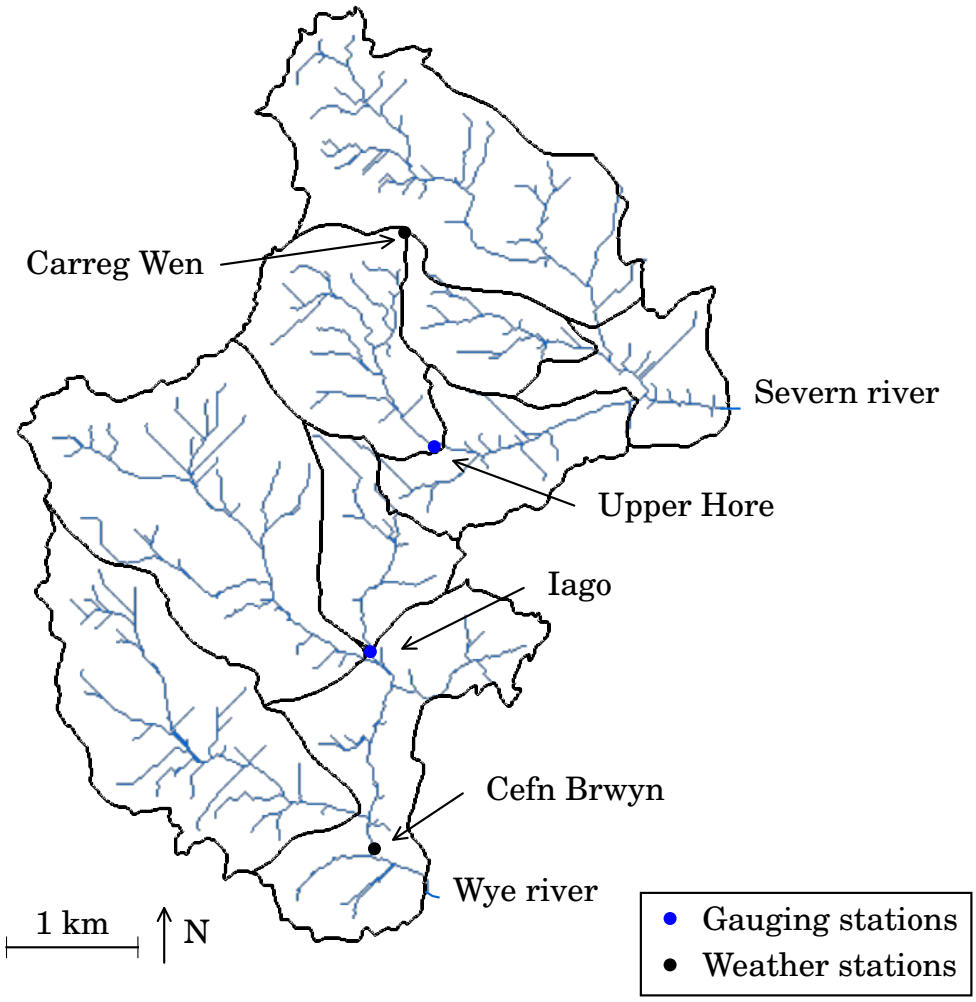

Figure 7.2: The headwaters of the Wye and Severn rivers. The catchments and sub-catchments (associated to gauging stations) are delimited by a black line (—). The blue dots (●) represent the gauging stations measuring the discharge of the Upper Hore and Iago streams. Finally, the rainfall rates used in the present study are measured by the weather stations, indicated by black dots (●).

higher altitudes, and of podzols (weathered sandstone) at lower altitudes. The most substantial difference between the two catchments is their vegetation cover: the Wye river catchment is mostly composed of grassland used for sheep pasture, whereas 70% of the Severn river catchment was forested with conifers at the time of the measurements (Brandt et al., 2004).

The climate is cool and humid. The average monthly temperature is typically 2-3°C in winter and 11-13°C in summer (Kirchner, 2009). The annual rainfall is around 2500-2600 mm y^{-1}, of which approximately 500 mm y^{-1} are lost to evapotranspiration (Brandt et al., 2004). Seasonal variations feature a larger rainfall during winter (280-300 mm $month^{-1}$) than during summer (135-155 mm $month^{-1}$). Finally, snow accounts for approximately 5% of annual rainfall (Kirchner, 2009).

Since the seventies, a Crump weir and a trapezoidal flume allow to measure continuously the discharges of the Wye and of the Severn rivers. Three of the upstream tributaries of the Wye river, and four of the upstream tributaries of the Severn river are additionally monitored by trapezoidal flumes. For the present study, we have had access to these data collected by the Centre for Ecology and Hydrology (CEH) of Wallingford and, more precisely, to the data set used in Kirchner (2009) (courtesy of M. Robinson and J. Kirchner). Here, we focus on only one tributary of each river.

Among the four tributaries of the Severn river, we analyse the Upper Hore stream, associated with the rainfall rate measured at the Carreg Wen weather station (figure 7.2). Identifying the groundwater drainage area with the overland flow drainage area (section 4.1), Neal et al. (1997a) estimate the area drained by the Upper Hore stream to about 178 ha. With a Digital Elevation Model of resolution 25×25 m and the Whitebox Geospatial Analysis Tool[1], we estimate the total stream length to about 7945 m. Inside the catchment, the altitude ranges between 405 and 736 m, with slopes reaching 30° (Brandt et al., 2004). During the five years of the data set, the average annual rainfall is 2703 mm y^{-1}, and the average annual discharge running off the Upper Hore stream is 2051 mm y^{-1}. With the units of a velocity, the discharge is here divided by the area it drains, as it is usually made in hydrogeology to compare a stream runoff to its rainfall. In units of a volumetric discharge, the mean discharge of the Upper Hore stream is 417 m^3 h^{-1}.

Among the three tributaries of the Wye river, we choose to analyse the Iago stream, because it drains the smallest area (figure 7.2). To do so, we use the rainfall rate measured in the weather station the closest to the Iago stream catchment (station known as Cefn Brwyn, see Kirchner (2009)). With the Whitebox Geospatial Analysis Tool, we estimate the length of the Iago stream channels to about 3940 metres. Identifying the groundwater drainage area with the overland flow drainage area, we estimate the area drained by the Iago stream to about 112 ha. Inside this catchment, the altitude ranges between 380 m and 620 m, with slopes reaching 30° (Brandt et al., 2004). During the five years of the present data set, the average annual rainfall is 2433 mm y^{-1}, and the average annual discharge running off the Iago stream is 1996 mm y^{-1}. This corresponds to a volumetric discharge of 255 m^3 h^{-1}.

[1] `http://www.uoguelph.ca/~hydrogeo/Whitebox/`

7.1.2 River hydrograph

In the present study, we use the five years long (from 1992 to 1996) data set used by Kirchner (2009). The discharge was measured every 15 minutes, and then averaged every hour. Figure 7.3 shows part of this data set, with 3-months hydrographs recorded in the Upper Hore and the Iago streams. The two rainfall signals are strikingly similar and, naturally, so are the two hydrographs. Comparing them to figure 4.9, we note that they also look similar to the Quiock Creek hydrograph. During flood events, the discharge increases rapidly and strongly. After a flood event, the discharge decreases rapidly at the beginning, and slowly afterwards. During the five years of the data set, both streams permanently flow — they never dry up. In the Iago stream for example, the minimum discharge recorded is $3.3{\cdot}10^{-2}\,\mathrm{mm\,h^{-1}}$, and the maximum discharge is $6.36\,\mathrm{mm\,h^{-1}}$.

In the next section, we analyse the drought flows of the two streams.

7.1.3 Drought flow

In order to analyse the drought flow of the two streams, we plot the negative time derivative of the discharge $-\dot{Q}$ with respect to the discharge Q (Brutsaert and Nieber, 1977), as in section 6.1.1. If the streams discharge evolutions follow the Dupuit-Boussinesq predictions, we can expect two asymptotic regimes. During the early stage of the drought flow, the discharge decreases as the inverse square root of time ($Q \sim 1/\sqrt{t}$, equation (2.23)), and $\dot{Q}$ depends on Q at the power 3. The long-times asymptotic regime predicts a discharge decrease as the inverse time squared ($Q \sim 1/t^2$, equation (2.29)), and a power 3/2 between $\dot{Q}$ and Q.

For this analysis, we selected 136 drought events in the Upper Hore stream, and 163 drought events in the Iago stream. For both streams, the mean duration of these drought flows is 2.5 days. We measure $\dot{Q}$ with respect to the discharge Q with the methods exposed in section 6.1.1. Figure 7.4 shows the results where $\dot{Q}$ is calculated as the mean slope over ten hours, and Q is the mean discharge over the same ten hours. The discharge derivative, $-\dot{Q}$, increases with the discharge Q. Averaging the data over bins of Q reduces the dispersion of the data.

The fit of a power law to these bins yields exponents of 2.10 ± 0.01 for the Upper Hore, and 2.30 ± 0.03 for the Iago stream. These exponents do not change when we vary the duration over which we calculate $\dot{Q}$. With the other method (with a threshold discharge value arbitrarily chosen at $3{\cdot}10^{-4}\,\mathrm{mm\,h^{-1}}$, see section 6.1.1), we find exponents of 1.90 ± 0.01 for the Upper Hore, and 2.05 ± 0.02 for the Iago stream. These results are in a good agreement with Kirchner (2009), who finds exponents of 1.97 for the Severn river, and 2.10 for the Wye river. Larger than one, these exponents mean that, in both rivers, the discharge does not decrease exponentially, but as a power law of time. An exponent 2 corresponds to a discharge decrease in proportion to the inverse time: $Q \sim 1/t$. This is problematic, because such regime is not integrable in time: the discharge cannot decrease infinitely as $1/t$, as it would induce an infinite volume of water. Only exponents lower than 2 in the $\dot{Q}$ Q plane correspond to an integrable

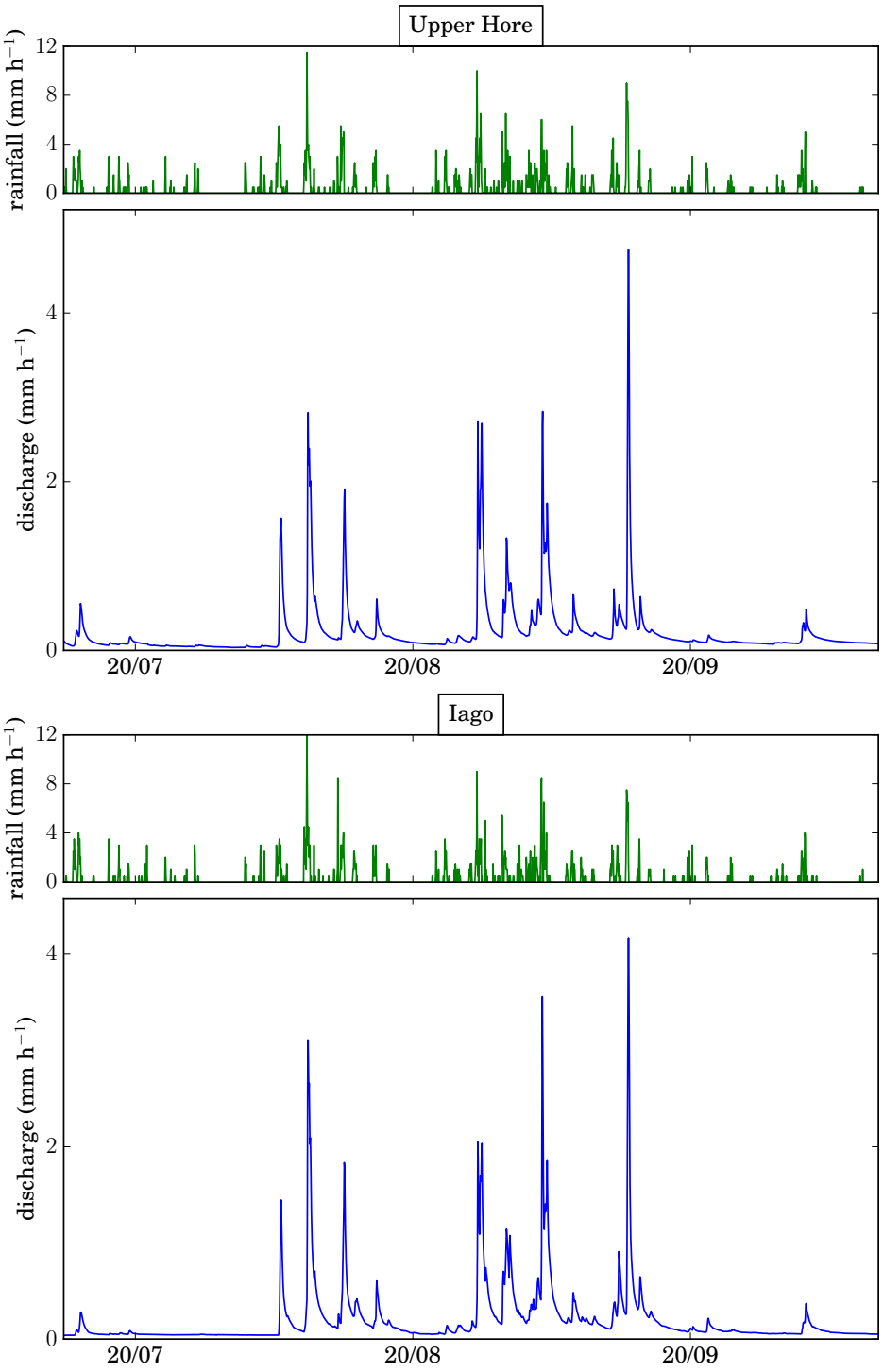

Figure 7.3: Rainfall rate (—) and discharge (—) of the Upper Hore stream, a tributary of the Severn river, and of the Iago stream, a tributary of the Wye river, during three months in the year 1992. The volumetric discharge of the stream is divided by the area it drains, such that it has the dimensions of a rainfall rate.

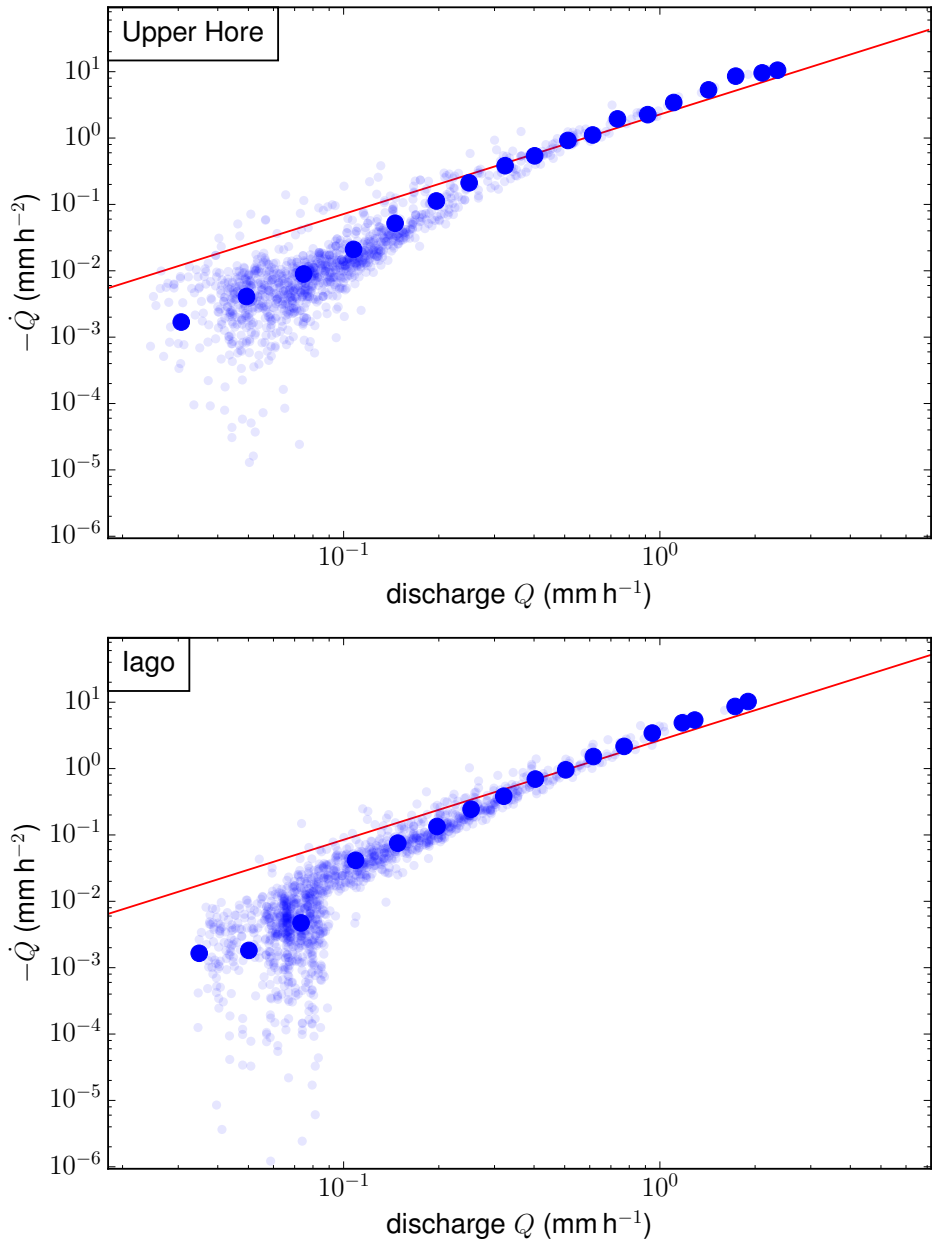

Figure 7.4: Time derivative of the discharge $-\dot{Q}$ as a function of the discharge Q for the two streams. For each data point (small blue points), $\dot{Q}$ is the mean slope over ten hours, and Q the mean discharge. (●) are averaged bins of all the data points. A 3/2 power law (—) fitted to the binned data yields a prefactor of $4.98 \cdot 10^{-2}\,\mathrm{m}^{-1/2}\,\mathrm{s}^{-1/2}$ for the Upper Hore stream, and $5.88 \cdot 10^{-2}\,\mathrm{m}^{-1/2}\,\mathrm{s}^{-1/2}$ for the Iago stream. The fit of a power law yields exponents of 2.10 ± 0.01 for the Upper Hore, and 2.30 ± 0.03 for the Iago stream.

discharge decrease.

These exponents do not seem to correspond to any Dupuit-Boussinesq asymptotic regime. Yet, the data present a large scatter, and we only have slightly more than one decade of discharges. A 3/2 power law cannot be excluded (figure 7.4). Besides its exponent, we can test this power law with its prefactor. This power law corresponds to the long-times asymptotic regime of the Dupuit-Boussinesq theory (equation (2.29)):

$$Q \sim a_d^2 \frac{s^2 W L^3}{K t^2} . \tag{7.1}$$

Here, we assume that the drought flow of both streams follows this asymptotic regime. We assume that the typical lateral length of the catchment is the ratio of the area over the total streams length divided by two: $L = A/(2W)$ (see section 6.2.5). Our discharge measurements Q_A are divided by the area of the catchment: $Q_\mathrm{A} = Q/(2WL)$. As a result, the time derivative of the measured discharge Q_A reads

$$-\dot{Q}_\mathrm{A} \sim 2\sqrt{2} \frac{\sqrt{K}}{a_d s L} Q_\mathrm{A}^{3/2} . \tag{7.2}$$

Fitting a 3/2 power law to the data yields prefactors of $4.98 \cdot 10^{-2}\,\mathrm{m}^{-1/2}\,\mathrm{s}^{-1/2}$ for the Upper Hore, and $5.88 \cdot 10^{-2}\,\mathrm{m}^{-1/2}\,\mathrm{s}^{-1/2}$ for the Iago stream. Identifying with expression (7.2), we measure the ratio of the hydraulic conductivity over the porosity squared:

$$\frac{K}{s^2} = 5.39\,\mathrm{m\,s^{-1}} \quad \text{in the Upper Hore} \tag{7.3}$$

and

$$\frac{K}{s^2} = 12.09\,\mathrm{m\,s^{-1}} \quad \text{in the Iago stream.} \tag{7.4}$$

It is uneasy to confirm these results because, to our knowledge, there is no information on the hydraulic conductivity in the Plynlimon aquifers (Haria and Shand, 2004). Yet, these values are compatible with a fractured aquifer.

This result must be confirmed by other methods. We now analyse the storm flow of the Upper Hore and Iago hydrographs.

7.1.4 Storm flow

The Iago and Upper Hore streams both respond promptly, and strongly, to rainfall events. For example, during the flood event of 5th August 1992, the Iago discharge increases from $4{\cdot}10^{-2}$ to $1.4\,\mathrm{mm\,h^{-1}}$, i.e. by a factor 35, in seven hours (figure 7.3). In the present section, we analyse the response of both streams to rainfall events, by plotting the discharge increase rate $\dot{Q}$ with respect to the rainfall rate, as in section 6.2.

As in section 6.2, we have carefully chosen numerous floods to be analysed. Here again, we apply three criteria to extract a well-defined flood event. First, the river discharge prior to the flood should be sufficiently low, such that the initial state of the aquifer prior to the flood be close to empty. Second, the rainfall event should be isolated

from other rainfall events, and regular: with only one local maximum. The last criterion is also that the discharge signal be regular enough: a distinct discharge increase, with a well-defined slope. With these three criteria, we have selected 187 flood events for the analysis of the Upper Hore, and 140 for the Iago stream.

With the same methods as in section 6.2, we have measured the discharge increase rate of each flood. By comparing the results of five different methods, we estimate a measurement error of 54% for the Upper Hore, and of 43% for the Iago stream.

In order to measure the rainfall rate of each rainfall event selected, we also used the same procedure as in section 6.2. However the present data set presents a relatively long sampling period of one hour, in contrast with the one minute sampling period in the Quiock creek. Here we only compared the rainfall rates measured with a sampling period of one hour, and with a sampling period of two hours. Calculating the average standard deviation between the two techniques, we estimate a measurement error on the rainfall rate of 8% in the Upper Hore, and of 7% in the Iago stream.

Figure 7.5 shows the results of the analysis. For both streams, the discharge increase rate $\dot{Q}$ is a growing function of the rainfall rate. This growing function is not linear, but resembles a power law, with an exponent larger than one. Fitting a power law to the data yields an exponent of 2.67 ± 0.91 in the Upper Hore, and of 2.08 ± 0.52 in the Iago stream. Both results seem to exclude the possibility of a 3/2 power law, as predicted by the Dupuit-Boussinesq asymptotic regime (equation (3.11)). However, a 3/2 power law is visually acceptable for the Iago stream.

Assuming that the storm flow of both streams conforms to the Dupuit-Boussinesq asymptotic regime (equation (3.11)), the fit of a 3/2 power law to the data yields a prefactor of $6.33 \cdot 10^{-3}\ \mathrm{m}^{-1/2}\,\mathrm{s}^{-1/2}$ for the Upper Hore, and $1.25 \cdot 10^{-2}\ \mathrm{m}^{3/2}\,\mathrm{s}^{-1/2}$ for the Iago stream. As the recorded discharge Q_A is rescaled with the area $A = 2\,W\,L$ of the catchment, equation (3.11) here leads to the following prediction:

$$\dot{Q}_A \sim \frac{a^2}{s\,L}\sqrt{\frac{K}{2}}\,R^{3/2}\,. \tag{7.5}$$

Identifying the prefactors with this expression, we find

$$\frac{K}{s^2} = 0.94\,\mathrm{m\,s^{-1}} \quad \text{in the Upper Hore} \tag{7.6}$$

and

$$\frac{K}{s^2} = 5.92\,\mathrm{m\,s^{-1}} \quad \text{in the Iago stream.} \tag{7.7}$$

These values are in reasonable agreement with the values found from the drought flow analysis. In the Iago stream, which seems the most compatible with the Dupuit-Boussinesq theory, only a factor of two differentiates the result of the drought flow analysis from the early response to rainfall.

The asymptotic regime of the early response to rainfall is valid until the front reaches the divide, that is for a flood duration

$$T = \frac{s\,L}{\sqrt{K\,R}}\,. \tag{7.8}$$

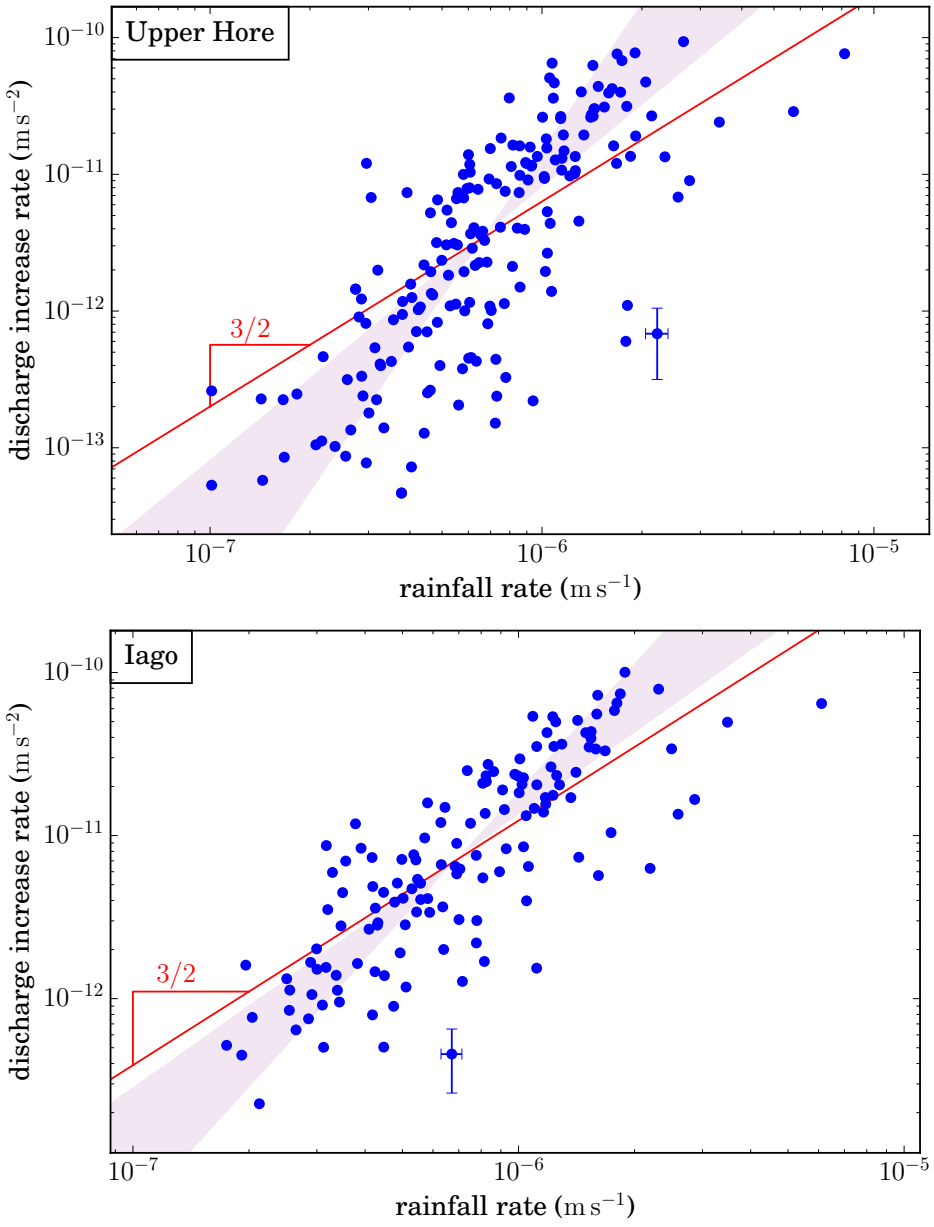

Figure 7.5: Discharge increase rate as a function of the rainfall rate in the Upper Hore and in the Iago streams (●). In both graphs, the red line represents a 3/2 power law fitted to the data (—), yielding prefactors of $6.33 \cdot 10^{-3}$ m$^{-1/2}$ s$^{-1/2}$ for the Upper Hore, and $1.25 \cdot 10^{-2}$ m$^{3/2}$ s$^{-1/2}$ for the Iago stream. The shaded area represents the minimum and maximum power-law fits.

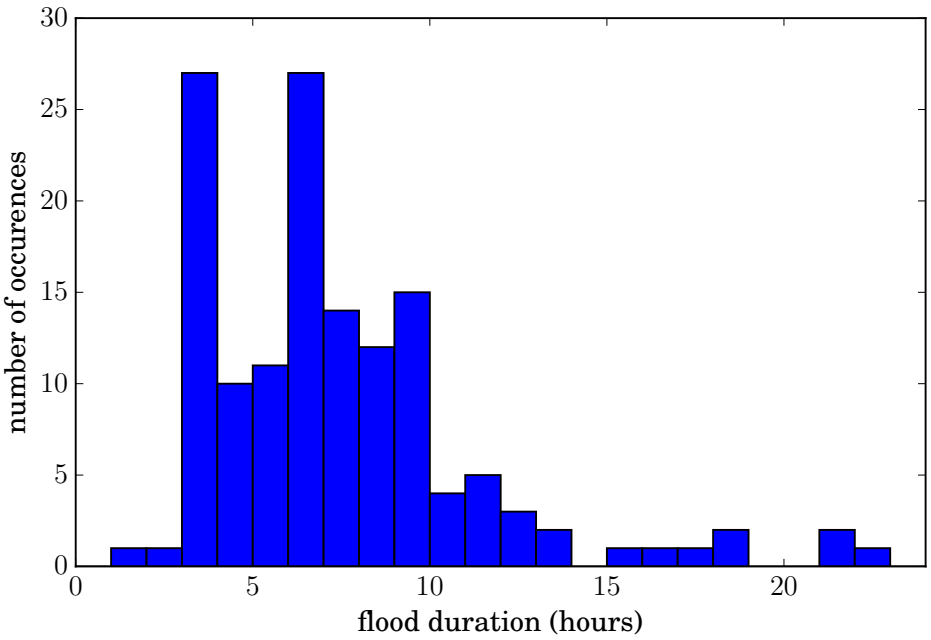

Figure 7.6: Duration of all the floods analysed for the Iago stream.

As we have measured the ratio K/s^2, we can estimate this limit of validity. Using the largest rainfall rate measured for the Iago stream $R = 6 \cdot 10^{-6}$ m s^{-1}, we estimate the duration of the asymptotic regime around 7 hours. Figure 7.6 shows the duration of all the floods analysed for the Iago stream. They are all shorter than one day, and most of them last between four and ten hours, that is of the order of the asymptotic regime duration limit. This emphasises the need of higher frequency measurements, to be able to measure shorter flood events. Yet, 77 flood events are shorter than seven hours. Fitting a power law to these 77 data points yields an exponent of 1.9 ± 0.4. This is slightly closer to the 3/2 exponent expected. However, this result is not drastically different from the result shown in figure 7.5, and the floods duration does not seem to play a major role here.

7.1.5 Discussion

Both the analyses of the drought flow and of the storm flow, in the Upper Hore and Iago streams, reveal a non-linear behaviour. During drought flow, in both streams, the discharge seems to decrease as a power law of time, and not exponentially. During storm flow, the discharge increase rate grows more than linearly with the rainfall rate.

Fitting a power law to the drought flow and storm flow data yields exponents compatible with the Dupuit-Boussinesq asymptotic regimes, if we take into account the large uncertainties of the data. Moreover, for both streams, the drought flow and storm flow analyses yield almost the same value of the ratio of the hydraulic conductivity over the porosity squared (table 7.1). This result supports the use of the Dupuit-Boussinesq approximation to analyse the dynamics of the groundwater flow in these catchments.

More generally, it is a strong indication that both Plynlimon catchments are dominated by groundwater flow, included during storm events. This confirms older studies, which noticed large and rapid responses of the water table to rainfall events (Hill and Neal, 1997; Haria and Shand, 2004).

However, we have no information of any impervious bottom of the aquifers, and we can wonder about the influence of two-dimensional groundwater flows on the rivers discharge dynamics (J. Kirchner, personal communication).

Unfortunately, in the present case, the analysis of the river discharge dynamics, on its own, is not sufficient to determine the aquifer hydraulic properties. As both the drought flow and the early response to rainfall provide an estimate of the ratio K/s^2, we are presently unable to separate hydraulic conductivity and porosity. Separate measurements of either K or s could allow to determine both and, furthermore, to confirm our conclusions. For example, high frequency measurements of the water table, even in a single borehole, would allow us to do so. If the borehole is sufficiently far from any stream, we could measure the rise of the water table during rainfall events. Assuming it is proportional to the ratio of the rainfall rate over the porosity, this would allow to estimate the porosity of the aquifer, as in section 5.1.

Finally, as for the Quiock Creek, we observe a large dispersion of the data. We suggest several reasons for this dispersion: the heterogeneity of the aquifer's properties and the spatial distribution of rainfall, the influence of the unsaturated zone, vegetation, or the inital state of the groundwater flow prior to a rainfall event.

7.2 The badlands of the Laval catchment, French Alps

7.2.1 Field site

The Draix experimental catchments are located in the southern French Alps near Digne-les-Bains. Six catchments, featuring varied lithology and various types of vegetation covers, are devoted to the study of floods and erosion. They are monitored by the Institut national de recherche en sciences et technologies pour l'environnement et l'agriculture (IRSTEA). Among these six catchments, we focus on the Laval catchment (44°08'26"N, 6°21'39"E).

The Laval catchment lies on Jurassic marine black marls belonging to Bajocian, Bathonian and Callovo-Oxfordian units. This marly formation, characterised by dense layering, is very sensitive to weathering and erosion. This results in characteristic badlands morphologies, with numerous V-shaped gullies and rills (Saez et al., 2011) (see figure 7.7). During floods, considerable bedload transport runs off the catchment (Badoux et al., 2012). A characteristic soil profile features a superficial loose detrital cover approximately 10 cm thick, a regolith of marl between 10 and 50 cm, and a very compact, structured and cohesive marl bedrock below 50 cm (Maquaire et al., 2002).

The climate is Mediterranean with mountaineous influences. The mean annual tem-

Figure 7.7: Picture of the Laval creek catchment, in the southern French Alps (*picture*: D. Richard, from `http://oredraixbleone.irstea.fr/`).

perature is 9.8°C with warm summers (28°C in July) and mild winters. The mean annual rainfall (1984-2004) is 900 mm, with an average of 200 days without rain and five days with rainfall depths larger than 30 mm (Saez et al., 2011). Important seasonal variations generally feature heavy rainfall in spring and autumn. Snow is not unusual but does not form a semi-permanent cover (Saez et al., 2011).

The Draix Creek drains about 86 ha (figure 7.8). The altitude of the catchment ranges between 850 and 1250 m, with a mean slope of 58%. With a 1×1 m Digital Elevation Model and the Whitebox Geoanalysis Tool, we estimate the total drainage length to about 33.9 km.

The data set used in the present section contains eight years (2000-2007) of continuous discharge and rainfall-rate measurements of the Laval creek, collected by the Base de Données pour les Observatoires en Hydrologie (*BDOH, Irstea*). The stage of the Laval creek is measured with a hydrostatic pressure probe, and converted into discharge with a calibration relationship (Duvert et al., 2012). Over the eight years of the present data set, the mean discharge is $1.64{\cdot}10^{-2}$ $m^3\,s^{-1}$, with a maximum of 10.7 $m^3\,s^{-1}$, and a minimum of 0 $m^3\,s^{-1}$. The discharge measurement time interval is highly variable, because it adapts to the discharge variations. During flood events, the time interval is generally one minute, whereas during low flow, it is around two hours. Comparing the average stream discharge with the average annual rainfall of 830 mm recorded at the Laval station, we estimate an evapotranspiration of 230 mm, which is $\approx 28\%$ of the total rainfall.

The rain gauge is a tipping bucket, which volume corresponds to 0.2 mm of cumulated rainfall. It records the minute at which the bucket tips over. We then obtain the rainfall rate signal as the cumulated volume over fifteen minutes, divided by the sampling period

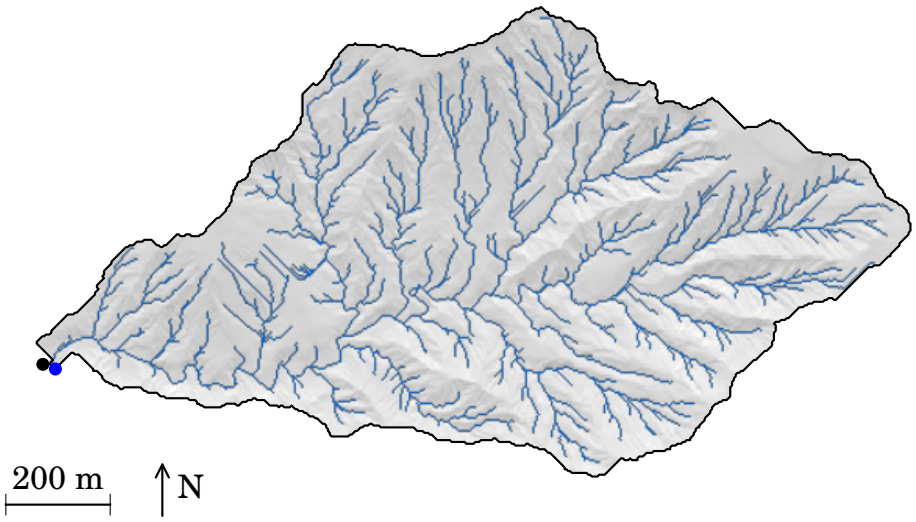

Figure 7.8: Laval creek catchment, from a 1×1 m Digital Elevation Model (courtesy of C. Le Bouteiller). The blue dot (●) represents the gauging station, and the black dot (●) the weather station.

of fifteen minutes.

7.2.2 River hydrograph

Figure 7.9 shows twenty-five days of the Laval creek hydrograph. The rainfall events are scarce but intense. As a result, the creek discharge increases strongly and quickly. For instance, during the flood of 23rd May 2002, the discharge increases from 0.02 to 0.78 $m^3 s^{-1}$, i.e. by a factor 40, in twenty minutes. This is typical of floods in the Laval creek. These flood events are typically followed by a rapid decrease of the discharge. In contrast with the Plynlimon rivers or the Quiock Creek, periods of low flow are short, and the creek rapidly dries up. As an example, three days after the flood event of 23rd May, the discharge was only $5 \cdot 10^{-4}$ $m^3 s^{-1}$.

In the next section, we analyse the drought flows of the Laval creek, with the same method as in sections 6.1.1 and 7.1.3.

7.2.3 Drought flow

We selected 80 drought flows during the eight years of the data set. As the time interval between each measurement varies with discharge variations, we measure the time derivative $\dot{Q}$ as the mean slope over a fixed number of points. We arbitrarily chose this number to be 6. During the periods where the time interval is approximately two

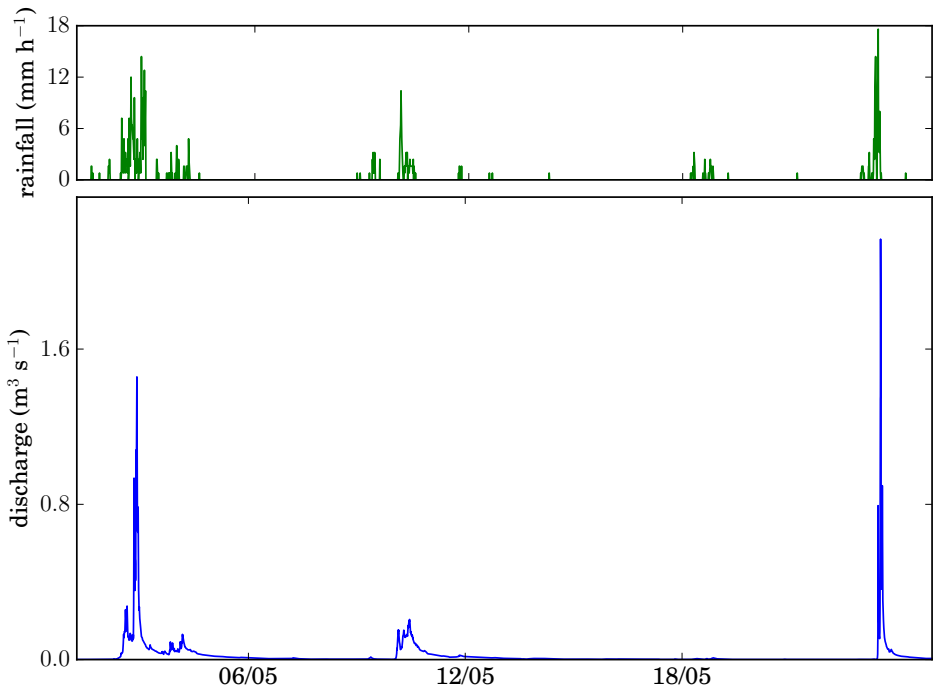

Figure 7.9: Rainfall rate (—) and discharge (—) of the Laval creek, French Alps, during 25 days in May 2002.

hours, we therefore measure the mean derivative of the discharge over half a day. Yet, during periods of large discharge decrease (early stage of drought flow), $\dot{Q}$ is measured over about 5 minutes. We have tested different values, and concluded that it does not significantly change the results.

Figure 7.10 shows the time derivative of the discharge $-\dot{Q}$ with respect to the discharge Q. Naturally, as the discharge increases, its derivative $-\dot{Q}$ increase. Averaging the data over bins of Q, the resulting averaged points seem to align on a power-law relationship. Fitting a power law to these binned points yields an exponent of 1.60 ± 0.02. As it is lower than 2, this exponent induces that the corresponding discharge decrease regime is integrable. On the other hand, as it is larger than one, this exponent reveals that the discharge of the Laval creek does not decrease exponentially.

This exponent is close to the 3/2 exponent expected with the long-times asymptotic regime of the Dupuit-Boussinesq regime (equation (2.29)):

$$Q \sim a_d^2 \, \frac{s^2 \, W \, L^3}{K \, t^2} \, . \tag{7.9}$$

If the discharge decreases as predicted by this equation, its variations $\dot{Q}$ depend on the discharge at the power 3/2:

$$-\dot{Q} = \frac{2\sqrt{K}}{a_d \, s \sqrt{W \, L^3}} \, Q^{3/2} \, . \tag{7.10}$$

Identifying with the prefactor obtained in figure 7.10, we measure the ratio of the hy-

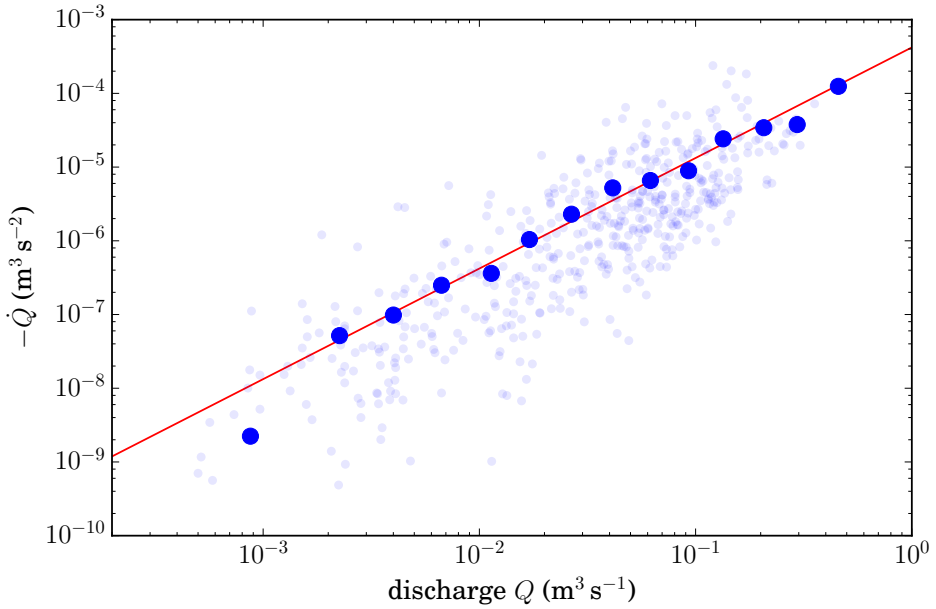

Figure 7.10: Time derivative of the discharge $-\dot{Q}$ as a function of the discharge Q for the Laval creek during drought flow. For each data point (small and transparent blue points), $\dot{Q}$ is the mean slope over six measurements, and Q the mean discharge. the blue points (●) are averaged bins of all the data points. A 3/2 power law (—) fitted to the binned data yields a prefactor of $4.20 \cdot 10^{-4}\,\mathrm{m}^{-3/2}\,\mathrm{s}^{-1/2}$. The fit of a power law yields exponents of 1.60 ± 0.02.

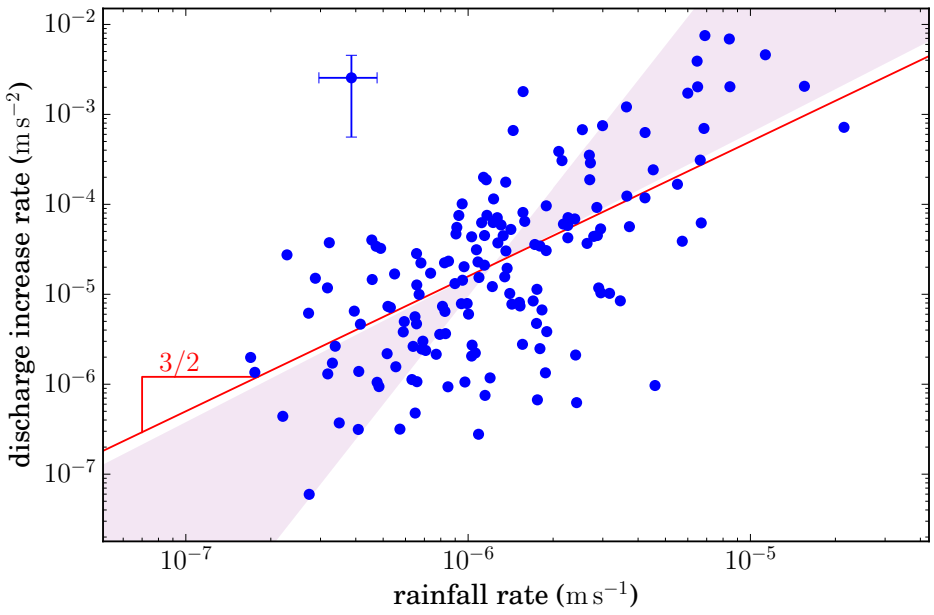

Figure 7.11: Discharge increase rate with respect to the rainfall rate (●). (—) represents a 3/2 power law fitted to the data, yielding a prefactor of $1.58{\cdot}10^4$ m$^{3/2}$ s$^{-1/2}$. The shaded area represents the minimum and maximum power-law fits.

draulic conductivity over the porosity:

$$\frac{K}{s^2} \approx 8.45\,\mathrm{m\,s^{-1}}\,. \tag{7.11}$$

This value is similar to the values found in the Plynlimon catchments in the previous section but, here again, we do not have any information on the porosity or on the hydraulic conductivity of the aquifer.

In the next section, we estimate the validity of this result by analysing the storm flow of the Laval creek.

7.2.4 Storm flow

With the same criteria as in sections 6.2 and 7.1.4, we selected 159 flood events in order to plot their discharge increase rate $\dot{Q}$ with respect to the rainfall rate R of the rainfall event. To reduce noise, we measured $\dot{Q}$ on a 5-minutes averaged signal. The method was the same as in sections 6.2 and 7.1.4, including for the measurement errors (estimated to about 78%). Also with the same method, the rainfall rate measurements are based on a 15-minutes signal. The measurement errors are estimated to about 23% (comparison with the measurements based on a 5-minutes signal and on a 30-minutes signal).

Figure 7.11 shows the results of this analysis. The discharge increase rate grows non-linearly with the rainfall rate. Fitting a power law to the data yields an exponent of 2.71 ± 1.2.

	Upper Hore	Iago	Laval
Catchment area A (m^2)	$1.78 \cdot 10^6$	$1.12 \cdot 10^6$	$8.6 \cdot 10^5$
Total streams length W (m)	7945	3940	33900
Lateral length of the aquifer L (m)	112	142	13
$\frac{K}{s^2}$ from the drought analysis ($m\,s^{-1}$)	5.39	12.09	8.45
$\frac{K}{s^2}$ from the flood analysis ($m\,s^{-1}$)	0.94	5.92	0.11

Table 7.1: Dimensions of the aquifers analysed in the present chapter, and results of the discharge dynamics analyses, which yield estimates of the ratio K/s^2.

This exponent seems to exclude the 3/2 power law expected with the Dupuit-Boussinesq asymptotic regime, although the large uncertainty keeps this theoretical exponent possible. Fitting a 3/2 power law to the data, we find a prefactor of $1.58 \cdot 10^4\ m^{3/2}\,s^{-1/2}$. Identifying the prefactor with expression (3.11), we measure the following ratio of the hydraulic conductivity over the porosity:

$$\frac{K}{s^2} \approx 0.11\,m\,s^{-1}\,. \tag{7.12}$$

This is two orders of magnitude lower than the result obtained with the drought flow analysis (equation (7.11)). This mismatch suggests that the floods of the Laval creek cannot be explained by the Dupuit-Boussinesq asymptotic regime, confirming the fact that a 3/2 power law hardly fits the plot of figure 7.11.

7.2.5 Discussion

The analysis of the Laval creek drought flow compares well with the long-times asymptotic regime of the Dupuit-Boussinesq equation, and the exponent of a power-law fit only slightly differs from the prediction. Moreover, this analysis yields a reasonable value of the ratio of the conductivity over the porosity squared, which supports the use of the late stage regime of the Dupuit-Boussinesq equation to describe the drought flows of the Laval creek. Yet, the drought flows observed on the hydrograph decrease very rapidly and, comparing with the Quiock Creek (section 6.1.1), we could have expected the early stage regime to manifest in the hydrograph.

In contrast, the storm flow analysis does not compare with the early-times asymptotic regime of the Dupuit-Boussinesq equation. As the Laval creek is known for regular overland flow, this is not surprising. On the contrary, our analysis suggests that the relationship between the discharge increase rate and the rainfall rate could be a power law with an exponent 2.5 or 3. If confirmed, this large exponent could be the signature of overland flow-dominated floods. Of course, this speculation requires further investigation, specially about the dynamics of floods generated by overland flow. Yet, we suggest

that plotting $\dot{Q}$ versus R during floods is an interesting tool to analyse the response of a catchment to rainfall.

7.3 Conclusion

In this chapter, we have analysed the discharge dynamics of three rivers. The Wye and the Severn rivers drain fractured aquifers in Wales, and the Laval creek drains marly badlands in the French Alps. The methods developed with the Dupuit-Boussinesq theory allowed us to analyse the drought flows by plotting $-\dot{Q}$ with respect to Q, and the response of the rivers to rainfall events by plotting $\dot{Q}$ with respect to R. During drought flows as well as storm flows, the three rivers behave non-linearly. During drought, the discharge does not decrease exponentially. During floods, $\dot{Q}$ increases with R faster than linearly. These observations are similar to the Quiock Creek observations.

The drought flows of the three rivers seem compatible with the late-times asymptotic regime of the Dupuit-Boussinesq equation, despite large uncertainties. Conversely, the storm flow analysis yields contrasted results. On the one hand, the groundwater-dominated Plynlimon catchments are compatible with the asymptotic regime of the Dupuit-Boussinesq theory, which confirms previous observations of extensive contribution of groundwater to streamflow during storm events (Hill and Neal, 1997; Haria and Shand, 2004). On the other hand, the relationship between $\dot{Q}$ and R in the Laval creek is more likely a power law with an exponent of 2.5 or 3, discarding the use of the Dupuit-Boussinesq approximation for this hydrograph, at least during storm events.

The $\dot{Q}$ R plot method, used to analyse the Quiock Creek, the two Plynlimon streams and the Laval creek hydrographs, proved its utility to identify the flow processes within a catchment. In the Quiock Creek catchment, it validates the use of the Dupuit-Boussinesq theory to describe the entire hydrograph. In complement to the drought flow analysis of Brutsaert and Nieber (1977), it also allows to provide estimates of the porosity and hydraulic conductivity at the catchment scale. In the Plynlimon catchments, it supports the use of the Dupuit-Boussinesq theory; yet, the drought flow and the storm flow analyses both provide the ratio K/s^2, and the $\dot{Q}$ R plot method is not sufficient to determine the hydraulic parameters of these aquifers. In the Plynlimon catchments, separate measurements would be necessary. In the Laval creek catchment, this method reveals a different behaviour, identifying a power-law relationship with an exponent of 2.5 or 3. This large exponent could be the mark of overland-flow dominated catchments.

Finally, the $\dot{Q}$ R plot could be a method to discriminate between groundwater-dominated and overland flow-dominated catchments. However, this suggestion requires further investigations. Indeed, a power 3/2 is characteristic of a Dupuit-Boussinesq groundwater flow. It implies a fully-penetrating stream, where the flow can be approximated as one-dimensional. Conversely, the dynamical behaviour of two-dimensional groundwater flows is still unknown. Our electric tomography of the Quiock Creek aquifer did not reveal any impermeable bottom layer. In the Plynlimon aquifers, deep groundwater circulations were observed. In section 8.3.2.2, we will additionally see that

groundwater head measurements from Haria and Shand (2004) strongly suggest that the flow becomes two-dimensional near the Severn river.

In the next chapter, we address the question of dynamical two-dimensional flows with a laboratory experiment. We then present our attempts to describe theoretically this problem.

Part IV

Beyond the Dupuit-Boussinesq theory: two-dimensional flows

Chapter 8

Deep aquifers: Two-dimensional flows

Contents

8.1 Introduction

In the previous chapters, we have shown that a groundwater flow can reproduce the main characteristics of a river hydrograph. Among these characteristics, the Dupuit-Boussinesq theory revealed that a groundwater flow features non-linear behaviours, during drought flow as well as during rainfall. In particular, we suggested that a 3/2 power-law relationship between the discharge increase rate $\dot{Q}$ and the rainfall rate R could be the signature of a groundwater-controlled hydrograph.

The Dupuit-Boussinesq theory implies a fully-penetrating stream: the aquifer has a finite depth, and the river flows on the impermeable bottom of the aquifer. Yet, it is difficult to evaluate the validity of this hypothesis in the field. The ground tomography of the Quiock Creek aquifer suggests that the bottom of the aquifer lies deep under the river (chapter 4). Several field studies, addressing the question of the aquifers depth with hydrochemical tracers, revealed significant contributions of deep groundwater to the streamflow (Neal et al., 1997a; Shand et al., 2005; Banks et al., 2009). Studying the groundwater flow of the Severn river headwaters, Plynlimon, Wales, Haria and Shand (2004) come to the same conclusions, and further emphasize that the deep groundwater flow reacts rapidly to rainfall events.

If the aquifer bottom is deeper than the river, the Dupuit-Boussinesq approximation does not hold any more, at least near the river (Bresciani et al., 2014). Indeed, below the river, groundwater must flow upwards to exit the aquifer. If the aquifer is a homogeneous porous medium, Darcy's law combined with the incompressiblity of water leads to the Laplace equation:

$$\Delta\phi = 0\,, \tag{8.1}$$

where $\phi = y + p/(\rho\, g)$ is the velocity potential (see section 1.2). This equation must be supplemented with boundary conditions, among which the water table plays an important role. Its free-surface condition is non-linear and time-dependant, which introduces analytical and numerical difficulties.

If this boundary condition is linearised, analytical studies of the problem show that groundwater flow in a deep aquifer is fully two-dimensional (Toth, 1963; Haitjema and Mitchell-Bruker, 2005; Jiang et al., 2011). Near a drainage divide, groundwater flows downwards; below a river, groundwater flows upwards (figure 8.1). If the aquifer depth is larger than the typical lateral length of the river catchment, these studies further show that, deep under the river, groundwater can bypass the river, and directly flow towards a lower river. In that case, the groundwater flow and the chemical elements it transports distribute over several scales, from first-order streams to the regional scale (Zijl, 1999; Cardenas, 2007). If Polubarinova-Kochina (1962) analytically solved the fully non-linear problem in several two-dimensional configurations, numerical models allow to resolve it in more realistic conditions, sometimes even in three dimensions (Bresciani et al., 2012; Goderniaux et al., 2013). Yet, these studies address static problems only.

Even though the numerical model MODFLOW allows to simulate time-varying three-dimensional flows, we are not aware of any systematic study of the dynamics of such flows. In the present chapter, we investigate the dynamics of a vertical two-dimensional

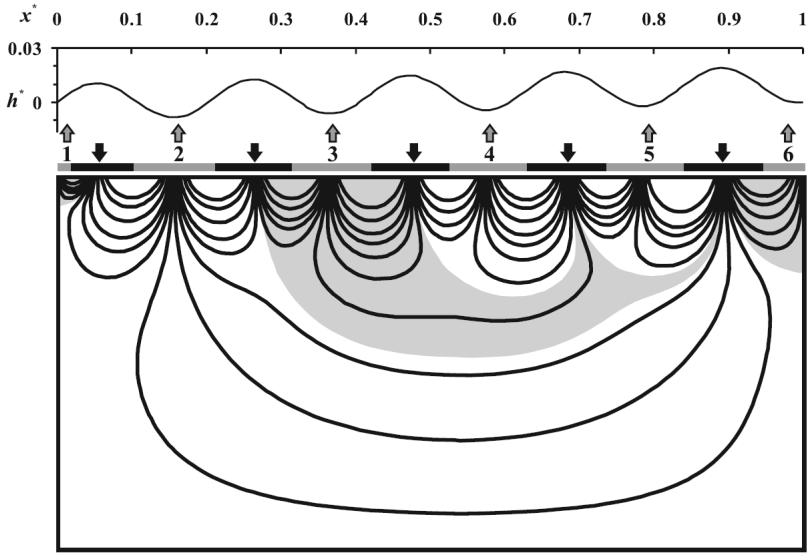

Figure 8.1: Streamlines from Laplace equation, with a linearised free-surface condition. At the top of the domain, the six outlets represent rivers. The grey shaded area represents the area of the flow domain which flows towards the river number 3. This figure, realised in Cardenas (2007), reproduces Toth (1963) solution, where a small perturbation of the potential ϕ is prescribed on the water table. This small perturbation, represented on the top graph, is sinusoidal with a large-scale slope s: $\phi = s\,x + a\,\sin(k\,x)$.

groundwater flow. With a laboratory aquifer, we analyse the drought flow and the early response to rainfall of a two-dimensional flow, with the particular purpose to compare these regimes with the field measurements of the previous chapter. We then propose various theoretical perspectives to address this problem. Although our theoretical analysis remains incomplete, it may provide some insight into the behaviour of two-dimensional flows.

The experimental and theoretical results presented in this chapter are part of a work in progress.

8.2 Two-dimensional flow in a laboratory aquifer

In the literature, only few studies of groundwater flow were devoted to laboratory experiments, and even fewer to deep aquifers. Abdul and Gillham (1984) study the effects of the capillary fringe on streamflow generation, whereas Hewlett and Hibbert (1963) and Nieber and Walter (1981) study the influence of the unsaturated zone in sloping aquifers. In this section, we describe the experimental setup which allows us to mimic two-dimensional groundwater flows in a deep aquifer.

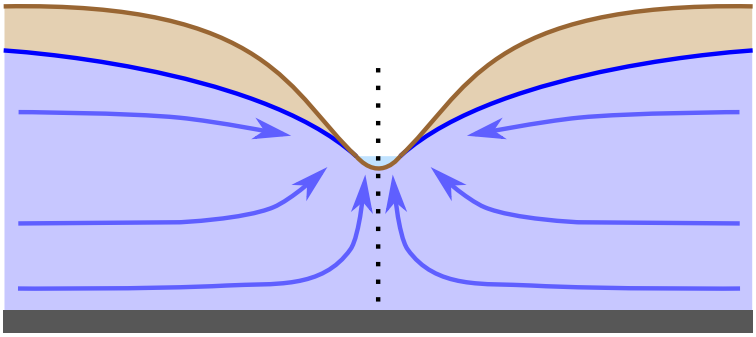

Figure 8.2: Two-dimensional groundwater flow in a deep aquifer. A vertical line halves the aquifer into two symmetric parts around the river.

8.2.1 Design of a deep laboratory aquifer

8.2.1.1 Experimental setup

In chapter 3, the geometry of the experiment was intended to reproduce the configuration of a fully-penetrating stream. Here, an additional boundary comes into play, underneath the river. Indeed, as the river flows on the porous material, groundwater can flow underneath the river (figure 8.2). Confining the groundwater flow to a vertical plane perpendicular to the river, we assume that the aquifer is symmetric with respect to the river. In this idealistic configuration, groundwater cannot cross the vertical line halving the aquifer around the river (contrary to Toth flow in figure 8.1). Under the river, this vertical line therefore represents a boundary for the groundwater flow. This boundary acts exactly as an impervious boundary: the flow can be parallel to it, but it cannot cross it. This boundary also exists in a non-symmetric aquifer, but its shape is more complicated than a simple vertical line. This boundary is the main difference with the configuration used in chapter 3.

To account for this boundary, we modified the geometry of the laboratory aquifer used in chapter 3. Two vertical glass plates ($90.5 \times 92\,\mathrm{cm}$) separated by a 5 cm gap hold a porous material in a quasi two-dimensional tank (figure 8.3). As in chapter 3, the right-hand side of the tank is an impervious wall, and the horizontal bottom is impervious. However, the left-hand side is composed of a vertical permeable grid placed on top of an impervious vertical wall (63 cm). This impervious wall represents the vertical line which halves an aquifer into two symmetric parts around the river. Above this impervious boundary, the outlet represents a river. The right-hand side represents the drainage divide of a natural aquifer. Finally, the horizontal bottom of the tank represents the impervious bottom of the aquifer, at a finite depth below the river. In this configuration, the depth of the aquifer is similar to its lateral extent.

We reproduce a porous aquifer with glass beads of diameter 3 mm. We have not measured the hydraulic conductivity of the porous material composed of these beads. In chapter 3 though, we measured a conductivity K of $0.97 \pm 0.06\,\mathrm{cm\,s^{-1}}$ with 1 mm beads, and $K = 5.7 \pm 1\,\mathrm{cm\,s^{-1}}$ with 4 mm beads. We expect the conductivity of 3 mm beads to lie between these two values. In this porous material, the capillary height

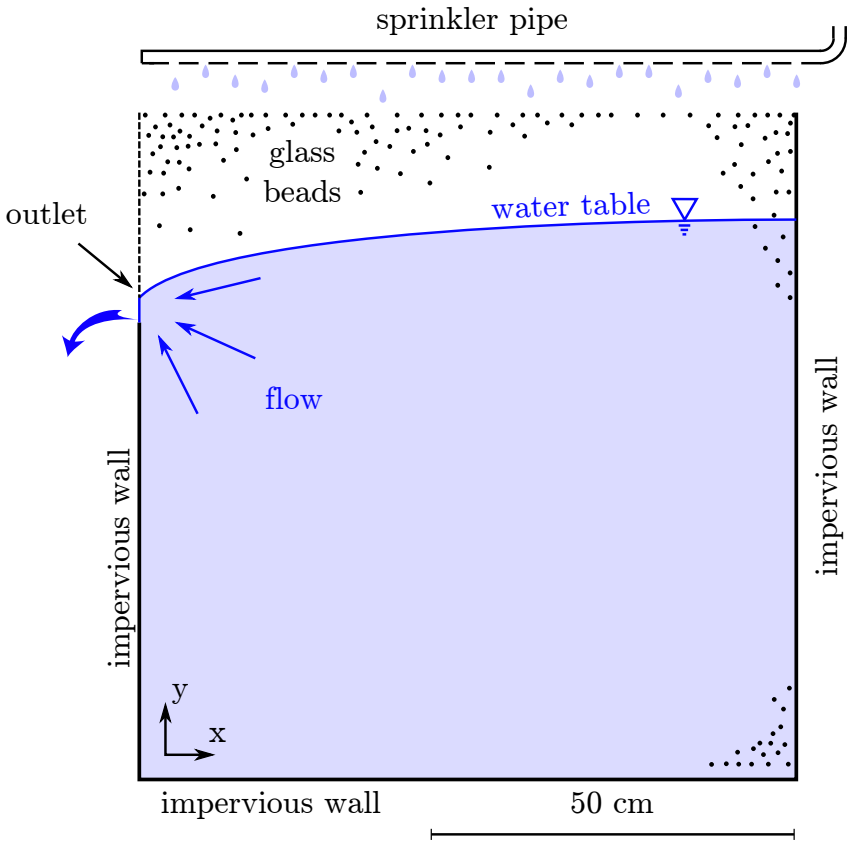

Figure 8.3: Experimental aquifer. The water table separates the unsaturated zone from the saturated zone (blue zone, bottom). At the outlet, we collect water flowing through the permeable grid in a bucket weighed every 0.1 second. Below the permeable grid, a vertical impervious wall represents the boundary halving an aquifer into two symmetric parts around the river.

is around 1 cm. In what follows, we neglect the capillary fringe, and approximate the water table as the top surface of the saturated zone.

Above this porous medium, we reproduce rainfall with a sprinkler pipe of section 2 cm. A series of 20 holes (1 mm in diameter) spreads regularly along the sprinkler pipe, fed with a water tower. An electromagnetic flowmeter (Kobold) measures the rainfall rate with discharges ranging from 0.83 to 16.67 $\mathrm{ml\,s^{-1}}$. In order to reproduce a larger range of rainfall rates, we installed a derivation in the water supply device, with a flowmeter ranging from 8.3 to 166.7 $\mathrm{ml\,s^{-1}}$. With this device, the rainfall rate of our experiments range from 1 to 53.3 $\mathrm{ml\,s^{-1}}$.

The last change of this experiment with respect to chapter 3 is the scale used to measure the cumulated weight of water flowing out of the aquifer. As we will see in section 8.2.2, the transient regimes of the experimental hydrographs obtained with the present setup are shorter than observed in the configuration of a fully-penetrating stream (chapter 3). In particular, the regime of early response to rainfall lasts only a few seconds (see figure 8.11). In order to measure precisely this regime, we used a more precise scale (Kern, PLJ-1200-3A) which measures the weight every 0.1 seconds, with a precision of 1 mg.

8.2.1.2 Outlet

Our deep laboratory aquifer produces fast transient regimes, which require more precision. Unfortunately, this precision revealed an instability triggered by the outlet device which induced significant noise (figure 8.4). This instability already existed in the experiments of chapter 3, but its influence was negligible compared to the measurement precision. It is induced by the rectangular spout about 10 cm long used to drive water from the aquifer outlet to the weighed bucket (figure 8.4a). On this spout, water flows in rivulets which spontaneously meander (Daerr et al., 2011). As the meanders are unstable, the discharge delivered to the bucket fluctuates around its average value. These fluctuations induced a significant measurement noise, so that we had to change the outlet device.

We started by creating a water reservoir which collects the groundwater almost immediately after it flows out of the aquifer (figure 8.4b). The purpose was to minimise the distance over which water flows until we can measure its weight. This intermediate reservoir is connected to the weighed bucket with a tube filled with water, such that the levels of the bucket and of the outlet reservoir are supposed to be equal. When the reservoir collects water, its level rises, and water consequently flows towards the bucket to equate their levels. Part of the outflowing water is therefore lost in the reservoir, and not weighed in the bucket. We reduce at maximum the proportion of water lost in the intermediate reservoir, by increasing the surface of the bucket. The latter is approximately 200 $\mathrm{cm^2}$, whereas the surface of the reservoir is approximately 5 $\mathrm{cm^2}$, which is approximately 2.5% of the bucket surface. We therefore hope to lose only approximately 2.5% of the outflowing water into the reservoir. Unfortunately, this device induced gravity oscillations between the water levels in the reservoir and in the bucket. The amplitude of these waves was too large to be neglected, and we had to

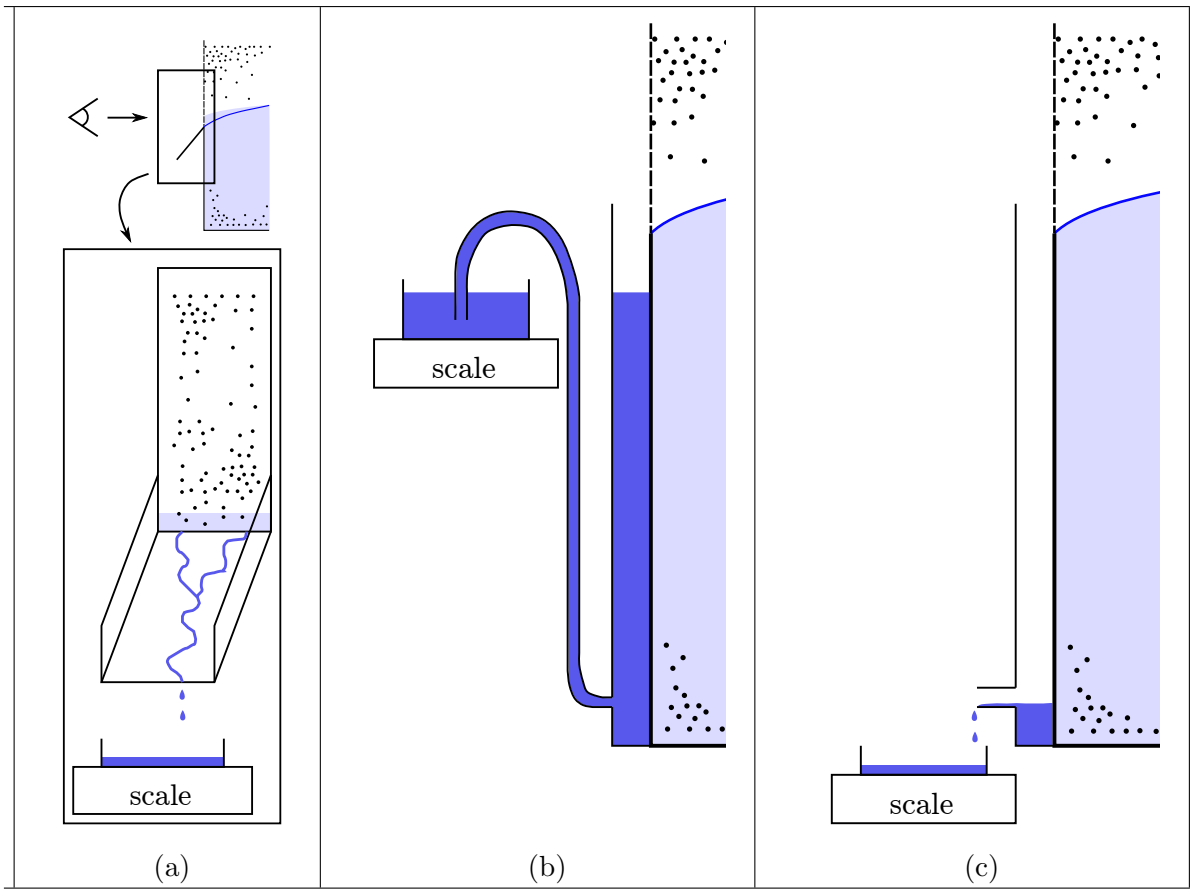

Figure 8.4: Three different outlet devices used to measure the most precisely possible the discharge of water flowing out of the experimental aquifer. *a)* Outlet used in the experiment of chapter 3. On this device, rivulets of water spontaneously meander while flowing down, inducing noise in the measurement. *b)* Second attempt of outlet device. At the outlet, an intermediate reservoir collects water immediately after it flows out of the aquifer. This intermediate reservoir is connected to the weighed bucket. *c)* Present configuration of the outlet. At the bottom of the intermediate reservoir, a small pipe drives water towards the weighed bucket.

develop a second device.

The present outlet device is illustrated in figure 8.4c. We use the same intermediate reservoir as in figure 8.4b but, now, the reservoir is almost empty. At the bottom, a small pipe drives the outflowing water towards the bucket. The advantage of this device compared to figure 8.4a is that the water flows in a pipe, which hinders the meandering of rivulets. Its drawback is that, before flowing into the small pipe, the outflowing water must flow down the vertical reservoir wall over approximately 50 cm. This drawback could again be improved in the future.

8.2.2 Observations

8.2.2.1 Two-dimensional streamlines

The experimental procedure is similar to the one described in chapter 3. We switch on rainfall and wait until equilibrium. Rainwater infiltrates down the porous material, until it reaches the groundwater reservoir. The water table then rises to accommodate more rainwater, and curves towards the outlet. The water table shape is qualitatively similar as in the fully-penetrating configuration of chapter 3. However, it rises much less than in a fully-penetrating configuration. For example, with a rainfall discharge of $28\,\mathrm{ml\,s^{-1}}$, the water level rises by about 3 cm at its maximum (right boundary). In comparison, with the 4 mm beads (with a larger conductivity, the water table is supposed to rise less), the water table rises by about 10 cm in the fully-penetrating configuration.

After a few minutes, the system reaches steady state. To visualize the streamlines, we introduce 3 ml of blue dye at four locations (19.1, 37.7, 56.9 and 75.6 cm away from the outlet) (figure 8.5). We then take pictures of the experiment every 20 seconds during twenty-two minutes. Figure 8.5 shows the pictures taken 30 seconds, three minutes and five minutes after injecting dye. After processing the 65 pictures, we select for each pixel the picture in which the pixel displays the minimum of light intensity. As a result, the bottom picture of figure 8.5 displays the minimum of intensity recorded in each pixel. This allows us to visualize the stationary flowlines.

As we introduce them, the four blue stains exhibit a lateral extent of about 3 cm. Then, they flow towards the outlet, following the streamlines. As they do so, they extend longitudinally (in the direction of the flow), but their lateral extent hardly changes (Van Genuchten and Wierenga, 1976, 1977).

According to their position relative to the outlet, the four stains flow downwards and towards the outlet. The furthest stain flows almost vertically downwards at the beginning, progressively changing its course as it gets closer to the outlet. As a result, the furthest stain also corresponds to the deepest streamline. Conversely, the closest stain flows almost horizontally.

Finally, the streamlines get closer to each other as they flow towards the outlet. In fact, the flow almost concentrates in a single line along the outlet — the area of outflowing water, on the outlet grid, is about 1 or 2 mm in height. As a result, flow accelerates as it gets closer to the outlet. To illustrate this observation, the closest stain has almost totally disappeared after approximately 1 minute, and the second flows out

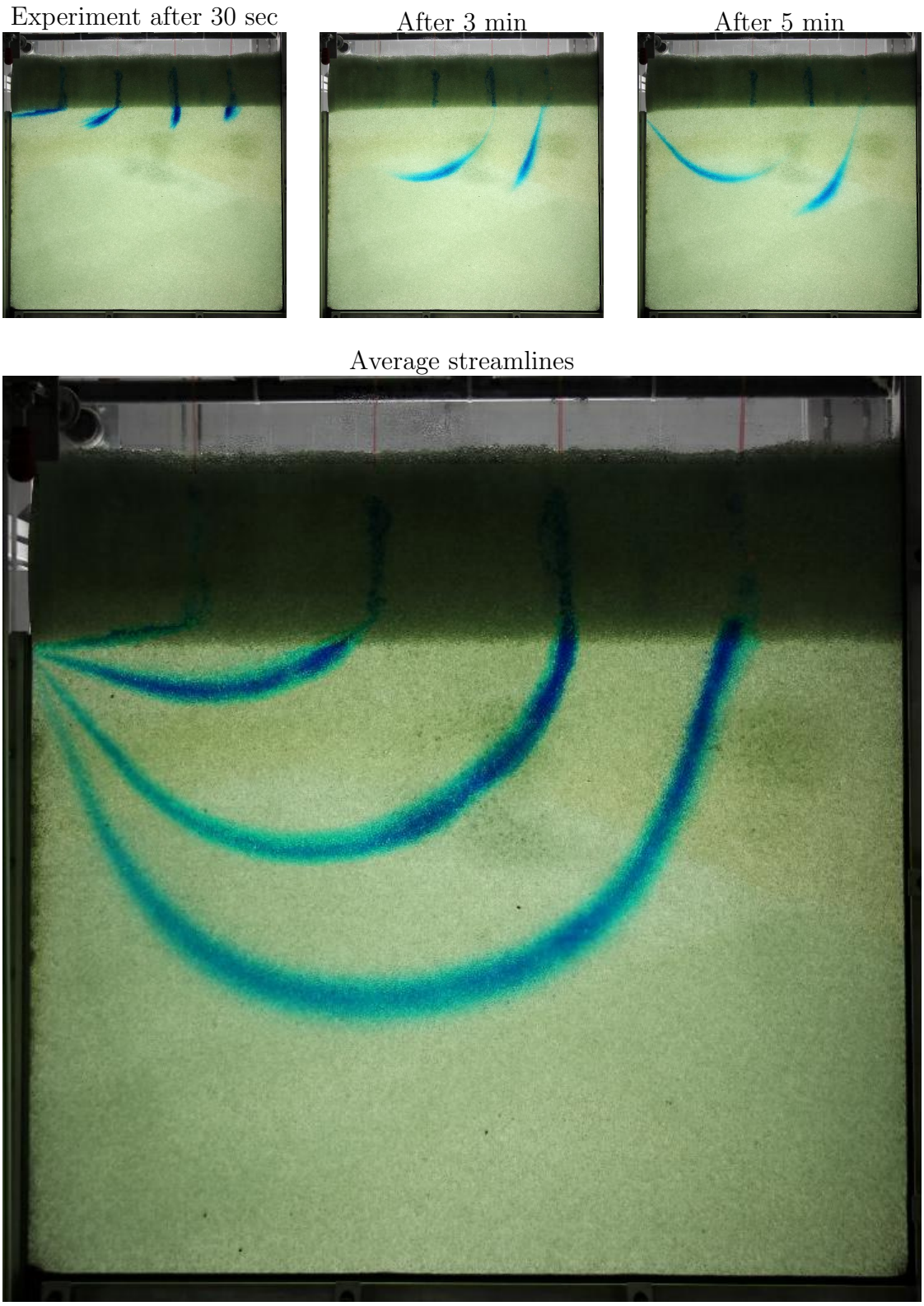

Figure 8.5: *Top:* Three pictures of the experiment thirty seconds (left), three minutes (middle), and five minutes after the injection of dye (right). After three minutes, the two closest stains have already exited the aquifer. *Bottom:* Streamlines revealed by displaying, for each pixel, its lowest intensity value.

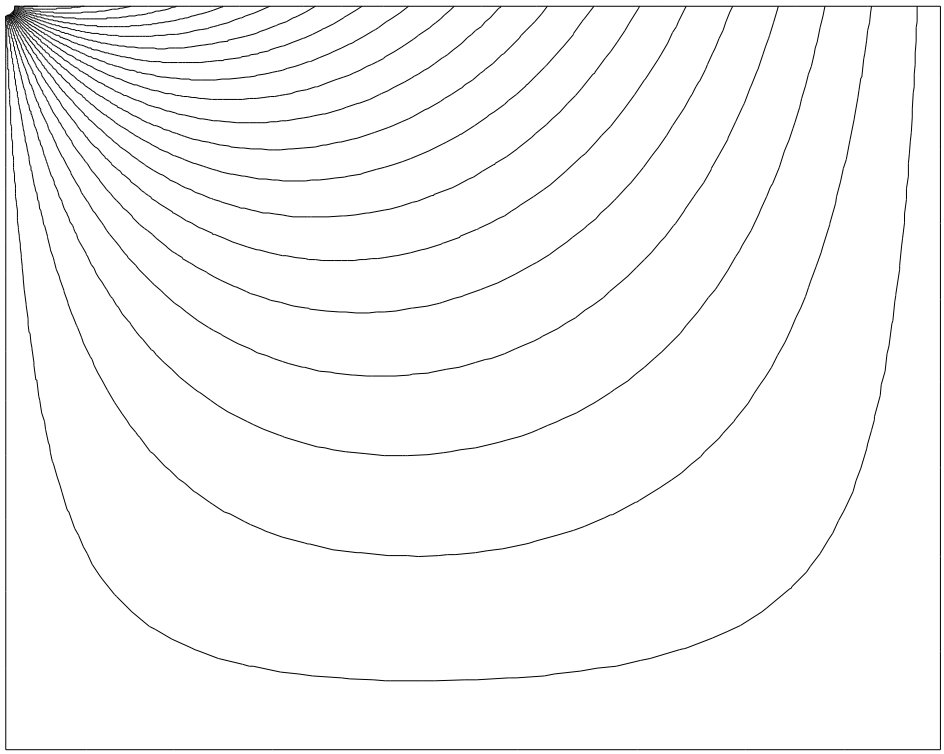

Figure 8.6: Resolution of the Laplace equation, with the free surface condition linearised.

of the aquifer in about 2 minutes and a half. Conversely, the furthest stain flows out of the aquifer in more than twenty minutes. These features, similar as in figure 8.1, emphasize the two-dimensionality of the flow in the present laboratory configuration.

8.2.2.2 Two-dimensional flow: linearisation of the free-surface condition

These experiments, realised in steady state, point to a remarkable feature of the groundwater flow in this deep configuration: the water table is almost horizontal, and its elevation h is close to the river elevation. This feature is an incentive to linearise the problem around this horizontal position. Here, we solve numerically the linearised problem of a groundwater flow in a rectangle (experimental configuration), receiving a constant rainfall rate R, and in steady state.

With a finite element method (with the solver FreFem++ (Hecht, 2012)), we solve the Laplace equation on the stream function, ψ (see section 8.3):

$$\Delta\psi = 0\,, \tag{8.2}$$

in order to visualise the stream lines. This is equivalent to solving the Laplace equation on the velocity potential ϕ.

This equation must be supplemented with boundary conditions. Along the impervious walls, normal fluxes vanish. On the right wall, on the bottom, and on the left wall, this condition imposes that the stream function is constant. Moreover, this constant is

the same for the three boundaries, because they all correspond to the same streamline. We arbitrarily fix this constant to:

$$\psi = -L\,, \tag{8.3}$$

where L is the lateral extent of the aquifer.

The part considered so far is linear. The last boundary, the water table, induces non-linearity. Two conditions on ϕ define it. First, it is connected to atmosphere, such that the pressure on the water table is atmospheric:

$$\phi = y \quad \text{on} \quad y = h\,. \tag{8.4}$$

The second condition is a mass balance, which reads in steady state:

$$R = K\left(\partial_x\phi\,\partial_x h - \partial_y\phi\right) \quad \text{on} \quad y = h\,. \tag{8.5}$$

We now linearise around the position $h = 0$:

$$\phi(h) \simeq \phi(0) + h\,\partial_x\phi(0)\,. \tag{8.6}$$

Then, equation (8.4) forces ϕ to be of the order h, and equation (8.5) linearises into

$$R = -K\,\partial_y\phi \quad \text{on} \quad y = 0\,. \tag{8.7}$$

On the stream function, the Cauchy-Riemann conditions (see section 8.3, equation (8.16)) translate this equation on ϕ into an equation on ψ:

$$R = K\,\partial_x\psi \quad \text{on} \quad y = 0\,. \tag{8.8}$$

We have therefore defined a rectangular domain, where all boundary conditions are linear. However, groundwater exits this rectangular domain through the single upper left corner, which represents the outlet. This point is singular, which complicates the numerical resolution. To avoid this problem, we introduce artificially a fifth boundary. We approximate the outlet as a small quarter circle of radius ϵ, where we impose a constant velocity potential. This implies that the streamlines are orthogonal to the quarter circle:

$$\partial_n\psi = 0\,. \tag{8.9}$$

Figure 8.6 shows the streamlines from our numerical resolution, with the dimensions of the experiment (see appendix A for the numerical code). In this resolution, the radius of the quarter circle is one percent of the total lateral length of the domain. Changing its value does not influence, at least qualitatively, the shape of the streamlines. Finally, the imposed rainfall rate is $R/K = 1$. As the problem is linear, the rainfall rate does not influence the shape of the flow; it only modifies the discharge exiting the domain, in proportion to the rainfall.

The streamlines thus obtained strongly resemble the streamlines of the laboratory experiment (figure 8.5). Far from the outlet, the groundwater first flows downwards,

progressively modifying its course to finish by flowing upwards and towards the outlet. Conversely, the streamlines starting near the outlet are nearly horizontal. As all the streamlines are directed towards the single upper left corner, they are forced to get closer to each other near the outlet, all concentrating towards this small boundary.

With a numerical trick, we have skirted the problem posed by the singularity of the outlet. As the numerical resolution seems to strongly resemble the laboratory experiment, the linearisation of the free surface seems to be a reasonable approximation. However, the resolution of the linear problem shows the importance played by the river. If we want to find the general features of a two-dimensional flow, we hope that the river shape plays a minor role. As its dimensions are small compared to the groundwater flow domain, a natural approach consists in reducing the outlet to a point. However, this point becomes singular, because it must accommodate the finite discharge exiting the aquifer. According to equation (8.6), this implies that $\partial_x \phi$ diverges near the outlet and, as a consequence, the linearisation of the free-surface condition (8.5) is impossible. If we consider it as a point, the outlet forces the problem to be non-linear.

In what follows, we investigate whether this non-linearity has a strong influence on the dynamics of the experimental two-dimensional flow.

8.2.2.3 Experimental hydrograph

Let us start by exploring the transient regimes of our deep experimental aquifer. A typical experiment begins with a horizontal water table, which level corresponds to the outlet level (about 63 cm). We then switch on the rainfall and maintain its rate R constant for a few tens of seconds. A few seconds after rainfall starts, the discharge of water exiting the aquifer starts rising (figure 8.7). It rises quickly during a few seconds. After about 5 s, the discharge increases less quickly, as it gradually reaches its steady state value of $16\,\mathrm{ml\,s^{-1}}$, imposed by the rainfall rate. In the experiment of figure 8.7, the rainfall lasts only about 35 s, and the discharge has almost already reached its equilibrium value. As a comparison, with the same rainfall rate, in the fully-penetrating configuration and with the 4 mm beads, the discharge reached its steady state in about 4 minutes (section 3.3). The transient regimes are therefore much shorter in the deep aquifer configuration. This can be interpreted as a geometrical effect. To accommodate the same discharge, the water table must rise less in the deep configuration than in a fully-penetrating configuration. The groundwater flow therefore adjusts faster to new conditions.

8.2.3 Drought flow

When the rainfall stops, the discharge starts to decrease. It decreases quickly at the beginning, and then relaxes slowly towards zero. In this section, we study the dynamics of this drought flow.

To study the drought flow of this deep laboratory aquifer, we pour a volume $V = 600\,\mathrm{ml}$ of water on the aquifer, close to the right-hand side boundary. All the water

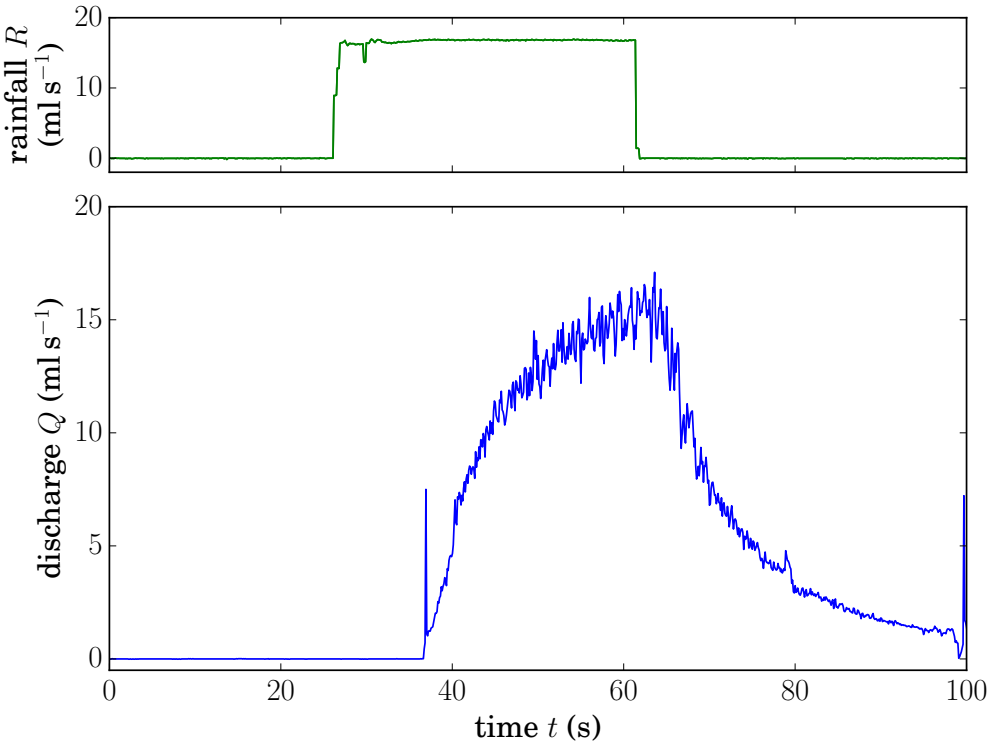

Figure 8.7: Rainfall rate R imposed to our laboratory aquifer (green line, top), and water discharge Q exiting the experiment (blue line, bottom). Measurements are collected at 10 Hz, with a precision of about 10^{-2} ml s^{-1}.

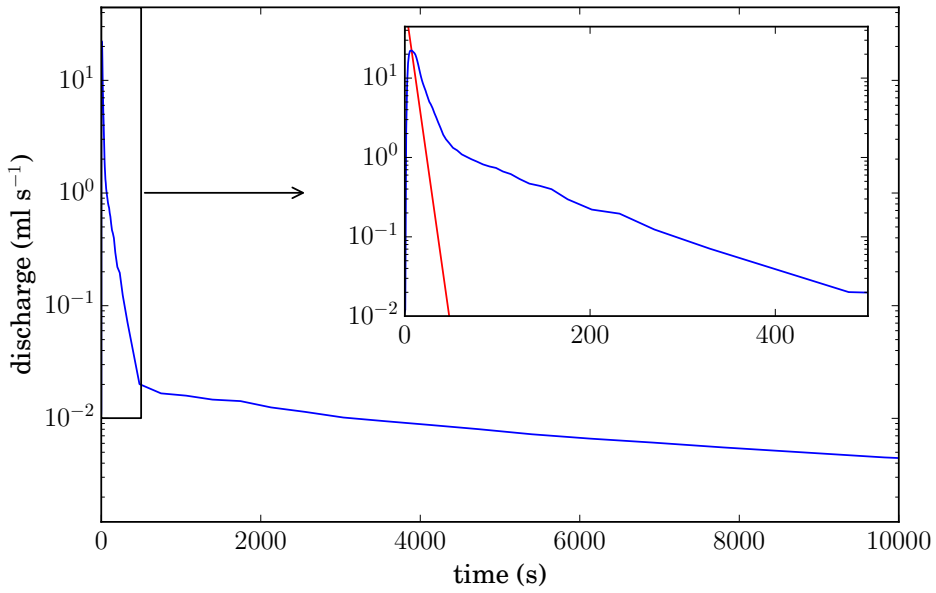

Figure 8.8: Drought flow in the deep aquifer (—). The inset displays only the early stages of the drought flow. The red line is the exponential decay (—) predicted, without any fit parameter, by the linearised Dupuit-Boussinesq equation. It may be valid at very early times, but the experimental drought flow rapidly deviates from it.

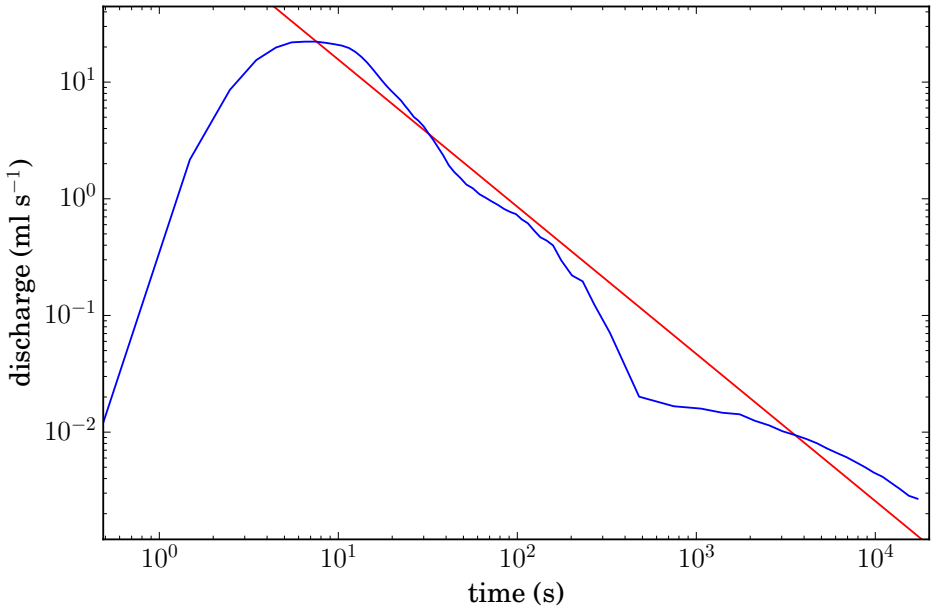

Figure 8.9: Drought flow in the deep laboratory aquifer. We pour a volume $V = 600\,\text{ml}$ on the porous material, and measure the discharge of water flowing out of the aquifer during 5.5 hours ($2 \cdot 10^4\,\text{s}$) (—). The fit of a power law (—) yields an exponent -1.26 ± 0.02.

infiltrates into the porous material, joining the groundwater reservoir. As the recharge is spatially localised, this forms a mound about 20 cm large, and about 10 cm high. This mound rapidly propagates towards the outlet, and the discharge of water flowing out of the aquifer increases quickly. Within 5 seconds, the discharge increases from zero to $22\,\text{ml}\,\text{s}^{-1}$. The discharge then starts decreasing.

During the first 200 seconds of the experiment, we weigh the outlet bucket every second. Afterwards, we weigh it every 15 seconds. We measure the water discharge during $2 \cdot 10^4\,\text{s}$, i.e. five hours and a half (figure 8.8). At the end of the experiment, groundwater still flows, delivering a discharge of $2.7 \cdot 10^{-3}\,\text{ml}\,\text{s}^{-1}$.

We first investigate the possibility of an exponential decay. On figure 8.8, we compare our drought flow with the theoretical exponential decay predicted by the linearisation of the Dupuit-Boussinesq equation (see section 2.2, equation (2.16)):

$$Q(t) \sim 2\,W\,h_c\,K\,\frac{H - h_c}{L}\,\exp\left(\frac{-\pi^2\,K\,h_c\,t}{4\,s\,L^2}\right)\,, \tag{8.10}$$

where W is the width of the tank, h_c is the depth of the aquifer below the river, K is the hydraulic conductivity, H is the depth of aquifer initially saturated with water, L is the lateral length of the aquifer, and s is the porosity. The experimental drought flow is comparable to this prediction during the very early stages of the experiment. However, it does not really seem exponential at long times. Very rapidly, the discharge deviates from the prediction (8.10). In the deep aquifer, the groundwater flow therefore exhibits a non-linear behaviour during drought.

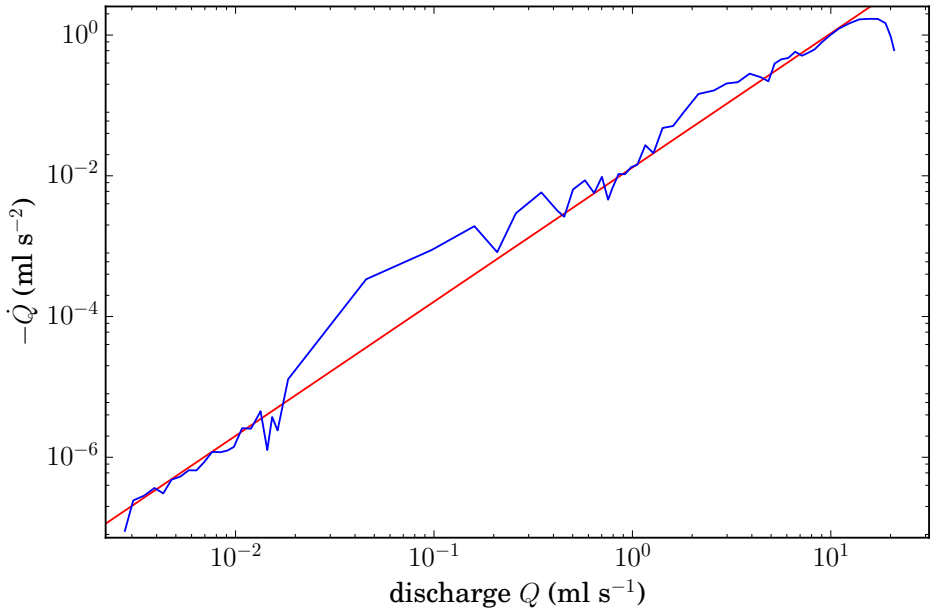

Figure 8.10: Time derivative $-\dot{Q}$ of the discharge with respect to the discharge, during the drought flow of the deep laboratory aquifer (—). The fit of a power law (—) yields an exponent 1.91 ± 0.02.

The fit of a power law to the drought flow yields an exponent -1.26 ± 0.02 (figure 8.9). We also compare this result with the method developed to analyse the drought flow of natural rivers, which consists in plotting the negative time derivative of the discharge $-\dot{Q}$ with respect to the discharge (figure 8.10). Fitting a power law to this data yields an exponent 1.91 ± 0.02. This exponent corresponds to a regime of discharge decrease slightly different from the previous method:

$$Q \sim \frac{1}{t^{1.1}} \,. \tag{8.11}$$

The exponents found by both methods, as they are larger than one, correspond to regimes of drought flow integrable in time. They do not compare to any of the Dupuit-Boussinesq asymptotic regimes, which predicted two possible exponents: $1/2$ and 2. However, they seem to be close to a regime in $Q \sim 1/t$, which we found in the Plynlimon catchments (see section 7.1 and Kirchner (2009)).

Yet, this preliminary result must be confirmed by further experiments. The experimental drought flow realised here needs to be improved. First, a better outlet device is necessary, such that the droplets flowing out of the aquifer, at the end of the experiment, must not flow down over about 50 cm to reach the weighed bucket. Second, at the point where the experiment stops, about 625 ml of water has exited the aquifer. This slightly exceeds the input volume. This excess probably results from the slowly draining unsaturated zone, which was certainly not totally empty before the experiment started.

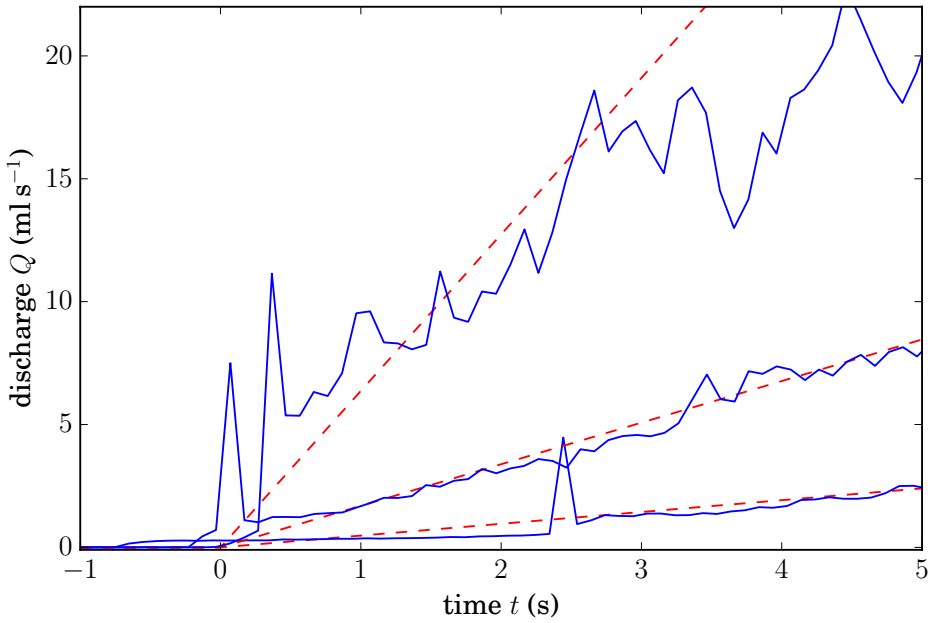

Figure 8.11: Increase of the water discharge just after the beginning of rainfall for various rainfall rates (—, $R = 51.7$, 17.2 and 7.8 mL s^{-1} from top to bottom). The curves are shifted horizontally so that time is zero at the beginning of the discharge increase. For each run, a linear increase is fitted to the data (- - -).

8.2.4 Early response to rainfall

In this section, we analyse the early response to rainfall of the experimental two-dimensional groundwater flow. The results presented here are only preliminary, because the outlet device used here might induce measurement errors.

The discharge delivered by the two-dimensional groundwater flow increases quickly after the beginning of rain. As shown in figure 8.7, the discharge reaches a steady state in a few tens of seconds. Before curving to reach its steady state asymptote, the early stages of this transient regime seem to be linear in time. Figure 8.11 shows the first five seconds after the discharge has started to increase, for three different experiments. The larger the rainfall rate, the larger the discharge increase. On this figure, the experiment made with the larger rainfall rate rapidly deviates from its linear behaviour — after only one or two seconds. The two other experiments, performed at lower rainfall rates, exhibit a linear behaviour during the five seconds displayed in figure 8.11.

The three signals exhibit a strong measurement noise. This noise is, in part, due to the high frequency of the weight measurements. However, each of them displays a strong peak at the beginning of the discharge increase. For each of them, this peak occurs at the precise moment when the discharge increases beyond about 0.65 ml s^{-1}. This threshold value being similar for all the experiments, this suggests a measurement bias due to the outlet device.

If the discharge indeed increases linearly with time, the weight of the bucket increases with the time squared. In order to measure the discharge increase rate $\dot{Q}$ of the early

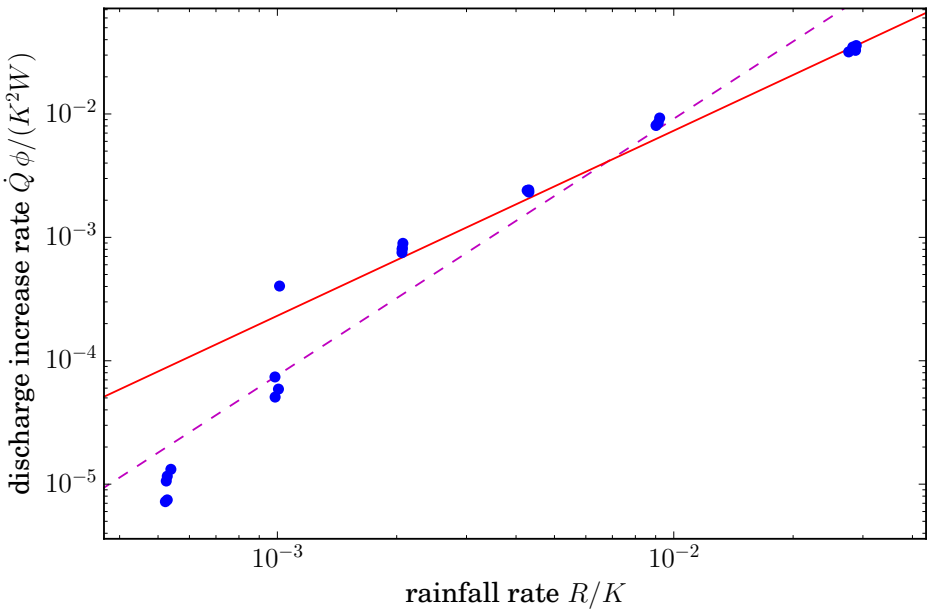

Figure 8.12: Dependence of the discharge increase rate with respect to the rainfall rate (●). The best fit of the data yields an exponent 2.08 ± 0.07 (- - -). A 3/2 power law (—) is also fitted to the data, rescaled as in the Dupuit-Boussinesq configuration (equation (3.12)). This fit yields a prefactor of 7.3, which is about 10 times the Dupuit-Boussinesq prefactor.

response to rainfall, as the discharge signals exhibit a strong noise, we fit a squared relationship to the weight signal. This method avoids differentiating our data. Repeating the experiment with various rainfall rates R, we measure the relationship between $\dot{Q}$ and R (figure 8.12). Not surprisingly, the discharge increase rate increases with the rainfall rate. However, as in the Dupuit-Boussinesq configuration, it increases faster than linearly. Fitting a power law to the data yields an exponent of 2.08 ± 0.07. This exponent is similar to the exponents found in the Plynlimon catchments (section 7.1).

Due to the large measurement noise, the points measured for low rainfall rates are highly uncertain. A 3/2 power law is plausible for the larger rainfall rates, which would be compatible with our results with the Quiock Creek hydrograph (chapter 6). Rescaling the data as suggested by the Dupuit-Boussinesq asymptotic regime (equation (3.12)), we fit a 3/2 power law, and obtain a prefactor of 7.3. This is about 10 times larger than the Dupuit-Boussinesq prefactor, confirming that the early response to rainfall is quicker in the present laboratory experiment than in a Dupuit-Boussinesq configuration.

For the moment, the quality of our experimental data does not allow us to clearly determine the relationship between $\dot{Q}$ and R. Further experiments are necessary. With these new experiments, it would also be interesting to explore the influences of hydraulic conductivity and aquifer depth.

Here, we also lack a theoretical background concerning the dynamics of a two-dimensional groundwater flow. In the next sections, we explore several theoretical

analyses of the problem, without reaching any definitive conclusion. Nonetheless, our analysis hopefully provides some insight on the general behaviour of a two-dimensional groundwater flow.

8.3 Analysis of two-dimensional flows

8.3.1 Two-dimensional flow in steady state

Complex analysis is an efficient method to solve the Laplace equation. In this section, we explain how the theory of analytic functions can help to solve the Laplace equation in two dimensions. We then illustrate this method with a simple example.

8.3.1.1 Properties of analytic functions

The problem of two-dimensional flow involves the resolution of the Laplace equation for the velocity potential $\phi(x, y)$. For that purpose, we introduce the real scalar field $\psi(x, y)$ and the complex scalar field $\Phi(x, y)$, defined as

$$\Phi = \phi + i\,\psi\,. \tag{8.12}$$

Noting $z = x + i\,y$ the complex variable and $\bar{z} = x - i\,y$, we now write Φ as a function of z and $\bar{z}$:

$$\Phi(x, y) = \Phi(z, \bar{z})\,. \tag{8.13}$$

We now suppose that Φ does not depend on $\bar{z}$:

$$\partial_{\bar{z}}\Phi = 0\,. \tag{8.14}$$

This condition is a very strong restriction, as Φ is now a function of the single variable z. If this function is differentiable, then we have

$$\begin{cases} \partial_x\Phi = \partial_z\Phi \\ \partial_y\Phi = i\,\partial_z\Phi\,. \end{cases} \tag{8.15}$$

Identifying the real and imaginary parts of equations (8.15), the condition (8.14) imposes that ϕ and ψ satisfy the Cauchy-Riemann conditions:

$$\frac{\partial\phi}{\partial x} = \frac{\partial\psi}{\partial y}\,, \quad \frac{\partial\phi}{\partial y} = -\frac{\partial\psi}{\partial x}\,. \tag{8.16}$$

As a result of the Cauchy-Riemann conditions, the real part of the complex potential, ϕ, satisfies the Laplace equation:

$$\Delta\phi = \frac{\partial}{\partial x}\frac{\partial\phi}{\partial x} + \frac{\partial}{\partial y}\frac{\partial\phi}{\partial y} = \frac{\partial}{\partial x}\frac{\partial\psi}{\partial y} - \frac{\partial}{\partial y}\frac{\partial\psi}{\partial x} = 0\,. \tag{8.17}$$

Similarly, we can show that the imaginary part ψ of the complex potential also satisfies the Laplace equation. From the Cauchy-Riemann equations, we also obtain

$$u = \frac{\partial\psi}{\partial y}\,, \quad v = -\frac{\partial\psi}{\partial x}\,, \tag{8.18}$$

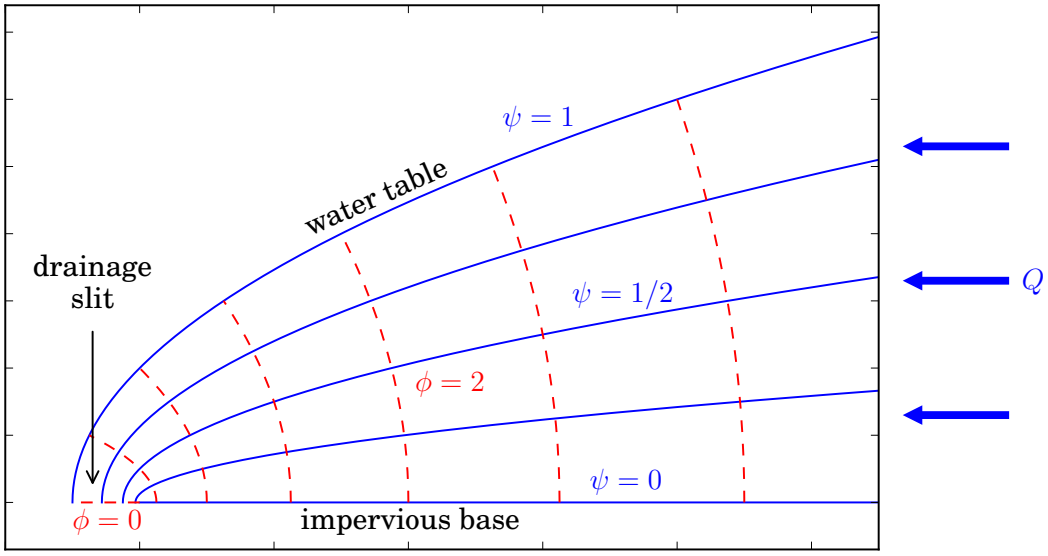

Figure 8.13: Example of a flow satisfying the Laplace equation: $\phi = \sqrt{z}$. The streamlines are defined by $\psi = const$ (—, equation (8.20)), and the isopotential lines are defined by $\phi = const$ (- - -, equation (8.21)).

where u and v denote for the horizontal and vertical components of the velocity. This defines ψ as the stream function of the flow. The stream function of a two-dimensional flow is useful, because the streamlines of the flow, defined as $\psi = \text{const}$, represent the trajectories of particles in a steady flow.

We have therefore shown that if the complex potential Φ is analytic — it is differentiable and satisfies condition (8.14) —, then its real and imaginary parts satisfy the Cauchy-Riemann equations and, in turn, the Laplace equation. The boundary conditions then provide supplementary constraints to the problem, and determine the single analytic function which represents the flow.

More information about the use of complex analysis for groundwater flows can be found in Polubarinova-Kochina (1962), Bear (1972) or Appel (2008).

8.3.1.2 Complex analysis

To illustrate how a function of the complex variable z can represent a flow, we begin with a simple example, given in Polubarinova-Kochina (1962): $\Phi(z) = \sqrt{z/A}$, where A is, for the moment, an undetermined real constant.

The streamlines of the flow are characterised by $\psi = \text{const}$. For a specific value of $\psi = \psi_0$, we write

$$z = x + iy = A\,\Phi^2 = A\,(\phi^2 - \psi_0^2 + 2\,i\,\phi\,\psi_0)\,. \tag{8.19}$$

Identifying the real and imaginary parts of z, we infer the equation of the streamline characterised by $\psi = \psi_0$:

$$y = 2\,A\,\psi_0\,\sqrt{\frac{x}{A} + \psi_0^2}\,. \tag{8.20}$$

Similarly, isopotential lines are defined by $\phi = \text{const}$. The isopotential line characterised by $\phi = \phi_0$ reads

$$y = 2\,A\,\phi_0\,\sqrt{\phi_0^2 - \frac{x}{A}}\,. \tag{8.21}$$

Figure 8.13 represents the streamlines and isopotential lines of the flow corresponding to $\Phi = \sqrt{2\,z}$. We have arbitrarily fixed $A = 1/2$. Because Φ is analytic, the streamlines and the isopotential lines are always orthogonal to each other.

To understand which physical flow may be represented by $\Phi = \sqrt{2\,z}$, we consider its boundaries.

Impervious base of the flow. The horizontal blue line, defined by $\psi = 0$ and delimiting the bottom of the flow (which we have arbitrarily fixed in $y = 0$), acts as an impervious boundary. Indeed, as $\psi = const$, the derivative of ψ along the horizontal coordinate x vanishes: $\partial_x \psi = 0$. According to the Cauchy-Riemann equations, this is equivalent to

$$\partial_y \phi = v = 0\,, \tag{8.22}$$

which is the condition defining an impervious boundary in a porous material.

Drainage slit. On the left of this impervious base, at the same vertical coordinate $y = 0$, a horizontal isopotential line $\phi = 0$ additionally delimits the bottom of the flow. On this segment we have $y = 0$ and $\phi = 0$. This segment therefore corresponds to a boundary where the pressure vanishes:

$$p = 0\,. \tag{8.23}$$

This corresponds to a boundary where the flow is directly in contact with air, such as a permeable grid for example. This grid drains the flow, as the fluid flows in the inverse direction of the potential gradient.

Water table. Finally, the top surface of the flow is characterised by a streamline, with a constant ψ: $\psi = 1$. Here, we will show that this streamline can be the free surface of the flow, or the water table.

Being a free surface, the water table is defined by two boundary conditions. One of the conditions is a mass balance, which determines the shape that the water table must adopt to accommodate for the flow. In steady state, and with the absence of rainfall, this condition simply translates into the condition of a vanishing normal flux:

$$\partial_n \phi = 0\,, \tag{8.24}$$

where $\mathbf{n}$ denotes the unit vector perpendicular to the surface. With the Cauchy-Riemann equations, this condition is equivalent to $\partial_s \psi = 0$, where $\mathbf{s}$ denotes the unit vector parallel to the surface. In other words, this condition states that, in steady state and in

the absence of rainfall, the free surface is a streamline — i.e. characterised by $\psi = \text{const}$. All the streamlines of the flow could therefore represent its free surface.

A second condition defines the free surface of the flow. As it is directly connected to the atmosphere, its pressure is atmospheric. For the velocity potential, this translates into

$$\phi = y\,. \tag{8.25}$$

As $z = \Phi^2/2$, this condition is satisfied on $\psi = 1$.

Discharge drained by the drainage slit. In the three previous paragraphs, we have shown that the flow represented in figure 8.13, which corresponds to $\Phi = \sqrt{2\,z}$, satisfies the Laplace equation. It is delimited by an impervious base, a water table and a permeable slit which drains the flow. Here, we show that the two values of the stream function ψ_b at the bottom and ψ_t at the top of the flow fix the discharge of fluid drained by the slit (of course, in general, one faces the inverse situation: the discharge of fluid fixes the extreme values of the streamlines). Indeed, if l is a line connecting the bottom to the top of the flow domain, the discharge q of fluid crossing this line reads

$$q = \int_l \vec{v}\cdot\vec{n}\;\mathrm{ds} = K\int_l \frac{\partial\,\psi}{\partial s}\;\mathrm{ds} = K\,(\psi_t - \psi_b) \tag{8.26}$$

where K is the conductivity. The flow represented in figure 8.13 therefore represents a porous material draining a discharge $q = K$ into a permeable slit.

With this simple example, we have shown how an analytic function can represent a flow satisfying the Laplace equation. However, determining a groundwater flow generally requires the inverse approach: we know that the flow satisfies the Laplace equation, and we want to find the analytic function which describes it, i.e. the analytic function which satisfies the boundary conditions. In the next section, we describe this inverse approach, with the same example.

8.3.1.3 Conformal mapping

We have shown that the function $\Phi = f(z)$, if it is analytic, describes a flow. In the physical plane, z geometrically represents a point, defined by its abscissa x and its ordinate y. Similarly, in a plane where ϕ and ψ define the abscissa and ordinate, Φ represents a point. Thus, the function f associates each point z_0 of the z-plane to a point Φ_0 in the Φ-plane. In this way, Φ_0 is the image of the point z_0 into the Φ-plane (see figure 8.14). The function f is then called a map, or a transformation. As f is analytic, it is a conformal map, which means it preserves angles locally (Bear, 1972).

In the physical plane, the boundaries of the flow are defined by specific conditions on ϕ and/or ψ. Let us consider the previous example, and assume we do not know the

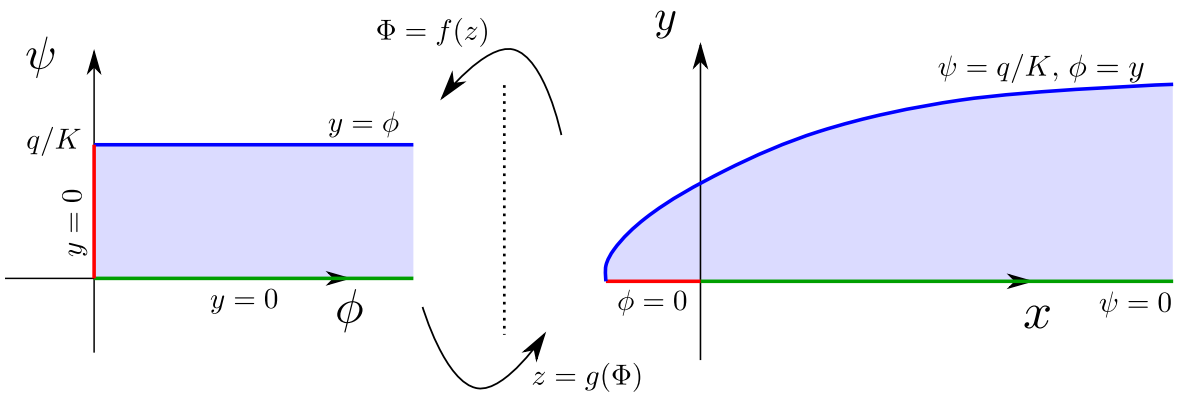

Figure 8.14: Conformal mapping. On the left, the Φ-plane is defined by ϕ on the abscissa axis, and ψ on the ordinate axis. On the right, the physical (or z-) plane. The boundary conditions (8.27) can be represented equivalently in both planes. However, the position of the water table is unknown in the physical plane, whereas it corresponds to a fixed line in the Φ-plane.

function f which describes it. We assume we only know its boundary conditions:

$$\begin{cases} \psi = 0 & \text{on the impervious base,} \\ \phi = 0 & \text{on the permeable slit,} \\ \psi = q/K & \text{on the water table} \\ \phi = y & \text{on the water table.} \end{cases} \tag{8.27}$$

These boundaries all have their image into the Φ-plane (figure 8.14). The flow domain, represented by the blue shaded area, has also its image into the Φ-plane, delimited by the boundaries images. A remarkable feature of the flow domain image into the Φ-plane is the position of the water table. As it is defined by $\psi = q/K$, the water table is fixed in the Φ-plane: it is a straight horizontal line.

The idea of conformal mapping is to find the function f which maps the boundaries of the z-plane into the boundaries of the Φ-plane. As f must be analytic, its inverse function $z = g(\Phi)$ exists, and is analytic (Bear, 1972). It is therefore possible to tackle the problem the other way around, and to look for the function g which satisfies the boundary conditions. In the Φ-plane, the boundary conditions are defined by

$$\begin{cases} y = 0 & \text{on the impervious base,} \\ y = 0 & \text{on the permeable slit,} \\ y = \phi & \text{on the water table.} \end{cases} \tag{8.28}$$

Note that, as the water table is not a free surface in the Φ-plane, it is defined by a single boundary condition. It is therefore easier to find the function g. We will now try to find the function g, assuming we do not know it from the previous section.

As we must have $y = \phi$ on the water table, the first natural proposition is $z = i\,\Phi$, which satisfies this condition everywhere. The drainage slit is defined by $\phi = 0$, so we indeed have $y = 0$. However, the impervious base is defined by $\psi = 0$, so with the function $g(\Phi) = i\,\Phi$, we do not have $y = 0$. We must find another function.

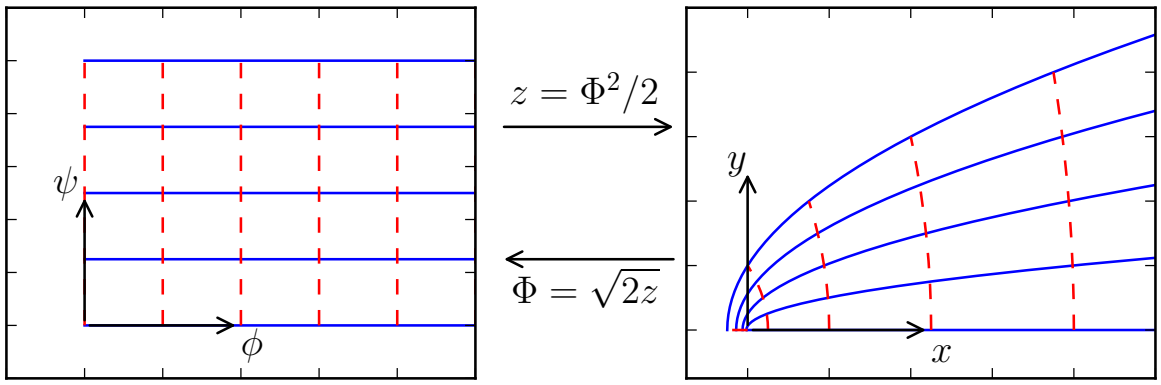

Figure 8.15: Streamlines and isopotential lines of a flow. *Left:* in the Φ-plane, isopotential lines are trivially vertical, and streamlines are horizontal. In this plane, the boundaries (equation (8.27)) are fixed. *Right:* in the z-plane, we must find the function which transforms the boundaries of the Φ-plane into the physical boundaries, in the z-plane.

We can get inspired from our first guess though, because it satisfied two of the three conditions. We want to have $y = 0$ on $\psi = 0$, so we multiply our first guess by $-i\,\Phi = \psi - i\,\phi$, such that $z = g(\Phi) = \Phi^2 = \phi^2 - \psi^2 + 2\,i\,\phi\,\psi$. On the impervious base, $\psi = 0$ such that $y = 0$. On the drainage slit, $\phi = 0$ and we also have $y = 0$. Finally, the water table is defined by $\psi = q/K$, so we obtain $y = 2\,\phi\,q/K$. Multiplying by the factor $K/(2\,q)$, we therefore obtain that the function $g(\Phi)$ such that

$$z = \frac{K}{2\,q}\,\Phi^2 \tag{8.29}$$

satisfies the boundary conditions (8.28). As it is analytic, we have found the solution to the problem defined by the Laplace equation on ϕ, supplemented by the boundary conditions (8.28). Inversely, the inverse function

$$\Phi = \sqrt{\frac{2\,q\,z}{K}} \tag{8.30}$$

is also analytic, such that ϕ satisfies the Laplace equation, and the boundary conditions (8.27). Figure 8.15 represents the isopotential lines and the streamlines defined by these transformations, in the Φ-plane and in the z-plane.

Before using conformal mapping to investigate the behaviour of a two-dimensional groundwater flow in deep aquifers, we match this two-dimensional solution of a shallow groundwater flow with the Dupuit-Boussinesq solution.

8.3.1.4 Matching with the Dupuit-Boussinesq solution

In chapter 3, we have shown that the Dupuit-Boussinesq equation admits a self-similar solution at early times of a rainfall event. This solution leads to the prediction

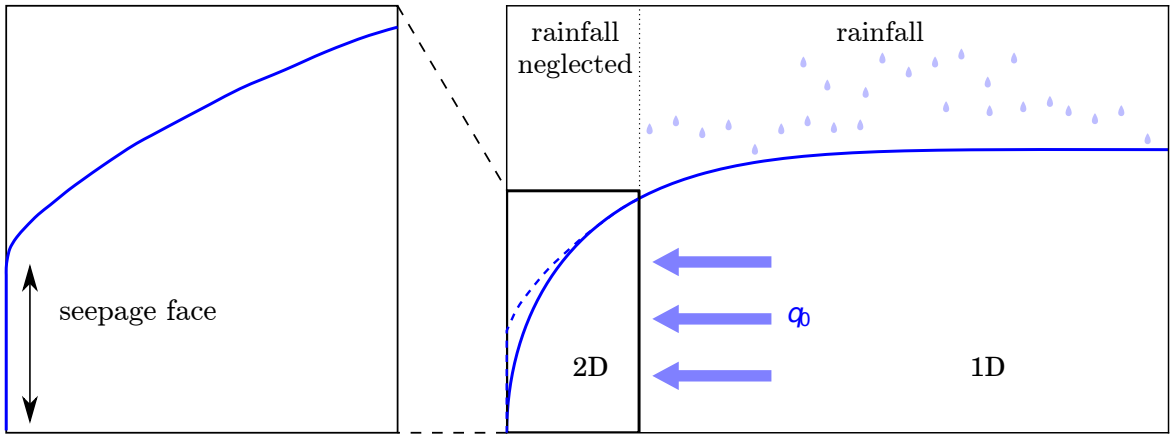

Figure 8.16: Illustration of the asymptotic matching between a Dupuit-Boussinesq solution, far from the outlet, and a two-dimensional solution, close to the outlet. Close to the outlet, the two-dimensional flow is insensitive to rainfall, and the water must only accommodate for the discharge q_0 coming from the one-dimensional flow, on the right.

that the discharge increases linearly with time, and in proportion to the rainfall rate at the power 3/2:

$$Q(t) \sim a^2 \frac{W}{s} \sqrt{\frac{K}{2}} R^{3/2} t \,, \tag{8.31}$$

where W is the width of the aquifer, s the porosity, K the hydraulic conductivity, R the rainfall rate and t the time. The mathematical constant a comes from the integration of the Dupuit-Boussinesq equation. Our experimental results conformed to this prediction, except for the prefactor of the scaling law. In the experiments, we found a prefactor about 3 times larger than the Dupuit-Boussinesq prediction. We attributed this mismatch to a singularity induced by the Dupuit-Boussinesq framework.

We mentioned the problem of this singularity in section 2.3. In the configuration of a fully-penetrating stream, the shallow water approximation imposes that the water table elevation is fixed at $h = 0$ at the river (in $x = 0$). Combined with Darcy's law (equation (2.2)), this implies that the water table behaves like

$$h \sim \sqrt{\frac{2\, q_o\, x}{K}} \,, \tag{8.32}$$

where q_0 is the discharge of water exiting the aquifer. This square root is incompatible with the shallow-water approximation, since the slope of the water table diverges near the outlet. This suggests that, close to the outlet, the groundwater flows in two dimensions, even in this shallow configuration. Here we propose to examine the asymptotic behaviour of the two-dimensional solution of the groundwater flow in a shallow configuration. We expect that, far from the river, it asymptotically exhibits a square root shape. In that case, matching this two-dimensional flow with the Dupuit-Boussinesq solution could change the prefactor in front of equation (8.32) and, in turn, the prefactor in front of equation (8.31).

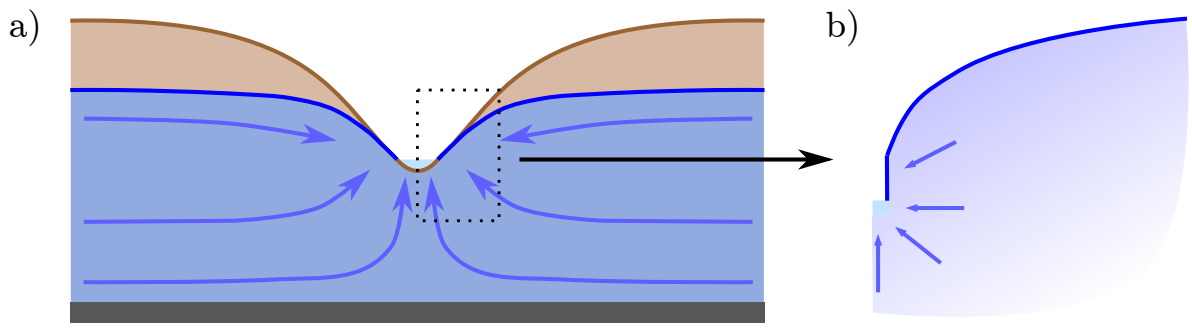

Figure 8.17: Illustration of a deep aquifer. *a)* Below the river, groundwater flows vertically upwards. *b)* At the beginning of a rainfall event, the perturbation imposed by rainfall to the groundwater flow may be insensitive to the aquifer bottom, if any.

For this purpose, we must solve the two-dimensional flow near the outlet, which is a vertical porous grid in the laboratory aquifer of chapter 3. Unfortunately, we are not aware of any analytical solution of the two-dimensional flow with a vertical permeable grid. Yet in the present chapter, we have found a solution with a horizontal grid (equation (8.29)). In what follows, we adopt this solution.

To match the two-dimensional solution (8.29) to a Dupuit-Boussinesq flow, we assume that rain falling in the immediate neighbourhood of the outlet represents a negligible fraction of the discharge exiting the aquifer. Sufficiently close to the outlet, the rainfall rate can be neglected, and the flow is essentially determined by the discharge q_0 coming from the right (figure 8.16). The discharge q_0 is determined outside of the two-dimensional area, where the shallow water approximation remains valid.

With the solution (8.29), we determine the shape of the water table of the two-dimensional flow:

$$y = \sqrt{\frac{2\,q_0}{k}\,x + \left(\frac{q_0}{K}\right)^2}\,. \tag{8.33}$$

Far from the outlet, the water table adopts asymptotically a square-root shape, as for a Dupuit-Boussinesq flow:

$$h \sim \sqrt{\frac{2\,q_o\,x}{K}}\,. \tag{8.34}$$

The prefactor of this square-root shape is exactly the same as for a Dupuit-Boussinesq flow (equation (8.32)). As a consequence, the asymptotic matching with solution (8.29) has no effect on the Dupuit-Boussinesq scaling laws. It would be interesting to test the matching of the Dupuit-Boussinesq solution with the two-dimensional flow, in the case where the river is modelled by a vertical grid at the outlet. The hodograph method could be a way to track this solution analytically (Polubarinova-Kochina (1962), p.162).

8.3.2 Infinitely deep aquifer

In this section, we investigate the two-dimensional flow in an infinitely deep, and infinitely large aquifer. The problem of an infinitely deep aquifer is interesting for three

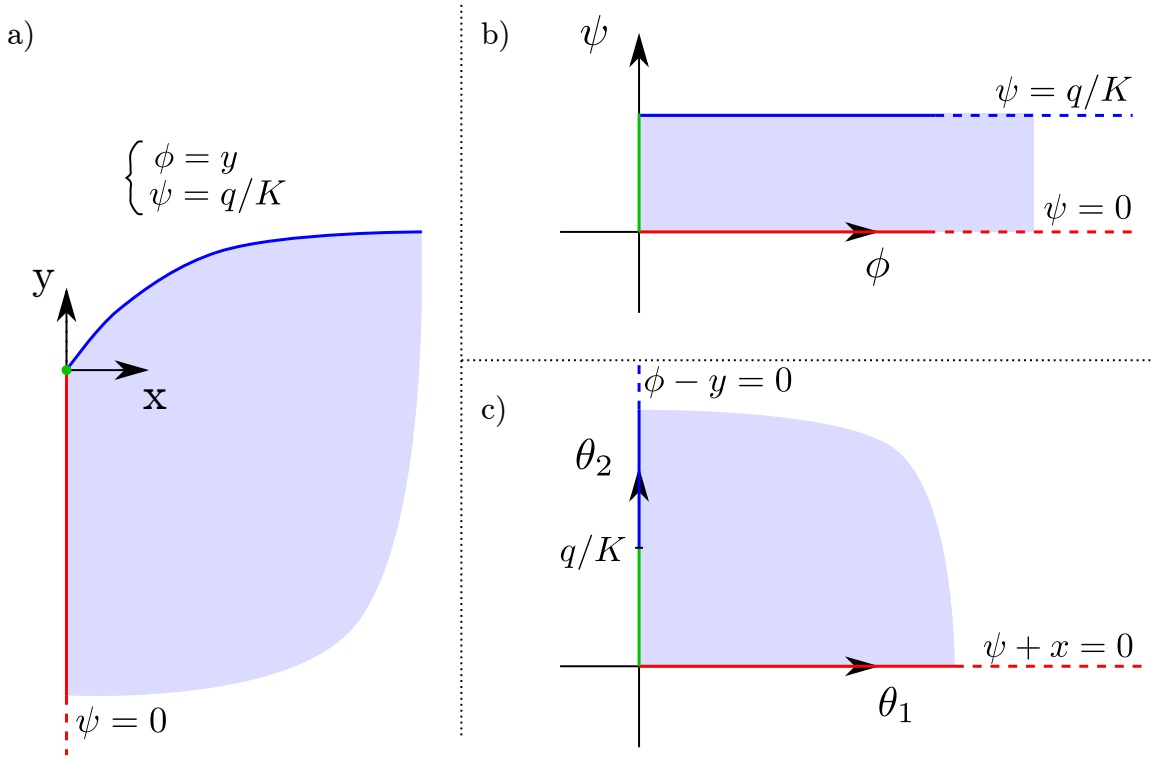

Figure 8.18: Representations of the groundwater flow domain in an infinitely deep aquifer, in three different planes: z, Φ and Θ. The vertical axis of symmetry halving the aquifer around the river is represented with a red line (—) in the three different planes. Similarly, the water table is represented with a blue line (—).

reasons. First, it is difficult to find any evidence that a tangible impermeable bottom layer delimits all aquifers. The possibility that some aquifers can be very deep cannot be excluded. Second, the analytic solution of a two-dimensional groundwater flow in steady state is easy to obtain in an infinitely deep aquifer. With this simple analytic solution, we can describe some characteristic features of two-dimensional flows in deep aquifers. Finally, we suggest that, at the beginning of a flood, rainfall induces only a small perturbation of the water table. In this case, even in an aquifer of finite depth, the perturbation may be insensitive to the aquifer bottom at the early stage of the response to rainfall (figure 8.17).

8.3.2.1 Steady state

Each specific shape of river induces a specific solution to the Laplace equation. However, we are looking for the general features of a groundwater flow in a deep aquifer. We hope that these general features do not depend much on the specific shape of each river, and that, sufficiently far from the river, the influence of the river shape can be neglected. In this section, we consider the river as a singular point (green point on figure 8.18a)

The groundwater flow in an infinitely deep and infinitely large aquifer thus presents

three boundaries (figure 8.18). First, the vertical axis of symmetry (red line on figure 8.18a), which halves the aquifer around the river, acts as an impervious boundary. On this boundary, the stream function is therefore constant. We arbitrarily fix the value of this constant, such that

$$\psi = 0 \tag{8.35}$$

on the vertical axis of symmetry.

The second boundary is the water table. The condition that the pressure is atmospheric on the water table reads, for the velocity potential:

$$\phi = y\,. \tag{8.36}$$

The second condition on the water table is given by mass balance. Here, we will consider the case of a discharge q flowing towards the river, without any rainfall. In steady state, as shown in the previous section, the absence of rainfall implies that the water table is a streamline, i.e. ψ is a constant. This constant is given by a mass balance (equation (8.26)):

$$\psi = \frac{q}{K}\,. \tag{8.37}$$

As in the previous section, the water table therefore corresponds to the fixed straight line $\psi = q/K$ in the Φ-plane (figure 8.18b). However, the situation is different here, because of the position of the streamline $\psi = 0$ in the z-plane: the positive part of the abscissa in the Φ-plane maps onto a vertical line in the z-plane.

The third boundary is the river, located in $x = 0$ and $y = 0$. In the river, the potential vanishes, such that

$$\phi = 0\,. \tag{8.38}$$

However, the stream function jumps from 0 on the axis of symmetry to $\psi = q/K$ on the water table:

$$0 < \psi < \frac{q}{K}\,. \tag{8.39}$$

This jump is the reason why the river is a singular point, which therefore transforms into a segment in the Φ-plane (figure 8.18b).

In order to find the function f which maps the boundaries of the flow from the Φ-plane to the z-plane, we introduce a new analytic function, the Zhukovsky function Θ (Zhukovsky, 1920; Polubarinova-Kochina, 1962):

$$\Theta = \Phi + i\,z\,. \tag{8.40}$$

The Zhukovsky function is analytic, because it is the sum of two analytic functions. Writing $\Theta = \theta_1 + i\,\theta_2$, the real and imaginary parts of the Zhukovsky function read

$$\begin{cases} \theta_1 = \phi - y \\ \theta_2 = \psi + x\,. \end{cases} \tag{8.41}$$

This new analytic function is useful because both the water table and the axis of symmetry are fixed in the Θ-plane. Indeed, equation (8.36) is equivalent to

$$\theta_1 = 0 \tag{8.42}$$

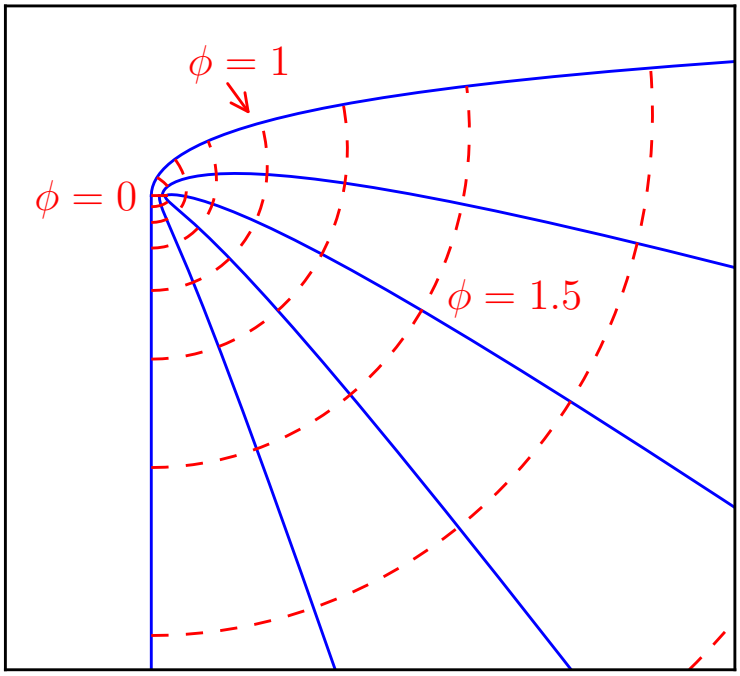

Figure 8.19: Streamlines (——) and isopotential lines (- - -) in an infinitely deep aquifer, corresponding to the analytic function (8.45).

on the water table. In the Θ-plane, the water table is therefore mapped onto the positive semi-infinite ordinate axis, with the minimum value $\theta_2 = q/K$ (figure 8.18c). The axis of symmetry is in $x = 0$, such that equation (8.35) leads to

$$\theta_2 = 0 \tag{8.43}$$

on the axis of symmetry. The image of the axis of symmetry is therefore the same in the Φ- and the Θ-planes (figure 8.18). Finally, the river is characterised by $y = 0$ and $\phi = 0$, such that $\theta_1 = 0$. Its image in the Θ-plane is therefore the same as in the Φ-plane.

The advantage of having introduced the Zhukovsky function is that in both the Φ- and Θ-planes, the three boundaries are fixed. Thus, it is easier to find a conformal map between those two planes. In the present case, a hyperbolic function maps Φ onto Θ:

$$\Theta = \frac{q}{K\sqrt{2}} \sqrt{\cosh\left(\frac{\pi K \Phi}{q}\right) - 1}\,. \tag{8.44}$$

This result, combined with the definition (8.40) of the Zhukovsky function, gives the function which maps the flow from the Φ-plane to the physical plane:

$$z = i\left(\Phi - \frac{q}{K\sqrt{2}} \sqrt{\cosh\left(\frac{\pi K \Phi}{q}\right) - 1}\right)\,. \tag{8.45}$$

Figure 8.19 shows the streamlines and the isopotential lines corresponding to this analytic function. As in the laboratory experiment, the streamlines get closer to each

other as they flow towards the outlet (see figure 8.5). Here, the analytic function also allows to observe that the isopotential lines concentrate as they get closer to the river. This implies that the flow accelerates as it gets closer to the river.

The isopotential line $\phi = 0$ is supposed to correspond to the river. The solution (8.45) gives, for $\phi = 0$:

$$\begin{cases} x = -\psi + \dfrac{q}{K\sqrt{2}}\sqrt{1 - \cos\left(\dfrac{\pi K \psi}{q}\right)} \\ y = 0\,. \end{cases} \tag{8.46}$$

It therefore maps the river as a segment of finite size in $y = 0$, and not as a singular point. Indeed, we would like to impose three conditions at the river: $x = 0$, $y = 0$ and $\phi = 0$ on the segment $0 < \psi < q/K$. However, we can only impose two conditions on a boundary. Here, our representation of the river in the Φ- and Θ-planes (figures 8.18a and b) implicitly imposes the two conditions $y = 0$ and $\phi = 0$. The solution (8.45) additionally satisfies $x = 0$ for the two points $(\phi = 0, \psi = 0)$ and $(\phi = 0, \psi = q/K)$.

However, the isopotential line $\phi = 0$ of solution (8.45) does not prescribe the real shape of the river. We simply found no analytic function which could take into account the singularity of the river. As we want the shape of the river to be neglected, solution (8.45) is rather an intermediate asymptotics: it is valid sufficiently far from the river, such that the shape of the river can be neglected; and sufficiently close to the river, such that the bottom and right boundaries of the aquifer can be neglected.

Naturally, as the flow satisfies the Laplace equation, the isopotential lines are perpendicular to the streamlines. Therefore, all the isopotential lines connect the vertical axis of symmetry to the water table, which is close to be horizontal. As a consequence, the isopotential lines describe circular curves turning around the river. This particularity, characteristic of any two-dimensional flow in a deep aquifer, points to an interesting observation. The isopotential lines are not vertical, as in a Dupuit-Boussinesq configuration. As a result, pressure is not hydrostatic in a deep aquifer. On the contrary, the value of ϕ increases with depth. This means that the pressure is larger than hydrostatic if we measure it deep into the aquifer.

In some field studies, the pressure measured deep into the aquifer happens to be larger than hydrostatic. This phenomenon, referred to as artesian, is generally explained by confining layers. Here, our results suggest that a two-dimensional free-surface flow could also generate non-hydrostatic flow. In the next section, we briefly investigate this particular feature of two-dimensional flows.

8.3.2.2 Two-dimensional flow near a river

Drilling a borehole into the ground sometimes causes water to flow out of the borehole. This means that the pressure at the bottom of the borehole is larger than hydrostatic. In this case, the borehole is referred to as artesian. This phenomenon is generally explained by the presence of an impermeable layer above the bottom of the

borehole. This impermeable layer confines groundwater and can, in specific geometrical conditions, lead to pressures larger than hydrostatic.

In the present section, we investigate the possibility that this phenomenon could also be due to a two-dimensional flow in a homogeneous aquifer. For that purpose, we compare qualitatively our analytic solution to field measurements performed in the aquifer of the Severn river headwaters, in Plynlimon, Wales.

Artesian boreholes in the Severn river catchment. In one of the Plynlimon catchments studied in section 7.1, close to the Severn river, Haria and Shand (2004) have investigated the deep groundwater flow. Motivated by hydrochemical studies highlighting the importance of deep groundwater in streamflow generation, they tested the hypothesis that groundwater inputs into the river are significant.

Their field set-up is similar to the installation we made in the Quiock Creek catchment (chapter 4). Along a transect perpendicular to the river bed, they installed pressure sensors at the bottom of boreholes to measure the water table level. At each location, they drilled three boreholes of different depth (figure 8.20). At the closest distance from the river though, access difficulties hindered them to drill deep into the aquifer, and they only drilled two shallow boreholes. In what follows, we will focus on the results given by the nests of boreholes 1, 2 and 3.

In order to measure the pressure field within the aquifer, care must be taken not to perturb the pressure field. They introduce a plastic tube in each borehole. Around this tube, there is an annular gap between the tube wall and the borehole wall. This gap, if filled with water, could impose hydrostatic pressure to the surrounding groundwater flow. To prevent this, they sealed this gap by filling it with an expanding resin. In this manner, the pressure sensors indeed measure the local pressure field, at the desired depth, without perturbing the rest of the flow.

Haria and Shand (2004) present a time series of the nine pressure sensors. This time series includes the height of water recorded in the boreholes, relative to the ground level at the location of the borehole. We estimated visually, on their time series, the value of the height recorded in the nine boreholes at a particular instant in December 2001. These values are representative of the whole time series. We estimate errors on these rough estimations of about $\approx 20\,\mathrm{cm}$. We call $h_i(y)$ the relative height measured in the borehole i of depth y. Figure 8.20 shows, for each nest of boreholes, the evolution of the height with respect to the depth of the borehole. In order to compare the three profiles, we plot the height relative to the height measured in the shallowest borehole: $h_i(y) - h_{i,\,top}$. If the pressure field were hydrostatic, the height would not depend on the depth of the borehole, and we would have $h_i(y) = h_{i,\,top}$.

On the contrary, in the three nests of boreholes, the height varies according to the depth of the sensor (figure 8.20, bottom). Yet, the relationship between the depth of the sensor and the height recorded is not similar in the three nests. In the first nest for example (blue points), the shallowest sensor records a larger pressure head ($\approx 15\,\mathrm{cm}$) than the "middle-depth" sensor, but lower ($\approx 2.5\,\mathrm{m}$) than the deepest sensor. We observe a similar trend for the second nest of boreholes (green points) but, for the third

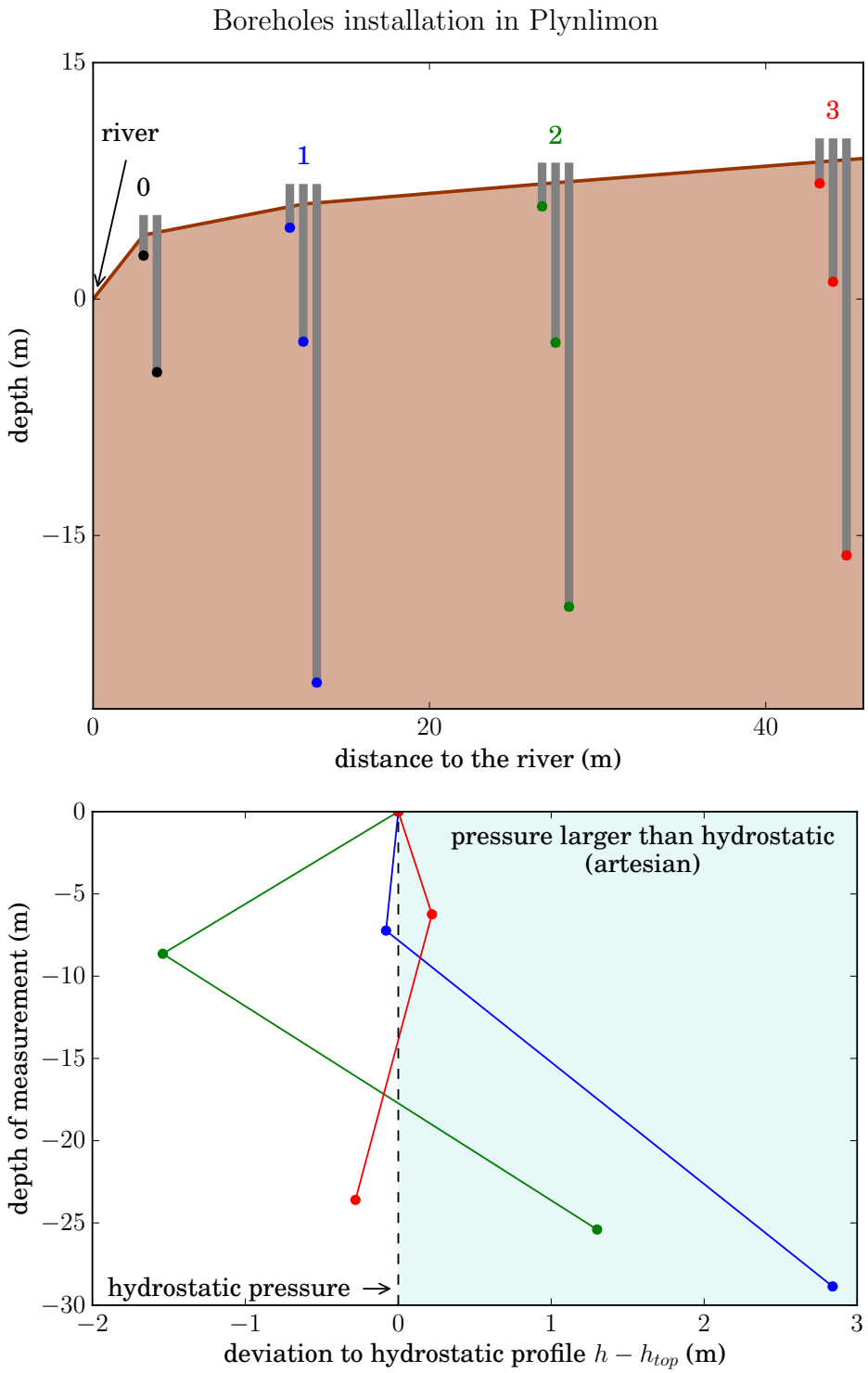

Figure 8.20: Artesian behaviour observed close to the Severn river. *Top:* Side view of the field installation in Haria and Shand (2004) to measure the pressure at different distances and different depths close to the Severn river. The points represent the locations of the sensors. Each colour corresponds to a different distance to the river. *Bottom:* Deviation to hydrostatic equilibrium $h = h_{top}$ of the height with respect to the depth of measurement. The three profiles correspond to the three nests of boreholes represented on the top illustration.

one (red points), the trend is different: the pressure head is larger in the "middle-depth" borehole, but lower in the deepest borehole. Also, the two closest nests of boreholes exhibit a strong departure from hydrostatic equilibrium. On the contrary, the third profile is closer to hydrostatic equilibrium.

Haria and Shand (2004) interpret these artesian pressures as a mark of the complexity of the aquifer geometry. Here, we show that these results could also be attributed to the behaviour of a two-dimensional flow in an infinitely deep aquifer.

Artesian behaviour of a two-dimensional flow. We now compare these results with the analytic solution (8.45) of two-dimensional flows provided in the previous section. This solution gives the profile of pressure with respect to depth, at any given distance to the river. For that purpose, we fix the distance to the river $x = x_i$ at which we want to infer the pressure profile with depth, and obtain a parametric relationship between the potential $\phi(x_i, y)$ and the depth y, ψ being the parameter. As $\phi = p/(\rho\, g) + y$, the hydrostatic equilibrium at a given distance x_i from the river is defined by $\phi(x_i, y) = h(x_i)$, where h is the height of the water table compared to the river elevation. At each distance x_i of the river, the difference $\phi(x_i, y) - h(x_i)$ therefore corresponds to the deviation to a hydrostatic profile.

Figure 8.21 shows three profiles $\phi(x_i, y) - h(x_i)$ at three distances from the river (0.5, 2 and 7), for $q = 1$ and $K = 1$. The three profiles deviate from the hydrostatic equilibrium. As the measurement point gets deep into the aquifer, it reaches isopotential lines which correspond to $\phi > h$, i.e. pressures larger than hydrostatic. The deeper into the aquifer, the larger the value of ϕ, and the larger the deviation to hydrostatic pressure. The distance of the borehole to the river also comes into play. The closer to the river, the larger the deviation. This is a geometrical effect: the isopotential lines concentrate as they approach the river. The variations of ϕ are therefore larger near the river. Finally, we notice that, at small depths, the deviation to hydrostatic pressure can be negative (i.e. pressures lower than hydrostatic). This effect gets stronger near the river.

Comparing these theoretical curves with the field measurements of figure 8.21, we observe a striking similarity. The closest nest of boreholes exhibits the strongest positive deviation to hydrostatic equilibrium, and the furthest almost exhibits hydrostatic equilibrium. Moreover, in the nests of boreholes 1 and 2, the "middle-depth" sensor exhibits a negative deviation to hydrostatic equilibrium, in a similar way as the theoretical curves show a negative departure from hydrostatic equilibrium at shallow depths.

The qualitative similarity between the field measurements and the theoretical curves of figure 8.21 suggests that these artesian boreholes could result from a deep two-dimensional flow in the aquifer. Furthermore, Haria and Shand (2004) observe that all boreholes rapidly rise during rainfall, and decline similarly after rainfall. The dynamics being similar in all the boreholes, this observation further suggests that the Severn river aquifer behaves as a large and deep porous material, where the deep groundwater flow contributes significantly to the stream flow generation, during floods as well as during

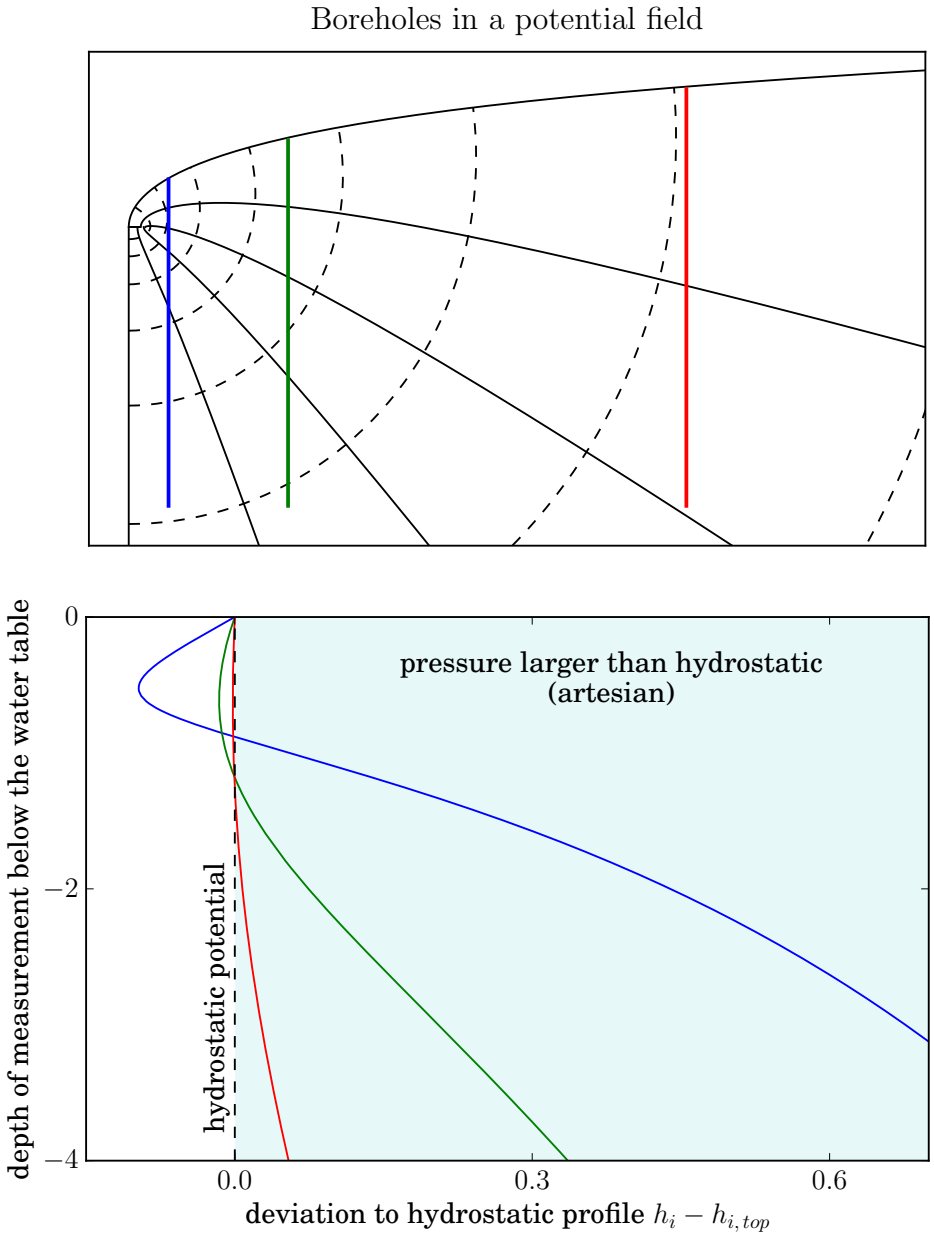

Figure 8.21: Deviation of the potential ϕ to its hydrostatic value $\phi = const$, in an ideal infinitely deep aquifer. *Top:* Representation of three boreholes in the potential field of the aquifer, at three distances from the river: 0.5 (—), 2 (—) and 7 (—). *Bottom:* Profiles of the potential $\phi = p/(\rho\, g) - y$ in the three boreholes. The hydrostatic equilibrium corresponds to $\phi = 0$. If $\phi > 0$, the pressure is larger than hydrostatic (artesian).

drought flow. If this is true, this two-dimensional groundwater flow also induces artesian effects.

However, the similarity between figures 8.20 and 8.21 is not perfect. Several reasons can explain this mismatch. First, it can be due to the finite depth of the aquifer. Second, local heterogeneities could affect the flow, especially in a fractured aquifer, where we expect strong heterogeneities at the local scale. Finally, the traditional explanation that an artesian well has been dug through a confining impervious layer could also hold here. Yet, this theory hardly explains the large negative departure from hydrostatic equilibrium in the second nest.

We now investigate whether the two-dimensionality of a flow has an influence on transient regimes.

8.3.2.3 Early response to rainfall: self-similarity

In the present section, we analyse the transient behaviour of the two-dimensional groundwater flow in an infinitely deep aquifer. The analysis proposed here is incomplete because of technical difficulties. Yet, it suggests that a self-similar solution may exist during the early stages of the reaction to rainfall.

As in steady state, we neglect the influence of the river, such that only two boundaries delimit the flow: the water table and the axis of symmetry. In transient regime, the mass balance on the water table reads:

$$s\,\frac{\partial h}{\partial t} = K\left(\frac{\partial \phi}{\partial x}\frac{\partial h}{\partial x} - \frac{\partial \phi}{\partial y}\right) + R\,, \tag{8.47}$$

where h is the water table elevation compared to the river. The second condition on the water table is that the pressure is atmospheric:

$$\phi = y \tag{8.48}$$

at the water table. The axis of symmetry stays a streamline, even during transient regimes. We chose to fix at 0 the value of the stream function:

$$\psi = 0 \tag{8.49}$$

on the axis of symmetry.

We now suggest that a self-similar solution exists at the early stages of the reaction to rainfall. We assume that the groundwater flow is at rest before the rainfall starts, and the water table level is $h = 0$ at $t = 0$. We now further assume that, far from the river in the horizontal direction, the groundwater flow is insensitive to the river, and fills up in proportion to rainfall:

$$h = \frac{R\,t}{s} \quad \text{for} \quad x \to \infty\,. \tag{8.50}$$

This assumption is the same as in chapter 3. However, contrary to the Dupuit-Boussinesq configuration, the configuration here allows groundwater to flow downwards, especially

far from the river. Therefore, the validity of this assumption is less obvious in the present case. In what follows, we proceed with this untested assumption. In the same way as in chapter 3, we now propose a self-affine transformation for the potential ϕ and for the elevation h of the water table:

$$\begin{cases} \Phi(x,y,t) = \dfrac{R\,t}{s}\ \tilde{\Phi}(\tilde{x},\tilde{y}) \\ h(x,t) = \dfrac{R\,t}{s}\ f(\tilde{x})\,, \end{cases} \tag{8.51}$$

where the tildes denote the self-affine functions and variables, and the self-affine variables read

$$\begin{cases} x = \dfrac{R\ t}{s}\ \tilde{x} \\ y = \dfrac{R\ t}{s}\ \tilde{y}\,. \end{cases} \tag{8.52}$$

With this self-affine transformation, the boundary conditions (8.48) and (8.49) translate into

$$\tilde{\phi} = \tilde{y} \tag{8.53}$$

and

$$\tilde{\psi} = 0\,. \tag{8.54}$$

Finally, incorporating the self-affine transformations into the mass balance equation (8.47), we obtain the second condition defining the water table in the self-affine plane:

$$\frac{R}{K}\ (f - \tilde{x}f' - 1) = \frac{\partial\tilde{\phi}}{\partial\tilde{x}}f'(\tilde{x}) - \frac{\partial\tilde{\phi}}{\partial\tilde{y}}\,. \tag{8.55}$$

The self-affine transformations (8.51) and (8.52) have therefore transformed the partial differential equation (8.47) into a two-dimensional ordinary differential equation. Removing the time-dependency from the problem, these transformations reduce its difficulty. We end up with a problem similar as the steady state one, except that the free surface condition (8.55) is now more complicated.

We have not found any analytical solution to this problem yet. This problem is also difficult numerically, because of the free surface.

8.4 Conclusion

The experiment presented in this chapter showed that the groundwater flow in a deep aquifer is two-dimensional. Far from the river, a water droplet feeding the groundwater reservoir begins its course by flowing downwards, and almost reaches the bottom of the aquifer. It then changes its course to progressively flow towards the river. If the aquifer is sufficiently deep, this two-dimensional feature of the flow breaks the Dupuit-Boussinesq approximation (Bresciani et al., 2014). One consequence is that the pressure, in a two-dimensional flow, is not hydrostatic. On the contrary, the isopotential lines wind around

the river. The deeper, the larger the velocity potential, and the larger the hydraulic head. Measuring the pressure — or, equivalently, the hydraulic head — deep into a two-dimensional groundwater flow therefore leads to artesian pressure. We suggest that a two-dimensional flow in the Severn river aquifer could explain the artesian pressures measured in Haria and Shand (2004).

In reaction to equivalent rainfall rates, the water table elevates less in the deep laboratory aquifer than in a fully-penetrating configuration. As a result, small variations of the water table elevation induce large variations of the discharge in a deep aquifer. This certainly explains the observation that the transient regimes in the deep aquifer are shorter than in the fully-penetrating configuration. This observation suggests that a larger system reacts faster than a smaller one. This result is counter-intuitive, as most flow paths are longer in a deep aquifer configuration. Far from the river, the velocity is also lower. As a result, the transit times distribution is certainly more extended in a deep aquifer than in an aquifer feeding a fully-penetrating stream.

The drought flow delivered by the two-dimensional groundwater flow seems to behave non-linearly. The discharge measured at the outlet of the experimental aquifer rapidly deviates from the exponential behaviour predicted by the linearised Dupuit-Boussinesq equation. Instead, the discharge seems to exhibit a power law with an exponent close to -1. This exponent is reminiscent of the exponent we found in section 7 in the Plynlimon catchments. New experiments in an improved set-up, as well as further theoretical investigations, are necessary to confirm this result.

As in a fully-penetrating configuration, the early response of the two-dimensional flow to rainfall grows non-linearly with the rainfall rate. A $3/2$ power law similar to the Dupuit-Boussinesq asymptotic regime could possibly fit our experimental data. This could explain the $3/2$ power-law relationship we found in the Quiock Creek hydrograph (chapter 6). Therefore, this relationship could be the general signature of groundwater flow-dominated floods, whatever the geometry of the aquifer. However, a power law with an exponent 2 fits better our experimental data. This result is similar to our observations on the Plynlimon catchments. A quadratic relationship between the discharge increase rate of a river during a flood and the rainfall rate could therefore be the signature of two-dimensional groundwater flows, thus differentiating a fully-penetrating configuration from a deep aquifer.

All these speculations would deserve new experiments, in improved experimental conditions — particularly concerning the aquifer outlet. Furthermore, we also lack theoretical investigations. Here, we propose that the early stages of a flood could be described by an infinitely deep and infinitely large aquifer. On the contrary, if the aquifer depth is sufficiently low compared to its typical lateral extent, the Dupuit-Boussinesq theory could be matched with a two-dimensional flow close to the river. In such case, the asymptotic regimes would certainly be similar to those found in chapter 3.

Part V

Conclusion and perspectives

Chapter 9

Conclusion and perspectives

River hydrographs generally exhibit a quick discharge increase during rainfall followed by a slowly decreasing discharge. The usual interpretation of these features invokes the superimposition of a fast surface runoff on a slow groundwater baseflow (figure 9.1). In this manuscript, we have shown that the dynamics of groundwater in an unconfined aquifer may account for these features as well. In this context, we interpret a hydrograph as a series of asymptotic regimes of the groundwater flow equations (figure 9.2).

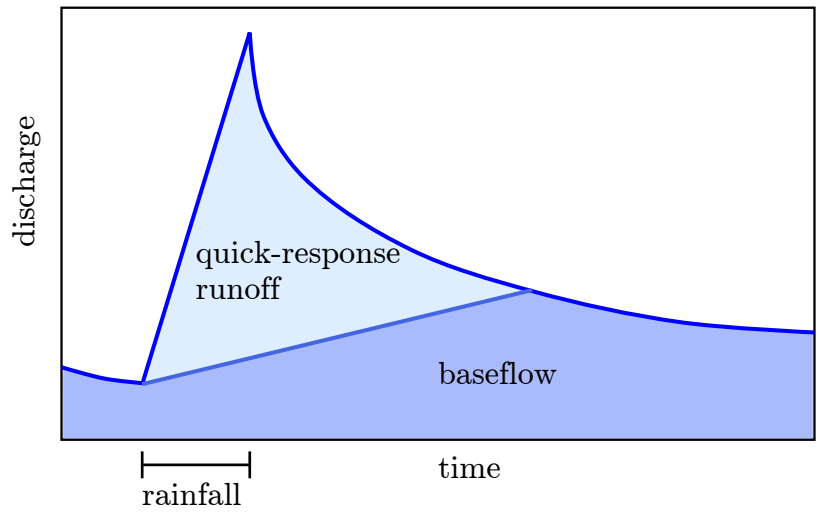

Figure 9.1: A typical flood hydrograph can be interpreted as the superimposition of the quick-response runoff on the baseflow.

The first regime, the storm flow, corresponds to the rapid discharge increase during rainfall (figure 9.2). Based on a laboratory experiment, we have shown that a homogeneous and two-dimensional aquifer submitted to artificial rainfall generates a realistic storm flow, in the absence of surface runoff. When the infiltrating rainwater reaches the water table, the latter begins to rise and causes the discharge to increase instantly. In the frame of the Dupuit-Boussinesq (shallow-water) approximation, the discharge

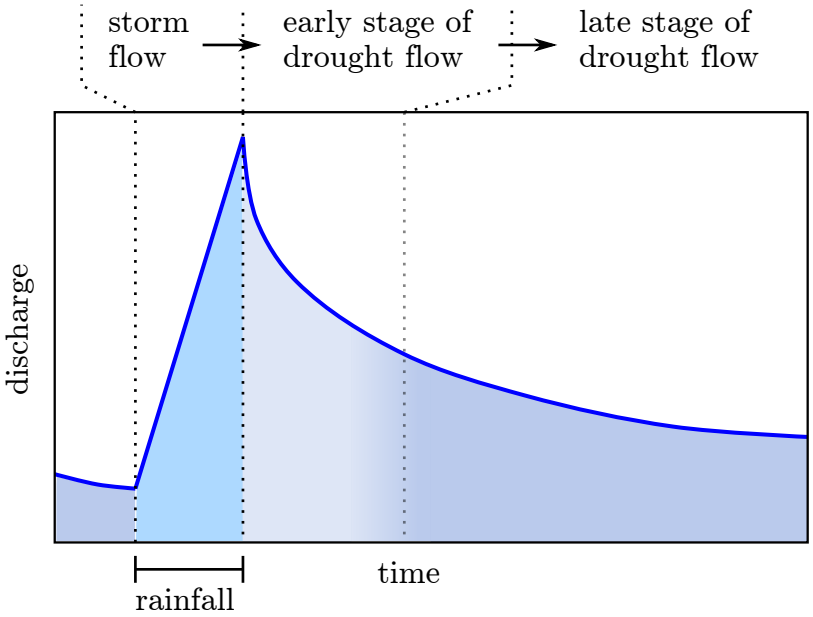

Figure 9.2: Typical flood hydrograph generated by a groundwater flow. It is a succesion of distinct asymptotic regimes of the groundwater flow.

increase rate is a non-linear function of the rainfall rate:

$$\dot{Q} \propto R^{3/2} . \tag{9.1}$$

After the rainfall has stopped, the drought flow begins, and the discharge decreases slowly. According to the Dupuit-Boussinesq theory, this relaxation involves two asymptotic regimes (figure 9.2). During the early drought flow, the discharge decreases as the inverse of the square root of time ($Q \sim 1/\sqrt{t}$). At longer times, the flow evolves towards a late drought flow regime. From then on, the discharge decreases as the inverse of the square of time ($Q \sim 1/t^2$).

To identify these regimes in nature, we designed a field experiment in the small catchment of the Quiock Creek, in Guadeloupe. High-frequency measurements show that the water table elevation and the river discharge react simultaneously and rapidly to rainfall. Plotting the discharge increase rate $\dot{Q}$ against the rainfall rate R during storm flows, we observe a power-law relationship with an exponent close to 3/2, as predicted by equation (9.1). In addition, the prefactor of equation (9.1) provides reasonable estimates of the porosity and hydraulic conductivity of the aquifer. The storm flow of the Quiock Creek is therefore compatible with the Dupuit-Boussinesq theory.

Once the rainfall has stopped, the Quiock Creek discharge decreases according to the early drought flow regime. The full Quiock Creek hydrograph can therefore be explained by the dynamics of a shallow groundwater flow equation, without invoking surface runoff.

Extending the above analysis to three other catchments, we found that they also respond non-linearly to rainfall ($\dot{Q} \propto R^n$, with $n > 1$), but with exponents n different from

3/2. This suggests a breakdown of the Dupuit-Boussinesq approximation, and points to possible vertical flow. Our preliminary experimental results with a two-dimensional laboratory aquifer also suggest a non-linear response to rainfall, with an exponent larger than one. Yet, this observation remains to be theoretically understood.

All the catchments we investigated, whether in the laboratory or in the field, respond non-linearly to the rainfall driving. We attribute this behaviour to the motion of the water table. This non-linearity has significant implications. First, in a catchment dominated by groundwater, the discharge increases more than linearly with the storm intensity (equation (9.1)), which is specially relevant to flood forecasting. Second, it precludes the use of Fourier analysis and transfer functions to investigate the response of a catchment to the rain signal.

As water travels within an aquifer, it interacts chemically with the surrounding rocks, turning them into secondary minerals. The transit time of a catchment, i.e. the time spent by water within the aquifer, thus controls chemical weathering. Yet, even in steady state and in simple aquifer geometries, there might not be any well-defined characteristic transit time (Chesnaux et al., 2005; Cardenas, 2007). We have established that, in addition, the groundwater flow can undergo dramatic variations in time. As a result, the transit time of a rain drop not only depends on the location where it enters the catchment, but also on its arrival time. This questions the very use of transit time to interpret weathering processes. Instead, we propose to couple chemical weathering with the groundwater flow.

Part VI

Appendix

Appendix A

Numerical resolution of the Laplace equation with FreeFem++

```
// define constants
real L = 673.-20.;
real H = 710-191;
real epsilon = 0.01*L;

int Npoints = 50;

// define borders
border top(t = -epsilon, -L){ x = t; y = 0.; }
border left(t = 0, -H){ x = -L; y = t; }
border bottom(t = -L, 0){ x = t; y = -H; }
border right( t = -H, -epsilon){ x = 0; y = t; }
border outlet( t = -pi/2., -pi ){ x = epsilon*cos(t); y =
   epsilon*sin(t); }

// build the mesh
mesh Th = buildmesh( top(Npoints) + left(Npoints) +
   bottom(Npoints) + right(Npoints) + outlet(Npoints) );

fespace Vh(Th,P2);

// define variables
Vh psi, ppsi;

problem Laplace( psi, ppsi ) =
        int2d(Th)( dx(psi)*dx(ppsi) + dy(psi)*dy(ppsi) )
        + on( top, psi=x )
        + on( left,bottom,right, psi=-L ) ;
```

```
// solve the problem
Laplace;
Th = adaptmesh(Th, psi);
Laplace;
Th = adaptmesh(Th, psi);
Laplace;
```

Bibliography

Abdul, A. and Gillham, R. (1984). Laboratory studies of the effects of the capillary fringe on streamflow generation. *Water Resources Research*, 20(6):691–698.

Alcamo, J., Döll, P., Henrichs, T., Kaspar, F., Lehner, B., Rösch, T., and Siebert, S. (2003). Development and testing of the watergap 2 global model of water use and availability. *Hydrological Sciences Journal*, 48(3):317–337.

Andermann, C., Longuevergne, L., Bonnet, S., Crave, A., Davy, P., and Gloaguen, R. (2012). Impact of transient groundwater storage on the discharge of himalayan rivers. *Nature Geoscience*, 5(2):127–132.

Andreotti, B., Forterre, Y., and Pouliquen, O. (2012). *Les milieux granulaires-Entre fluide et solide: Entre fluide et solide*. EDP sciences.

Appel, W. (2008). *Mathématiques pour la physique et les physiciens*. H. et K. Editions.

Aquilina, L., Ladouche, B., and Dörfliger, N. (2006). Water storage and transfer in the epikarst of karstic systems during high flow periods. *Journal of Hydrology*, 327(3):472–485.

Arneodo, A., Couder, Y., Grasseau, G., Hakim, V., and Rabaud, M. (1989). Uncovering the analytical saffman-taylor finger in unstable viscous fingering and diffusion-limited aggregation. *Physical review letters*, 63(9):984.

Badoux, A., Turowski, J., Mao, L., Mathys, N., and Rickenmann, D. (2012). Rainfall intensity–duration thresholds for bedload transport initiation in small alpine watersheds. *Natural Hazards and Earth System Science*, 12(10):3091–3108.

Banks, E. W., Simmons, C. T., Love, A. J., Cranswick, R., Werner, A. D., Bestland, E. A., Wood, M., and Wilson, T. (2009). Fractured bedrock and saprolite hydrogeologic controls on groundwater/surface-water interaction: a conceptual model (australia). *Hydrogeology Journal*, 17(8):1969–1989.

Bear, J. (1972). *Dynamics of fluids in porous media*. Dover, New York.

Bergström, S., Singh, V., et al. (1995). The hbv model. *Computer models of watershed hydrology.*, pages 443–476.

Berkowitz, B., Cortis, A., Dentz, M., and Scher, H. (2006). Modeling non-fickian transport in geological formations as a continuous time random walk. *Reviews of Geophysics*, 44(2).

Beven, K. (1981). Kinematic subsurface stormflow. *Water Resources Research*, 17(5):1419–1424.

Beven, K. and Freer, J. (2001). A dynamic topmodel. *Hydrological processes*, 15(10):1993–2011.

Booij, M. (2005). Impact of climate change on river flooding assessed with different spatial model resolutions. *Journal of hydrology*, 303(1):176–198.

Boussinesq, J. (1877). *Essai sur la théorie des eaux courantes*, volume 2. Imprimerie nationale.

Boussinesq, J. (1903). Sur un mode simple d'écoulement des nappes d'eau d'infiltration à lit horizontal, avec rebord vertical tout autour lorsqu'une partie de ce rebord est enlevée depuis la surface jusqu'au fond. *CR Acad. Sci*, 137:5–11.

Boussinesq, J. (1904). Recherches théoriques sur l'écoulement des nappes d'eau infiltrées dans le sol et sur le débit des sources. *Journal de mathématiques pures et appliquées*, pages 5–78.

Bouwer, H. (1989). The bouwer and rice slug test—an update. *Groundwater*, 27(3):304–309.

Bouwer, H. and Rice, R. (1976). A slug test for determining hydraulic conductivity of unconfined aquifers with completely or partially penetrating wells. *Water Resources Research*, 12(3):423–428.

Brandt, C., Robinson, M., and Finch, J. (2004). Anatomy of a catchment: the relation of physical attributes of the plynlimon catchments to variations in hydrology and water status. *Hydrology and Earth System Sciences Discussions*, 8(3):345–354.

Brantley, S. L. and Lebedeva, M. (2011). Learning to read the chemistry of regolith to understand the critical zone.

Bresciani, E. (2011). *Modélisation des contrôles climatiques, topographiques, géologiques et anthropiques sur les écoulements souterrains en domaine de socle*. PhD thesis, Université Rennes 1.

Bresciani, E., Davy, P., and de Dreuzy, J.-R. (2014). Is the dupuit assumption suitable for predicting the groundwater seepage area in hillslopes? *Water Resources Research*, 50(3):2394–2406.

Bresciani, E., Davy, P., and Dreuzy, J. (2012). A finite volume approach with local adaptation scheme for the simulation of free surface flow in porous media. *International Journal for Numerical and Analytical Methods in Geomechanics*, 36(13):1574–1591.

Brutsaert, W. (1968). A solution for vertical infiltration into a dry porous medium. *Water Resources Research*, 4(5):1031–1038.

Brutsaert, W. (1994). The unit response of groundwater outflow from a hillslope. *Water resources research*, 30(10):2759–2763.

Brutsaert, W. (2005). *Hydrology: an introduction*. Cambridge Univ Pr.

Brutsaert, W. and Lopez, J. (1998). Basin-scale geohydrologic drought flow features of riparian aquifers in the southern great plains. *Water Resources Research*, 34(2):233–240.

Brutsaert, W. and Nieber, J. (1977). Regionalized drought flow hydrographs from a mature glaciated plateau. *Water Resources Research*, 13(3):637–643.

Buss, H., White, A., Dessert, C., Gaillardet, J., Blum, A., and Sak, P. (2010). Depth profiles in a tropical, volcanic critical zone observatory: Basse-terre, guadeloupe. In *Proc. of the 13th Intl. Symp. on Water–Rock Interaction.*

Calder, I. (1977). A model of transpiration and interception loss from a spruce forest in plynlimon, central wales. *Journal of Hydrology*, 33(3):247–265.

Cardenas, M. B. (2007). Potential contribution of topography-driven regional groundwater flow to fractal stream chemistry: Residence time distribution analysis of tóth flow. *Geophysical Research Letters*, 34(5).

Carslaw, H. S. and Jaeger, J. C. (1959). Conduction of heat in solids. *Oxford: Clarendon Press, 1959, 2nd ed.*, 1.

Chapman, T. (1999). A comparison of algorithms for stream flow recession and baseflow separation. *Hydrological Processes*, 13(5):701–714.

Chapman, T. G. (2003). Modelling stream recession flows. *Environmental Modelling & Software*, 18(8):683–692.

Chesnaux, R., Molson, J., and Chapuis, R. (2005). An analytical solution for ground water transit time through unconfined aquifers. *Groundwater*, 43(4):511–517.

Chevigny, E. (2014). *Cartographie de la diversité des sols viticoles de versant par imagerie à haute résolution: contribution à la connaissance des terroirs.* PhD thesis, Université de Bourgogne.

Childs, E. (1971). Drainage of groundwater resting on a sloping bed. *Water Resources Research*, 7(5):1256–1263.

Clergue, C. (2015). *Apport de l'étude des isotopes du Li et du Sr à différentes échelles pour la caractérisation des cycles biogéochimiques et de l'altération chimique en milieu tropical, Exemple de la Guadeloupe.* PhD thesis, Paris 7.

Colmet-Daage, F. and Lagache, P. (1965). Caractéristiques de quelques groupes de sols dérivés de roches volcaniques aux antilles françaises. *Cahiers de l'ORSTOM serie pédologie*, 8:91–121.

Cooper, H. H., Bredehoeft, J. D., and Papadopulos, I. S. (1967). Response of a finite-diameter well to an instantaneous charge of water. *Water Resources Research*, 3(1):263–269.

Daerr, A., Eggers, J., Limat, L., and Valade, N. (2011). General mechanism for the meandering instability of rivulets of newtonian fluids. *Physical review letters*, 106(18):184501.

Dagan, G. (1967). A method of determining the permeability and effective porosity of unconfined anisotropie aquifers. *Water Resources Research*, 3(4):1059–1071.

Dannowski, G. and Yaramanci, U. (1999). Estimation of water content and porosity using combined radar and geoelectrical measurements. *Eur. J. Environ. Eng. Geophys*, 4(1):71–85.

Darbandi, M., Torabi, S., Saadat, M., Daghighi, Y., and Jarrahbashi, D. (2007). A moving-mesh finite-volume method to solve free-surface seepage problem in arbitrary geometries. *International Journal for Numerical and Analytical Methods in Geomechanics*, 31(14):1609–1629.

Darcy, H. (1856). *Les fontaines publiques de la ville de Dijon*. V. Dalmont.

Darnault, C. J. (2008). *Overexploitation and Contamination of Shared Groundwater Resources: Management,(bio) technological, and Political Approaches to Avoid Conflicts*. Springer Science & Business Media.

Davy, P., Bour, O., De Dreuzy, J.-R., and Darcel, C. (2006). Flow in multiscale fractal fracture networks. *Geological Society, London, Special Publications*, 261(1):31–45.

de Dreuzy, J.-R., Darcel, C., Davy, P., and Bour, O. (2004). Influence of spatial correlation of fracture centers on the permeability of two-dimensional fracture networks following a power law length distribution. *Water resources research*, 40(1).

de Gennes, P.-G., Brochard-Wyart, F., Quéré, D., Fermigier, M., and Clanet, C. (2002). *Gouttes, bulles, perles et ondes*. Belin Paris.

De Marsily, G. (1986). *Quantitative hydrogeology*.

Devauchelle, O., Petroff, A., Lobkovsky, A. E., and Rothman, D. H. (2011). Longitudinal profile of channels cut by springs. *Journal of Fluid Mechanics*, 667:38–47.

Devauchelle, O., Petroff, A. P., Seybold, H. F., and Rothman, D. H. (2012). Ramification of stream networks. *Proceedings of the National Academy of Sciences*, 109(51):20832–20836.

Döll, P., Kaspar, F., and Lehner, B. (2003). A global hydrological model for deriving water availability indicators: model tuning and validation. *Journal of Hydrology*, 270(1):105–134.

Dupuit, A. (1863). *Études théoriques et pratiques sur la mouvement des eaux*. Dunod, Paris.

Duvert, C., Nord, G., Gratiot, N., Navratil, O., Nadal-Romero, E., Mathys, N., Némery, J., Regüés, D., García-Ruiz, J. M., Gallart, F., et al. (2012). Towards prediction of suspended sediment yield from peak discharge in small erodible mountainous catchments (0.45–22km 2) of france, mexico and spain. *Journal of Hydrology*, 454:42–55.

Erhel, J., De Dreuzy, J.-R., and Poirriez, B. (2009). Flow simulation in three-dimensional discrete fracture networks. *SIAM Journal on Scientific Computing*, 31(4):2688–2705.

Forchheimer, P. (1901). Wasserbewegung durch boden. *Z. Ver. Deutsch. Ing*, 45(1782):1788.

Gaillardet, J., Dupré, B., Louvat, P., and Allegre, C. (1999). Global silicate weathering and co 2 consumption rates deduced from the chemistry of large rivers. *Chemical Geology*, 159(1):3–30.

Gelhar, L. W. (1986). Stochastic subsurface hydrology from theory to applications. *Water Resources Research*, 22(9S):135S–145S.

Gelhar, L. W. (1993). *Stochastic subsurface hydrology*. Prentice-Hall.

Gleick, P. H. (1996). Water resources. *Encyclopedia of climate and weather*, 2:817–823.

Goderniaux, P., Davy, P., Bresciani, E., Dreuzy, J.-R., and Borgne, T. (2013). Partitioning a regional groundwater flow system into shallow local and deep regional flow compartments. *Water Resources Research*, 49(4):2274–2286.

Godsey, S., Kirchner, J., and Clow, D. (2009). Concentration–discharge relationships reflect chemostatic characteristics of us catchments. *Hydrological Processes*, 23(13):1844–1864.

Guérin, A., Devauchelle, O., and Lajeunesse, E. (2014). Response of a laboratory aquifer to rainfall. *Journal of Fluid Mechanics*, 759:R1.

Guyon, E., Hulin, J., and Petit, L. (2001). *Hydrodynamique physique*. EDP sciences.

Haitjema, H. (1995). On the residence time distribution in idealized groundwatersheds. *Journal of Hydrology*, 172(1):127–146.

Haitjema, H. M. and Mitchell-Bruker, S. (2005). Are water tables a subdued replica of the topography? *Groundwater*, 43(6):781–786.

Halley, R. B. and Schmoker, J. W. (1983). High-porosity cenozoic carbonate rocks of south florida: progressive loss of porosity with depth. *AAPG Bulletin*, 67(2):191–200.

Harbaugh, A. W. (2005). *MODFLOW-2005, the US Geological Survey modular groundwater model: The ground-water flow process*. US Department of the Interior, US Geological Survey Reston, VA, USA.

Haria, A. H. and Shand, P. (2004). Evidence for deep sub-surface flow routing in forested upland wales: implications for contaminant transport and stream flow generation. *Hydrology and Earth System Sciences Discussions*, 8(3):334–344.

Hecht, F. (2012). New development in freefem++. *J. Numer. Math.*, 20(3-4):251–265.

Hele-Shaw, H. S. (1898). Flow of water. *Nature*, 58:520.

Henderson, F. and Wooding, R. (1964). Overland flow and groundwater flow from a steady rainfall of finite duration. *Journal of Geophysical Research*, 69(8):1531–1540.

Hewlett, J. D. and Hibbert, A. R. (1963). Moisture and energy conditions within a sloping soil mass during drainage. *Journal of Geophysical Research*, 68(4):1081–1087.

Hill, T. and Neal, C. (1997). Spatial and temporal variation in ph, alkalinity and conductivity in surface runoff and groundwater for the upper river severn catchment. *Hydrology and Earth System Sciences Discussions*, 1(3):697–715.

Huyck, A. A., Pauwels, V., and Verhoest, N. E. (2005). A base flow separation algorithm based on the linearized boussinesq equation for complex hillslopes. *Water resources research*, 41(8).

Ibrahim, H. and Brutsaert, W. (1965). Inflow hydrographs from large unconfined aquifers. *J. Irrig. Drain. Div. Am. Soc. Civ. Eng*, 91:21–38.

Jiang, X.-W., Wang, X.-S., Wan, L., and Ge, S. (2011). An analytical study on stagnation points in nested flow systems in basins with depth-decaying hydraulic conductivity. *Water Resources Research*, 47(1).

Jiménez-Martínez, J., Longuevergne, L., Borgne, T., Davy, P., Russian, A., and Bour, O. (2013). Temporal and spatial scaling of hydraulic response to recharge in fractured aquifers: Insights from a frequency domain analysis. *Water Resources Research*, 49(5):3007–3023.

Johnson, N., Likens, G., Bormann, F., Fisher, D., and Pierce, R. (1969). A working model for the variation in stream water chemistry at the hubbard brook experimental forest, new hampshire. *Water Resources Research*, 5(6):1353–1363.

Kalinski, R., Kelly, W., Bogardi, I., and Pesti, G. (1993). Electrical resistivity measurements to estimate travel times through unsaturated ground water protective layers. *Journal of Applied Geophysics*, 30(3):161–173.

Kirby, C., Newson, M. D., and Gilman, K. (1991). *Plynlimon research: the first two decades*. Institute of Hydrology Wallingford, UK.

Kirchner, J. (2003). A double paradox in catchment hydrology and geochemistry. *Hydrological Processes*, 17(4):871–874.

Kirchner, J. (2009). Catchments as simple dynamical systems: Catchment characterization, rainfall-runoff modeling, and doing hydrology backward. *Water Resources Research*, 45(2):W02429.

Kirchner, J., Feng, X., Neal, C., et al. (2000). Fractal stream chemistry and its implications for contaminant transport in catchments. *Nature*, 403(6769):524–527.

Kirchner, J. W., Feng, X., and Neal, C. (2001). Catchment-scale advection and dispersion as a mechanism for fractal scaling in stream tracer concentrations. *Journal of Hydrology*, 254(1):82–101.

Kreft, A. and Zuber, A. (1978). On the physical meaning of the dispersion equation and its solutions for different initial and boundary conditions. *Chemical Engineering Science*, 33(11):1471–1480.

Lajeunesse, E. and Couder, Y. (2000). On the tip-splitting instability of viscous fingers. *Journal of fluid mechanics*, 419:125–149.

Le Borgne, T., Bour, O., De Dreuzy, J., Davy, P., and Touchard, F. (2004). Equivalent mean flow models for fractured aquifers: Insights from a pumping tests scaling interpretation. *Water Resources Research*, 40(3).

Le Borgne, T., Bour, O., Paillet, F., and Caudal, J.-P. (2006a). Assessment of preferential flow path connectivity and hydraulic properties at single-borehole and cross-borehole scales in a fractured aquifer. *Journal of Hydrology*, 328(1):347–359.

Le Borgne, T., Dentz, M., and Carrera, J. (2008). Lagrangian statistical model for transport in highly heterogeneous velocity fields. *Physical review letters*, 101(9):090601.

Le Borgne, T., Paillet, F., Bour, O., and Caudal, J.-P. (2006b). Cross-borehole flowmeter tests for transient heads in heterogeneous aquifers. *Groundwater*, 44(3):444–452.

Le Goc, R. (2009). *Caractérisation et modélisation des écoulements dans les milieux fracturés*. PhD thesis, Université Rennes 1.

Le Grand, N., Daerr, A., and Limat, L. (2005). Shape and motion of drops sliding down an inclined plane. *Journal of Fluid Mechanics*, 541:293–315.

Le Maitre, D. C., Scott, D. F., and Colvin, C. (1999). Review of information on interactions between vegetation and groundwater.

Lindström, G., Johansson, B., Persson, M., Gardelin, M., and Bergström, S. (1997). Development and test of the distributed hbv-96 hydrological model. *Journal of hydrology*, 201(1):272–288.

Lloret, E. (2010). *Dynamique du carbone organique dans des petits bassins versants tropicaux : exemple de la Guadeloupe*. PhD thesis, Paris 7.

Lloret, E., Dessert, C., Pastor, L., Lajeunesse, E., Crispi, O., Gaillardet, J., and Benedetti, M. (2013). Dynamic of particulate and dissolved organic carbon in small volcanic mountainous tropical watersheds. *Chemical Geology*, 351:229–244.

Loke, M. (1999). Electrical imaging surveys for environmental and engineering studies. *A practical guide to*, 2.

Long, J., Remer, J., Wilson, C., and Witherspoon, P. (1982). Porous media equivalents for networks of discontinuous fractures. *Water Resources Research*, 18(3):645–658.

Maher, K. (2010). The dependence of chemical weathering rates on fluid residence time. *Earth and Planetary Science Letters*, 294(1):101–110.

Maher, K. and Chamberlain, C. (2014). Hydrologic regulation of chemical weathering and the geologic carbon cycle. *science*, 343(6178):1502–1504.

Małoszewski, P. and Zuber, A. (1982). Determining the turnover time of groundwater systems with the aid of environmental tracers: 1. models and their applicability. *Journal of hydrology*, 57(3):207–231.

Malvicini, C. F., Steenhuis, T. S., Walter, M. T., Parlange, J.-Y., and Walter, M. F. (2005). Evaluation of spring flow in the uplands of matalom, leyte, philippines. *Advances in water resources*, 28(10):1083–1090.

Maquaire, O., Ritzenthaler, A., Fabre, D., Ambroise, B., Thiery, Y., Truchet, E., Malet, J.-P., and Monnet, J. (2002). Caractérisation des profils de formations superficielles par pénétrométrie dynamique à énergie variable: application aux marnes noires de draix (alpes-de-haute-provence, france). *Comptes Rendus Geoscience*, 334(11):835–841.

Marc, V. and Robinson, M. (2007). The long-term water balance (1972–2004) of upland forestry and grassland at plynlimon, mid-wales. *Hydrology and Earth System Sciences*, 11(1):44–60.

Marchand, A., Weijs, J. H., Snoeijer, J. H., and Andreotti, B. (2011). Why is surface tension a force parallel to the interface? *American Journal of Physics*, 79(10):999–1008.

McDonnell, J. (1990). A rationale for old water discharge through macropores in a steep, humid catchment. *Water Resources Research*, 26(11):2821–2832.

McDonnell, J. J. (2003). Where does water go when it rains? moving beyond the variable source area concept of rainfall-runoff response. *Hydrological processes*, 17(9):1869–1875.

McDonnell, J. J., McGuire, K., Aggarwal, P., Beven, K. J., Biondi, D., Destouni, G., Dunn, S., James, A., Kirchner, J., Kraft, P., et al. (2010). How old is streamwater? open questions in catchment transit time conceptualization, modelling and analysis. *Hydrological Processes*, 24(12):1745–1754.

McGuire, K., McDonnell, J. J., Weiler, M., Kendall, C., McGlynn, B., Welker, J., and Seibert, J. (2005). The role of topography on catchment-scale water residence time. *Water Resources Research*, 41(5).

McGuire, K. J. and McDonnell, J. J. (2006). A review and evaluation of catchment transit time modeling. *Journal of Hydrology*, 330(3):543–563.

Molenat, J., Davy, P., Gascuel-Odoux, C., and Durand, P. (1999). Study of three subsurface hydrologic systems based on spectral and cross-spectral analysis of time series. *Journal of Hydrology*, 222(1):152–164.

Naff, R. L. and Banta, E. R. (2008). The us geological survey modular ground-water model-pcgn: a preconditioned conjugate gradient solver with improved nonlinear control. Technical report, Geological Survey (US).

Naumburg, E., Mata-Gonzalez, R., Hunter, R. G., Mclendon, T., and Martin, D. W. (2005). Phreatophytic vegetation and groundwater fluctuations: a review of current research and application of ecosystem response modeling with an emphasis on great basin vegetation. *Environmental Management*, 35(6):726–740.

Neal, C. (1997). A view of water quality from the plynlimon watershed. *Hydrology and Earth System Sciences Discussions*, 1(3):743–753.

Neal, C., Robson, A., Shand, P., Edmunds, W., Dixon, A., Buckley, D., Hill, S., Harrow, M., Neal, M., Wilkinson, J., et al. (1997a). The occurrence of groundwater in the lower palaeozoic rocks of upland central wales. *Hydrology and Earth System Sciences Discussions*, 1(1):3–18.

Neal, C. and Rosier, P. (1990). Chemical studies of chloride and stable oxygen isotopes in two conifer afforested and moorland sites in the british uplands. *Journal of Hydrology*, 115(1):269–283.

Neal, C., Wilkinson, J., Neal, M., Harrow, M., Wickham, H., Hill, L., and Morfitt, C. (1997b). The hydrochemistry of the headwaters of the river severn, plynlimon. *Hydrology and Earth System Sciences Discussions*, 1(3):583–617.

Neuman, S. P., Walter, G. R., Bentley, H. W., Ward, J. J., and Gonzalez, D. D. (1984). Determination of horizontal aquifer anisotropy with three wells. *Groundwater*, 22(1):66–72.

Nieber, J. and Walter, M. (1981). Two-dimensional soil moisture flow in a sloping rectangular region: Experimental and numerical studies. *Water Resources Research*, 17(6):1722–1730.

Parlange, J.-Y. and Brutsaert, W. (1987). A capillarity correction for free surface flow of groundwater. *Water Resources Research*, 23(5):805–808.

Pauwels, V. and Troch, P. A. (2010). Estimation of aquifer lower layer hydraulic conductivity values through base flow hydrograph rising limb analysis. *Water resources research*, 46(3).

Petroff, A. P., Devauchelle, O., Abrams, D., Lobkovsky, A., Kudrolli, A., and Rothman, D. (2011). Geometry of valley growth. *Journal of Fluid Mechanics*, 673(245-254):6.

Petroff, A. P., Devauchelle, O., Seybold, H., and Rothman, D. H. (2013). Bifurcation dynamics of natural drainage networks. *Philosophical Transactions of the Royal Society A: Mathematical, Physical and Engineering Sciences*, 371(2004):20120365.

Polubarinova-Kochina, P. (1962). Theory of ground water movement princeton university press. *Princeton, NJ*.

Renard, P. and De Marsily, G. (1997). Calculating equivalent permeability: a review. *Advances in Water Resources*, 20(5):253–278.

Richards, L. A. (1931). Capillary conduction of liquids through porous mediums. *Journal of Applied Physics*, 1(5):318–333.

Rotaru, M., Gaillardet, J., Steinberg, M., and Trichet, J. (2006). *Les climats passés de la Terre*. Vuibert.

Rupp, D. E. and Selker, J. S. (2006a). Information, artifacts, and noise in dq/dt- q recession analysis. *Advances in water resources*, 29(2):154–160.

Rupp, D. E. and Selker, J. S. (2006b). On the use of the boussinesq equation for interpreting recession hydrographs from sloping aquifers. *Water resources research*, 42(12).

Saez, J. L., Corona, C., Stoffel, M., Rovéra, G., Astrade, L., and Berger, F. (2011). Mapping of erosion rates in marly badlands based on a coupling of anatomical changes in exposed roots with slope maps derived from lidar data. *Earth Surface Processes and Landforms*, 36(9):1162–1171.

Saffman, P. G. and Taylor, G. (1958). The penetration of a fluid into a porous medium or hele-shaw cell containing a more viscous liquid. *Proceedings of the Royal Society of London. Series A. Mathematical and Physical Sciences*, 245(1242):312–329.

Samouëlian, A., Cousin, I., Tabbagh, A., Bruand, A., and Richard, G. (2005). Electrical resistivity survey in soil science: a review. *Soil and Tillage research*, 83(2):173–193.

Sanford, W., Parlange, J., and Steenhuis, T. (1993). Hillslope drainage with sudden drawdown: Closed form solution and laboratory experiments. *Water resources research*, 29(7):2313–2321.

Shand, P., Haria, A., Neal, C., Griffiths, K., Gooddy, D., Dixon, A., Hill, T., Buckley, D., and Cunningham, J. (2005). Hydrochemical heterogeneity in an upland catchment: further characterisation of the spatial, temporal and depth variations in soils, streams and groundwaters of the plynlimon forested catchment, wales. *Hydrology and Earth System Sciences*, 9(6):621–644.

Sloan, W. (2000). A physics-based function for modeling transient groundwater discharge at the watershed scale. *Water Resources Research*, 36(1):225–241.

Snoeijer, J. H. and Andreotti, B. (2013). Moving contact lines: scales, regimes, and dynamical transitions. *Annual review of fluid mechanics*, 45:269–292.

Sophocleous, M. (2002). Interactions between groundwater and surface water: the state of the science. *Hydrogeology journal*, 10(1):52–67.

Şorman, A. A., Şensoy, A., Tekeli, A., Şorman, A., and Akyürek, Z. (2009). Modelling and forecasting snowmelt runoff process using the hbv model in the eastern part of turkey. *Hydrological processes*, 23(7):1031–1040.

Szilagyi, J. and Parlange, M. (1998). Baseflow separation based on analytical solutions of the boussinesq equation. *Journal of Hydrology*, 204(1):251–260.

Tallaksen, L. (1995). A review of baseflow recession analysis. *Journal of hydrology*, 165(1):349–370.

Theis, C. V. (1935). *The relation between the lowering of the piezometric surface and the rate and duration of discharge of a well using ground water storage*. US Department of the Interior, Geological Survey, Water Resources Division, Ground Water Branch Washington, DC.

Todd, D. K. (1954). Unsteady flow in porous media by means of a hele-shaw viscous fluid model. *Eos, Transactions American Geophysical Union*, 35(6):905–916.

Toth, J. (1963). A theoretical analysis of groundwater flow in small drainage basins. *Journal of geophysical research*, 68(16):4795–4812.

Trinchero, P., Beckie, R., Sanchez-Vila, X., and Nichol, C. (2011). Assessing preferential flow through an unsaturated waste rock pile using spectral analysis. *Water Resources Research*, 47(7).

Troch, P. A., Berne, A., Bogaart, P., Harman, C., Hilberts, A. G., Lyon, S. W., Paniconi, C., Pauwels, V., Rupp, D. E., Selker, J. S., et al. (2013). The importance of hydraulic groundwater theory in catchment hydrology: The legacy of wilfried brutsaert and jean-yves parlange. *Water Resources Research*, 49(9):5099–5116.

Troch, P. A., De Troch, F. P., and Brutsaert, W. (1993). Effective water table depth to describe initial conditions prior to storm rainfall in humid regions. *Water Resources Research*, 29(2):427–434.

Van Genuchten, M. T. and Wierenga, P. (1976). Mass transfer studies in sorbing porous media i. analytical solutions. *Soil Science Society of America Journal*, 40(4):473–480.

Van Genuchten, M. T. and Wierenga, P. (1977). Mass transfer studies in sorbing porous media: Ii. experimental evaluation with tritium (3h2o). *Soil Science Society of America Journal*, 41(2):272–278.

Wittenberg, H. (1994). Nonlinear analysis of flow recession curves. *IAHS Publications-Series of Proceedings and Reports-Intern Assoc Hydrological Sciences*, 221:61–68.

Woessner, W. W. (2000). Stream and fluvial plain ground water interactions: rescaling hydrogeologic thought. *Groundwater*, 38(3):423–429.

Younes, A., Ackerer, P., and Delay, F. (2010). Mixed finite elements for solving 2-d diffusion-type equations. *Reviews of Geophysics*, 48(1).

Zecharias, Y. B. and Brutsaert, W. (1988). Recession characteristics of groundwater outflow and base flow from mountainous watersheds. *Water Resources Research*, 24(10):1651–1658.

Zhukovsky, N. (1920). Seepage through dams. *Collected works*, 5:297–332.

Zijl, W. (1999). Scale aspects of groundwater flow and transport systems. *Hydrogeology Journal*, 7(1):139–150.

Résumé

L'évolution du débit d'une rivière présente généralement des épisodes de crue intenses, au cours desquels le débit augmente rapidement, suivis par une diminution lente du débit lorsque la pluie s'arrête. Dans ce manuscrit, nous montrons que l'écoulement souterrain dans un aquifère non confiné permet de comprendre cette dynamique.

Dans le cadre de l'approximation de Dupuit-Boussinesq (eau peu profonde), la vitesse de montée de crue $\dot{Q}$ est une fonction non-linéaire du taux de précipitations R : $\dot{Q} \propto R^{3/2}$. Après la pluie, on distingue deux régimes asymptotiques de décrue. Au début de la décrue, le débit décroît proportionnellement à l'inverse de la racine du temps ($Q \propto 1/\sqrt{t}$ (Polubarinova-Kochina, 1962)). En fin de décrue, le débit décroît comme l'inverse du temps au carré ($Q \propto 1/t^2$ (Boussinesq, 1903)).

L'étude d'un aquifère de laboratoire soumis à une pluie artificielle confirme l'existence de ces régimes asymptotiques. Ce dispositif expérimental simplifié (aquifère homogène et bidimensionnel) génère des montées de crue réalistes, en l'absence de ruissellement.

L'instrumentation d'un site de terrain dans le bassin versant de la Ravine Quiock, sur l'île de Basse-Terre en Guadeloupe, révèle un comportement similaire. La surface de la nappe phréatique et le débit de la rivière évoluent simultanément pendant la pluie, et se conforment aux prédictions théoriques. Comme dans l'expérience de laboratoire, cet aquifère réagit donc non-linéairement au forçage induit par les précipitations.

L'analyse de données acquises dans trois autres bassins versants (Plynlimon, Pays de Galles, et Laval, France) confirme le caractère non-linéaire de la réponse d'un aquifère à la pluie : $\dot{Q} \propto R^n$, avec $n > 1$. Cependant, l'exposant n obtenu est différent de 3/2. Une expérience préliminaire en laboratoire suggère que cet écart à la théorie de Dupuit-Boussinesq pourrait être induit par l'écoulement vertical dans l'aquifère.

Abstract

River hydrographs generally exhibit intense flood events during which the discharge increases quickly during rainfall, and decreases slowly afterwards. In this manuscript, we show that the dynamics of groundwater in an unconfined aquifer can account for these features.

In the frame of the Dupuit-Boussinesq (shallow-water) approximation, the discharge increase rate $\dot{Q}$ is a non-linear function of the rainfall rate R: $\dot{Q} \propto R^{3/2}$. After the rain, two consecutive asymptotic regimes compose the drought flow. During the early drought flow, the discharge decreases as the inverse square root of time ($Q \sim 1/\sqrt{t}$ (Polubarinova-Kochina (1962)). Later, the discharge decreases as the inverse square of time ($Q \sim 1/t^2$ (Boussinesq, 1903)).

A laboratory aquifer (homogeneous and bidimensional) submitted to artificial rainfall confirms the existence of these asymptotic regimes. This simplified experimental setup generates a realistic flood signal, in the absence of surface runoff.

Field observation in the catchment of the Quiock Creek, Guadeloupe reveals a similar behaviour. The water table and the river discharge evolve simultaneously during rainfall, and conform to theory. Like in our laboratory experiment, this aquifer reacts non-linearly to forcing by rainfall.

The river discharge from three other catchments (Plynlimon, Wales and Laval, France) confirms this non-linear reaction: $\dot{Q} \propto R^n$, with $n > 1$. The exponent, however, is different from 3/2. A preliminary laboratory experiment suggests that this breakdown of the Dupuit-Boussinesq theory is due to vertical groundwater flow.